Simplified model for the d.c. planar magnetron discharge

Guy Buyle

Proefschrift voorgelegd tot het behalen van de graad van
Doctor in de Wetenschappen: Natuurkunde

Promotor: Prof. Dr. ir. R. De Gryse

Copromotor: Prof. Dr. D. Depla

December 2005

Simplified model for the d.c. planar magnetron discharge

Guy Buyle

Proefschrift voorgelegd tot het behalen van de graad van
Doctor in de Wetenschappen: Natuurkunde

Promotor: Prof. Dr. ir. R. De Gryse

Copromotor: Prof. Dr. D. Depla

December 2005

"Seeing what everyone else has seen
and thinking what no one else has thought."

Albert Szent-Gyorgi

Aan Karin, Johanna en Frank.

Dankwoord

Uiteraard zou dit werk nooit zijn geworden wat het is zonder de steun en hulp van een heleboel mensen.

Vooreerst dank ik oprecht mijn promotor, Prof. De Gryse. Naast alle dingen die van een promotor verwacht kunnen worden, heeft hij me nog iets extra gegeven wat uiterst zeldzaam aan het worden is: de tijd en de vrijheid om mijn ding te doen.

Uiteraard ook dank aan mijn copromotor, officieel Prof. Depla maar eigenlijk gewoon Diederik. Naast, weerom, de dank voor alle dingen die men logischer wijze kan verwachten van een copromotor nog twee "directe" uitspringers: zijn directe beschikbaarheid en zijn directe mening.

Iemand die ik ook speciaal wil bedanken is "Jo" (officieel Ereprof. J. Haemers): de mix van zijn eeuwige aanwezigheid, zijn experimentele avonturen, zijn plagerigheid en zijn bezorgdheid maakte mijn tijd doorgebracht op de S1, zowel tijdens als na de "kantooruren", meer dan aangenaam. Hij en/of Diederik vormden bovendien het ideale klankbord: een onnoemelijk aantal verheven modellen en theorieën i.v.m. de magnetronontlading zijn, gelukkig voor mijn geloofwaardigheid, nooit verder geraakt dan hun bureau.

In de aanvangsperiode van mijn doctoraat was de inbreng van Dr. De Bosscher van cruciaal belang. Ook al verwaterde dit later door zijn drukke agenda, toch bleef ik op kritieke momenten op zijn steun kunnen rekenen. Hij is het die me "de juiste filosofie" bijbracht voor dit werk. Bovendien is hij de "aanstoker van alles": dit doctoraat was een logisch vervolg op het eindejaarswerk dat ik maakte onder zijn begeleiding.

Verder wil ik ook "de collega's" van de S1 bedanken, zowel voor de praktische hulp bij mijn (schaarse) experimentele ondernemingen, het luisterende oor als voor de leuke werkatmosfeer. Heel in het bijzonder wil ik Mevr. Van Nevel (Nadine) vermelden: haar "kwiekheid" en motivatie maakten de "administratieve dinges" een stuk aangenamer.

Tenslotte wil ik nog speciaal mijn ouders bedanken (die altijd bereid waren om te luisteren naar en zich in te leven in wat hun zoon nu weer kwam vertellen) en natuurlijk ook Karin: *in critical times you managed the family in such a way that the kids and you felt like a wonderful support.*

Guy Buyle

Gent, oktober 2005.

Acknowledgement

This research was financed with a grant from the Institute for the Promotion of Innovation by Science and Technology in Flanders (IWT).

Table Of Contents

Introduction....1

List of Acronyms....5

Part I....7

1 FUNDAMENTAL ASPECTS OF THE MAGNETRON DISCHARGE....9

1.1 Overview of the magnetron sputter process....9

1.2 Different processes in the magnetron discharge....13

1.2.1 Processes in the plasma....13

1.2.2 Interactions with surfaces....19

1.3 Typical discharge characteristics....25

1.3.1 Erosion profile....25

1.3.2 Discharge voltage....27

1.3.3 Cathode sheath....28

1.3.4 Current-voltage characteristic....37

1.3.5 Bulk plasma characteristics....41

1.3.6 Electron transport....48

1.4 Influence of the external parameters....53

1.4.1 Magnetic field....53

1.4.2 Gas pressure....56

1.4.3 Electrical power input....58

1.4.4 Target material....61

1.4.5 Discharge gas....62

1.4.6 Anode....64

1.5 Conclusions....66

2 MODELLING OF THE MAGNETRON DISCHARGE 67
2.1 Modelling magnetron sputter deposition 67
2.1.1 The magnetic field 68
2.1.2 The magnetron discharge 69
2.1.3 The particle-target interaction 69
2.1.4 Particle transport in the gas phase 70
2.1.5 Film growth on the substrate 71
2.2 Magnetron discharge simulation models 72
2.2.1 Particle-In-Cell Monte Carlo method 73
2.2.2 Monte Carlo method 75
2.2.3 Kinetic model 77
2.2.4 Fluid model 78
2.2.5 Hybrid model 79
2.2.6 Simplified models 81
2.3 Challenges related to MD modelling 82
2.3.1 SE yield 82
2.3.2 Recapture 82
2.3.3 Electron mobility 83
2.3.4 Modelling "industrially relevant" magnetron discharges 83
2.4 Conclusion: simplified model for the magnetron discharge 85

Part II 87

1 RECAPTURE OF SECONDARY ELECTRONS 89

1.1 Introduction 89

1.2 Model 90

1.2.1 Magnetron model 90

1.2.2 Initial starting conditions of the SE 91

1.2.3 Solving the Lorentz equation 92

1.2.4 Electron interactions 94

1.2.5 MC model 94

1.2.6 Analytical model 95

1.2.7 The average EGIP <*f*> 97

1.3 Results and discussion 97

1.3.1 Verifying the model 98

1.3.2 Influence of the initial starting conditions of the electron 101

1.3.3 Influence of the reflection coefficient R 103

1.3.4 Influence of the gas pressure 104

1.3.5 Influence of the magnetic field 104

1.3.6 Influence of the electric field 105

1.4 Conclusion 107

2 IONISATION MODEL 109
2.1 Introduction 109
2.2 Concept of thin and thick sheath and individual sheath 111
2.3 Thin sheath ionisation model 112
2.3.1 Determination of the arches A_i 113
2.3.2 Modelling of the transfer of HEE among arches 115
2.3.3 Deduction of the HEE-density H 117
2.3.4 Deduction of the ionisation distribution 119
2.4 Thick sheath ionisation model 120
2.4.1 Determination of the arches 121
2.4.2 Modelling of the transfer of HEE among arches 126
2.4.3 Deduction of the HEE-density H 128
2.5 MC model 130
2.6 Results and discussion 133
2.6.1 Determination of W and f_{ion} 133
2.6.2 AIM: example of the different arch types 134
2.6.3 Multiplication factor m and ionisation distribution I 135
2.6.4 MIM: Influence of the scattering angle 142
2.6.5 MIM: Comparison of relative ionisation and excitation distribution 143
2.7 Conclusions 144

3 SELF-CONSISTENT MODEL 147
3.1 Introduction 147
3.2 Model 147
3.2.1 Ion bombardment of the target 148
3.2.2 Deduction of the steady state emission profile r_{SS} 149
3.2.3 Steady state emission profile taking into account recapture 150
3.2.4 Principle of the self-consistent model 151
3.2.5 Practical self-consistent model 152
3.3 Results and discussion 154
3.3.1 Verifying independence of initial conditions 154
3.3.2 Discharge properties for a given configuration 156
3.3.3 Extended Thornton relation for the discharge voltage 158
3.3.4 Basic result for simulating dependences 160
3.3.5 Influence of γ and R on the self-consistent gas pressure 161
3.4 Conclusions 163

4 DISCHARGE CURRENT CALCULATION 165
4.1 Introduction 165
4.2 Model 165
4.2.1 Discharge current based on the ion flux at the target 165
4.2.2 Individual ion motion 166
4.2.3 Model for discharge current 167
4.3 Results and discussion 178
4.3.1 Understanding the IV characteristic 178
4.3.2 Pressure dependence of the MD 182
4.3.3 Influence of γ and R on the IV characteristic 184
4.3.4 Pressure dependence of the IV characteristic 186
4.3.5 Magnetic field dependence of the IV characteristic 187
4.4 Conclusions 189

5 MAGNETIC FIELD DEPENDENCE OF THE CYLINDRICAL MAGNETRON DISCHARGE....191

5.1 Introduction....191

5.2 Experimental results....192

5.3 Discussion: explanation by recapture?....193

5.4 Extension of the MC model....196

5.4.1 Bohm diffusion....196

5.4.2 Coulomb collisions....197

5.5 Results and discussion....198

5.5.1 General influence of Bohm diffusion....198

5.5.2 General influence of Coulomb collisions....199

5.5.3 Application to the experimental results....200

5.6 Conclusions....201

6 INFLUENCE OF BOHM DIFFUSION AND VALIDATION OF THE MODEL....203

6.1 Introduction....203

6.2 Model....203

6.3 Influence of Bohm diffusion: results and discussion....205

6.3.1 Influence of the Bohm diffusion collision frequency....205

6.3.2 Influence of Bohm diffusion on the pressure dependence of the MD....209

6.3.3 Conclusion....212

6.4 Comparison of simulations with experiments....212

6.4.1 Experimental conditions....212

6.4.2 Optimising the accuracy of the model....214

6.4.3 Comparison of the simulation and experimental results....215

6.5 Conclusions....224

Summary....227

Nederlandse samenvatting....233

Appendix: Magnetic Field Calculation....239

Publications and Conference Contributions....243

References....247

Introduction

The magnetron discharge

Magnetron sputtering is a deposition technique that enables the production of coatings with unique properties in an economically and ecologically sound way. As such, it has become the established process of choice for the deposition of a wide range of industrially important coatings, e.g. hard, wear-resistant, low friction or corrosion-resistant coatings or even coatings with specific optical or electrical properties [Kelly00].

This deposition technique is based on the generation of a magnetically enhanced gas discharge at reduced pressure, which will further be referred to as magnetron discharge. Note the distinction between the magnetron sputter deposition process and the magnetron discharge (MD) itself.

Although MD research is stimulated (financially) by its industrial relevance, the MD on itself is also scientifically attractive. Here a plasma interacting with a magnetic field is concerned. This can lead to very complex behaviour, as also shown by the problems encountered in the plasma confinement needed for nuclear fusion.

Objective

The aim of the presented work is to obtain a fundamental understanding of the MD, i.e. the identification and modelling of the processes crucial for the generic MD behaviour. A first reaction might be to investigate the MD experimentally to reach this goal. However, a wealth of experimental data already exists. Moreover, most of these experimental measurements are accompanied by models and possible theories for their explanation. Unfortunately, the vast majority of these seem only valid for the accompanying experimental results, i.e. they lack general validity. Hence, at second thoughts, a better strategy seems to be the analysis of the already existing wealth of experimental measurements and proposed theories and to distil the generic magnetron discharge behaviour from them.

If the different processes are identified, they can be modelled, i.e. they are described in mathematical terms. The collection of these models should lead to a self-consistent model for the MD that is able to reproduce the MD behaviour. When this reproducing is so calculation intensive that it requires a computer, it is usually referred to as a simulating. Through simulation one can study the response of the model to stimuli. This is not the same as an experiment where the response of the physical device to stimuli is investigated. As a result there will always be a difference between the simulation results and the experiments. Consequently, an important aspect of each model is its accuracy. One should also take into account that a model is only valid within certain boundaries: it never includes "all the physics" but only the physics relevant for the investigated process or technique. This implies that for each model one should consider its applicability.

A wide variety of processes occurs in a MD: as well typical plasma processes, particle-particle interactions as solid-particle interactions occur. Moreover, the range of as well the energy as the time scale of the different processes is large. This effect is enhanced by the large range of operating conditions: as well current density, as gas pressure and even the magnetic field strength can vary over an order of magnitude. This turns the modelling of the MD into an interesting but challenging effort.

Even when using what is considered now a powerful personal computer, the range of length and time scales increases the required computation time of very accurate MD

simulations (up to several days). Consequently, a simplified model is preferred. This choice is enhanced by the fact that a simplified model is often more appropriate to get a global overview of the most relevant processes (see citation from [Anderson78] in section I.2.4zzg).

To come to a simplified model, simplifications need to be made. In practice this means that processes and aspects are neglected, accounted for or nurtured. The latter means they are accounted for very accurately. However, as the exact importance of the different processes and aspects is difficult to assess, different people will find different processes important. Bluntly stated, everybody has his own "personal simplified model" of the magnetron discharge. This is an example of the theory that each individual looks at the world using his or her own framework [Goleman98]. Hence, by proposing a simplified model, the developers' judgement of the importance of processes or aspects will inevitably lead to discussion. Fortunately, an outcome to this is the direct confrontation of the simulation results with experiments.

As mentioned before, it is important to discuss the accuracy and applicability of a model. This is especially true for a simplified model. If one wants a simplified model to reproduce the generic behaviour, it is clear that the peculiarities of an individual situation might not be reproduced very accurately. Hence, the emphasis of the simplified model will be on the reproduction of general dependences. In the MD, the most important of these are the influence of the electrical power, of the magnetic field and of the gas pressure. In practice, magnetron sputter deposition occurs using pulsed discharges, reactive discharges, r.f. driven discharges, ... However, the simplified model discussed here is only meant to be applicable to the most basic form of magnetron sputtering: d.c. planar magnetron sputtering using a balanced magnetron.

Some guidelines to the text

The structure of this thesis follows the above discussed approach. Part I is dedicated to the analysis of existing data and theories. It gives a (non-exhaustive) overview of existing literature of the MD (Chapter 1) and also discusses the different methods used to model and simulate it (Chapter 2). Part II concerns the simplified model and its results. The development of the simplified model is given step by step. Per step, the most relevant results are given. The first step is the calculation of the recapture of secondary electrons (Chapter 1). The second step deals with the ionisation distribution of a secondary electron (Chapter 2). The combination of these two steps leads to a self-consistent model for the MD (Chapter 3). This self-consistent model is extended with a model for the discharge current (Chapter 4). Then a side step is made to the cylindrical MD (Chapter 5). Finally, Bohm diffusion is included in the simplified model and simulation and experimental results are compared (Chapter 6). At the end, the main conclusions and some suggestions for further modelling are phrased. Also a short summary in Dutch is provided.

In the MD the discharge voltage V_d is a negative value. However, when using the symbol V_d in mathematical expressions, it is common to "forget" its sign. For the sake of consistency and ease of notation, the discharge voltages are always treated as positive values in this work. For example, when it is mentioned that "the discharge voltage V_d increases", it actually means that the absolute value of V_d increases. It is stressed again that in reality, these values are negative.

Throughout the text, several acronyms are used, e.g. SE (Secondary Electron), HEE (High Energy Electron),... All these acronyms are used for both the singular and plural form, e.g. "*A SE is emitted from the target ...*" but also "*The SE are recaptured because...*". The reason is that some of these acronyms are used with sub- or superscripts, e.g. HEE^{SI}, which

makes the addition of the plural *s* not so evident. The only exception is the abbreviation for the current-voltage characteristic (IV), for which a plural *s* is added.

In principle, the gas pressure should be expressed in Pascal (Pa). However, it is also very common to use milliTorr (mTorr) in magnetron sputtering. The relationship between the two is: 1mTorr = 0.133 Pa. In this work, own results are always expressed in Pascal but for referencing the pressure unit of the reference is kept.

A similar unit problem exists for the magnetic field strengths: the official unit is Tesla (T) but the most commonly used unit is Gauss (G) as it is much more convenient. The relation is $1\ T = 10^4\ G$. For the units of the magnetic field strength, we followed the typical convention in magnetron sputtering: the field strengths are expressed in Gauss and the magnet strengths in Tesla.

Sometimes, at the beginning of a subsection, a text is printed in a different font type. This text gives a short summary of the subsection.

List Of Acronyms

AIM	Analytic Ionisation Model
BDC	Bohm Diffusion Collisions
BE	Bulk Electron
CC	Coulomb Collisions
CMD	Cylindrical Magnetron Discharge
d.c.	direct current
EGIP	Effective Gas Interaction Probability
HEE	High Energy Electron
HEE^{ta}	HEE that originate from the target, i.e. accelerated SE
HEE^{SI}	HEE that originates from SI
FWHM	Full Width at Half Maximum
ID	Ionisation Degree
IM	Ionisation Model
IS	Individual Sheath
IS^{K}	Individual Sheath that is considered thicK
IS^{N}	Individual Sheath that is considered thiN
IS^{T}	Individual Sheath that is in the Transition region, i.e. between a IS^{K} and IS^{N}
IV	Current - Voltage characteristic
MC	Monte Carlo
MD	Magnetron Discharge
MDP	Magnetron Discharge Properties
MIM	MC Ionisation Model
PIC-MC	Particle-In-Cell Monte Carlo
r.f.	radio-frequency
SC	Self-Consistent
SCM	Self-Consistent Model
SE	Secondary Electron
SI	Sheath Ionisation
SS	Steady State

PART I

1 FUNDAMENTAL ASPECTS OF THE MAGNETRON DISCHARGE

This chapter describes the magnetron discharge (MD): first a general description of the MD is given (section 1.1), the second part focuses on the separate processes that occur in the discharge (section 1.2). Of these, only the ones relevant for the remaining part of the thesis are discussed in more detail. The third part of the chapter describes some of the typical characteristics of the MD (section 1.3). The chapter ends with a discussion of the influence of the external parameters on the MD characteristics (section 1.4).

1.1 Overview of the magnetron sputter process

Magnetron sputtering is based on the generation of a magnetically enhanced glow discharge in vacuum. When a sufficiently high DC voltage is applied between two electrodes in a confined area at a reduced gas pressure, the gas can be ionised and an electrical discharge can form. The electrical discharges are categorised according to the current density. When the current density is sufficiently high, a self-maintaining discharge is formed, referred to as Townsend or dark discharge. Further increasing the current turns the discharge into a corona discharge and then into a glow discharge. The term "glow" refers to the light emission that can be observed in such discharges. The light originates from the de-excitation of metastable energy states of the gas atoms and ions. A glow discharge for which increasing the discharge current increases the discharge voltage, is referred to as being of the abnormal type. In a sputter magnetron, the ionisation degree of the generated abnormal glow discharge is increased by the presence of a magnetic field. Here, this "magnetically enhanced abnormal glow discharge" is referred to as the "magnetron discharge (MD)". When this type of discharge is used for thin film deposition, the process is referred to as magnetron sputter deposition.

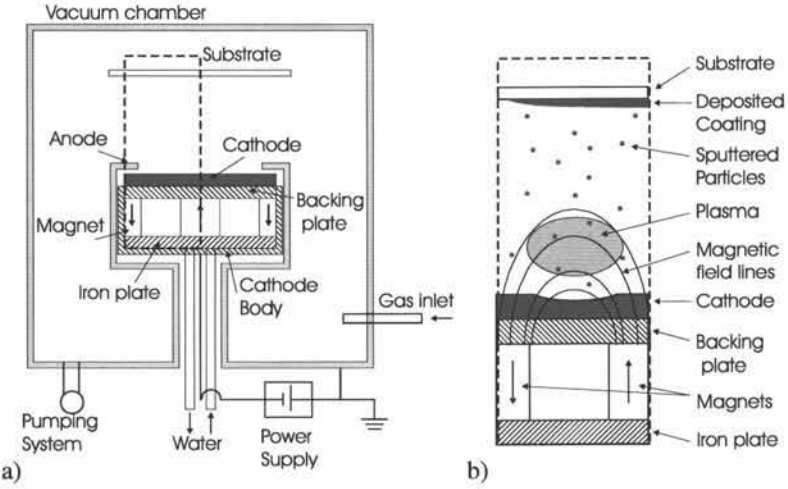

Fig. 1.1 *a)* Typical system for magnetron sputter deposition: the magnetron consists of the cathode body which contains the target, the magnets and the cooling system. It is surrounded by an anode housing. Also the substrate, vacuum chamber, electrical power supply, gas inlet and pumping system are sketched. *b)* Sketch of the magnetron discharge (enclosed region of part *a*).

A typical configuration used in magnetron sputtering is given in Fig. 1.1: shown is the general setup of the vacuum chamber containing a planar magnetron (part *a*), the discharge

region is shown in more detail in part *b*. The principal parts of the configuration are the vacuum chamber, the electrical power supply, the pumping system, the target (which acts as cathode), the backing/cooling plate, the magnets on top of a soft iron plate, the anode and the substrate.

To generate a discharge, the pressure in the vacuum chamber is first reduced to typically 10^{-4} Pa (= 10^{-6} mbar) or below. Then the sputter gas, usually argon, is introduced into the chamber such that a pressure typically in the range 0.1 to 2 Pa is obtained. To start the MD, a large d.c. voltage (range 600 – 1000 V) is applied. Also r.f. driven discharges are possible but such discharges are not considered in this work. Once an electron-ion pair is formed, e.g. due to cosmic radiation, the discharge is started and evolves rapidly to a steady state. During this process the discharge voltage drops to a value typical in the range of 300-500 V. The current density varies strongly according to the applied electrical power but lies usually in the range of 20-80 mA/cm^2. Hence, for a small circular magnetron (race-track area about 10 cm^2) typical discharge currents are 0.2 to 0.8 A. On the other hand, large rectangular magnetrons (race-track area about 500 cm^2) can easily carry several tens of Amperes. A major limitation for power input is the cooling of the magnetron. According to [Braithwaite00] "virtually all energy ends up as heat". This can result in a strong increase of the cathode temperature, possibly leading to demagnetisation of the permanent magnets and/or melting of the target. Hence, an effective cooling of the magnetron is absolutely necessary. This is achieved by a water flow through the magnetron assembly (Fig. 1.1a).

The discharge is maintained because positive argon ions are accelerated towards the cathode. The resulting ion bombardment leads to the emission of secondary electrons (SE) from the target. The emitted SE can be recaptured by the target or can be accelerated into the discharge. Because they are accelerated over the cathode sheath, they become energetic. Hence, they can ionise argon atoms which leads to the generation of new ions, thus sustaining the discharge. The ion bombardment at the target does not only release electrons but also target atoms. These atoms have an average energy of around 10 eV and travel through the vacuum chamber. Part of them reaches the substrate and forms the desired coating. Interaction of the sputtered particles with the sputter gas can heat the sputter gas, which gives rise to gas rarefaction (sputtering wind) [Rossnagel87b, Rossnagel88b].

As mentioned, the electrons emitted from the target are referred to as secondary electrons. When these electrons are accelerated into the discharge, they are referred to as primary electrons of the discharge. These primary electrons create electron-ion pairs. The electrons of these electron-ion pairs are referred to as the secondary electrons of the discharge. In order to avoid problems with the nomenclature, the following convention is used in this work. The electrons emitted from the target are referred to as secondary electrons (SE). The electrons that are accelerated into the discharge are referred to as high energy electrons (HEE) as long as their energy is larger than a certain threshold energy E_{th}. When their energy drops below this threshold, they are referred to as bulk electrons (BE). The major source of BE are not these slowed down HEE but the electrons that originate from the generation of an electron-ion pair in the discharge. The large majority of the electrons in the MD are BE: in standard glow discharges their density is four orders of magnitude larger than the HEE density [Bogaerts96]. According to self-consistent magnetron discharge simulations about one in thousand electrons is a HEE [Shidoji01a]. Nevertheless, the HEE are extremely important as they are responsible for sustaining the MD.

The charged particle density in a MD is of the order of 10^{10} - 10^{11}/cm^3, corresponding to an ionisation degree of less than 1%. The electron temperature is typically around 5 eV in the bulk of the plasma. The ionisation rate according to self-consistent simulation results is of

the order of 10^{16}/cm^{3}s [Kondo99a]. It is of course strongly dependent on the electrical power input.

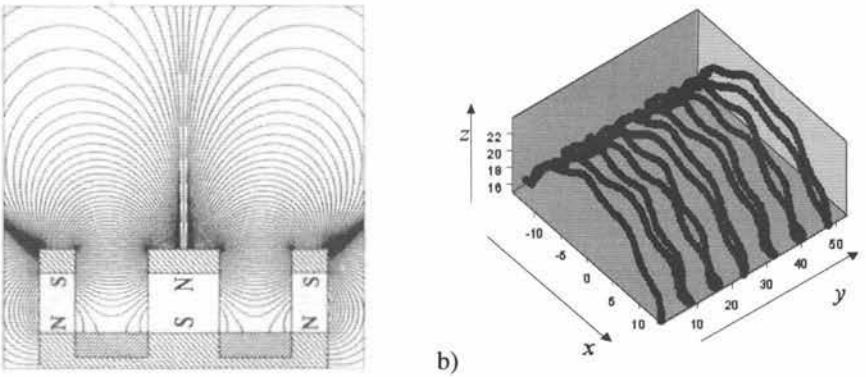

a) b)

Fig. 1.2 *a*) 2D cross section of the magnetic field of a generic magnetron, taken from [Penfold95]. *b*) Sketch of the electron movement in a planar magnetron discharge. Three components can be distinguished: (i) along the magnetic field lines, (ii) gyrating around the field lines and (iii) a drift in the E×B direction.

Fig. 1.2a gives a 2D cross section of a sputter magnetron, showing the magnetic field lines. The maximum value of the horizontal magnetic field component at the target surface is referred to as B_{max} in this work. This B_{max} is the standard quantity to denote the magnetic field strengths in magnetrons. In older works, typical values for B_{max} are around 200-300 G but, due to improvements in the production of strong permanent magnets, typical values are nowadays 500-600 G. An important aspect of the magnetic field is its balancing. A magnetic field is balanced when the flux from the inner pole is equal to, i.e. is balanced by, the flux to the outer pole(s). Unbalanced magnetrons can be of type I (flux of the outer poles smaller than the one from the inner pole) or type II (flux of the outer poles larger than the one from the inner pole) [Window86].

As the electrons move in a region that is subjected to an electric and magnetic field, their movement is described by the Lorentz equation:

$$\frac{d\mathrm{v}}{dt} = \frac{q}{m}(E + \mathrm{v} \times B) \qquad (1.1)$$

with v the electron velocity, q the electron charge and m the electron mass. The typical behaviour of a HEE is schematically shown in Fig. 1.2b: the HEE gyrates around the magnetic field lines with a radius defined by the Larmor radius r_L:

$$r_L = \frac{m\mathrm{v}_\perp}{qB} \qquad (1.2)$$

with $\mathrm{v}_\perp$ the velocity component perpendicular to the target. As the velocity component along the magnetic field lines is not altered, the electron also moves along these field lines. The third component of the motion is the drift in the direction perpendicular to both E and B, the so-called $E \times B$ or Hall drift. Because of this drift there is a Hall current in the discharge. For a 6-inch target this current can be up to ten times as large as the discharge current [Rossnagel87a]. The $E \times B$ velocity $\mathrm{v}_{E \times B}$ of the electrons varies from approximately 5×10^5m/s (15 mm above target) to 10^5m/s at 40 mm above the target [Sheridan98].

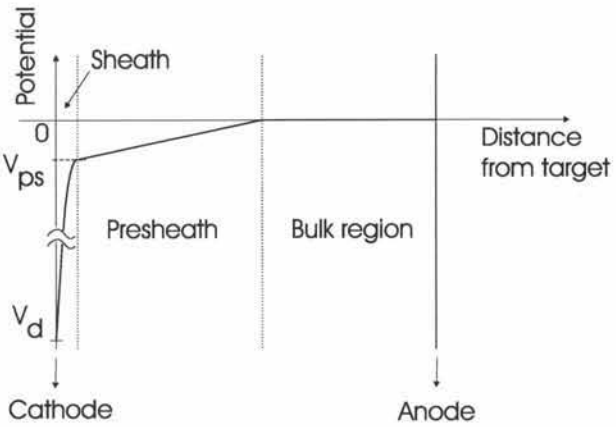

Fig. 1.3 Sketch of the "typical" potential distribution in a MD in the direction perpendicular to the target surface. Three regions can be distinguished: the sheath, presheath and bulk region.

The potential distribution in a MD is as sketched in Fig. 1.3. The largest part of the potential drop is over the cathode sheath, which has a linearly increasing electric field. The cathode sheath thickness is typically one to two millimetres. A presheath with constant electric field exists: it has a potential drop of the order of kT_e so that the Bohm criterion is satisfied (section 1.3.3.1). The plasma potential is shown in Fig. 1.3 at ground level: in reality, it is slightly positive (some volts) but the exact potential distribution in the bulk region depends on the geometry and on the magnetic field (balancing) (section 1.3.5.4).

Most ions are created at the end of the cathode sheath and are accelerated towards the cathode. Their typical residence time in the discharge is approximately 0.7-0.8 μs [Sheridan89a]. However, simulation results show that this average value is not so meaning full [Goeckner91]: it is more useful to differentiate among the ions born in the sheath (residence time approximately 0.2 μs) and the ones born in the presheath (residence time around 5 μs). As mentioned, the HEE start at the cathode and are accelerated into the discharge. Their maximum energy is practically equal to the discharge voltage. For a sufficiently strong magnetic field, they will lose nearly all their energy before they leave the discharge. An effective ionisation energy of 30 eV means they can generate between 10 and 17 electron-ion pairs (for discharge voltages from 300 to 500 V). At 0.5 Pa, the time between two ionisations is approximately 6×10^{-8}s. Hence, they are a HEE for about 0.6 to 1 μs and during that time they travel a distance of roughly 4 to 10 m.

In a MD a wide variety of processes occurs: typical plasma processes, as well as particle-particle and solid-particle interactions occur. Moreover, the energy range and the time scale of the different processes vary strongly. Also the external parameters have a large operating range: the applied electrical power, gas pressure, cathode size and magnetic field strength can vary over an order of magnitude according to the type of magnetron used. This turns the MD into an interesting but also complex topic. Because of this, simplifications are needed for a workable model. In the next section, the different processes and their role in the MD are discussed.

1.2 Different processes in the magnetron discharge

1.2.1 Processes in the plasma

From the interactions in the plasma, only collision processes are considered. Hence, global effects are neglected. Nevertheless, these global processes may contribute significantly too, e.g. they might contribute to the anomalous electron transport observed in the MD (section 1.3.6.2). The collision processes that occur in the plasma can be split up in elastic collisions (section 1.2.1.1), inelastic collisions (section 1.2.1.2), de-excitations (section 1.2.1.3) and ion-electron recombinations.

A positive ion-electron recombination is the reverse process of an ionisation. This means that an electron and an ion combine to form a neutral atom. Because of the energy and momentum conservation laws it follows that these processes cannot be two-body processes but have to be three-body processes. The "third body" can be any particle present in the discharge (or even a chamber wall). Consequently, the occurrence of a three-body process is not only related to the argon ion and electron density but also to the neutral density, i.e. the gas pressure. In diode discharges typical ionisation rates for electron impact are of the order of 10^{16}/cm^{3}s whereas the typical rate for three-body processes is of the order of 10^{11}/cm^{3}s [Bogaerts96], meaning that recombination processes can be neglected compared to electron impact ionisation. For a MD, the ionisation rate and the electron and ion density are of the same order as in a diode discharge but the neutral density is much lower. Consequently, the occurrence of the three-body processes can be neglected in the MD and will not be considered here.

1.2.1.1 Elastic collisions

The characteristic of elastic collisions is that they do not alter the internal energy of the collision partners. Instead, they redistribute their kinetic energy. Elastic collisions occur between the atoms, ions and electrons. Four types of elastic collisions are discussed in this section: electron-atom, atom-atom, ion-atom and Coulomb collisions.

A. Electron – atom

The electron-argon elastic collisions change the direction of the electron velocity vectors but the electron energy remains practically constant.

The occurrence of this type of collision is characterised by its cross section σ_{ela} (Fig. 1.4): it has a maximum of 1.3×10^{-15}cm^2 around 12 eV and decreases for increasing energy to reach 1.8×10^{-16} cm^2 at 600 eV. In this region, σ_{ela} is approximately proportional with the inverse of the square root of the electron energy, i.e. $\sigma_{ela}\sim1/E^{0.5}$.

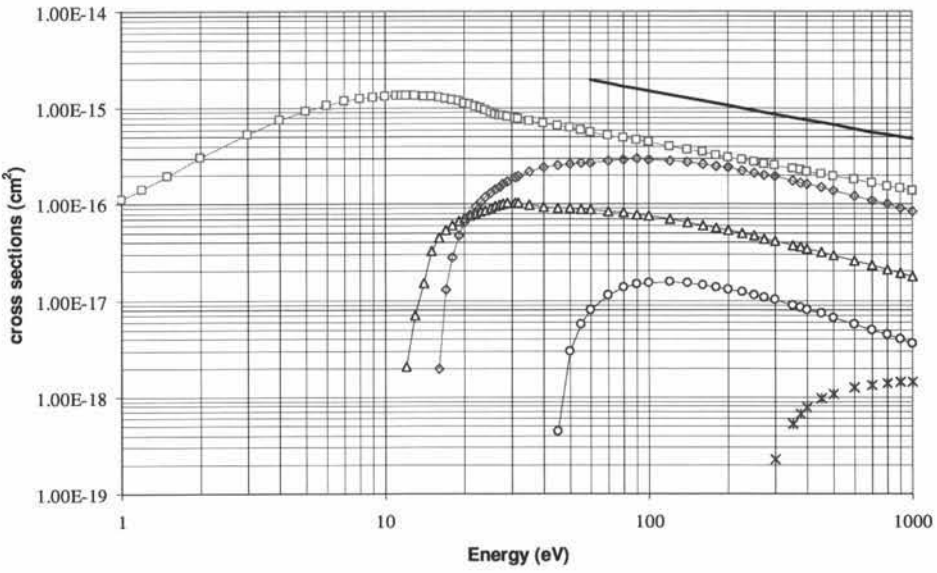

Fig. 1.4 The energy dependence of the electron cross sections for elastic collisions (□), excitations (△) and the "standard" ionisations (M-shell) (◇). For completeness, also the ionisation by ejecting an electron from the L-shell (×) and the cross section for creating Ar^{++} (O) is shown. The thick solid line indicates the dependence $1/E^{0.5}$. Based on data from [Bretagne86a].

Defining E (E_0) as the electron energy after (before) the elastic collision, the relation between energy before and after the collision is given by [Lieberman94]:

$$E = E_0\left[1-2\frac{m_1 m_2}{(m_1+m_2)^2}(1-\cos\chi)\right] \tag{1.3}$$

for two particles with masses m_1 and m_2 and χ the axial scattering angle. In the case of an electron-argon interaction, the formula can be simplified to:

$$E = E_0\left[1-2\frac{m}{M}(1-\cos\chi)\right] \tag{1.4}$$

as the electron mass m is much smaller than the argon atom mass M. Because of the large difference in m and M it is clear that the energy of the electron before and after the interaction will be practically the same. The scattering angle χ is determined by the angular differential cross section $\sigma(E,\chi)$. Experimental data for $\sigma(E,\chi)$ are given in e.g. [Srivastava81, Nahar87]. A recent overview of the elastic differential cross sections is given in [Jablonski04]: it lists lots of experimental data as well as the fits obtained using the Dirac-Hartree-Fock and Thomas-Fermi-Dirac potential. A plot of the differential cross sections for electron energies from 150 to 300 eV is shown in Fig. 1.5a.

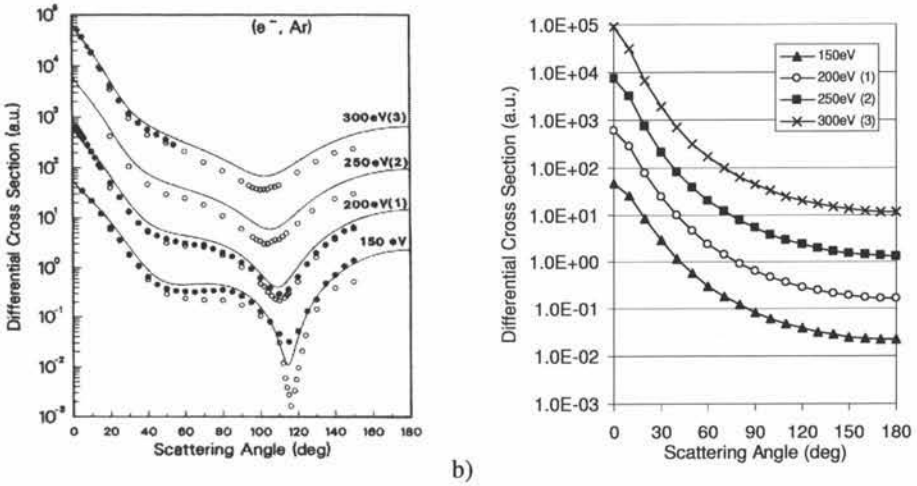

a) b)

Fig. 1.5 *a*) Plot of the differential cross section for elastic electron Argon collisions: experimental results as well as a theoretical curve are presented, taken from [Nahar87]. *b*) Plot of the differential cross sections based on eq. (1.6). The number in parenthesis following an energy value indicates the power of ten by which the cross section values are multiplied.

Surendra et al. modelled this angular dependence of $\sigma(E,\chi)$ by introducing the normalised differential scattering cross section $I(E,\chi)$ based on screened Coulomb scattering [Surendra90]:

$$I(E,\chi)=\frac{1}{4\pi}\frac{\varepsilon}{\left[1+\varepsilon\sin^2(\chi/2)\right]\ln(1+\varepsilon)} \qquad (1.5)$$

This result is commonly used, also in magnetron discharge simulations, e.g. [Kondo99a, Shidoji99a]. However, in [Okhrimovskyy02] it is pointed out that the proposed expression "*is incorrect and misses some scientific background...*". Instead, the following expression is proposed for $I(E,\chi)$:

$$I(E,\chi)=\frac{1}{4\pi}\frac{1+8\varepsilon}{(1+4\varepsilon-4\varepsilon\cos\chi)^2} \qquad (1.6)$$

with $\varepsilon = E/E_u$ with E_u the atomic unit of energy (= 27.21 eV). As can be seen (Fig. 1.5b) this approximation agrees rather well with the experimental values (Fig. 1.5a), except at large scattering angles. Okhrimovskyy scattering is used in [Kolev04a]. Sometimes also isotropic scattering is assumed in magnetron simulations, see e.g. [Shidoji00]. To investigate the influence of the model for χ, different models have been implemented in the MC model of section II.2.5, the results are discussed in section II.2.6.4.

B. Atom-atom

The relevant collisions of this type are argon-argon and argon-sputtered atom interactions. In this case the masses of both particles are of the same order and eq. (1.3) needs to be used. Hence, the energy transfer is considerable. Although collisions of this type are not considered in the developed model (Chapter II.2), they are mentioned as they give rise to gas density rarefaction (section 1.4.3.4). The cross section for an elastic atom-atom collision is approximately 1.4×10^{-15}cm^2 at 1 eV and decreases with increasing atom energy. Around

500 eV it already decreased to $2.4\times10^{-16}cm^2$ according to the fitting formula proposed in [Phelps94]. Due to the low concentration of sputtered atoms in the MD, a collision between these species is more unlikely.

C. Ion-atom: symmetric charge transfer

In principle elastic collisions can occur between argon ions and argon atoms/sputtered atoms and between sputtered ions and argon atoms/sputtered atoms. Given the relative occurrence of all these particles only the collisions between argon ions and argon atoms need to be considered. The cross section for such an elastic collision between an argon ion and an argon atom is approximately $1.2\times10^{-14}cm^2$ for ion energies of a few eV and decreases slowly with increasing energies to reach a value of $4\times10^{-15}cm^2$ at 1000 eV [Phelps94]. A special case of the elastic collisions is symmetric charge transfer: it occurs when during a collision an electron is exchanged between an argon ion and an argon atom:

$$Ar^+ + Ar^0 \rightarrow Ar^0 + Ar^+$$

When disregarding the fine structure levels or isotopic mass, the incident and scattered ion are indistinguishable, implying that the interaction can be considered as an elastic one. Its cross section is half of the one for elastic scattering collisions [Phelps94]. At 0.5 Pa and ion energies of a few eV, the mean free path length for elastic collisions and for symmetric charge transfer is approximately 7 and 14 mm, respectively. The typical cathode sheath length is of the order of 2-3 mm, the presheath can extend up to a centimetre and more into the discharge. Hence, for the given pressure, it seems likely that a "slow" ion, i.e. one at the onset of being accelerated in the presheath, undergoes at least one interaction with an argon atom. This process is not crucial although it adds to the heating of the argon sputter gas. In standard diode discharges the process of symmetric charge transfer between fast ions and atoms leads to the generation of fast atoms in the discharge [Bogaerts96]. However, fast ions only appear in the cathode sheath region. Given the typical cathode sheath thickness in the MD, the probability for such an interaction is very low and the process of charge exchange between a fast ion and a slow argon atom can be neglected.

D. Coulomb collisions

Coulomb collisions are crucial for the energy exchange of the low energy electrons (<10 eV) but can be neglected for the high energy electrons (>25 eV) in the discharge.

Coulomb collisions (CC) occur between two charged particles q_1 and q_2, representing an electron-electron, electron-ion or ion-ion collision. To determine the cross sections for this type of interaction, we introduce the classical distance of closest approach b_0, defined as [Lieberman94]:

$$b_0 = \frac{q_1 q_2}{4\pi\varepsilon_0 W_R} \qquad (1.7)$$

with ε_0 the dielectric constant and W_R the centre of mass kinetic energy defined as $W_R = m_R v_R^2/2$ with $v_R = v_1 - v_2$ and m_R the reduced mass, i.e. $m_R = m_1 m_2/(m_1+m_2)$. To determine the influence of the Coulomb collisions on the charged particle motion, the cross section σ_{90} for a deflection of 90 degrees is determined. Such a deflection can occur through a single scattering or through multiple small angle scatterings. The latter has the largest probability and it can be deduced that σ_{90} is given by:

$$\sigma_{90} = \frac{8}{\pi} b_0^2 \ln \Lambda \tag{1.8}$$

with Λ the classical Spitzer parameter. For the typical plasmas used in material processing, $\ln \Lambda$ is approximately equal to 10 [Lieberman94]. Given the formula for b_0 it follows that $\sigma_{90} \sim 1/v_R^4$. This implies that the cross section decreases very rapidly with increasing kinetic energy of the charged particles. It is important to estimate whether the influence of Coulomb collisions needs to be taken into account when retracing electron orbits in the MD.

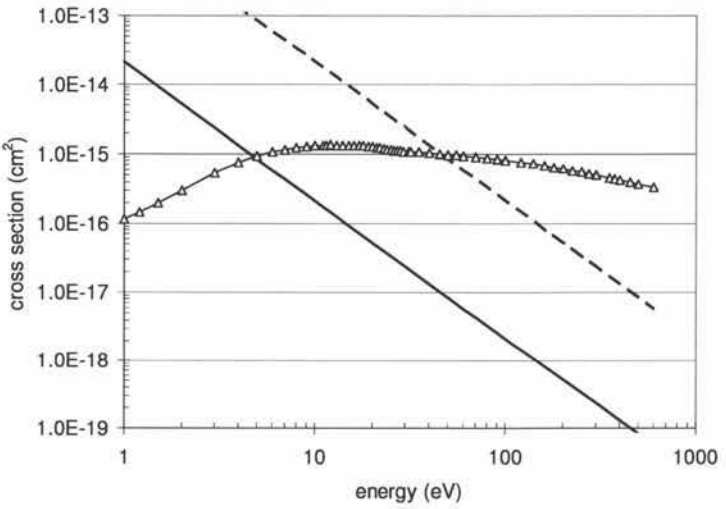

Fig. 1.6 Comparison of the electron cross section σ_{90} for Coulomb collisions (dashed line) and the total electron cross section σ_{tot} (△). To compare the relative occurrence of the processes it needs to be taken into account that the target particles of CC are much less available than the ones for the collision processes included in σ_{tot} as the ionisation degree in MD is typically below 1%. This "adapted" cross section for CC (solid line) clearly indicates that CC are only important at small electron energies.

To determine σ_{90} it is assumed that the first charged particle is a fast electron and the second a slow electron or ion. Hence, $v_R \approx v_1$ and $m_R = m/2$ for electron-electron and $m_R \approx m$ for electron-ion interaction. Hence, the cross section for electron-ion interaction is a factor four smaller than for electron-electron interaction. The cross section for electron-electron interaction is given in Fig. 1.6 (dashed line) together with the "total" electron cross section σ_{tot}, which is defined as $\sigma_{ela}+\sigma_{ion}+\sigma_{exc}$. The target species for CC (electrons or ions) are much less abundant than for the other collisions (argon atoms). For typical MD, the ionisation degree is well below 1% (section 1.3.5.2). Hence, to compare the relative occurrence of CC the cross section σ_{90} needs to be divided by 100 to compare it with σ_{tot}. This is shown in Fig. 1.6: already at 20 eV the probability for a CC is 20 times smaller than the total cross section. On the other hand, at low electron energies CC can no longer be ignored.

From the deduction of σ_{90} in [Lieberman94], it follows that for an arbitrary scattering angle χ the CC cross section σ_χ is given by:

$$\sigma_\chi \chi^2 = \sigma_{90} 90^2 \tag{1.9}$$

Hence, another way of looking at Fig. 1.6 is to interpret the dashed line as the cross section σ_χ for a CC with angle χ where χ is determined by $\chi^2/90^2 = 1/100$ (i.e. $\chi = 9$). At 45 eV a deflection of $\chi = 9$ has the same probability to occur as one of the other collisions (ionisation, excitation or elastic collision). Given that 1% is an upper limit of the actual ionisation degree, we conclude that CC will only be important at low electron energies. This is confirmed by the results for the EEDF (electron energy distribution function) obtained in [Guimarães91] where it is reported that the influence of Coulomb collisions on the EEDF is limited to electron energies below 25 eV. In that work it is shown that the lower energy part of the EEDF is strongly determined by the CC. This is no surprise: the only interactions possible for the bulk electrons with energy below the excitation threshold (11.55 eV) are elastic collisions. As the energy transfer for collisions with argon atoms is only of the order of m/M, the electron energy loss due to elastic argon-electron collisions remains marginal, even at low energies. Hence, the only way for the electrons to exchange energy is through CC.

1.2.1.2 Inelastic collisions: Ionisation and excitation

In the MD two kinds of atoms are present: the argon atoms and the sputtered atoms. Both can be ionised or excited. Although the ionisation and excitation of the sputtered atoms can be of practical importance, e.g. in self-sustained sputtering or in ion assisted deposition, these processes will not be discussed.

A. Ionisation of argon atoms

One of the most important processes in the MD is the ionisation of argon atoms by electron impact. If a ground state argon atom is directly ionised this process is referred to as direct electron impact ionisation:

$$Ar^0 + e^- \rightarrow Ar^+ + 2e^-$$

The ejected electron can result from the K, L or M-shell of the argon atom. The ionisation threshold of these shells is 3205, 245 and 15.76 eV, respectively. The cross sections for the L and M shell are plotted in Fig. 1.4, based on data from [Bretagne86a]. Also the ionisation cross section for the generation of Ar^{++} is shown. Given the electron energies in the MD (typically below 600 eV), only ionisation from the M-shell is considered. Hence, in the remaining part of the thesis "ionisation" stands for "M-shell ionisation of the argon atom", although it will not be mentioned explicitly anymore. The cross section σ_{ion} of the considered ionisation process increases with electron energy, reaches a maximum of approximately 3×10^{-16}cm^2 around 100 eV and decreases again. In this decreasing part σ_{ion} is practically inversely proportional with the square root of the electron energy as indicated in Fig. 1.4.

Because of the ionisation of the argon atom, the electron energy is reduced with an amount equal to the sum of E_{ion}, the ionisation energy, and E_{eject}, the energy of the ejected electron. The average energy E_{eject} is around 10 eV for incoming electron energies of some hundreds of eV [Bretagne86a, Carman89]. Differential cross sections for ejection of an electron with E_{eject} are given in [Bretagne86b] for an incoming electron energy of 1000 eV.

A metastable argon atom can also be ionised (two-step electron impact ionisation), the required energy is only 4 eV. As the density of the metastable argon atoms is much lower than the ground state atoms, this process is much less frequent than direct electron impact ionisation. For the same reason, ionisation through collision of two argon metastable atoms is of minor importance and not considered here.

Next to electron impact, also impact of a fast argon ion (Ar_f^+) or atom (Ar_f^0) can cause ionisation:

$$Ar^0 + Ar_f^+ \rightarrow Ar^+ + Ar_f^+ + e^-, \quad Ar^0 + Ar_f^0 \rightarrow Ar^+ + Ar_f^0 + e^-$$

These processes only become important for higher atom or ion energies, the maximum of the cross sections is reached above 1000 eV [Bogaerts96]. Given the rather low discharge voltages in MD (typically below 600 eV), these processes can be neglected. Again, this process can also occur for argon metastable atoms, but this is even less frequent.

B. Excitation of argon atoms

Excitation of an argon atom by electron impact is similar to direct impact ionisation but less energy is transferred to the atom: no electron is ejected but an electron of the atom is moved to a higher energy level. As an electron can be excited from different energy levels and as it can be transferred to different energy levels, there is a wide variety of excitations possible. For example, 25 different excitations are taken into account for the MD simulations in [Kondo99a]. The threshold for excitation is 11.55 eV. Instead of accounting for each of these individual excitation levels it is common to consider the sum of all these cross sections. The cross section σ_{exc} plotted in Fig. 1.4 is the sum of all these different excitation possibilities. Several sets for these cross sections exist. In [Yanguas-Gil05] a new set is proposed based on recent experimental measurements and the other most common sets (from Bretagne, Vleck and Hayashi) are discussed in view of these recent measurements. Also thermal excitation and photo-excitation are in principle possible but they can be neglected.

1.2.1.3 De-excitation

De-excitation is the inverse process of excitation: the excited levels of the atoms are only short-living and the atom returns to its ground state by one or more transitions. Such an electron transition results in the emission of photons. The part of the emission in the visible range is observed by the eye as "the plasma". De-excitation also allows more advanced optical studies of the discharge, e.g. computer-tomography [Itoh96, Miyake92] or OES (optical emission spectroscopy) [Rossnagel89, Debal00, Christou02]. Given the life-time of the excited levels (order of 10^{-8}s [Miyake92]), and the speed of the excited species (order 10^3-10^4m/s), the de-excitation and excitation occur practically at the same position.

1.2.2 Interactions with surfaces

In this section we discuss the interactions of the different species in the MD with solid surfaces. The surfaces are the chamber walls, the anode and the cathode (target). The following species can interact with these surfaces: electrons, argon atoms and ions, sputtered atoms and ions, and photons. The plasma-surface interaction can lead to different processes. To understand a typical dc MD three types of plasma-solid interactions occurring at the target are sufficient: emission of secondary electrons (section 1.2.2.1), emission of sputtered particles (section 1.2.2.2) and the reflection and recapture of electrons (section 1.2.2.3).

For reactive sputtering the situation is more complex: the added reactive gas interacts also with the surfaces, which leads to (partial) covering of both the cathode and anode surfaces. The latter causes the disappearing anode effect when the compound layer is an insulator [Sellers97]. In reactive sputtering also the implantation of certain species has to be taken into account because this gives, together with the covering of the cathode surface, rise to the poisoning of the process [Berg87, Berg05, Depla04a-c].

1.2.2.1 Secondary electron emission

When a particle hits a surface, an electron can be emitted. The number of secondary electrons (SE) emitted per incoming particle is defined as the SE yield γ. For the MD, the ion induced SE yield is by far the most important. The other types of SE emission (by atoms, electrons, photons and the electric field) are also discussed here to show that they are really of minor importance. In what follows, except for this section, the term "SE emission" stands for "ion induced SE emission", even when not explicitly mentioned; the same holds for the SE yield γ.

A. Ion and atom induced SE emission

Ions bombarding a surface give rise to the emission of SE. The emitted electrons have a small initial energy, typically in the range of 2 to 6 eV [Chapman80]. These experimental findings can be simulated, see e.g. [Nishimura96]. The angular distribution of the emitted SE is a three-dimensional cosine distribution because the free path length of the electrons in the solid is so small that any information of the origin of the electron is lost by the time it is emitted [Reimer85].

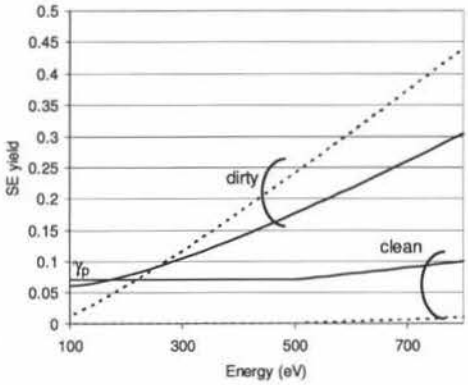

Fig. 1.7 Sketch of the energy dependence of the SE yield for clean and dirty surfaces. The full line indicates the yield of the argon ions, the dashed line the one from the argon atoms. In MD, only the yield of the argon ions on a clean surface is of importance. The constant value of the SE yield induced by ions on a clean surface is referred to as γ_p. The plots are based on the expressions for the SE yield given in [Phelps99].

More difficult to determine is the SE yield. The experimental results show the need to differentiate between clean and dirty surfaces [Phelps99]. A clean surface is, of course, a surface of pure metal without contamination. A dirty surface is a surface that is partially contaminated, e.g. by oxygen or nitrogen. In general, there are two mechanisms responsible for electron emission: kinetic and potential emission (see e.g. [Baragiola94, Nishimura96]). For kinetic emission the main source of energy to emit the electrons is the kinetic energy of the incoming ion. In this case the ion induced SE coefficient γ depends on the ion energy. SE emission is considered kinetic emission down to ion energies of approximately 500-1000 eV [Baragiola94, Nishimura96]. Below this, the kinetic emission is overwhelmed by potential emission. For the latter mechanism, the energy to release the electron is related to the ionisation energy of the atom (see further). For clean metal surfaces, the SE yield at low energies is independent of the kinetic energy of the incoming ion and is typically in the range 0.05-0.15. This constant value of the SE yield due to potential emission is referred to as γ_p. However, for dirty surfaces γ depends on the ion energy, even in the low energy range

Fig. 1.7). This indicates that for dirty surfaces the kinetic emission dominates down to the lowest ion energies.

To judge the cleanliness of the cathode in a MD we consider the following example for aluminium and oxygen. For a current density of 10 mA/cm^2 the ion flux at the target is approximately 6×10^{16}/cm^{2}s. Given the low sputter yields of the aluminium oxide (0.03-0.04) [Kelly87, Depla02], it follows that 1.8 to 2.4×10^{15}/cm^{2}s atoms are sputtered from the target. At 5 mTorr the impinging flux of argon atoms on a surface is approximately 1.8×10^{18}/cm^{2}s [Chapman80]. Given an impurity of 0.1% and a sticking coefficient of the order of 1% for oxygen [Depla04b], the depositing flux on the target is 1.8×10^{13}/cm^{2}s. As this is more than 100 times smaller than the removing flux, the target surface can be considered clean. Consequently, only SE yields for clean surfaces will be considered.

overview SE yields							
metal	φ (eV)	ε_F (eV)	eq. (2.9)	eq. (2.10)	eq. (2.11)	experim.	Reference
Au	5.1	7.25	0.063	0.063	0.086	0.062 0.040 0.030	[Oechsner78] [Lakits90] [Töglhofer93]
Al	4.28	11.3	0.069	0.115	0.113	0.120 0.075 0.070 0.071	[Chapman80] [Yamauchi83] [Lewis89] [Smith94]
Ti	4.33	8.84	0.086	0.112	0.111	0.148 0.075	[Oechsner78] [Lewis89]
Cu	4.65	9.03	0.070	0.092	0.101	0.030 0.200 0.100 0.082	100eV [Chapman80] 400eV [Chapman80] [Guntherschulze30] [Oechsner78]
Ag	4.26	7.48	0.106	0.117	0.113	0.088	[Oechsner78]
W	4.55	11.47	0.059	0.098	0.104	0.095 0.089	[Hagstrum56] [Oechsner78]

Table 1.1 Overview of the SE yields for some commonly sputtered metals. First, the work function φ and the Fermi energy ε_F are given as these values are needed for the calculated SE yields based on eqs. (1.10), (1.11) and (1.12). Then, different experimental SE yields found in literature are listed.

For some commonly sputtered metals (Al, Ag, Au, Cu, Ti and W) experimental reported values are listed in Table 1.1. It is clear that there is a rather large scatter in the values. A possible explanation is the fundamental difference between clean and dirty surfaces because it is not always clear how clean the actually measured surface is. Furthermore, the SE yield is also very sensitive to surface properties (e.g. morphology, crystal surface) that are not always characterised. From the behaviour of the different SE yields sketched in Fig. 1.7 it is clear that some reported measurements for metals are most likely in reality for (partially) dirty surface. Examples are the SE yields taken from [Chapman80] in Table 1.1 for copper: according to this reference the SE yield varies from 0.03 at 100 eV to 0.2 at approximately 400 eV, which does not correspond with potential emission at all. In Table 1.1 also the values obtained in [Oechsner78] are listed. However, except for W, these values are reported only at 1.05 keV. By comparing the results with the ones from [Lewis89] for Al and Ti it follows that

at 1.05 keV the kinetic emission process already starts to participate. The same holds for the Oechsner-value for Au by comparing it with the results from [Lakits90].

Based on the experiments listed in Table 1.1 an average experimental value for γ_p is calculated. These averaged values are used for Fig. 1.8. Given the apparent contribution of kinetic emission at 1.05 keV for Au, Al and Ti these values are not included. Also the values for copper from [Chapman80] are not included because of the lack of a potential emission regime. The error bars are determined by the maximum and minimum reported experimental value.

Theoretical efforts have been done to model the SE yield for ion induced potential SE emission. An expression that agrees rather well with the experimental results is the one proposed in [Kishinevsky73]:

$$\gamma_p = \frac{0.2(0.8E_i - 2\phi)}{\varepsilon_F} \tag{1.10}$$

with ε_F the Fermi energy, E_i the ionisation energy of the incoming ion and φ the work function of the target material. Also Baragiola has proposed an expression for γ_p [Baragiola79]:

$$\gamma_p = 0.032(0.78E_i - 2\phi) \tag{1.11}$$

Baragiola et al. mention that this expression gives a better fit than eq. (1.10) to the set of experimental data they used, which included SE yields obtained with different ion species. In contrast to eq. (1.10), the Fermi energy is not needed in eq. (1.11). However, this means that metals with the same work function also have the same γ_p. Baragiola et al. [Baragiola81] also proposed another fit to the experimental data:

$$\gamma_p = 0.016(E_i - 2\phi) \tag{1.12}$$

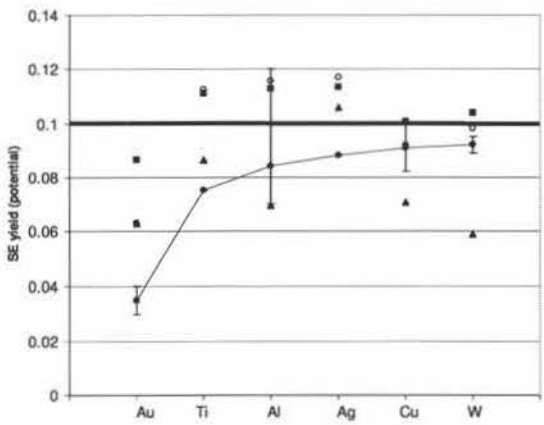

Fig. 1.8 The experimentally obtained secondary electron yield γ_p for some commonly sputtered metals (Au, Al, Ti, Cu, Ag and W). The average values (●) are plotted from the results shown in Table 1.1, the error bars are determined by the minimum and maximum of the experimental values. The calculated values for γ_p, using eqs. (1.10) (▲), (1.11) (○) and (1.12) (■), are also shown. As can be observed, there is quite a spread in the results. The metals are ordered so that the experimental γ_p increases from left to right.

The three eqs. (1.10), (1.11) and (1.12) are also plotted in Fig. 1.8 for different materials. As can be seen do the results vary quite strongly. This shows that γ_p is not accurately known. Hence, most often the value of 0.1 is used in magnetron discharge simulation as it represents an average of the different values, although Fig. 1.8 shows that practically all of the experimental values are below 0.1.

Neutral bombardment of a surface gives rise to SE emission, just like ion bombardment. However, there is an important difference: for clean surfaces the neutral SE yield does not exhibit the constant SE yield at low ion energies but decreases (Fig. 1.7). Although some high energy neutrals (originating as sputtered atoms or argon ions that were reflected and neutralised at the cathode) do hit the surfaces in a MD, the vast majority of the atoms in the MD have a low energy. Consequently, the contribution of atom induced SE emission can be neglected.

B. Electron induced SE emission

When an electron strikes a solid, electrons can be emitted. Conventionally, the emitted electrons have been arbitrarily split in three categories according to their energy as "true secondaries" (energy <20 eV), "elastically reflected electrons" (energy equal to the energy of the incident electron) and "intermediate electrons". Maximum yields of 1 to 2 are measured at incident electron energies of several hundreds of electron volt [Henrist02]. The yield drops with decreasing energy but does not become zero for zero incident energy: as by definition the reflected electrons are also considered in the yield, the yield becomes equal to the reflection coefficient at low energies. Measurements in [Henrist02] show an increase in the yield at energies below 5 eV for impact on copper. This agrees with the measured increase of the reflection coefficient for very low electron energies on copper, e.g. [Andersson70, McRae76a]. Hence, in this case, the concept of SE yield is quite ambiguous.

In a MD, there is in principle no interaction of high energy electrons with the walls as only low energy electrons escape the discharge region because of the magnetic trap. Hence, the effect of electron induced SE emission can be neglected. However, due to the spiralling along the magnetic field lines, electrons with very low energies can interact with the cathode. Although this process can be considered as electron stimulated SE emission, we refer to this process as electron reflection and recapture at a solid (section 1.2.2.3).

C. Photon induced SE emission

The ejection of electrons due to photon bombardment is called photoemission. The SE yield for most pure metals is of the order of 10^{-4} to 10^{-3} in the visible and near uv range, which is the typical emission range for the excited argon atoms and ions. With decreasing wavelengths the yield increases to reach approximately 0.1 at 100 nm [Chapman80]. The typical de-excitation rate in the MD is of the order of 10^{16}/cm^{3}s [Kondo99a]. Assuming that half of the photons hit the target and that the SE yield equals 10^{-3} results in an electron emission of 5×10^{12}/cm^{2}s from the target due to photo-ionisation. A current density of 10 mA/cm^2, a lower limit for the MD, results in an ion flux at the target of approximately 6×10^{16}/cm^{2}s. For the typical ion induced SE yield of 0.1 this gives an electron emission of 6×10^{15}/cm^{2}s. This is more than three orders of magnitude larger than the photoemission. Hence, the process of photoemission can be neglected.

D. Electric field induced SE emission

SE emission can also occur, especially at (micro) protrusions at the surface, under the influence of a strong electric field, i.e. of the order 10^7V/m or more [Bogaerts96]. In the

typical MD the maximum electric field is 2 orders of magnitude lower. Hence, this effect can be neglected.

1.2.2.2 Sputtering and sputter yield

The positive ions generated in the discharge are accelerated in the cathode sheath before they reach the target. When striking the target, their typical energy is in the range 300-500 eV. This leads to the ejection of target atoms (sputtering of the target), which results in target erosion. Because of the non-uniform plasma distribution, an erosion groove is formed (Fig. 1.1b). The sputter yield Y is the average amount of particles removed from the target per incoming ion. It is dependent on the energy and type of the incoming particle, the incoming angle, the texture of the target and the target material. This yield can be determined using empirical formulas; one of the best known is probably the formula of Matsunami [Yamamura83, Matsunami84]. These sputter yields can also be calculated using a numerical approach. A reference here is TRIM [Eckstein91, Biersack80]. A theoretical background to sputtering is given in [Sigmund69].

There exist models for the angular distribution and energy distribution of the sputtered particles. A recent overview of particular interest is [Stepanova01]: it investigates the sputtering of metals (e.g. Cu, W, Ti) with sub-keV argon atoms at normal incidence. The angular distribution and the (angularly resolved) energy distribution of the sputtered particles are studied. Results obtained by experiments and both numerical and analytical modelling are given. In the model developed in the second part of this thesis, the erosion groove formation is considered but the sputtered particles are not followed. Hence, their angular and energy distribution is not needed in the model and will not be further considered here.

1.2.2.3 Reflection and recapture of electrons

The SE electrons emitted at the target follow the magnetic field lines (Fig. 1.2b). As these electrons have a small initial energy of some eV (section 1.2.2.1), they can interact with the target surface. In that case the SE are either reflected or adsorbed. The latter process is in MD usually referred to as the recapture of SE. The process is determined by the reflection coefficient R. Because of energy conservation the maximum energy an electron can have when it reaches the cathode surface is equal to its initial energy (2-6 eV).

Some examples of measurements of R as a function of energy for impinging electron energies below 10 eV are mentioned in the literature for Ni [McRae76b, Andersson70], Cu [Lee65, Anderson69, Andersson70, McRae76a], W [Zollweg64, Babout77] and Fe [Kisker85, Tamura85]. In [Tamura85] it is shown that the total reflection is practically independent of the impinging angle in the range 0 to 20. An overview of experiments on W and Cu is given in [Babout77]. The influence of (partial) oxygen covering of the surface is discussed in [McRae76a, Babout77]: the higher the oxygen covering, the lower the reflection coefficients. The influence of both nitrogen and oxygen on the surface of Cu is discussed in [Lee65]. The influence of the crystal orientation on the electron reflection coefficient for W is reported in [Zollweg64]. For Fe/MgO(001) the reflection/absorption depends on the spin polarisation of the electrons [Bertacco99].

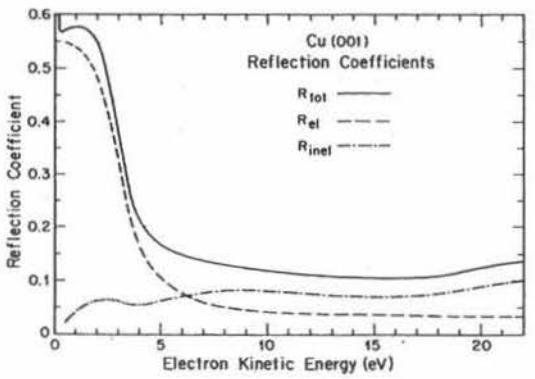

Fig. 1.9 Electron reflection coefficient at low impinging electron energies for a Cu(001)-surface, taken from [McRae76a].

The energy dependence of R for copper is given in Fig. 1.9. In [Babout77] is shown that, for a clean Cu (100) surface, reported R-values at 3 eV lay typically between 40 and 55%; although also a value of less than 10% has been measured. Hence, these electron reflection coefficients are not known very accurately. In general, the exact position of the minima and maxima of R as a function of the energy is related to the band structure of the metal around the vacuum level, see e.g. [Kisker85]. The reflection coefficient is split up in an elastic and inelastic part. The latter is quite small for Cu (001) (Fig. 1.9).

1.3 Typical discharge characteristics

In this part some of the more important characteristics and properties of the MD are discussed, namely the erosion profile, the discharge voltage, the cathode sheath, the current-voltage characteristic and the bulk plasma properties.

1.3.1 Erosion profile

Models exist to estimate the erosion profile width but they are more qualitative than quantitative of nature. The rule of thumb is that the maximum erosion occurs where the magnetic field lines are parallel to te cathode.

Since the ions in a MD bombard the target, they remove target atoms, leading to erosion of the target. Because of the magnetic field, the plasma is restricted to a limited region. Hence, also the ions hit the target in a limited region and the target is not uniformly eroded but an erosion groove is formed (Fig. 1.2b). From a practical viewpoint, this is of great importance because the target has to be replaced once a critical thickness is reached. For a standard planar magnetron, this point is reached after approximately 25% of the total target material is removed [DeBosscher99]. The low target utilisation is very cost inefficient, not only because of target price but also because of the down time of the system. As a result, a lot of "exotic configurations" encountered in magnetron sputtering are designed with the aim of reducing the non-uniform target erosion.

Because of its practical importance, determination and/or prediction of the erosion profile has always been a main topic. However, it is very difficult to analytically determine the erosion. As a rule of thumb, the strongest erosion appears where the magnetic field component parallel to the target has its maximum strength [Westwood03]. This is illustrated

in [Ido93a, Ido93b] where the position of the horizontal magnetic field lines is shifted using a "compressing coil", i.e. a solenoidal coil around the target.

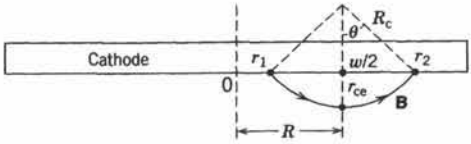

Fig. 1.10 Sketch for the determination of the erosion width: R_c is the radius of curvature of the magnetic field line that reaches a height r_L (in the figure r_{ce}) above the target. This magnetic field line intersects the target at r_1 and r_2. Taken from [Lieberman94].

A simple analytical model has been developed in [Lieberman94]. To estimate the width w of the erosion profile, the behaviour of a HEE is examined (Fig. 1.10). The reasoning is repeated here. It is assumed that the cathode sheath thickness d_S is much smaller then the Larmor radius r_L of the HEE. A HEE is trapped along the magnetic field lines and oscillates back and forth between r_1 and r_2. Hence, its ionisation and the resulting ion bombardment is limited to the region between r_1 and r_2, which implies that w is roughly equal to r_2-r_1. Of course, different magnetic field lines result in different r_1 and r_2. The field line of choice is the one that has height r_L above the target. Given that this magnetic field line has a radius of curvature R_c, it follows that:

$$\frac{w/2}{R_c} = \sin\theta \tag{1.13}$$

and

$$r_L + R_c\cos\theta = R_c \tag{1.14}$$

From these equations, w can be determined as a function of r_L and R_c. A simple solution is obtained for small θ (i.e. $w/2 << R_c$):

$$\frac{w}{2R_c} \approx \theta \tag{1.15}$$

and

$$\frac{2r_L}{R_c} = 2(1-\cos\theta) = 4\left(\sin\frac{\theta}{2}\right)^2 \approx \theta^2 \tag{1.16}$$

By eliminating θ following expression is found as an approximation of the width w:

$$w \approx 2\sqrt{2r_L R_c} \tag{1.17}$$

Given the proportionality of r_L with $v_\perp/B$ (see eq. (1.2)) and given that the electron velocity v is proportional with the square root of the maximum electron energy eV_d, one finds:

$$w \sim \frac{V_d^{1/4}}{B^{1/2}} \tag{1.18}$$

Although experiments show that this dependence is not exact [Wendt90], the model captures the fact that the width of the erosion profile decreases with decreasing discharge voltage and increasing magnetic field strength. Better agreement is obtained assuming a thick sheath [Wendt90]: in this case the maximum height of the electron is not given by r_L but by d_S. Replacing r_L by d_S in eq. (1.17) and using the Child-Langmuir law for d_S (see further, eq. (1.27)), the following dependence for w was deduced:

$$w \sim \frac{V_d^{1/10} I^{1/5}}{B^{4/5}} \tag{1.19}$$

Note that in the above equations B represents the magnetic field strength at the target surface, i.e. what is referred to in this text as B_{max}. According to [Wendt90], this relation gives much better agreement with experimental results but at strong magnetic fields the experimental width w is systematically underestimated. Another shortcoming of the model is the electrical power dependence, which is at low pressures much stronger than predicted by the model.

1.3.2 Discharge voltage

A simple model presented in [Thornton78a] gives an estimate of the MD discharge voltage. It shows that the discharge voltage is influenced by the target material and by the sputter gas. The first because of the influence on the SE emission coefficient γ, the latter because of the influence on both γ and the effective ionisation energy W. However, the model gives no indication of the discharge voltage dependence on the magnetic field strength, the gas pressure or the electric power. Also ionisation in the cathode sheath is disregarded.

The discharge voltage is a characteristic of the MD that is straightforward to measure, and hence, it is one of the most used techniques to characterise the MD. To estimate the discharge voltage in steady state the following reasoning, originally derived for cylindrical or post magnetrons [Thornton78a], can be applied. As mentioned (section 1.1) the MD is maintained by the SE which, due to acceleration into the plasma, become energetic and ionise sputter gas atoms. Given this mechanism, the minimum discharge voltage $V_{d,min}$ needed to maintain the discharge is given by [Thornton78a]:

$$V_{d,\min} = \frac{W}{\gamma_{eff} \varepsilon_i \varepsilon_e} \tag{1.20}$$

with W the effective ionisation energy (in eV), γ_{eff} the amount of SE that effective leave the cathode, ε_i the ion collection efficiency and ε_e the fraction of the theoretical amount of ions that the electron effectively generates before it is lost from the discharge. The theoretical amount of ion-electron pairs is given by $eV_{d,min}/W$. For sufficiently strong magnetic fields, the electrons are trapped in close vicinity of the target. Escape from this trap is only possible through several interactions with the sputter gas. Consequently, ε_e can be considered close to unity. Because of the trapping of the electrons, most ionisation takes place close to the target surface. Hence, the vast majority of the ions reaches the cathode, which implies ε_i practically equal to unity. The effective ionisation energy W varies only slightly for different MD conditions (see section II.2.6.1), a typical value is 30 eV [Thornton78a, Lieberman94]. The only remaining unknown to determine $V_{d,min}$ from eq. (1.20) is γ_{eff}. Experiments with ion beams reveal that for clean metal surfaces, the SE yield γ is typically around 0.1 (section 1.2.2.1). However, a substantial part of these electrons is recaptured by the target in the MD. Consequently, γ_{eff} is given by:

$$\gamma_{eff} = f\gamma \tag{1.21}$$

with f the fraction of the electrons that is not recaptured but effectively interacts with the discharge gas (see Chapter 1 of part II). Thornton estimated that for his cylindrical magnetron with magnetic field strength of 200 G about half of the SE are recaptured. This results in $V_{d,min} = 600$ V, which is indeed close to the typical discharge voltages encountered. However, this neglects the ionisation caused by electrons that are generated in the cathode sheath. This effect can be characterised by the multiplication factor m as will be discussed further (section II.2.4.3). Because of this the effective SE yield is given by:

$$\gamma_{eff} = fm\gamma \tag{1.22}$$

A more advanced model for V_d, taking into account that HEE can leave the discharge is developed in [Wang99]. In the limit of the electrons leaving the discharge with neglectable energy, eq. (1.20) is found back.

1.3.3 Cathode sheath

Where the plasma is in contact with physical borders, e.g. a chamber wall, a plasma sheath is formed. The most important one of the different sheaths is the cathode sheath because it is responsible for the acceleration of the SE into the plasma, and thus, is crucial for maintaining the discharge. Before the complex situation of the cathode sheath of a planar magnetron is considered, more simple situations will be discussed: first the standard low voltage sheath is treated, followed by the standard high voltage sheath. Afterwards, the sheath in the presence of a uniform 1D magnetic field is discussed. Then, the situation of a cathode sheath with a 1D magnetic field will be considered. Finally, the cathode sheath in a typical planar magnetron is contemplated. When discussing plasma sheaths, one should keep in mind the title of a recent article: "*Sheaths: more complicated than you think*" [Hershkowitz05].

1.3.3.1 Low voltage plasma sheaths

When the wall adjacent to a plasma is at a potential of the same order as the plasma potential, a low voltage sheath is formed. Its thickness is of the order of a few Debye lengths. The length of the accompanying presheath is of the order of the ion mean free path.

At the edge of a bounded plasma, a potential exists to contain the more mobile species (in general the electrons). Hence, the plasma will have a higher potential than the surrounding walls. The non-neutral region in front of the walls is referred to as sheath. Assume a plasma with ion (electron) density n_i (n_e), electron temperature kT_e, plasma potential V_p. The plasma makes contact with a wall at potential V_w with V_w of the same order as kT_e. The potential distribution and the ion and electron density vary as sketched in Fig. 1.11. The actual sheath is the part closest to the wall and has a thickness of a few Debye lengths λ_{De}. This Debye length is defined as [Chapman80]:

$$\lambda_{De} = \sqrt{\frac{\varepsilon_0 kT_e}{en_0}} \tag{1.23}$$

with ε_0 the dielectric constant and n_0 the equilibrium density of the ions and electrons in the bulk plasma. In the sheath the electron density drops quickly.

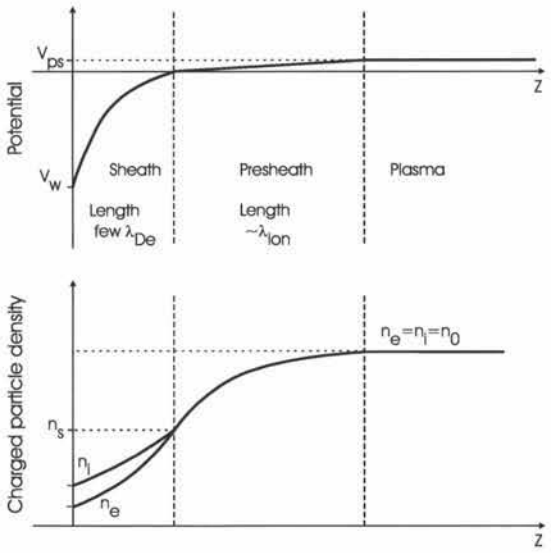

Fig. 1.11 Potential and charged particle density distribution along the direction perpendicular to the wall at potential V_w for a low voltage sheath, i.e. V_w/kT_e small. The figure is based on a similar one in [Lieberman94].

It can be shown that a stable sheath is only possible when the ions enter it with a minimum velocity, the Bohm velocity, given by [Chapman80]:

$$v_B = \sqrt{\frac{kT_e}{M}} \tag{1.24}$$

with M the ion mass. The ions can only acquire the Bohm velocity if a presheath exists with a minimum potential drop V_{ps} equal to $kT_e/2$. This presheath is assumed to be quasi-neutral, i.e. $n_e = n_i$, which implies that the electric field in the presheath is constant. The presheath length is of the order of the ion mean free path λ_{ion}, which is much longer than the Debye length (factor 100 or more). Due to the acceleration in the presheath the charged particle density n_s at the sheath edge is reduced [Chapman80]:

$$n_s = n_0 e^{-\frac{V_{ps}}{kT_e}} \approx 0.61 n_0 \tag{1.25}$$

1.3.3.2 High voltage sheath without magnetic field

For large wall potentials the boundary region can be split in three regions, according to the electron density n_e: in the presheath n_e is equal to the ion density, in the Debye region n_e drops to zero, followed by the electron-free ion sheath. One has to be very careful with the splitting of the sheath region in different parts as these parts "only exist in our minds" [Chapman80].

We consider again the situation of a plasma in front of a wall at a potential V_w (section 1.3.3.1). Assume that the absolute value of V_w is continuously increased. At a certain moment, no electrons can reach the wall anymore. A further increase of V_w will lead to a region in front of the wall with only positive ions, the ion sheath (Fig. 1.12). The region between the presheath and the ion sheath is the Debye region/sheath. The larger V_w, the larger the ion sheath thickness. This thickness can be calculated using the assumption of a space charge limited current, the so-called Child-Langmuir law. The distinction is made between the

physical length of the sheath (d_s) and the modelled length for it (here d_{CL}). The Child-Langmuir law (CL law) relates the current density j_d at the wall, the sheath thickness d_{CL} and the wall potential V_w:

$$j = \frac{4}{9}\varepsilon_0 \left(\frac{2e}{M}\right)^{1/2} \frac{V_w^{3/2}}{d_{CL}^2} \tag{1.26}$$

or alternatively:

$$d_{CL} = \frac{\sqrt{2}}{3}\lambda_{De}\left(\frac{2V_w}{kT_e}\right)^{3/4} = \frac{\sqrt{2}}{3}\lambda_{De}\left(2\phi_w\right)^{3/4} \tag{1.27}$$

with the normalised wall potential ϕ_w defined as $\phi_w = eV_w/kT_e$. The thickness d_{CL} can be substantially longer (up to 100 times and more) than the Debye length.

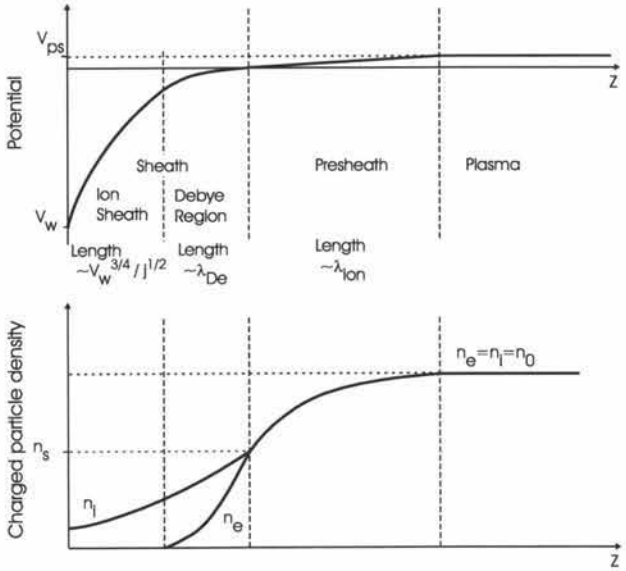

Fig. 1.12 Potential and charged particle density distribution along the direction perpendicular to the wall at potential V_w for a high voltage sheath (large ϕ_w). The figure is based on a similar one in [Lieberman94].

The influence of ϕ_w on the validity of the CL law was studied in [Sheridan89b]. They investigated the region between a low and high voltage sheath by taking into account that a non-zero electron density can exist in the sheath. They found that the zero electron density approximation, needed to deduce the CL law, is accurate within 1% for $\phi_w > 10^4$. The agreement is still acceptable down to $\phi_w \sim 100$. The CL law is compared with experimental results in [Goeckner92]: it is accurate close to the wall but gives poor results near the plasma-sheath boundary.

The CL law can be improved by taking into account the region where the electron density is not zero yet. Such models are presented in [Sheridan89b] and in [Kono04]. In the latter the following expressions are derived for the ion sheath:

$$d_{K,ion} = \left[\frac{\sqrt{2}}{3} \left(\sqrt{1-2\phi_w} - 2 \right)^{3/2} + 2\sqrt{2} \left(\sqrt{1-2\phi_w} - 2 \right)^{1/2} \right] \lambda_{De} \tag{1.28}$$

and for the thickness of the transition region (Debye sheath) is given by:

$$d_{K,De} = 3.411 \lambda_{De}^{4/5} \lambda_{ion}^{1/5} - 0.34 \lambda_{De} \tag{1.29}$$

The total sheath thickness according to Kono is then given by the sum of both contributions:

$$d_{Kono} = d_{K,ion} + d_{K,De} \tag{1.30}$$

The thicknesses d_{CL} and d_{Kono} become equal in the limit of kT_e going to zero. The application of both d_{CL} and d_{Kono} to a MD is discussed in section 1.3.3.5.

1.3.3.3 Plasma sheath in the presence of a 1D magnetic field

For the magnetic field strengths encountered in magnetrons the ion sheath is not influenced. On the other hand, the presheath and Debye sheath are already at low magnetic field strengths magnetised because of the electron density. Experimental measurements of the magnetic field influence are burdened with the difficulty to distinguish between the different parts of the boundary region. Nevertheless, an important observation is the widening of the region containing the largest potential drop with increasing magnetic field strength.

In this part we focus on a plasma sheath in front of a "wall" that has a one dimensional uniform oblique magnetic field in front of it. In the case of a high voltage potential, the boundary region consists of the ion sheath, the Debye sheath and the presheath. As the first is electron free, it is only influenced when the magnetic field influences the ion motion. Such magnetic field strengths are not encountered in MD and will not be considered.

Kim et al. are the first to report a direct measurement of the magnetic effects on presheaths [Kim95]. They distinguish between a collisional and collisionless presheath. The first type, which is encountered in MD, is investigated using an ECR source with N_2 as discharge gas. Nevertheless, the plasma characteristics are similar to the ones in MD: plasma density $10^{10}/cm^3$, electron temperature 3-5 eV, gas pressure 0.75-2 mTorr and magnetic field strength 150-200 G. The plasma potential is measured in the region close to a grounded plate with a uniform oblique magnetic field in front of it. The angle between the normal of the plate and the direction of the magnetic field is given by ψ: for $\psi = 90$ the magnetic field is parallel with the plate. Because of the magnetic field the presheath consists of two parts: a collisional and a magnetic part. The collisional part (length $d_{ps,c}$) is the one next to the actual sheath, the magnetic part (length $d_{ps,m}$) is between the collisional presheath and the bulk plasma. The length of the magnetic part of the presheath fits the expression:

$$d_{ps,m} = K r_{L,is} \sin\psi \sim \frac{1}{B} \tag{1.31}$$

with $r_{L,is}$ the Larmor radius of the ions with the speed of sound and constant $K \approx 0.5$-0.9. For the given plasma characteristics, $d_{ps,m}$ is of the order of some centimetres. The length $d_{ps,c}$ is approximately 0.5-0.6 λ_{ion} with λ_{ion} the ion mean free path length. The potential drop V_{ps} over the presheath is split over the two parts but remains of the order of kT_e, as in the non-magnetised case (eq. (1.25)). Because of the grounded anode plate, these results regard a low voltage sheath.

The only measurements found for a high voltage sheath are the ones of [Singha02]: they measured the potential distribution in front of a negatively biased plate (up to -100 V) with an oblique magnetic field. They split up the boundary region in an unmagnetised collisionless sheath (here called ion sheath), a magnetic presheath (probably what is here called Debye sheath) and a presheath. However, the measurements of the potential distribution show that it is very difficult to distinguish the different regimes. Their results for the magnetic field dependence of the collisionless magnetised presheath length agree with the ones obtained in [Kim95]. The unmagnetised collisionless sheath thickness increases with increasing magnetic field. Increasing the absolute value of the negative bias potential leads to a decrease in the magnetic presheath length.

1.3.3.4 Cathode sheath in the presence of a 1D magnetic field

Increasing the magnetic field at the cathode of an electrical discharge decreases the Larmor radius of the high energy electrons, which is expected to lead to a thinner cathode sheath. Although this behaviour has been observed, this reasoning appears only valid for certain discharge conditions. The sheath can also be insensitive to, or even widen with, an increasing magnetic field.

The cathode of a MD is negatively biased with respect to the plasma (Fig. 1.3). Hence, the situation is similar to the one used in [Singha02] (previous section). However, there is an important difference: in the experiments discussed in the previous section, the biased plate does *not* play a role in maintaining the plasma. Hence, the sheath formed in front of the plate only needs to prevent the more mobile species to escape from the plasma. In contrast, the voltage drop at the cathode has to ensure the maintaining of the discharge. Consequently, when one of the external parameters (e.g. magnetic field, discharge voltage) at the cathode is changed, the plasma characteristics (charged particle density, current density, electron temperature) change too, making it difficult to isolate the influence of that parameter on the sheath.

Kuwahara and Fujiyama describe a MD with a uniform magnetic field parallel to the cathode [Kuwahara94, Fujiyama95, Kuwahara98]. In this case the magnetron consists of three parallel plates of which the middle one is negatively biased with respect to the two outer ones. A magnetic field is created by the use of a Helmholtz coil. Measurements of the cathode fall thickness, defined as the length between the cathode and the position of the maximum in the light emission from the plasma, are presented. The cathode fall thickness is represented in this text by Δ (section 1.3.3.5). They report $\Delta = 16$ mm (0.67 Pa, 86 G, 0.05 mA/cm^2). The actual sheath is reported to be approximately 3.7 mm, which is approximately the Larmor radius corresponding with the average energy of the HEE [Kuwahara98]. Most of the ionisation occurs in the region 7 to 16 mm above the cathode. In [Kuwahara94], measurements of Δ show a decrease from 75 to 7 mm with increasing magnetic field from 10 to 190 G (30 mTorr, 550 V). The current density varied from 0.003 to 1 mA/cm^2 and is modelled using the CL law in which the cathode sheath thickness d_{CL} is replaced by the Larmor radius corresponding with the average energy of the HEE.

Hence, the length of the cathode sheath seems to be related to the Larmor radius of the HEE for the investigated discharge conditions. This is not so surprising: in diode discharges, the cathode sheath thickness is related to the mean free path of the HEE because the electrons are accelerated away from the cathode in a straight line. In case of a magnetic field in front of the cathode, the electrons are bound by the magnetic field lines and the height they can reach, and hence the position where they ionise for the first time, is determined by their Larmor radius instead of the mean free path. With increasing magnetic field, the discharge is

contained in a smaller area closer to the cathode, leading to higher plasma densities. This explains why the sheath thickness reduces with increasing magnetic field strength.

Unfortunately, the situation is more complex because the decrease of the cathode sheath thickness with magnetic field does not seem to hold for all circumstances. Cylindrical or post magnetrons also have a uniform 1D magnetic field when the magnetic field is generated by an external Helmholtz coil, which is usually the case. Measurements of the cathode sheath thickness as a function of the magnetic field in the case of a uniform B-field are reported in [Yeom89, Vanderstraaten98b, Behnke00]. In [Vanderstraaten98b] the floating potential was found to be relative insensitive to magnetic field changes from 266 to 532 G at 4.65 mTorr and from 348 to 674 G at 1.2 mTorr. In [Behnke00] sheath thicknesses of approximately 5 mm (4 Pa, 150-350 G, 125 mA) are reported. With increasing magnetic field, the spatial extension of the potential drop at the cathode increases, in agreement with the measurements in [Yeom89] where a slight increase in the thickness was observed when the magnetic field was increased from 100 to 200 G.

This increase in sheath thickness with increasing magnetic field was modelled in [Lister96]: a 1D model was used to asses the effect of the magnetic field on the sheath. The model is similar to the CL law but it does not neglect the electron current in the sheath. Lister differentiates between classical and Bohm mobility (section 1.3.6.2). He deduced that the sheath thickness should increase with magnetic field strength if the classical electron mobility is valid. For Bohm electron mobility, the sheath should be independent of the magnetic field strength.

1.3.3.5 Cathode sheath in planar magnetron discharges

Given the shape and strength of the magnetic field in planar magnetrons, the cathode sheath is difficult to describe analytically. The Child-Langmuir law cannot be applied as such because of the relatively small V_d to kT_e ratio, the non-uniform current, the sheath ionisation and the non-zero electron density in the sheath. The cathode sheath thickness is typically one to two millimetres; the electric field is linear and has a maximum value at the cathode of typically 500 V/mm or more.

A. Definition

A first difficulty with defining the cathode sheath in a MD is that because of the non-uniform magnetic field, the plasma and current density are also non-uniform. This implies that the sheath thickness will vary along the target. Conventionally, the "sheath thickness" of a MD stands for the sheath thickness at the point where the plasma is the most intense and the sheath the thinnest. By definition, the sheath region is the region where there is a net electric charge.

In diode discharges, the electric field is linear in the cathode sheath as mentioned in [Lieberman94]. Also in [Chapman80] the spatial variation of the electric field in the cathode sheath is discussed. Choi et al. measured the electric field near the cathode in a planar MD and reported a linear electric field [Choi96]. This is confirmed by self-consistent simulations [Nanbu97], although the linearity is not exact. On the other hand, in the presheath the electric field is constant because of the quasi-neutrality. Hence, the transition from sheath to presheath is marked by a change in the slope of the plasma potential. The cathode sheath thickness defined this way is referred to as d_E in this text. In reality, the transition from quasi-neutral to non-neutral can occur gradually and is sometimes difficult to retrieve.

Another concept used to denote the cathode sheath is the dark space (thickness d_{ds}). It is defined as the region in front of the cathode where no plasma glow is observed. In

magnetron sputtering the situation is in principle the same as in diode discharges: close to the cathode there is a region where the electrons cannot ionise yet. However, given the electron trapping in the vicinity of the target and the strong magnetic fields this dark space is very thin. Typical electric field strengths at the target are in the order of 500 V/mm or more. Hence, the energy of maximum cross section for ionisation (100 eV) is already reached after 0.2 mm and the concept of dark space is not so useful.

To get more information about the cathode sheath of a MD, it is more interesting to investigate another optical property of the magnetron plasma: the position of the maximum in the light emission. The height of this maximum above the target is represented by Δ.

B. Sheath Dimensions

As mentioned, d_E can be determined from plasma potential measurements. An example is given in [Shidoji94]: d_E is approximately 3 mm for a rectangular target (0.4 Pa, B_{max} = 250 G, 400 V). Rossnagel and Kaufman also measured the plasma potential and report d_E = 5 and 1.2 mm for 5 and 30 mTorr, respectively (B_{max} = 165 G, 0.1 A, target diameter not mentioned but >110 mm) [Rossnagel86]. They mention that the potential distribution in the actual sheath is difficult to probe: when measuring in the sheath the discharge voltage increases in constant current mode. They stopped measuring when the increase was higher than 10%. In [Bradley98a] it is mentioned that when the probe was close to the target (<4 mm) the discharge current was decreased (up to 30%) in constant voltage mode. Also in [Špatenka97] difficulties are mentioned when measuring close to the cathode.

A direct measurement of d_E, based on LIF (Laser Induced Fluorescence) is given in [Bowden93]: d_E-values are 1.7, 2.2 and 3.1 mm (+/-0.3 mm) for B_{max} = 450, 400 and 200 G respectively (50 mTorr, I_d= 40 mA, stainless steel target with diameter 100 mm).

Reports of the dark space thickness d_{ds} are given in [Rossnagel87b]: the thickness decreases with increasing pressure and discharge voltage, measured thicknesses vary from 1.0 to 0.3 mm. The proposed relation between d_{ds} and V_d at constant pressure is:

$$d_{ds} = aV_d^m \qquad (1.32)$$

with m ranging from -3.9 at 3 mTorr to -5.8 at 10 mTorr. Gvozdev et al. also reported that at constant pressure the dark space increases with decreasing discharge voltage [Gvozdev98]. Typical thicknesses are in the region 0.5 to 1 mm, reaching up to 2 mm at low pressures (2 mTorr) and low discharge voltage (330 V).

Experimental measurements of Δ are reported in [LanGu88]: Δ varies from roughly 4.0 to 1.5 mm for magnetic fields varying from 100 to 600 G (5 and 10 mTorr, 0.5 A, 9-inch target) and from 5.0 to 2.8 mm for magnetic fields varying from 100 to 900 G (5 mTorr, 0.1 A, same target). Miyake et al. measured Δ using emission-selected computer-tomography: they reported the maximum in emission at 3.1, 1.3 and 0.6 mm at 0.3, 1 and 10 Pa, respectively, at low current: 40 mA on a 100 mm diameter Al target [Miyake92].

The quantities d_E and Δ are also obtained in self-consistent simulations. Shidoji et al. investigated the dependence of the MD on the pressure [Shidoji01a]. Also the influence of the balancing [Shidoji01b] and the strength of the magnetic field [Shidoji03] on the discharge are investigated. From the simulations of Kondo et al. d_E and Δ as a function of magnetic field [Nanbu97, Kondo99a, Kondo01], discharge voltage [Kondo01], pressure [Nanbu97] and SE yield [Kondo99a] can be deduced. An overview of all these self-consistent results is given in Table 1.2. For the magnetic field dependence, the scaling proposed by Lan Gu (eq. (1.33)) is

confirmed [Nanbu97, Kondo99a]. A general remark is that the simulated cathode sheath thicknesses (2 to 9 mm) are (very) large compared to the experimental measurements.

p (Pa)	B_{max} (G)	I_d (mA)	V_d (V)	γ	d_E (mm)	Δ (mm)	Reference
0.67	175	73.3	500	0.12	7.00	9.80	[Nanbu97]
0.67	350	187.8	500	0.12	3.90	4.40	
0.67	700	226.9	500	0.12	2.90	2.20	
0.33	350	160.2	500	0.12	4.10	8.40	
0.67	325	34.9	500	0.12	5.80	7.20	[Kondo99a]
0.67	487.5	45.9	500	0.12	4.80	5.20	
0.67	650	46.2	500	0.12	4.50	4.40	
0.67	325	49.5	500	0.15	5.00	5.40	
0.67	162.5	21.8	300	0.12	3.20	4.10	[Kondo01]
0.67	162.5	28.2	400	0.12	4.10	4.40	
0.67	162.5	15.6	500	0.12	6.90	6.90	
0.67	162.5	13.4	600	0.12	9.10	9.40	
0.67	325	74.5	300	0.12	2.00	2.20	
4.00	110	0.4	160	0.1	4.00	5.00	[Shidoji99a]
0.67	100	-	340	0.17	5.30	5.00	[Shidoji01a]
0.67	240	-	240	0.12	2.40	2.00	
0.67	180.00	7.00	200	0.10	4.00	4.00	[Shidoji03]
0.67	360.00	8.10	170	0.085	3.00	2.00	

Table 1.2 Overview of self-consistent simulation results. Listed are the gas pressure p, the magnetic field strength B_{max}, the discharge current I_d, the discharge voltage V_d, the SE yield γ, the cathode sheath thickness d_E (based on the electric field) and Δ (based on the ionisation rate). The results are obtained using 2D models except for [Nanbu97] where a 3D rectangular magnetron geometry is used.

C. Sheath Models

A first trial to model the cathode sheath thickness, given the results for the 1D magnetic field, is to investigate whether the thickness is again related to the Larmor radius of the HEE. Because of the typical curvature of the magnetic field (Fig. 1.2), this is not the case: the maximum height an electron can reach depends on its starting position as the HEE follow the magnetic field lines. Hence, the height at which the electrons ionise the first time varies according to their emission position. Consequently, the cathode sheath thickness is not related to the Larmor radius, as confirmed by the measurements of [LanGu88].

A point of interest is whether the cathode sheath can be considered collisionless or not. According to [Sheridan91b], to determine the thickness of a plasma sheath, it can be considered collisionless when the thickness is smaller than five times the mean free path length of the ions. Given the typical sheath thicknesses (<3 mm) and the ion mean free path lengths ($\approx$ 8 mm) (section 1.2.1.1.C), the collisionless regime can be assumed. Even the ion energy for impact at the cathode will hardly be influenced because for this the limit is one-half of the mean free path length.

Applying the CL law is not straightforward: in principle the ion current density of the centre is needed but this quantity is not known because of the non-uniform current density. A typical way around the problem is to use the average current density. As the current density varies very strongly over the race-track area the validity of this approach can be questioned. Another problem is that, regardless of the magnetic field, the CL law becomes less accurate for ϕ_w<100 (section 1.3.3.2). In MD the electron temperature is usually around 5 eV, which means that the discharge voltage should be at least 500 V. Hence, for standard discharge voltages (300 to 400 V), the CL law is at the edge of its applicability. The situation is even

more problematic because the electrons are trapped by the magnetic field, violating the assumption of zero electron density in the sheath.

Given the range for the cathode sheath thickness, the question appears whether a MD has a thin or thick sheath. These terms were used in [Wendt90] to describe the relation between the cathode sheath and the Larmor radius of the HEE. If d_E is thinner than r_L, it is referred to as a thin sheath. The opposite case is referred to as thick sheath (see also section II.2.1). Typical Larmor radii are from 6 to 1 mm for magnetic field strength from 100 to 600 G. As the corresponding Δ-values are 4 and 1.5 mm (see section 1.3.3.4B), it is clear that the magnetron discharge has a thick sheath, except for the weakest magnetic fields. Wendt et al. found that the dependence of the erosion width agreed indeed much better when using a thick instead of a thin sheath model [Wendt90]. This means that sheath ionisation, i.e. the generation of ions in the sheath, occurs. This violates the assumption of a source-free sheath, which is required for the deduction of the CL law.

In spite of the problems with the application of the CL law, Lan Gu and Lieberman tried to model their results using an adapted CL law [LanGu88]: they accounted for the dependence of the race-track width, and hence of the average current density, on the magnetic field and discharge voltage. Their resulting scaling law for the cathode sheath thickness d_{GL} is:

$$d_{GL} = C\frac{V_d^{7/8}}{I^{1/2}B^{1/4}} \tag{1.33}$$

with C a constant depending on the magnetic field geometry. The sheath thickness d_{GL} is roughly half of the measured Δ-values. However, some deviation of the scaling is seen for lower currents and very high magnetic fields.

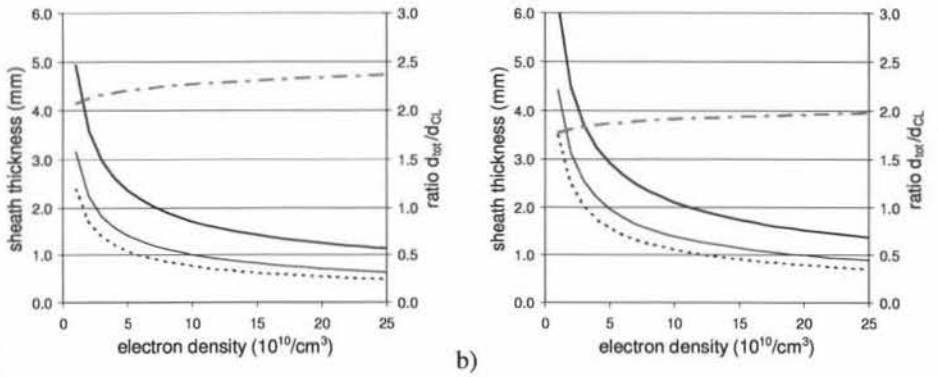

Fig. 1.13 Comparison of the sheath thickness d_{CL} obtained with eq. (1.27) (thick solid line), $d_{K,ion}$ obtained with eq. (1. 28) (thin solid line) and d_{Kono} obtained with eq. (1.30) (dotted line) as a function of the electron density for V_d = 300 V (*a*) and 500 V (*b*). The electron temperature is set to 10 eV and the gas pressure to 0.5 Pa. The ratio d_{Kono}/d_{CL} is also plotted (dash-dotted line, right vertical axis).

The fact that d_{GL} is on the order of half the observed Δ-values should be related to the fact that the CL law does not take into account the Debye sheath. Hence, the sheath thickness d_{Kono} (eq. (1.30)) is more appropriate to use. The thicknesses d_{CL}, d_{Kono} and $d_{K,ion}$ (eq. (1.28)) and the ratio d_{Kono}/d_{CL} are plotted in Fig. 1.13 as a function of the electron density in the range 1-25×10^{10}/cm^3 for V_d = 300 and 500 V. To calculate λ_{ion}, needed for d_{Kono}, the pressure is assumed to be 0.5 Pa. Hence, the highest electron density (25×10^{10}/cm^3) corresponds with

an ionisation degree of 0.2 %. The electron temperature is set to 10 eV. This might seem high but measurements show that the electron temperature increases towards the cathode sheath (section 1.3.5.6). It is interesting to see that d_{Kono} is approximately a factor two larger than d_{CL}. This agrees rather well with the results in [LanGu88] that Δ is twice as large as d_{GL} and confirms that the inaccuracy of the CL law is partially due to the assumption of an electron-free sheath.

1.3.4 Current-voltage characteristic

The typical $I_d = kV_d^n$ formula is a good fitting formula for the current-voltage characteristic (IV) but, unfortunately, it has no physical background. Models for the IV based on a physical reasoning appear only valid for specific magnetron discharge conditions.

1.3.4.1 Typical current-voltage characteristic

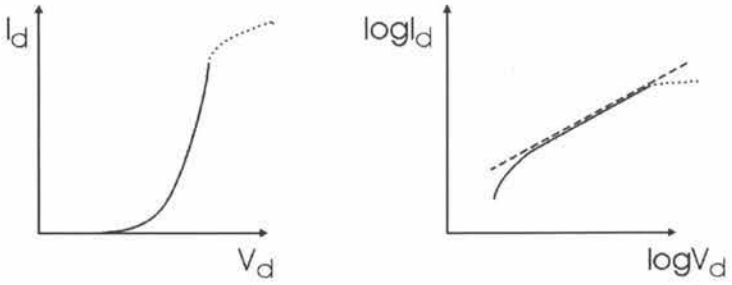

Fig. 1.14 Sketch of a typical current-voltage relation (IV) of a MD, both for standard (*a*) and logarithmic scales (*b*). In the latter the exponential increase of I_d with V_d is indicated by the dashed line. At high powers, the IV can change dramatically: a large increase of V_d becomes necessary for a small increase in current (indicated by the dotted line). At low powers the discharge current decreases typically stronger with decreasing discharge voltage.

The relationship between the discharge current I_d and the discharge voltage V_d of a MD is referred to as the current-voltage characteristic or IV. A typical IV is shown in Fig. 1.14a: at low currents, a relatively strong increase in the discharge voltage is needed to increase the current while at high currents the current can increase strongly at almost constant discharge voltage. Except for the extremities, the $\log I_d$-$\log V_d$ plot (Fig. 1.14b) reveals a linear relationship between $\log I_d$ and $\log V_d$. Based on this dependence Thornton proposed the following relationship [Thornton78a]:

$$I_d = kV_d^n \tag{1.34}$$

with k and n constants. The value n is typically in the range 5 to 15.

From practical/economical viewpoint of sputter deposition it is desired to have a high deposition speed at low electrical power input. Hence, if the dependence of the sputter yield on the ion energy is sublinear, it is favourable to have a high discharge current at relatively low discharge voltages. This means a very steep IV, which corresponds with a high n in eq. (1.34). For diode discharges, the IV is given by [Maniv82]:

$$I_d \sim (V_d - V_0)^{3/2} \tag{1.35}$$

with V_0 the minimum discharge voltage at which the discharge can be maintained. Hence, the n-value of the IV allows for checking whether the magnetron is really working as a magnetron or whether it behaves as a diode discharge. Consequently, n is sometimes referred

to as the efficiency of the magnetron and can be interpreted as a number indicating the trapping of the SE [Waits78].

The constants k and n are determined by the magnetron configuration (e.g. B-field, geometry, anode position) and by the process parameters (e.g. gas pressure and composition, target material). Although it is generally accepted that n increases with increasing magnetic field strength and increasing pressure, e.g. [Maniv80, Nyaiesh81, Wendt90], exceptions exist. This together with the behaviour of the IV at the extremities is discussed more extensively in section 1.4.

1.3.4.2 Explanation for the standard characteristic

Relationship (1.34) was based on experimental measurements, there is no physical model behind it. Rossnagel and Kaufman did some trials to make the relationship physically meaningful. In [Rossnagel87b] it is shown that the CL law and eq. (1.34) are basically the same when taking into account eq. (1.32), the relationship between the sheath thickness d_{ds} and the discharge voltage V_d. Substituting this relation in the CL law (eq. (1.26)) results in an expression for the current density j as a function of V_d:

$$j \sim V_d^{1.5-2m} \tag{1.36}$$

The experimental values for m (see below eq. (1.32)) result in realistic n-values. However, for more accuracy it should be taken into account that the current density j and the discharge current are not just proportional: instead eq. (1.19) should be used, leading to:

$$I \sim V_d^{1.25(1.5-2m+0.1)} \tag{1.37}$$

Hence, the exponent n is split up in three contributions: the CL law, the dependence of the sheath on the discharge voltage and the dependence of the race-track width on the discharge voltage.

Another trial to model eq. (1.34) was performed assuming that the IV is mainly the result of gas rarefaction [Rossnagel88b]. The basis of the gas density reduction is discussed in section 1.4.3. Using the gas density reduction model, it was explained why n is material dependent: metals with a high sputter yield are sputtered more for the same discharge current which leads to a stronger gas rarefaction. This reduces the increase of the current, resulting in a lower n for materials with a large sputter yield. According to [Rossnagel88b] the relative reduction of the gas pressure enlarges with increasing gas pressure. Hence, the effect of the gas density reduction on the n-value should be the strongest at high pressures. Nevertheless, they report that n increases from 10.1 to 14 when the pressure increases from 3 to 10 mTorr.

1.3.4.3 Other models

Another approach for modelling the IV of a MD can be found in [Westwood83]. Starting from the experimental observations from Soxman (Ref. 4 in [Westwood83]), the following relation is proposed:

$$I_d = \beta\left(V_d - V_0\right)^2 \tag{1.38}$$

with β and V_0 constants for the given discharge parameters. In [Westwood83] the constants V_0 and β could be given a physical meaning. V_0 is the minimum discharge voltage needed to sustain the discharge as determined in eq. (1.20). The constant β is given by:

$$\beta \sim \frac{w\mu_{\perp}}{d_{ds}^3} \tag{1.39}$$

with d_{ds} the dark space/sheath length as used in the CL law, $\mu_{\perp}$ the electron mobility in the direction perpendicular to the magnetic field lines and w the race-track width. Hence, the calculation of the current is based on the electron current towards the anode.

Westwood and Maniv report the good agreement between the experimental results and eq. (1.38) [Westwood83]: the parameter V_0 decreases with increasing pressure as could be expected. Moreover, their experimental values for β increase with increasing pressure, consistent with eq. (1.39): when the pressure increases, $\mu_{\perp}$ will increase and d_{ds} will decrease. Kelly and Arnell tested this model for the IV [Kelly98]: although they could fit their IVs with eq. (1.38), the pressure dependence of both V_0 and β was rather irregular and material dependent. Also Depla et al. fitted their experimentally obtained IVs using eq. (1.38) [Depla05a]. They investigated the pressure dependence of β: at low magnetic fields β is found to decrease with decreasing pressure but at stronger magnetic fields β displays a rather constant value at high pressure and it increases strongly at low pressures. This pressure dependence conflicts with eq. (1.39), i.e. with the physical interpretation assigned to β in [Westwood83].

Another problem of the relationship is its magnetic field dependence. The sheath thickness decreases with the magnetic field strength: $\sim 1/B^{0.25}$ (eq. (1.33)). The electron mobility decreases for increasing magnetic field: $\sim 1/B^2$ for classical diffusion and $\sim 1/B$ for Bohm diffusion. Hence, according to eq. (1.39), β should decrease with increasing magnetic field, even when Bohm diffusion is assumed. However, experiments show that the IV becomes steeper with increasing magnetic field [Nyaiesh81, Wendt90, Depla05a], which indicates that also β should increase. Hence, also the experimentally measured magnetic field dependence of β at constant pressure conflicts with eq. (1.39), another indication that the physical interpretation given to β is very questionable.

Guimarães and Bretagne developed an interesting model for the IV of a MD [Guimarães91]: they related the electron current I_e, the current caused by the emission of SE from the target, with the discharge current I_d. At the cathode the relation between both is:

$$I_d = I_i + I_e = (1+\gamma) I_i \tag{1.40}$$

which leads to :

$$I_e = \frac{\gamma}{1+\gamma} I_d \tag{1.41}$$

with γ the SE yield. To deduce I_d at the anode from I_e at the cathode they developed a model to calculate the electron energy distribution function (EEDF) taking into account electron interactions with argon atoms and ions and other electrons. Two loss mechanisms for electrons are considered: electron-ion recombination and the scattering of electrons out of the plasma region. The latter happens when an electron undergoes a collision within the border of the discharge. The thickness of the border region is of the order of the Larmor radius. The discharge current I_d is then given by the amount of collisions occurring in the border region of the plasma and no electric field is needed to extract the electrons from the plasma. The ratios found for I_e/I_d in this way are in good agreement with the ones deduced from eq. (1.41) using $\gamma = 0.07$, the SE yield of molybdenum for which the model was applied. Hence, the electron

current to anode is calculated without the electric field in the bulk region or the electron diffusion coefficient across the magnetic field lines.

Kuwahara and Fujiyama report the IVs of a multi-target planar magnetron with a uniform but rather weak (<200 G) magnetic field [Kuwahara94]. They proposed a model for the IV based on the CL law (eq. (1.26)) in which the sheath thickness d_{CL} was replaced by the Larmor radius corresponding with the average energy of the high energy electrons in the discharge. The wall potential V_w is replaced by V_d-V_0, with V_0 the "*voltage at J=0 on the prolongation of the current-voltage characteristic*". Hence, they find basically the same IV as for the diode discharge (eq. (1.35)).

1.3.4.4 Non-typical magnetron discharge conditions/configurations

It is also interesting to look at the IVs measured in "non-standard" magnetron conditions as they sometimes reveal interesting characteristics. Wang and Cohen reported IVs for a hollow cathode magnetron [Wang99]: for high pressures the results could be fitted using eq. (1.34), for low pressures they used the expression

$$I_d = k\left(V_d - V_r\right)^n \tag{1.42}$$

Note that the voltage V_r is not the same as V_0: "*The physical meaning of V_r has something to do with the residual energy of a primary electron leaving the plasma*" [Wang99]. V_r is approximately 350 V and higher below 1 mTorr and drops sharply to become zero around 5 mTorr.

Musil and co-workers investigated the influence of holes (∅ 2 mm) in the target through which the discharge gas was fed [Musil01]: the hollow cathode discharges created in the holes enabled magnetron operation at lower discharge voltages and at lower pressures. The influence of the race-track length on the IV was investigated in [Musil99]: for a given target they recorded the IV of one short discharge, one long discharge and two short, simultaneously run discharges and concluded that the longer the race-track length, the lower the discharge voltage needed to draw a certain discharge current.

Posadowski and Radzimski measured IVs in the case of high power/self-sustained sputtering [Posadowski93]. For materials that can be run in self-sustained mode (Ag and Cu) the discharge voltage saturates with increasing discharge current and even decreases again at high currents. For materials that cannot be run in self-sustained mode (Al) such a saturation is not observed: the slope $\Delta I_d/\Delta V_d$ remains practically constant. Posadowski reported the influence of the B-field, target diameter and thickness on the IVs in the case of high power sputtering of Cu and Ni [Posadowski01, Posadowski04]. These IVs show as well positive as negative $\Delta I_d/\Delta V_d$ values and do not fit eq. (1.34) at all.

Cuomo and Rossnagel measured the IV of a magnetron in which electrons (from a hollow cathode discharge) were injected: for large enough electron addition in the magnetic trap of the discharge, large currents (>1 A) could be achieved for discharge voltages as low as 30 V [Cuomo86].

Bradley and Cecconello used an unbalanced magnetron to study IVs [Bradley98b]. For a new target, i.e. no erosion groove formed yet, the measured IVs could be fitted using eq. (1.38). However, as the erosion profile evolved with time a change in the IV occurred: below -600 V the discharge current increased (up to a factor two) compared with the non-eroded target. At higher V_d the effective plasma impedance was negative and the I_d decreased

with increasing V_d. By drilling holes in the target they could increase the discharge current by a factor 1.8 at a given discharge voltage and working pressure.

1.3.4.5 Simulation results

Simulations of the IV are scarce. Shidoji et al. reproduced an IV [Shidoji01a]: compared with experiments it appeared that the IV was shifted to lower discharge voltages. A good result was obtained when the SE yield was reduced by a factor two. Although Shidoji et al. found this an unrealistic solution, recapture of SE can very well account for this low SE yield (section 1.2.2.3). Also Kondo and Nanbu simulated an IV [Kondo01]. They report a negative slope, i.e. the discharge current decreases with increasing discharge voltage above 400 V. They attributed this effect to the short cathode-anode spacing (20 mm) used in the simulation.

1.3.5 Bulk plasma characteristics

The term "bulk plasma" is used here to define the plasma region that is neutral or quasi-neutral. Hence, it is the MD region except for the cathode sheath. A first problem when describing the bulk plasma is that the region is not uniform at all: the further away from the cathode, the smaller the charged particle density. This will also influence other plasma characteristics, making this region difficult to characterise. The extension of the bulk plasma is determined by the anode and the balancing of the field. For a balanced magnetic field, the situation is sketched in Fig. 1.15a: because the electrons follow the magnetic field lines, the anode extends along the magnetic field line that it intersects. This way a virtual anode is created and the MD is limited to a well-defined region. However, the plasma can also be allowed to spread out (Fig. 1.15b). Unfortunately, the anode position and the balancing of the magnetic field are aspects of the magnetron that tend to be neglected when documenting the magnetron properties, which makes it difficult to clarify their role in the reported experiments.

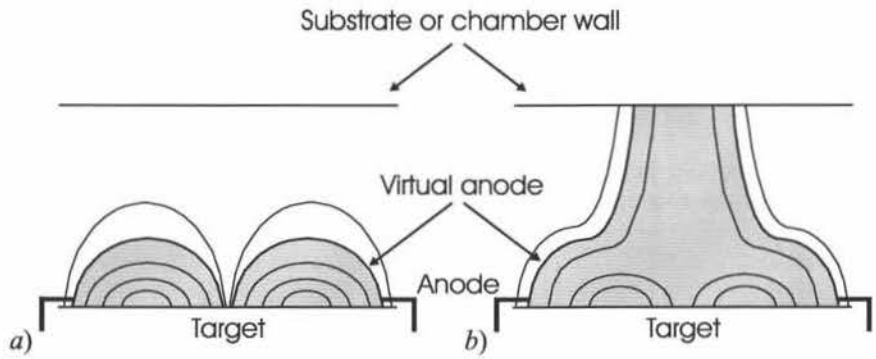

Fig. 1.15 Sketch of the bulk plasma region as bounded by the virtual anode for a balanced (*a*) and unbalanced (*b*) magnetron. For the balanced magnetron the plasma is limited to a well-defined region whereas the plasma region in an unbalanced magnetron is not limited by the virtual anode. Hence, it needs another boundary, e.g. the substrate or chamber wall.

First, the spatial profile of the plasma (section 1.3.5.1), the plasma density (section 1.3.5.2) and the sputtered particle density in a MD (section 1.3.5.3) are discussed. This is followed by the potential distribution in the bulk region (section 1.3.5.4). Afterwards, the ion and electron energies are treated (sections 1.3.5.5 and 1.3.5.6, respectively).

1.3.5.1 Spatial profile

To assess the distribution of the plasma in a MD, the plasma emission of the different species (argon atoms and ions and sputtered particle atoms and ions) can be used because it allows determination of their relative density in the discharge. The techniques used are plasma emission monitoring, optical emission spectroscopy, computer-tomography or laser-induced fluorescence.

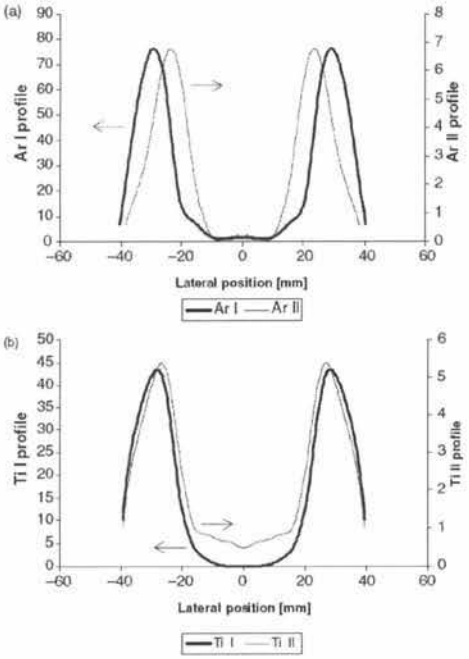

Fig. 1.16 Profiles of plasma emissivity at 2.5 mm above the target for argon (*a*) and titanium emission (*b*) at 5 Pa and 18.6 W and B_{max} = 300 G. The bold line is the atomic emission, the thin line the ionic emission. Taken from [Christou02].

One would expect the radial argon ion density to reflect the erosion profile, because the ions are accelerated in a straight line to the target where they cause the erosion. This is confirmed in [Debal98] where it is reported that the emission of the ArI (argon atoms) and the AlI (aluminium atoms) lines is similar and can be correlated with the erosion profile (50 mTorr, 0.133 A). However, in [Christou02] the MD in the case of Ti sputtering in argon (5 Pa, 18.6 W) is studied. They recorded a two-dimensional profile for the emission lines ArI (argon atoms), ArII (argon ions), TiI (Ti atoms) and TiII (Ti ions). They report that for both Ar and Ti the radial distribution of the atoms is radially more outward than the one from the ions (Fig. 1.16). The radial shift is attributed to the temperature gradient in the plasma: at the edges the temperature is lower which leads to relatively less ions. Based on this work there should be a small discrepancy between the atomic emission profile (Ar and/or Ti) and the erosion profile.

The pressure dependence on the 2D spatially-resolved emission of a MD is reported in [Debal00] for aluminium sputtering in an argon/nitrogen mixture: increasing the total pressure from 50 to 150 mTorr brings the Ar emission clearly closer to the target whereas it hardly affects the Al emission. In pure argon, a power increase at 50 mTorr from 20 to 60 W had

practically no influence on the distribution. From their measurements it follows that the emission of Al is radially slightly more outward than the one of Ar.

1.3.5.2 Plasma density

Typical plasma densities in a MD are around 10^{10}-10^{11}/cm^3, depending on the discharge current density. For a given current density, the plasma density is practically independent of the gas pressure. Consequently, the maximum ionisation degree, which is below 1%, decreases with increasing pressure.

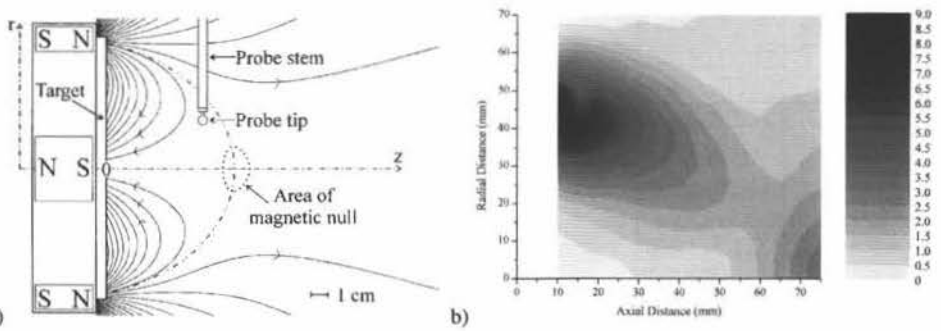

Fig. 1.17 *a*) Schematic diagram of the magnetron showing the magnetic field configuration and the emissive probe. The broken line represents the boundary between the open and closed field lines. *b*) The corresponding ion density in the bulk plasma at 0.26 Pa and V_d = 330 V. The ion density increases towards the region of the magnetic trap. A local maximum occurs in the area of the magnetic null. Taken from [Bradley01].

An important property of the plasma is the charged particle density. This density can also be expressed using the ionisation degree, the ratio of the charged and neutral densities. The absolute density of the charged particles can be measured using a Langmuir-probe (LP) or using optical absorption measurements. An example of a 2D spatial overview of the ion density is reported in [Bradley01]. The magnetron configuration and measured ion density distribution are reproduced in Fig. 1.17: as expected the ion density increases towards the region where the HEE are trapped. The blank region close to the cathode is due to the measurement difficulties encountered there as mentioned before (section 1.3.3.5).

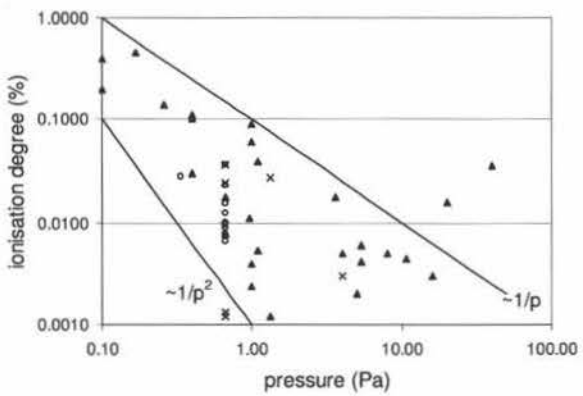

Fig. 1.18 The ionisation degree (in %) as a function of gas pressure based on the data of Table 1.3. The symbols differentiate between experimental results (▲) and self-consistent simulation results from Shidoji et al. (×) and Kondo and Nanbu (○). The full lines indicate a pressure dependence $1/p$ and $1/p^2$.

p (Pa)	B_{max} (G)	I_d (A)	V_d (V)	P (W)	n (10^{10}/cm^3)	z (mm)	ID (%)	kT_e (eV)	comment	Reference
Experimental results										
0.67	165.00	0.10			1.30	8.00	0.0078	23.00	peak	[Rossnagel86]
4.00	165.00	0.10			5.00	2.00	0.0050	6.00	peak	
40.00	280.00		-450		350.00	5.00	0.0350	8.00	peak	[Fujita86]
1.10	245.00	0.05			1.49	6.80	0.0054	4.50	II	[Sheridan89a]
1.10		0.30			10.50	6.80	0.0382	3.10	II	
0.96	245.00	0.15	-400	60	2.70	10.00	0.0113	3.00	II	[Goeckner90]
0.10	245.00	0.02	-400	8	5.00	10.00	0.2000	-	II	[Sheridan90b]
20.00	245.00	0.60	-400	240	80.00	10.00	0.0160	-	II	
1.33			-400		0.40	5.00	0.0012	-	peak	[Ido93a]
0.40		1.00			10.00	75.00	0.1000	5.50	II	[Ivanov94]
5.33		0.03			8.00	10.00	0.0060	-		[Dony95]
8.00		0.03			10.00	10.00	0.0050	-		
10.67		0.03			12.00	10.00	0.0045	-		
16.00		0.03			12.00	10.00	0.0030	-		
1.00	245.00	0.05	-400	20	0.60	25.00	0.0024	2.00	II	[Sheridan95]
0.17	250.00	1.00			19.20	10.00	0.4608	6.50		[Bradley96]
0.40		0.75			3.00	15.00	0.0300	1.00		[Spatenka97]
5.00		0.75			2.50	20.00	0.0020	0.40		
0.10		2.00	-400	800	10.00	230.00	0.4000	7.00	II,peak, rectangular	[Serianni00]
1.00	300.00			300	15.00	13.00	0.0600	2.30	II	[Martines01]
1.00	300.00			500	22.50	13.00	0.0900	2.30	II	
1.00	300.00			40	1.00	13.00	0.0040	2.20	II	
0.26	300.00	0.50	-330	165	9.00	10.00	0.1385	8.00	II	[Bradley01]
0.67	214.00	0.60	-575	345	3.00	30.00	0.0180	3.50	rectangular	[Field02]
5.33	214.00	0.60	-409	245	5.50	30.00	0.0041	1.70		
0.40	300.00		-350		11.00	70.00	0.1100	3.25	II	[Seo04b]
3.60	300.00		-350		16.00	70.00	0.0178	3.25	II	
Self-consistent simulation results										
0.67	175.00	73.30	500	37	2.10	10.00	0.0126	-	rectangular	[Nanbu97]
0.67	350.00	187.80	500	94	2.60	4.00	0.0156	-	rectangular	
0.67	700.00	226.90	500	113	1.60	2.00	0.0096	-	rectangular	
0.33	350.00	160.20	500	80	2.30	10.00	0.0276	-	rectangular	
0.67	325.00	34.90	500	17	1.10	8.00	0.0066	-		[Kondo99a]
0.67	487.50	45.90	500	23	1.30	5.00	0.0078	-		
0.67	650.00	46.20	500	23	1.60	4.00	0.0096	-		
0.67	325.00	49.50	500	25	1.70	5.50	0.0102	-		
0.67	162.50	21.80	300	7	2.60	4.00	0.0156	-		[Kondo01]
0.67	162.50	28.20	400	11	3.80	5.00	0.0228	-		
0.67	162.50	15.60	500	8	1.50	7.00	0.0090	-		
0.67	162.50	13.40	600	8	1.50	9.00	0.0090	-		
0.67	325.00	74.50	300	22	6.00	2.00	0.0360	-		
4.00	110.00		-160		3.00	10.00	0.0030	-		[Shidoji99a]
0.67	100.00		-340		4.00	12.00	0.0240	-		[Shidoji01a]
0.67	240.00		-240		6.00	7.00	0.0360	-		
1.33	240.00		-240		9.00	7.00	0.0271	-		
0.67	180.00	9.70	-200	1.9	0.20	5.00	0.0012	-		[Shidoji01b]
0.67	180.00	1.40	-200	0.3	0.08	11.00	0.0005	-	II	
0.67	180.00	7.00	-200	1.4	0.20	6.00	0.0012	-		[Shidoji03]
0.67	360.00	8.10	-170	1.4	0.22	4.00	0.0013	-		

Table 1.3 Overview of reported plasma densities, both experimentally measured (upper part) as well as self-consistently calculated (lower part). The table lists the gas pressure p, the maximum magnetic field B_{max}, the discharge current I_d and discharge voltage V_d, the electrical power P, the plasma density n and its height above the target z, the ID and the (highest) kT_e when these properties are reported. In the comment column it is indicated when the measured density is a peak density (i.e. an absolute maximum). For the simulation results all the densities are peak values. If explicitly mentioned in the reference, also the type of balancing (I or II) of the magnetron is given. The data are obtained for cylindrical planar magnetrons, except when mentioned otherwise.

An overview of different plasma density measurements reported in literature is given in Table 1.3. Also self-consistent simulation results are included. When a radial and/or axial profile is given in the reference, the highest reported density is listed. Typical plasma densities are clearly in the range 10^{10}-10^{11}/cm^3. The ionisation degree (ID) was calculated, assuming a neutral particle density of 2.5×10^{13}/cm^3 at 0.1 Pa and is shown as a function of gas pressure (Fig. 1.18). Of course, the ID depends also on the electrical power input (section

1.4.3.4), but the general trend is a decrease in ID with increasing pressure. This is due to the fact that for a given discharge current, the plasma density is only very weakly pressure dependent (see e.g. [Špatenka97, Field02]). From the cited plasma density measurements, it follows that the ID is at most 1% in magnetron discharges.

1.3.5.3 Density and ionisation degree of sputtered particles

According to the applied power sputtered particle densities vary from 10^{10} to 10^{11}/cm^3 in a typical MD. Because of the low ionisation threshold for metals, the ionisation degree of the sputtered particles is of the order of 1 to 10%.

Measurements of the absolute density of sputtered particles based on optical adsorption are performed in [Dony97] for Al sputtering in argon: the reported Al-densities are approximately 10^{11}/cm^3 at 6 Pa (8 mm above the target, 30 mA), which corresponds with an Al/Ar ratio of 1/15000. Using the same technique, Leroy et al. measured sputtered Ti densities [Leroy04]: the density varies from approx. 2×10^{10}/cm^3 (95 mm above target, 0.1 A) to almost 4×10^{11}/cm^3 (25 mm above target, 1 A) at 4 Pa. This corresponds with an Ti/Ar density of respectively 1/50000 and 1/2500. According to [Christou02] the density at 2.5 mm is about 10 times as high as at 17.5 mm above the target. Combining both results leads to the estimate that, close to the cathode, the ratio of the sputtered particles and the argon atoms would be at most 1/250.

From a practical view-point, the ionisation degree of the sputtered particles is important: the energy and arrival direction of the ionised sputter particles can be controlled by a bias voltage, which allows for tailoring the film properties (see e.g. [Ivanov94]). This explains the recent interest in high power pulsed sputtering as this technique leads to a large fraction of ionised sputtered particles (see e.g. [Ehiasarian02, Christie05]. Initially, no positively ionised sputtered particles can leave the negatively charged target. However, during transport through the discharge, the sputtered particles can become ionised. Whereas the argon atoms are practically exclusively ionised by one step impact ionisation, the low ionisation threshold of the sputtered metal particles (6 to 9 eV) turns Penning ionisation into a relevant process. According to [Schulte97] this process becomes important at higher pressures, in their experiments above 2 Pa.

Christou and Barber measured the ionised fraction of Ti in Ar at 3 Pa at the target [Christou00]: the fraction decreases from above 10% at very low powers (<5 W) to below 2% at 60 W. They obtained the ionisation degree by comparing Ti and Ti^+ emission lines. Leroy et al. report an ionisation degree of Ti of around 2% in Ar at 4 Pa and $I_d = 1$ A using an optical absorption diagnostic technique [Leroy04].

1.3.5.4 Potential distribution

For balanced magnetrons with a well-defined discharge area, the bulk plasma is electric field free, except for the presheath where a typical electric field strength of the order of 1 V/mm is observed. The plasma potential is slightly positive (some volts) and depends on the pressure. For unbalanced magnetrons the situation is less clear: large potential drops might occur far from the cathode but the "*discrepancy in spatial structure of the plasma potential in the bulk discharge region has not yet been elucidated*" [Seo04a].

In principle the bulk plasma is the region with charge neutrality and without potential gradients. An exception is the presheath, which is assumed quasi-neutral. The potential drop over the presheath is of the order of $kT_e/2$, i.e. some eV (section 1.3.3.1), which is very small compared with the potential drop over the cathode sheath. As the presheath extends about one centimetre in the plasma, e.g. [Shidoji94], a good estimate for its electric field is 1 V/mm.

This is in agreement with measurements reported in [Rossnagel86, Bowden93, Field02, Seo04a-c]. Also MC-PIC simulations confirm these results, e.g. [Kondo99a, Shidoji99a]. These flat potentials in the bulk plasma agree also with the measurements for post magnetrons [Behnke00, Yeom89]. The plasma potential is slightly positive, e.g. from 1 to 3 V from 1.5 to 8 cm above the target at 0.4 Pa [Špatenka97], from 1 to 3 V from 3 to 10 cm above the target (40 mTorr) [Field02]. The floating potential is around -5 to -10 V and practically flat at some centimetres above the target but it decreases rather strongly closer to the target: in [Fujita86] the floating potential drops to approximately -30 V at some millimetres above the target.

In the previous case, the measurements of the plasma potential in the planar magnetron case were for balanced magnetrons, it is to say the authors do not mention anything specific about the balancing. Hence, the situation sketched in Fig. 1.15a can be assumed. From the mentioned results, only the ones in [Seo04a-c] were acquired using an unbalanced magnetron (type II). This is surprising as other measurements show a rather strong variation in the plasma potential for unbalanced magnetrons: potential differences far into the plasma of 20 V [Bingsen92] and 40 V (at 100 W) [Bradley97, Bradley01] are observed. Measurements reported in [Spolaore99] on an unbalanced magnetron of type II show that for high power (100 W) the plasma potential is practically flat in the region 15 to 35 mm above the target, for low power (25 W) the plasma potential varies with approximately 10 V. Simulations in [Shidoji01b] show that for an unbalanced magnetron (type II) a potential drop of approximately 20 V is formed in front of the anode in order to extract the electrons from the discharge. For a balanced magnetron on the other hand, the simulations show that the potential is basically flat in the bulk plasma.

1.3.5.5 Ion energy

The plasma in a MD is a non-equilibrium plasma, hence it is not possible to define an ion temperature: ions are accelerated in the presheath and become energetic. The average ion confinement time is too short in comparison with the collision rate so that no equilibrium can be reached. Nevertheless, Goeckner et al introduced an effective ion temperature which gives the velocity of the ions [Goeckner90]: their measurements show that the ions have an energy of approximately 0.26 eV in the radial direction and a higher energy (0.64 eV) in the azimuthal direction. They conclude that it is unclear why the effective temperature is higher in the azimuthal than in the radial direction.

1.3.5.6 Electron energy: electron temperature and EEDF

As the electron energy distribution function in a MD is not Maxwellian, the concept of electron temperature is not fully applicable but it can be used as average electron energy. The electron temperature in the bulk is typically 1 to 5 eV and increases up to some tens of eV towards the cathode.

To characterise the energy distribution of the electrons in a plasma the *E*lectron *E*nergy *D*istribution *F*unction (EEDF) $g(E)$ is used. It is defined such that:

$$n_e = \int_0^\infty g(E)dE \tag{1.43}$$

Another function that is often used is the *E*lectron *E*nergy *P*robability *F*unction (EEPF) $g_p(E)$, defined as:

$$g_p(E) = \frac{g(E)}{\sqrt{E}} \tag{1.44}$$

Based on the EEDF the average electron energy E_{avg} is given by:

$$E_{avg} = \frac{1}{n_e}\int_0^{\infty} Eg(E)dE \qquad (1.45)$$

For a Maxwellian distribution, the electron temperature kT_e is given by $2/3E_{avg}$.

Typical values reported for kT_e are in the order of 1-5 eV for the bulk plasma. The radial dependence is reported in e.g. [Sheridan95, Špatenka97], the dependence in the direction perpendicular to the target in e.g. [Rossnagel86, Rossnagel87b, Kuwahara98, Sheridan98]. A 2D spatial overview can be found in e.g. [Fujita86, Tao96, Field02]. The non-uniformity of the MD is responsible for the (strong) increase of the electron temperature towards the cathode. In [Tao96] close to the target electron temperatures up to 60 eV are reported, in [Rossnagel86] up to 23 eV at 5 mTorr and in [Bradley98a] up to 13 eV at 1.25 mTorr. The kT_e close to the cathode have to be interpreted with care because LP measurements close to the cathode region can influence the discharge (section 1.3.5.2).

Furthermore, as the electrons in a MD have an ExB drift component which is around 10% of the thermal velocity (section 1.3.6.1), this drift velocity needs to be taken into account when interpreting the Langmuir probe characteristics as shown in [Sheridan94]. If the drift is neglected the calculated electron temperature kT_e is too large and the plasma potential V_p too low: using a stationary model (no drift) they calculated V_p = -2.35 V and kT_e = 4.47 eV, using the correct drift-model they found V_p = -0.038 V and kT_e = 1.33 eV.

Moreover, a problem is that the EEDF in a MD is not Maxwellian. This means that the concept of electron temperature is not fully applicable and that "*the electron temperature deduced from probe measurements can characterise no more than the mean electron energy, and cannot be used for calculations of excitation or ionisation rates*" [Godyak90]. A first deviation from the Maxwellian distribution is that the EEDF has a high energy tail. This is shown in [Guimarães91]: the calculated results show that the EEDF is almost constant in the range 100 to 500 eV. The upper limit corresponds with the discharge voltage. The results also show that it is necessary to account for the Coulomb collisions to reproduce the EEDF correctly at low energies.

A second deviation from the Maxwellian distribution occurs at low energies: several authors report the existence of two electron temperatures, e.g. [Sheridan91a, Ivanov92, Sheridan95, Špatenka97, Serianni00, Bradley01, Field02, Seo04a]. Both in [Sheridan91a] and [Bradley01] it is shown that within the region with closed magnetic field lines there is only one electron temperature, in the region outside this region there exists a hot and cold electron temperature. The hot one corresponds with the electron temperature inside the closed magnetic field lines. Serianni et al. reported a similar result for two facing magnetrons in the closed field configuration [Serianni00]: in the region between the two magnetrons one electron temperature was observed within the region enclosed by the magnetic field lines, outside this region two electron temperatures were observed. The phenomenon of two electron temperatures is explained by considering the loss mechanism for the electrons: Seo et al. showed the transition from a bi-Maxwellian distribution to a single Maxwellian distribution by increasing the bias of the anode from +5 V to -30 V [Seo04a]. In [Seo04b] it is shown that the structure of the electron energy probability function at low electron energies can give rise to large discrepancies between the kT_e measured using a planar and cylindrical Langmuir probe (see also section 1.4.2.4).

1.3.6 Electron transport

Probably one of the least understood aspects of the planar d.c. MD is the transport of the low-energetic bulk electrons. First, the E×B drift of the electrons is discussed, then follows the anomalous electron transport.

1.3.6.1 E×B drift

Charged particles in a crossed electric and magnetic field undergo a drift in the direction perpendicular to both the electric and magnetic field, the so-called E×B drift or Hall drift with drift velocity v_{ExB} given by [Garcia03]:

$$v_{E\times B} = \frac{E \times B}{B^2} \tag{1.46}$$

Of course, this equation applies only when the movement of the charged particle is magnetised in the considered time or space interval. This is easily understood by comparing the electron and ion behaviour: although the E×B drift is charge and mass independent, eq. (1.46) is only valid for the electrons in the MD. The reason is that the electron Larmor radius is of the order of one millimetre while the ion Larmor radius is of the order of one metre. Hence, on the length scale of the discharge region the ions can be considered non-magnetised.

Experimental measurements show a E×B velocity v_{ExB} of the electrons from approximately 5×10^5m/s (15 mm above target) to 10^5m/s at 40 mm above the target at 1 Pa [Sheridan98] and 1.3×10^6m/s (13 mm above the cathode) at 0.42 Pa [Sheridan94]. In [Fujita86] a practically constant drift velocity of 7.3×10^4m/s from 2 to 35 mm above the target was reported. Bradley et al. differentiated between the drift velocity in the sheath, the presheath and the bulk region [Bradley01]. The drift velocity was *estimated* to be 2×10^6m/s in the sheath and 1×10^5m/s in the presheath. Because of the large potential gradients (~10 V/cm) measured in the bulk region, Bradley et al. estimated that the sheath and presheath region only account for 20% of the total E×B current, the remaining 80 % is carried by the bulk plasma. Given the typical drift velocities, v_{ExB}~1×10^5m/s, and the velocity corresponding with the electron temperature kT_e, 1.3×10^6m/s at 5 eV, it follows that the drift velocity v_{ExB} is roughly 10% of the thermal speed. Hence, the electron drift needs to be taken into account when measuring kT_e (section 1.3.5.6).

Shidoji et al. found Hall drift velocities in the range 4 to 10×10^5m/s [Shidoji00]. The result was obtained using a Monte Carlo method in which only the HEE were considered (until their energy dropped below the ionisation threshold). The electric field in the cathode sheath was used as an input parameter; no presheath was taken into account.

1.3.6.2 Anomalous electron transport

Experimental observations show that the electron transport in the direction perpendicular to the magnetic field lines is higher than can be expected from classical theory. This anomalous electron transport is generally attributed to instabilities in the discharge and does not only appear in magnetron discharges. Although its origin seems to become unravelled, anomalous electron transport seriously hampers self-consistent magnetron modelling

A. Indications for anomalous electron transport in the MD

The problem of the anomalous electron transport becomes apparent when looking at the current carriers in the plasma. At the cathode side the total discharge current I_d is given by eq. (1.40). Given the typical values of γ (section 1.2.2.1), it follows that the current is carried mostly by the positive argon ions. At the anode side, the current is carried exclusively by the electrons. As the HEE are trapped in front of the cathode by the magnetic field, the current to the anode is mostly due to the low-energetic bulk electrons. Experimental evidence of the electron-drift towards the anode is presented in [Sheridan95]. Of course, the transport of the bulk electrons towards the anode is hampered by the magnetic field. According to classical theory, the standard electron mobility μ in the absence of a magnetic field is defined as:

$$\mu = \frac{e}{m\nu} \tag{1.47}$$

with ν the collision frequency of the electrons and e the elementary charge unit. The mobility $\mu_\perp$ in the direction perpendicular to the magnetic field lines is given by [Chen03]:

$$\mu_\perp = \frac{\mu}{1+\frac{\omega^2}{\nu^2}} \tag{1.48}$$

with ω the Larmor frequency:

$$\omega = \frac{eB}{m} \tag{1.49}$$

In magnetron discharges the electron collision frequency ν is of the order 10^7-10^8Hz (pressure dependent), ω of the order 1 to 10 GHz (magnetic field dependent). Given this large ω/ν ratio, eq. (1.48) simplifies to:

$$\mu_\perp = \mu\frac{\nu^2}{\omega^2} \sim \frac{1}{B^2} \tag{1.50}$$

The dependence of the mobility on the magnetic field is given in Fig. 1.19a.

The ion mobility μ_i in an electric field is also given by eq. (1.47) when m is replaced by M and ν by ν_i, the ion collision frequency (around 10^5 Hz at 0.5 Pa). Hence, μ_i is much lower than the electron mobility μ. However, the ions are not magnetised and their mobility remains unchanged for increasing magnetic field. This means that the ion mobility becomes larger than the electron mobility above a certain magnetic field strength as illustrated in Fig. 1.19a for 0.1 and 5 Pa. This has an important consequence for the discharge: instead of a positive space charge that forms the cathode sheath, a negative space charge sheath should form in front of the anode as discussed in [Pekker95] and as illustrated by the PIC-MC simulations in [Vanderstraaten98a,b]. However, experimental evidence exists that such a negative space charge is not formed in MD for the considered magnetic field strengths [Vanderstraaten98b], which is a first indication of anomalous electron transport in the direction perpendicular to the magnetic field.

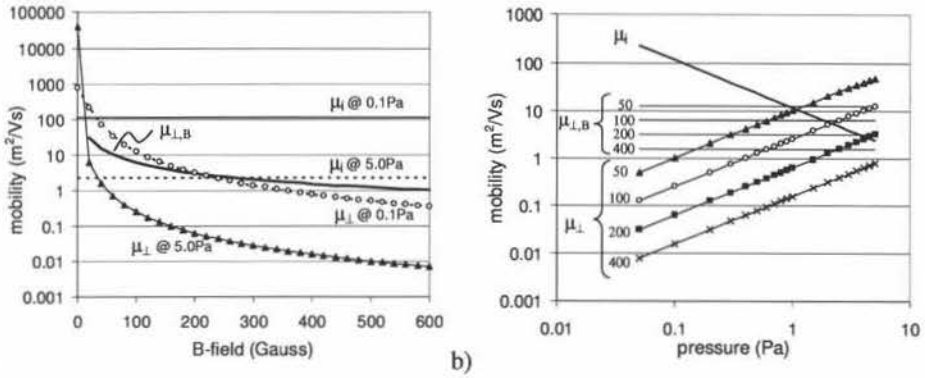

Fig. 1.19 *a*) Magnetic field dependence of the Bohm and classical electron mobility (at 0.1 and 5 Pa) in the direction perpendicular to the magnetic field. Also the ion mobility μ_i at 0.1 and 5 Pa is indicated. *b*) Pressure dependence of the Bohm and classical electron mobility in the direction perpendicular to the magnetic field at 50, 100, 200 and 400 G. Also the ion mobility μ_i, which is independent of the B-field, is indicated.

In a plasma the current density in a region with electric field E is given by:

$$j = \sigma_p E \tag{1.51}$$

with the plasma conductivity σ_p defined as:

$$\sigma_p = ne\mu_\perp \tag{1.52}$$

Hence, the current density j_d related to the discharge current is given by:

$$j_d = ne\mu_\perp E \tag{1.53}$$

Assuming classical diffusion (i.e. using eq. (1.50)) combined with the definition of the Larmor frequency ω (eq. (1.49)) the current density can be written as:

$$j_d = ne\frac{e\nu}{m\omega^2}E = \frac{ne\nu E}{B\omega} \tag{1.54}$$

On the other hand, given eq. (1.46), the E×B current density $j_{E\times B}$ can be written for perpendicular E and B as:

$$j_{E\times B} = ne\nu_{E\times B} = ne\frac{E}{B} \tag{1.55}$$

From eq. (1.54) and eq. (1.55) it follows that:

$$\frac{j_{E\times B}}{j_d} = \frac{\omega}{\nu} \tag{1.56}$$

Note that this equality is only valid in the assumption of classical diffusion. For 0.2 Pa and an electron energy of 10 eV ν is approximately 10^7 Hz, taking into account ionisations, excitations and elastic collisions (both with electrons and atoms). The Larmor frequency ω is around 5×10^9 Hz for 300 G. Hence, the ratio $j_{E\times B}/j_d$ is approximately 500. The ratio $j_{E\times B}/j_d$ has been measured experimentally [Rossnagel87a, Bradley01]. Bradley et al. deduced the ratio

from the estimated and measured v_{ExB}-values (section 1.3.6.1). Rossnagel and Kaufman measured total Hall drift current by measuring the induced magnetic field [Rossnagel87a]: I_{ExB} varied between 2 and 9 times the discharge current I_d, the highest values occurring at the lowest pressures and highest powers. By estimating the surface area for I_d and I_{ExB}, they were able to estimate j_{ExB}/j_d. In [Rossnagel87a] the ratio is estimated to be at most 16, in [Bradley01] the ratio is for the whole discharge around 8 with localised values up to 25. Hence, both report ratios much smaller than the classical value for ω/ν, a second indication of anomalous electron transport in the direction perpendicular to the magnetic field.

Both in [Rossnagel87a] and [Bradley01] it is suggested that the results are in line with Bohm diffusion. In this case the mobility in the direction perpendicular to the magnetic field lines $\mu_{\perp,B}$ is defined as:

$$\mu_{\perp,B} = \frac{1}{16B} \tag{1.57}$$

Hence, the mobility is inversely proportional with the magnetic field strength B (Fig. 1.19b). For Bohm diffusion the ratio ω/ν is equal to 16, which agrees rather well with the mentioned experimental ratios for j_{ExB}/j_d. However, although Bohm diffusion is at low pressure clearly stronger than classical diffusion, the electron mobility remains smaller than the ion mobility for the typical working parameters of the MD. Fig. 1.19b shows that close to the target (strong B) Bohm diffusion is stronger, but further away from the target (weak B) classical diffusion might still be stronger.

B. Possible origins of the anomalous transport

Experimental efforts to clarify the anomalous transport mechanism in magnetrons have been done. Fluctuations in the electric field have been observed and could be responsible for the phenomenon. Instabilities in the electric field in the low-frequency range, *low* meaning below the plasma-ion frequency which is 3.3 MHz at a plasma density of $10^{10}/cm^3$, are reported: Sheridan and Goree found a peak at 5 kHz which they attributed to the ion cyclotron resonance and some secondary peaks around 200 kHz [Sheridan89a]. However, they concluded that these instabilities are *not* responsible for the anomalous electron transport [Sheridan89a].

Martines et al. reported oscillations in the order of 100 kHz and attributed them to the density gradient caused by the ExB drift [Martines01]. This agrees with the fluid model developed in [Vanderstraaten00] which predicts unstable oscillations with frequencies above the ion-neutral collision frequency (~100 kHz) in the ExB direction. It is suggested that these oscillations "*may contribute to the anomalous transport*". Oscillations below 15 kHz are also reported in [Bilyk04] for two different cylindrical magnetrons. The observed peaks in the spectra are explained as a "*result of non-linear coupling (deterministic chaos) rather than result of certain simple phenomena (e.g. ion gyromotion)*" [Bilyk04]. Also in this work is suggested that "*the stochastic fluctuations helped the transport of charged particles across the magnetic field*".

Next to these low-frequency instabilities, also instabilities at higher frequencies have been measured: in [Pal04] instabilities in the ExB flow with a characteristic frequency between 50 and 100 Mhz are measured for a cylindrical magnetron, but only below 0.4 Pa. This frequency is in between the ion collision frequency ν_i (~20 MHz) and the electron cyclotron frequency ν (~1 to 10 GHz). For these instabilities, the amplitude peaks as a function of the magnetic field strength, the frequency increases with magnetic field strength.

Oscillations at even higher frequencies are reported by Gopalraja and Forster who observed oscillations at 22, 240 and 262 MHz in a planar magnetron [Gopalraja00].

More in general, promising fundamental recent investigations regarding the electron transport across inhomogeneous magnetic fields are reported in [Kumar02, Kumar04] where a plasma created in a multicusp bucket source is allowed to diffuse across inhomogeneous magnetic fields. The existence of shear in the electric field near the magnetic sheath is reported. In that magnetic sheath the plasma is turbulent, outside the sheath it is quiescent. The turbulent electrostatic fluctuation has a frequency between the ion and electron Larmor frequencies. They mention that the fundamental reason for the plasma turbulence is the trapping of energetic electrons. These results agree with the afore mentioned measured electric field oscillations of [Sheridan89a] and [Martines01].

It is also interesting to look at stationary plasma thrusters, a kind of Hall effect thrusters. In the exhaust region of such devices a similar situation as in MD is encountered: electrons in a region with a crossed electric and magnetic field diffuse in the direction perpendicular to the magnetic field lines and the classical expression for $\mu_\perp$ underestimates the transport. The observed anomalous transport in the exhaust region is generally linked to electric field fluctuations or turbulence, although also the electron-wall interaction is mentioned as a possible explanation, e.g. [Hagelaar03]. More about this topic can be found in [Ahedo03]. Here, we only mention that this link was made for the first time in [Janes66] (according to [Ahedo03]). In that work, the plasma density was found to oscillate in the azimuthal direction, i.e. the E×B direction. The accompanied density gradients cause an oscillating electric field in the same direction. As the oscillations of the electric field and the plasma density are correlated a net electron current flows in the direction perpendicular to both B and the azimuthal direction. This net electron current gives the anomalous diffusion. In [Janes66] the possible origin for these non-uniformities is suggested to be the ionisation mechanism. However, in [Chable05] an overview is given of measured low frequency (<100 kHz) oscillations and they are classified in four groups, each with different (possible) origins.

C. Modelling of the anomalous drift

In Hall effect thrusters, it has been tried to include anomalous diffusion in the simulations. The empirical relation proposed for $\mu_{\perp,H}$, the electron mobility across the magnetic field lines in the exhaust region is [Hagelaar03, Bareilles04]:

$$\mu_{\perp,H} = \mu_\perp + K\mu_{\perp,B} \tag{1.58}$$

with K an empirical parameter. Hence, they combine the classical and Bohm diffusion. Good agreement between the experiments and simulations is obtained for K~0.2 [Bareilles04]. Another way to introduce the anomalous electron transport is by introducing an extra type of collisions for the electrons, the Bohm diffusion collisions ν_B, with frequency:

$$\nu_B = \alpha\omega_L \tag{1.59}$$

with α an empirical parameter, see e.g. [Ahedo03, Smirnov04]. For "true" Bohm diffusion α should be equal to 1/16. However, both numerical simulations and experiments indicate $\alpha \approx 1\times10^{-2}$ in Hall thrusters. Hence, using a phenomenological approach, the influence of anomalous diffusion can be modelled. To our knowledge, no similar approach exists for the MD.

1.4 Influence of the external parameters

In this part, the influence of the external parameters on (some of) the characteristics treated in the previous section will be discussed. The considered external parameters are: magnetic field (section 1.4.1), gas pressure (section 1.4.2), electrical power (section 1.4.3), target material (section 1.4.4), discharge gas (section 1.4.5) and anode (section 1.4.6).

1.4.1 Magnetic field

The magnetic field is crucial for the MD as it distinguishes the MD from the glow discharge. Because of the magnetic field, the MD can operate at lower pressures and discharge voltages. This allows a higher plasma density, which leads to a steeper IV-characteristic and higher current densities. Increasing the magnetic field strength enhances all these effects although at very high magnetic field strengths the effect becomes minimal.

1.4.1.1 Erosion profile

The magnetic field is the main reason for the formation of the erosion profile. Consequently, a change in the magnetic field structure and/or strength can influence the shape and position of the erosion profile.

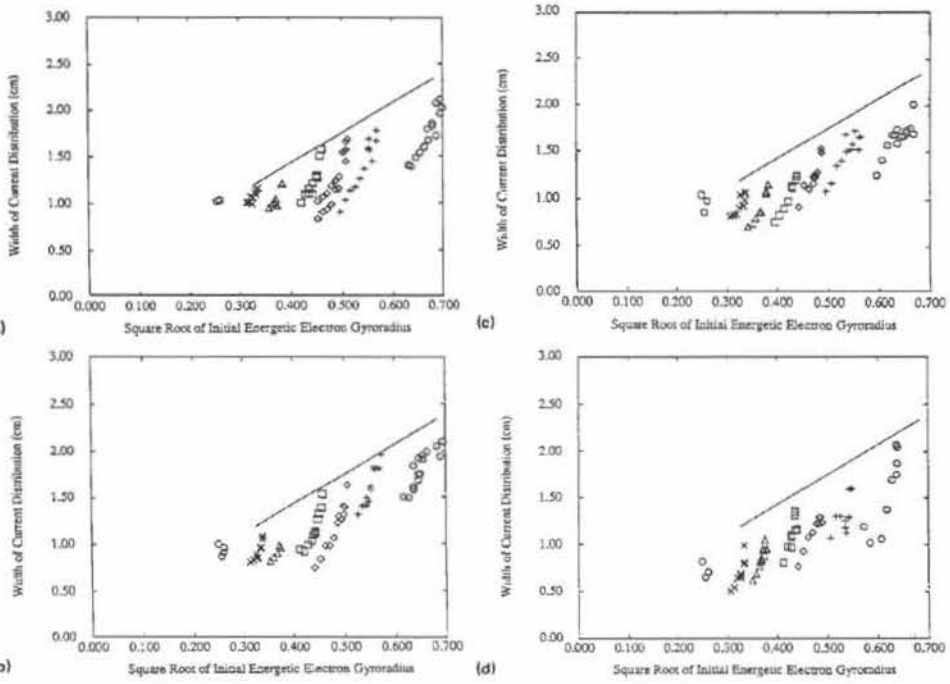

Fig. 1.20 Measured cathode current distribution width w as a function of the square root of the Larmor radius r_L, which is referred to in the graphs as "Square Root of Initial Energetic Electron Gyroradius" for 5 mTorr (a), 10 mTorr (b), 20 mTorr (c) and 50 mTorr (d). The solid lines represent the solution obtained with the thin sheath model (eq. (1.18)). The symbols indicate the strength of the magnetic field: B_{max} = 171 G (⊙), 228 G (+), 285 G (◇), 342 G (□), 456 G (△), 570 G (×) and 855 G (○). Taken from [Wendt90].

The influence of the strength of the magnetic field on the width of the erosion profile is discussed in [Wendt88a, Wendt90]. In these references, eqs. (1.18) and (1.19) are deduced based on the simple model explained in section 1.3.1. These equations show that the width

decreases with increasing magnetic field because the Larmor radius of the HEE decreases, which restricts the region accessible to the HEE. From Fig. 1.20 it is clear that eq. (1.18) is not able to reproduce the influence of the electrical power at a given magnetic field strength. Therefore, the model was adapted such that also thick sheaths could be modelled. This yielded a much better agreement between the model and the experiments. However, at high magnetic field strengths the thick sheath model consistently underestimates the width of the current distribution.

More difficult to model is the influence of the structure of the magnetic field on the erosion profile. For deducing eq. (1.18) and eq. (1.19), it is assumed that the magnetic field is symmetrical, for which a Gaussian profile with maximum on the symmetry-axis applies. However, in reality the magnetic field is mostly asymmetric and a Gaussian profile is questionable, as e.g. in [Ido93a, Kusumoto04]. In [Ido93a] it is shown how the shape and position of the erosion profile are influenced by the magnetic field structure. In [Fukami87] the influence of the vertical magnetic field component on the erosion profile is studied.

1.4.1.2 Discharge voltage/Discharge current/ IV

Measurements of the behaviour of the discharge voltage V_d as a function of the gas pressure at constant discharge current I_d for different magnetic field strengths are reported in [Chang86]: it follows that the higher the magnetic field, the lower the required V_d to obtain a given I_d at fixed gas pressure. In [Wendt90] the IVs move to lower discharge voltages and become steeper with increasing magnetic field strength. Similar results are also reported in [Nyaiesh81]. These results agree with the enhanced trapping of the HEE with stronger B-field.

Self-consistent simulations were also used to investigate the influence of the magnetic field on the MD. The influence of the magnetic field strength B_{max} on the properties of the MD was simulated at a discharge voltage of 500 V and gas pressure 5 mTorr for a rectangular magnetron [Nanbu97] and for a circular magnetron [Kondo99a]. The results (Table 1.3) show that for the circular magnetron the electron density n_e increases with increasing B_{max} whereas for the rectangular magnetron n_e exhibits a maximum as a function of B_{max}. In contrast, in [Shidoji01a] at 5 mTorr the electron peak density for $B_{max} = 100$ G ($V_d = 340$ V) is smaller than the one for $B_{max} = 240$ G ($V_d = 240$ V).

Theoretical considerations related to the influence of the magnetic field on the MD are formulated in [Goree91]. They define the efficiency η as the ratio of the actual amount and the theoretical maximum amount of generated electron-ion pairs [Sheridan90c]:

$$\eta = \frac{\langle N_i \rangle}{N_{i,max}} \tag{1.60}$$

with $\langle N_i \rangle$ the average of "*the number of ionisations that a single electron performs*" and $N_{i,max}$ "*the number of ionisations performed by a well-confined electron in the absence of excitation and elastic collisions*". This definition appears rather inconsistent as for N_i excitations and elastic collisions are included but for $N_{i,max}$ not. According to [Goree91] $N_{i,max}$ for $V_d = 400$ V is 17, which corresponds with an "effective" ionisation energy of 23.5 eV. This value is between the ionisation energy of argon (15.8 eV) and the actual effective energy (30 eV). Hence, it is not exactly clear what $N_{i,max}$, and consequently, η physically represent. Nevertheless, the results show a strong increase in η at low B_{max} but above a certain B_{max} η saturates. They deduced a similarity law to specify the optimal magnetic field. Therefore the dimensionless magnetic field strength β is introduced [Goree91]:

$$\beta = aB_{max}\sqrt{\frac{e}{2mV_d}} \tag{1.61}$$

with a the radius of the position where the magnetic field is parallel to the target surface. The optimal magnetic field occurs around $\beta = 10$. For the magnetron they used, a equals 17 mm and the optimal magnetic field is around 500 G. They argue that from practical viewpoint, a further increase in magnetic field strength has a negative effect as it narrows the erosion profile without promoting the trapping of the electrons. Experiments [Chang86, Wendt90] show that increasing the magnetic field keeps reducing the discharge voltage, even at strong magnetic fields. The amount of ionisation in the sheath increases with increasing magnetic field. Consequently, one emitted SE can create an avalanche of electrons in the discharge. As this effect is enhanced by the magnetic field strength, it might explain why the discharge voltage decreases. In [Depla05a] it is observed that at 0.25 A increasing the magnetic field from about 250 to 1000 G leads to a continuous decrease in the discharge voltage at high pressures (>1 Pa) but the discharge voltage remains constant for a magnetic field increase above 600 G at low pressures (<0.3 Pa). The saturation of the discharge voltage is most likely due to the increased recapture of secondary electrons at strong magnetic fields as this reduces the effective SE yield.

As in the case of the erosion profile, the balancing of the magnetic field will have a strong influence on the discharge properties. An example is shown in [Muralidhar95] where the magnetic field of the magnetron is generated by an inner (current I_1) and outer (current I_2) coil. With increasing I_1/I_2, B_{max} increases but the balancing also shifts from type II to type I. The extinction pressure p_{ext} was recorded at fixed discharge current ($I_d = 0.3$ A) as a function of the ratio I_1/I_2. At low I_1/I_2 ratios p_{ext} decreases, at high ratios it increases again in spite of the increasing B_{max}. The reason for the increase of p_{ext} at high ratios is that the target area within the tunnel of magnetic field lines decreases at high I_1/I_2 ratios. In [Kadlec95] it is shown that the maximization of this area leads to the minimization of the extinction pressure. Komath et al. also conclude that, using a similar magnetron system, the most efficient sputtering occurs when the discharge covers the maximum target area [Komath99]. However, they claim that this condition is satisfied when the ring where the vertical magnetic field is zero "*takes a position where the circular area inner to it equals the annular area outside*" (sic).

1.4.1.3 Cathode sheath

The cathode sheath was already extensively discussed in section 1.3.3.5. From that discussion it is clear that for the planar MD the magnetic field is crucial for its thickness. Here, only a short summary is given.

Because of the magnetic field the electrons cannot move freely in the region of the cathode sheath. Consequently, the electron density is non-zero which implies that the CL law cannot be applied directly. Experimental observations of the cathode sheath thickness are reported in [Bowden93] and [LanGu88]. In the first, the sheath thickness decreases from 3.1 to 1.7 mm with increasing B from 200 to 450 G. In the latter the sheath thickness, which varies within 1 to 4 mm, is found inversely proportional with $B^{0.25}$ (eq. (1.33)). At high magnetic fields, the sheath thickness is almost independent of the magnetic field strength. In contrast to cylindrical or post magnetrons, no increase of d_E with increasing magnetic field is experimentally observed.

The decrease of sheath thickness with increasing B_{max} is also retrieved in self-consistent simulations as can be deduced from [Nanbu97, Kondo99a, Kondo01, Shidoji01a]

(see data in Table 1.3). However, in [Shidoji03] B_{max} was varied from 180 to 360 G to investigate the influence of a "*strong*" magnetic field on the MD. With increasing magnetic field the cathode sheath thickness decreases and the peak position of the electron density shift towards the target as expected, but the peak in the net ionisation rate decreases. Instead, the net ionisation rate in the bulk region (20-40 mm above the target) increases substantially (see also section 2.2.5).

1.4.1.4 Bulk plasma

The discharge region of the MD is determined by the structure of the magnetic field as shown in Fig. 1.15. Hence, the plasma properties in the bulk region are to a large extent determined by the magnetic field shape. An example is given in [Ivanov94]: three different configurations are considered: strongly unbalanced type II, weakly unbalanced type II and unbalanced type I. At 70 mm above the centre of the target the electron density was $1\times10^{17}/m^3$, $2\times10^{16}/m^3$ and $3\times10^{15}/m^3$, respectively. The plasma potential varied from -11.2 over -7.4 to -1.2 V. In [Shidoji01b] the balancing of the magnetron is investigated by comparing the self-consistent simulation results for a balanced and an unbalanced (type II) magnetic field. For the unbalanced magnetron the anode is partially shielded by the magnetic field lines, which forces the plasma potential to change such that the electrons are guided to the anode.

1.4.2 Gas pressure

When the gas pressure is decreased the MD becomes more difficult to maintain, which leads to an increase in the discharge voltage and a widening of the cathode sheath. The erosion profile becomes wider and the electron temperature increases. At very high pressures (>30 Pa) the discharge evolves to a diode mode.

1.4.2.1 Erosion profile

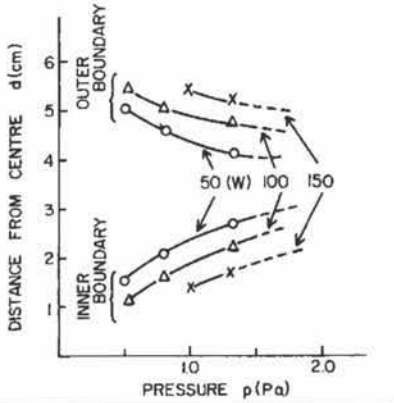

Fig. 1.21 Dependence of the outer and inner radius of the erosion profile on the gas pressure at 50, 100 and 150 W. Taken from [Fukami87].

The variation of the width of the erosion profile is dependent on the gas pressure as reported in [Musil95, Musil98]: at low pressures, there is a strong increase of the width, at high pressures the width becomes relatively independent of the gas pressure. A similar experiment was performed in [Fukami82, Fukami87] where also an increase of the race-track width is observed with decreasing pressure (Fig. 1.21). In [Wendt90] the width of the discharge

current distribution w at the target was observed at different pressures. From Fig. 1.20 it is clear that w is not directly influenced by the pressure as for a given Larmor radius the observed widths are practically pressure independent.

1.4.2.2 Discharge voltage/Discharge current/ IV

With decreasing pressure the discharge voltage V_d remains relatively constant at high pressures while at low pressures V_d increases sharply [Chang86]. According to the simulation results this pressure dependence is due to the decrease in the effective SE yield because the lower the pressure the larger the recaptured fraction of SE (section II.4.3.2). At (very) high pressures the discharge voltage increases again, e.g. [Fujita86].

The influence of the pressure on the IV was already briefly mentioned (section 1.3.4.1): in general the exponent n in eq. (1.34) decreases with decreasing pressure. However, the behaviour of n can be more complex: measurements in [DeBosscher99] show n practically constant in the range 0.05 to 0.2 Pa. The measurements of Musil show that the steepness of the IV decreases very slightly with increasing pressure from 0.2 to 10 Pa, which implies a decrease of n with increasing pressure [Musil98]. In [Depla05a] the steepness of the IVs was studied for a wide range of pressures and magnetic field strengths: at strong magnetic fields n decreases with increasing pressure, at weak magnetic fields n increases with increasing pressure. The pressure dependence of n changes around 300-400 G for the type of magnetron used. These measurements can explain the previously mentioned difference in pressure dependence of n.

Another interesting influence of the pressure on the MD appears when the discharge current is measured as function of the gas pressure at constant discharge voltage. Seo and Chang measured the discharge current I_d between 1 and 30 mTorr [Seo04b]: I_d increases strongly at low pressures, between 5 and 20 mTorr it increases slowly, at higher pressures it increases again strongly. They could relate this to the electron density: in the region 10 to 18 mTorr the electron density decreases with increasing pressure. This is due to an enhanced loss of low energy electrons as in this region the electron temperature increases with increasing pressure. In [Escrivão03] the same experiment is done but at high pressures: from 3.3 to 66.7 Pa. At the low end of their pressure range a strong increase in discharge current with increasing pressure is seen. At higher pressures, the behaviour depends on the discharge voltage: for low V_d (350 V) I_d goes through a maximum at 10 Pa, then decreases with increasing pressure and becomes practically constant above 40 Pa. For higher V_d (370V and more), I_d flattens around 20-30 Pa, followed by a linear increase of I_d with pressure. They explain this behaviour by assuming a magnetron mode at low pressures, which gradually evolves to a diode mode and becomes the only mode at high pressures (>30 Pa).

1.4.2.3 Cathode sheath

The influence of the discharge pressure on the dark space is reported in [Rossnagel87b] and in [Gvozdev98]. Both mention that the dark space thickness increases with decreasing pressure, especially at low pressures.

1.4.2.4 Bulk plasma / Electron transport

As already mentioned in section 1.3.5.2, the plasma density for a given discharge current is only slightly dependent on the gas pressure, see e.g. the data of [Rossnagel86, Field02]. In [Špatenka97] the density was found slightly higher at 0.4 Pa than at 5 Pa but the measurement point was 5 mm closer to the target. At 80 mm from the target the density at

5 Pa (2×10^{10}/cm^3) was higher than at 0.4 Pa (1×10^{10}/cm^3). In [Seo04b] it was reported that a region existed where the electron density decreased with increasing pressure (section 1.4.2.3).

The influence of the pressure on the 3D spatial distribution of the plasma (emission) is investigated in [Debal00]: with increasing pressure from 50 to 150 mTorr at constant power (40 W) the argon emission comes closer to the cathode and the emission is shifted slightly inward (this was not for a pure argon gas but an argon-nitrogen mixture). This agrees with the results for the width of the erosion profile and the current distribution (section 1.4.2.1).

The plasma potential V_p in the bulk plasma at two different pressures is reported in [Rossnagel86]: at 30 mTorr ($V_p = 1$ V) it is slightly lower than at 5 mTorr ($V_p = 4$ V). For the latter pressure the presheath extends further into the plasma. The decrease in plasma potential with increasing pressure is also observed in [Field02, Seo04b]. In [Špatenka97] the plasma potential is practically the same at both 0.4 and 5 Pa.

The behaviour of the electron temperature kT_e as a function of pressure can be deduced from the experimental data in Table 1.3: kT_e is consistently higher at lower pressures [Rossnagel86, Špatenka97, Field02]. This pressure behaviour is also reported in [Bradley98b]. In [Rossnagel88b] the electron temperature is reported as a function of the gas density: it varies from 2 eV at 7×10^{14}/cm^3 (2.8 Pa) to 7 eV at 1×10^{14}/cm^3 (0.4 Pa). In [Seo04b] kT_e is measured as a function of the pressure at constant discharge voltage: with a planar probe the general trend of decreasing kT_e with increasing pressure is measured. However, using a cylindrical probe the result is entirely different: kT_e is at 1 mTorr (3.1 eV) and at 27 mTorr (3.25 eV) almost the same but in between it has two local maximums (3.6 eV at 5 mTorr and 4.0 eV at 20 mTorr) and one minimum (2.8 eV at 7.5 mTorr). The origin of the discrepancy is the sensitivity of the cylindrical probe to the detailed shape of the electron energy probability function at low electron energies. This shows that Langmuir probe measurements of kT_e need to be approached with care (see also section 1.3.5.6).

1.4.3 Electrical power input

Increasing the electrical power input intensifies the discharge: the plasma density increases, which leads to a narrowing of the cathode sheath and a widening of the erosion profile. At high powers the effect of the sputtered particles on the MD cannot be neglected anymore as they heat the discharge gas, which leads to gas density reduction (GDR) or gas rarefaction. At even higher power levels sputtering in the self-sustained mode occurs for certain materials.

1.4.3.1 Erosion profile

The effect of the electrical power on the erosion profile was investigated in [Fukami82, Fukami87]: they observed a widening of the erosion profile with increasing power (Fig. 1.21). In [Wendt90] the effect of the electrical power on the width w of the current distribution on the cathode was investigated. Fig. 1.20 shows w as a function of the square root of the Larmor radius r_L. As r_L is proportional with the square root of V_d, the horizontal axis scales as $V_d^{0.25}$ at fixed magnetic field. It is clear that w increases with increasing V_d. Interestingly the width is not uniquely determined by the Larmor radius.

1.4.3.2 Discharge voltage/Discharge current/ IV

The influence of the electrical power on the discharge voltage/discharge current is in principle given by the current-voltage characteristic or IV (section 1.3.4). Here, only the limits of the IV are discussed. The reason for the extinction of the discharge at low powers can be deduced from eq. (1.20) for the discharge voltage. When V_d drops below $V_{d,min}$, an

electron does not have enough energy to produce the necessary amount of ions. However, eq. (1.20) is not suitable to determine this minimum voltage accurately: in reality the amount of ion-electron pairs resulting from one SE emitted at the target can be increased by ionisation in the cathode sheath because the electron of an electron-ion pair generated in the sheath can become energetic. To enhance this effect the cathode sheath increases strongly at low powers. However, the cathode sheath can only be stretched to a certain limit because at too large cathode sheath thickness the electric field becomes too weak to accelerate the electrons to ionise efficiently. Consequently, once a critical sheath thickness is reached, the discharge extinguishes.

Usually the upper limit of the IV is a practical limit: the power supply cannot deliver enough power or the magnetron cooling does not allow higher powers. However, sometimes a deviation from the IV can be seen before these practical limitations occur. Sometimes above a certain discharge voltage, a further increase does not lead to a current increase anymore (dotted line in Fig. 1.14). This is reported in e.g. [Nyaiesh81, Muralidhar95, Fukami87] and seems to occur at low pressures and rather weak magnetic fields. In [Muralidhar95] this phenomenon, which is equivalent with saying that the discharge cannot be maintained beyond a certain maximum discharge current, is attributed to gas density reduction with increasing current.

For certain materials another transition is observed at high powers: with increasing power the discharge voltage saturates and even decreases slightly with increasing power. This indicates the transition to the self-sustained sputtering mode [Posadowski93]. A discussion of this topic is beyond the scope of this work.

1.4.3.3 Cathode sheath

The influence of the discharge voltage on the dark space thickness is reported in [Rossnagel87b] and in [Gvozdev98]. Both report a decrease in d_{ds} with increasing V_d at constant pressure. The dependence of d_{ds} on V_d is given by eq. (1.32) (section 1.3.3.5). Lan Gu [LanGu88] compared the position of the maximum in the plasma emission Δ (see also section 1.3.3.5) at 0.5 and 0.1 mA and found that Δ was consistently smaller at higher discharge currents. This is also reflected in eq. (1.33) for Δ. Although this equation has V_d in the denominator, it does not contradict eq. (1.32) because an increase in V_d will nevertheless lead to a decrease in Δ because the current in the nominator will increase much stronger than V_d itself.

The influence of V_d on the cathode sheath thickness was simulated by Kondo and Nanbu [Kondo01]. They report an increase in the cathode sheath thickness with increasing V_d (Table 1.2), which contradicts the experiments mentioned in the previous paragraph. The deviation of the simulation results from the experiments is attributed to the short distance (20 mm) between the cathode and anode.

1.4.3.4 Bulk plasma / Electron transport

A. Gas density reduction or gas rarefaction

In the context of magnetron sputtering, gas density reduction (GDR) or gas rarefaction is the process in which the discharge gas is heated and therefore diluted. The effect of gas heating was shown by Hoffman [Hoffman85]. He measured the pressure increase during cylindrical magnetron sputtering in a very well sealed vacuum chamber without pumping and could relate the discharge current to the pressure increase. The maximum pressure increase observed was 25% at 12 A. The relative pressure increase was almost independent of the base

pressure. As the pressure increase was direction dependent, Hoffman concluded that there existed circulation cells in the gas, the so-called *sputtering wind*. For planar magnetrons, GDR is reported in [Rossnagel88a]. The heating of the discharge gas is due to momentum transfer with the sputtered particles. As these are emitted from the target with an average energy around 10 eV they can increase the average discharge gas temperature considerably. Rossnagel reports that for Ar on Cu at 1 Pa the particle density is reduced to half of its original density at 1.5 A and to approximately one third at 3.6 A. According to these measurements the sputtered particles reduce the discharge gas density seriously. However, these results can be questioned when considering the following observations.

First, using the same magnetron set-up and the same discharge gas and target material as in [Rossnagel88a], Rossnagel and Saenger reported the optical emission from the MD as a function of the discharge current I_d [Rossnagel89]. The increase in emission intensity is found to be proportional with I_d up to 1 A, above 1 A the dependency slowly decreases and around 5 A the emission intensity is proportional with the square root of I_d (see also part B of this section). This decreased dependence is attributed in [Rossnagel89] to GDR, a plausible explanation. However, according to the experiments mentioned in the previous paragraph, the major decrease in gas density is below 1 A. Consequently, the effect of GDR should be strongest in the region up to 1 A, but there the emission is reported to be proportional with the discharge current.

Second, in [Serianni00] the electron density is found to be proportional with the discharge current in the entire measured region (from 1 to 8 A) for Al sputtering with Ar. If the gas density would be strongly reduced with increasing I_d, the proportionality should become weaker.

Additionally, some simple reasoning can shed some light on the problem. The mean free path length of a sputtered particle is dependent on the kind and the energy of the sputtered particles but is typically some centimetres at 1 Pa. Hence, the energy deposited by the sputtered particles is spread over a volume of several cubic centimetres. Given the size of this volume and given the typical ratios for the sputtered particle/argon density (section 1.3.5.3), a sputtered particle/argon atom ratio of 1/10000 seems a good estimate for typical MD conditions, a ratio of 1/1000 can be considered an upper limit. Now, assume a discharge gas particle energy of 0.025 eV (room temperature) and a sputtered particle energy of 10 eV. When the sputtered particle loses all its energy the average energy of the discharge gas atoms increases to 0.026 eV for a sputtered particle/argon atom ratio of 1/10000 and to 0.035 eV for a ratio of 1/1000. The total pressure of the system can be considered constant, i.e.

$$n_0 kT_0 = n_1 kT_1 \tag{1.62}$$

with index 0 (1) for the situation where the magnetron is off (on). The relative pressure decrease is defined as:

$$\frac{\Delta n}{n_0} = \frac{n_0 - n_1}{n_0} = 1 - \frac{T_0}{T_1} \tag{1.63}$$

This results in a gas density reduction of roughly 4% and 30% for sputtered particle/argon ratios of 1/10000 and 1/1000, respectively. Of course, this simple reasoning is only a very rough estimate but it shows that although at high relative sputtered particle densities (1/1000) GDR can indeed be significant, the effect will be minor for typical discharge conditions (1/10000).

B. Plasma species densities

It appears logical that the higher the discharge current I_d, the higher the plasma density. Hence, a power law is expected:

$$n_s = aI_d^{\alpha} \tag{1.64}$$

with a and α constants and n_s the density of species s of the MD. This relation was experimentally investigated by increasing the current at constant pressure: from the reported measurements of the electron density n_e in [Sheridan89a, Bradley98b, Serianni00] it follows that α is close to one. The optical emission I^s_{emis} of plasma species s can be written as:

$$I^s_{emis} = bI_d^{\beta} \tag{1.65}$$

with b and β constants. Relative density measurements based on this plasma emission have been performed, e.g. [Dony95, Rossnagel89]. In the latter, Ti sputtering with Ar was investigated. The results show $\beta = 1$ for the Ar-emission at low powers, decreasing to $\beta = 0.5$ at high I_d (>5 A). This decrease is attributed to GDR (see above). The sputtered particles emission was found to have β close to 2 (Ar on Ti-target used) and the ionised sputtered particles emission had β close to 3. In both cases β is practically independent of I_d. In [Dony95] the emission from argon ions and sputtered particles (represented by M) scales with the square of the discharge current ($\beta = 2$). As I^s_{emis} is proportional with both n_s and n_e [Rossnagel89], α can be deduced. The results for α and β are summarised in Table 1. 4.

Species	α	β
e^-	1	0
Ar	0	1
Ar^+	1	2
M	1	2
M^+	2	3

Table 1. 4 The approximate values for α (eq. (1.64)) and β (eq. (1.65)) for the different species. Based on results from [Sheridan89a, Rossnagel89, Dony95, Serianni00].

Note that these dependences on I_d are obtained by varying I_d at constant pressure. In [Sheridan90b] the discharge voltage was kept constant and I_d was increased by increasing the gas pressure. For copper sputtering with argon they found $\alpha = 1.63$ for the relation between the electron density and I_d, which is significantly higher as α obtained at constant pressure.

The charged particle confinement time is measured as a function of the discharge current in [Sheridan89a]. Interestingly, the confinement time of the particles increases as I_d increases. Hence, the increase in I_d is not because of "faster" charge carriers but due to the increase in the density of the charge carriers (see also section II.4.3.1).

1.4.4 Target material

In non-reactive mode and using non-magnetic conductive (metal) targets, the choice of target material influences the MD mainly because of the material dependent SE coefficient.

In general, the target material influences a lot of aspects of the MD, e.g. the reactivity of the material or the angular dependence of the sputtered particles. Here, the discussion is limited to metal targets in a non-reactive d.c. mode. Even then, a change of material can have a strong influence on the discharge properties.

First, the target material determines the SE yield γ: as the SE yield is mainly due to potential emission, it follows from eqs. (1.10), (1.11) and (1.12) (section 1.2.2.1) that the work function φ (and for eq. (1.10) also the Fermi energy) of the metal determines γ. Hence, the influence of the target material on the MD is similar to the change of the SE yield. From eq. (1.20) (section 1.3.2) it follows that V_d is inversely proportional with the effective SE yield. Depla et al. recorded at a given discharge current and gas pressures the discharge voltage for different target materials [Depla05a]. They concluded that, as a first approximation, V_d can be considered proportional with $1/\gamma$. The influence of the SE yield on the discharge properties has been self-consistently simulated. In [Shidoji01a] et al. it is mentioned that reducing the SE yield by 50% can decrease the currents with a factor four to five. In [Kondo99a] the increase of the SE yield from 0.12 to 0.15 increases the plasma density (from 1.1 to $1.7\times10^{10}/cm^3$) and discharge current (from 34.9 to 49.5 mA) and decreases Δ (from 7.2 to 5.4 mm) (Table 1.2). As the SE yields for the different metals (Fig. 1.8) vary roughly within the range of 0.04 to 0.09, it is clear that the choice of target material will have a strong influence on the discharge properties.

Second, the choice for the target material also influences the gas density reduction (GDR). For materials with a high sputter yield, there will be relatively more sputtered particles in the discharge and hence the heating of the discharge gas will be stronger. Moreover, the momentum transfer of the sputtered particles to the discharge gas, the main cause for GDR, depends on the kind of sputtered particles. It follows that from the viewpoint of Rossnagel and Kaufmann, who assume that the IV is largely determined by GDR [Rossnagel88b], the n-value of materials with high sputter yield should be lower as the one of materials with a low sputter yield. This was experimentally observed by comparing Cu (high sputter yield) and Al (lower sputter yield) [Rossnagel88b]. However, in their work the effect of the difference in the effective SE yield was neglected, although this effect can very well explain the observed lower n-values [Depla05a].

Third, the target material determines the electron reflection coefficient R and the initial energy E_{init} of the SE. As both these properties influence the recapture probability of the SE, this is another way for the target material to influence the MD characteristics.

A special category of materials that have a stronger influence on the MD are the magnetic materials. These materials can hardly be magnetron sputtered using a typical target thickness and a typical set of permanent magnets because the magnetic field lines will practically all be confined within the target material. Hence, a thin target needs to be used in combination with very strong magnets. Even then magnetron sputtering of magnetic materials poses problems: because of the strong magnetic field gradient within the target material, even a small onset of an erosion profile will lead to a strong increase in the magnetic field at the eroded positions. Hence, the erosion at these positions will be reinforced so that a very narrow and steep erosion profile is formed. An example of a MC simulation of this problem is shown in section 2.2.2. Several "exotic" magnetron designs exist to overcome this problem, see e.g. [Manley93, Devine05].

1.4.5 Discharge gas

In non-reactive mode, i.e. using a noble gas, the choice of discharge gas influences the MD mainly because of the change in the effective ionisation energy although it also has an influence on the SE yield and on the confinement times of the charged particles. Hence, the IVs are discharge gas dependent.

In reactive sputtering, when the discharge gas is not only a noble gas but mixed with one or more reactive gases, the choice and composition of the discharge gases have a very strong influence on the MD and its stability, see e.g. [Sproul03, Sproul05]. However, this is out of the scope of the present discussion where only inert gases are discussed. The influence of the discharge gas on the angular and energy distribution of the sputtered particles is not treated either, even though this can be of practical concern.

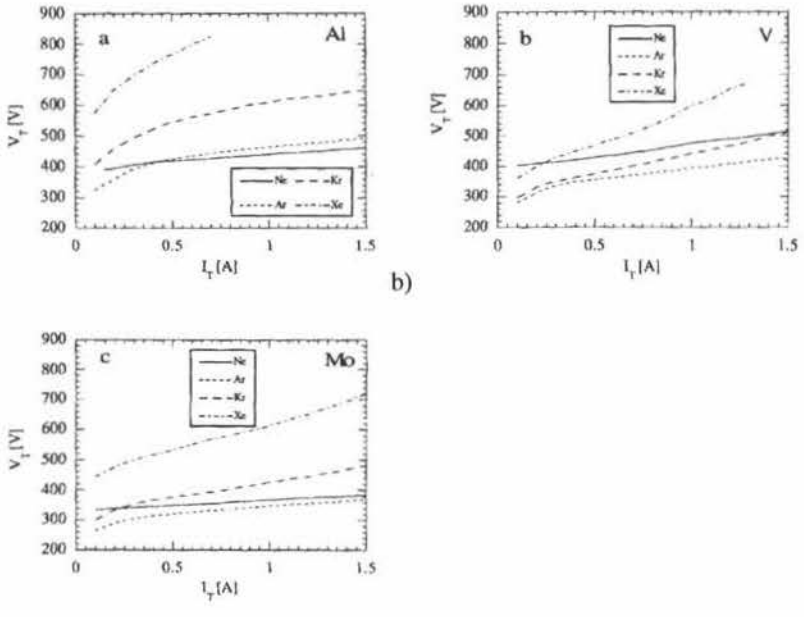

Fig. 1.22 The IV for Al (a), V (*b*) and Mo (*c*) at 1 Pa obtained with Ne, Ar, Kr and Xe. Taken from [Petrov93].

The influence of the inert discharge gas on the MD properties was investigated in [Petrov93]. Using four different noble gases (Ne, Ar, Kr and Xe) three different materials (Al, V and Mo) were sputtered. The discharge voltage at 1 Pa increases from Ar over Kr to Xe for all materials and currents (Fig. 1.22). The deviating results obtained with Ne are attributed to "*the considerably higher ionisation potential and the lower electron scattering cross section for Ne compared to the other three noble gases*" [Petrov93].

The increase of V_d from Ar over Kr to Xe can be understood by considering the SE yield γ. The presence of the ionisation E_i energy in eqs. (1.10), (1.11) and (1.12) (section 1.2.2.1) shows that the discharge gas influences this yield: E_i of Ne, Ar, Kr and Xe is 21.6, 15.8, 14.0 and 12.1 eV, respectively. Hence, the effect of the discharge gas will be similar to the influence of the SE yield, which was discussed in the previous section (section 1.4.4). This explains the results of Ar, Kr and Xe.

The discharge gas influences the MD also through the ionisation and excitation cross sections. It is clear that the ionisation cross section will be related to the minimum pressure at which the discharge can be maintained: this is shown in [Petrov93] where the Ne-discharge can only be maintained for pressures above 0.6-0.8 Pa whereas for the other three discharge gases a stable discharge was obtained down to 0.1 Pa. This is expected to be due to the low ionisation cross section for Ne. Moreover, the relative magnitudes of the excitation and ionisation cross sections will also result in different effective ionisation energies W. The

influence of W on the discharge voltage is given by eq. (1.20). The higher W, the more external energy input needed to obtain the same discharge intensity.

Sheridan et al. measured the charged particle confinement times τ using He, Ne, Ar, Kr and Xe as discharge gas and observed an increase in τ with ion mass [Sheridan90b]. They proposed a model in which τ is proportional with the square root of the discharge gas mass. However, the experimental results show a weaker dependence, except at the highest discharge currents (1 A). Although the influence of γ and W are neglected in this work, the experiments show that the mass of the discharge gas also influences the discharge.

The discharge gas influences the gas density reduction: the transfer of momentum from the sputtered particles to the discharge gas, the main cause for GDR (section 1.4.3.4), depends on the discharge gas. Although this effect cannot be denied, the importance of it is questionable. In [Rossnagel88a] magnetron sputtering of Ti with Ar and Ne was compared. The measured n-values of the IV (see eq. (1.20)) are 9.48 for Ar and 10.53 for Ne. The lower n for Ar was explained using the gas density reduction theory.

Finally, also the ratio of the E×B current and the discharge current is affected by the choice of the discharge gas [Rossnagel87a]: for He, Ne, Ar and Kr on a W target this ratio has the same pressure and discharge current dependence but this ratio is consistently lower for He.

1.4.6 Anode

The anode is a crucial part of the magnetron system as it ensures that the electrical circuit is closed. However, when the anode is well placed it hardly seems to influence the discharge. As a consequence, it is an aspect of the MD that can be commonly neglected but it is necessary to realise that this is only true within limited operating conditions.

The anode is sometimes overlooked when describing a magnetron configuration. This is understandable as, at first sight, it does not play such an important role. When describing the motion of the HEE, only the electric field at the cathode side and the magnetic field are needed (see also section 1.1). As the HEE determine the ionisation position and the resulting target bombardment, the anode seems redundant. However, for any self-consistent model the anode is needed as it determines the electric field in the plasma. Moreover, a magnetic field line that intersects the anode becomes a virtual anode and limits the extension of the discharge region (Fig. 1.15).

Thornton mentioned that the positioning of the anode is crucial for optimal discharge voltages in cylindrical magnetrons as "*an anode of insufficient size or with poor placement can cause a significant anode voltage drop*" [Thornton78b]. Hence, he designed for a cylindrical magnetron an end wing with anode shroud (Fig. 1.23a): it was suggested to take D, the distance between the target and the anode, at least three times larger than the Larmor radius of the HEE. If D becomes too small, the discharge will be shortened and the HEE will leave the discharge without being able to generate the theoretical maximum amount of electron-ion pairs. Hence, the delivered energy to the discharge will not be used optimally which requires higher discharge voltages.

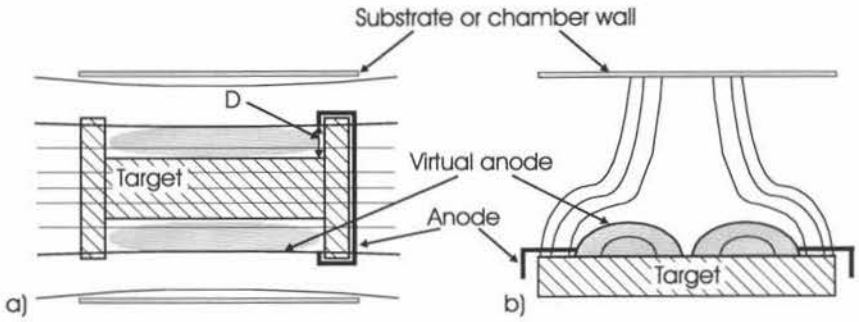

Fig. 1.23 Positioning of the anode in a cylindrical (*a*) and planar (*b*) magnetron.

The foregoing reasoning also applies for planar magnetrons: if the anode is placed too far from the centre of the target the anode might not be efficient and another part of the system can become the effective anode. This becomes clear by comparing the situations sketched in Fig. 1.15b and Fig. 1.23b. On the other hand, if the anode is placed to close to the centre of the target, the discharge area becomes too small. This leads to a decreased effective SE yield because relatively more SE will be recaptured. Moreover, the HEE will leave the discharge with a considerable amount of energy (ε_e no longer equal to one in eq. (1.20)). The increase in the discharge voltage when the anode is shifted into the discharge area has been experimentally observed [Depla05a]. Hence, the positioning of the anode is crucial for an efficient magnetron working.

It is interesting to look at situations where the anode is obstructed, as in [Seo04a] where an unbalanced magnetron of type II is used with two anodes: an anode ring at 25 mm above the target and an anode plate 80 mm above the target. If both anodes are grounded, the plate on top carries practically all the current. The more negative the top "anode" is biased, the more the current is carried by the grounded anode ring. Because of this the electron loss mechanism changes, which causes the reported change from a bi-Maxwellian to a single Maxwellian EEDF (see also section 1.3.5.6).

In [Sieck94] a segmented anode is placed along a rotatable magnetron. The different segments can be grounded or left floating, which prevents them to act as anode. If all segments are grounded, the anode segment immediately after the turn (in the sense of the E×B drift of the electrons) carries the largest current. The target position next to this anode segment is eroded the strongest. If only one segment is grounded and the others are left at floating potential, the target position next to the grounded segment experiences the highest target erosion rate, regardless the position of the grounded segment.

An extreme case of anode obstruction can occur when depositing insulating layers during reactive sputtering. If no special care is taken, the insulating layer does not only form on the substrate but also on the anode. Hence, after a while, the path for the electron current to the anode is blocked. This gives rise to the so-called disappearing anode effect which leads to instability of the process, see e.g. [Sellers97].

1.5 Conclusions

From this literature review, it follows that the general processes related to the working of the MD are well-known. However, some aspects are not completely clarified. The ones that will receive further attention in this work are briefly summarised:

- The secondary electrons emitted from the target are brought back to the vicinity of the target, which leads to electron-target interaction, resulting in recapture of the electrons. Although it has been known for a long time that this process occurs and that it can strongly influence the discharge voltage, practically no work has been done to quantitatively calculate the influence of this process.

- In a MD, the Child-Langmuir law cannot be applied because, due to the magnetic field, the cathode sheath is neither electron-free nor source-free. The latter is due to the generation of ions within the sheath. In spite of this, the Child-Langmuir law is frequently applied to the MD.

- Characteristic for the MD is the very steep current-voltage characteristic. Although efforts are made to physically clarify this relationship, basically only phenomenological models exist.

- Experimental measurements of the ratio of the Hall current and the discharge current reveal values that are substantially lower than theoretically predicted. Consequently, there is anomalous electron diffusion. The anomalous transport is especially important at strong magnetic fields and/or low gas pressures. It is suggested that this enhanced transport is related to electric field oscillations. However, no quantitative models exist for this phenomenon.

In part II of this work, these issues will return: (simplified) models will be proposed for the first three whereas the last one will be dealt with empirically. This way they all will be included in the simplified self-consistent magnetron discharge model that will be discussed.

2 MAGNETRON DISCHARGE MODELLING

This chapter gives an overview of MD modelling. This modelling is scientifically challenging as it concerns a plasma interacting with a magnetic field. Such an interaction can lead to complex behaviour as also shown by the problems encountered in Hall thrusters or nuclear fusion in a tokamak. More information about the simulation of these subjects can be found in [Post04] and [Bareilles04], respectively. Of course, simulation of a tokamak plasma is of an entirely different scale as of a MD.

First, we consider the modelling of the whole magnetron sputter deposition process as this places the MD modelling in a broader perspective (section 1.1). Second, the different methods encountered in MD modelling are treated (section 2.2). Third, some challenges and limitations when simulating the MD are discussed (section 2.3). Finally, the choice for a simplified model is motivated (section 2.4).

2.1 Modelling magnetron sputter deposition

Magnetron sputtering is a widely applied coating technology in industry. Examples of coatings deposited by magnetron sputtering are numerous. A review of relatively recent developments in magnetrons and examples of (the advantages of) magnetron sputtered coatings is given in [Kelly00]. Here we mention specifically the coatings put on glass to control its heat transmission: yearly more than 200 million square metres of glass is plasma coated for this application, with magnetron sputtering the preferred deposition technique [Fellenberg03].

Because of the industrial importance, there is a strong drive to simulate the entire magnetron deposition process in order to replace trial-and-error experiments. This can lead to serious cost reduction, both for the manufacturers as users of magnetron sputter equipment. The reasons are straightforward. For a typical coating plant, one of the main costs is the installation cost. Hence, it is a major advantage to have equipment that from the start can realise a large throughput that fits specifications like required deposition speed, uniformity, reproducibility or target lifetime. This means that magnetron manufacturers strive to a minimum "setup time", which requires from them the ability to predict whether the proposed design will work or not before the machine is actually built. This could be achieved by simulating the machines' characteristics. Of course, also the possibility of optimising the deposition parameters without actually performing any real world experiment is attractive.

The ideal magnetron sputter deposition simulation would use as input the desired coating characteristics (e.g. electrical resistance, adhesion, refractive index, ...) and process requirements (e.g. deposition speed, price per square metre,...). It would yield as output the necessary process parameters, e.g. sputter mode (d.c., r.f., pulsed, ...), gas pressure, magnetic field strength, electrical power input,... In reality, one is still far away from such a model. The model becomes more realistic when the in- and output are switched (Fig. 1.1). This way the parameters defining the deposition process are the input; the deposited film properties form the output. Such model is referred to as a "*virtual sputter magnetron*". Efforts are made to develop such a simulation tool, e.g. [Yamazaki02, Pflug02, Kools04a, Kwon05]. This trend of virtualising is not limited to magnetron sputtering but is generally found back in plasma related processes, e.g. high intensity discharge lamps, inductively and capacitively coupled plasmas or plasma displays panels. A short history and future of plasma modelling and simulation with respect to microelectronics fabrication is given in [Graves03]. Some of the university groups that are working more in general on plasma simulation are the groups of A. Bogaerts [Bogaerts05], M. Kushner [Kushner05], K. Nanbu [Nanbu05] and C. Birdsall

[Birdsall05]. The latter is in that sense unique because the software they develop can be freely downloaded.

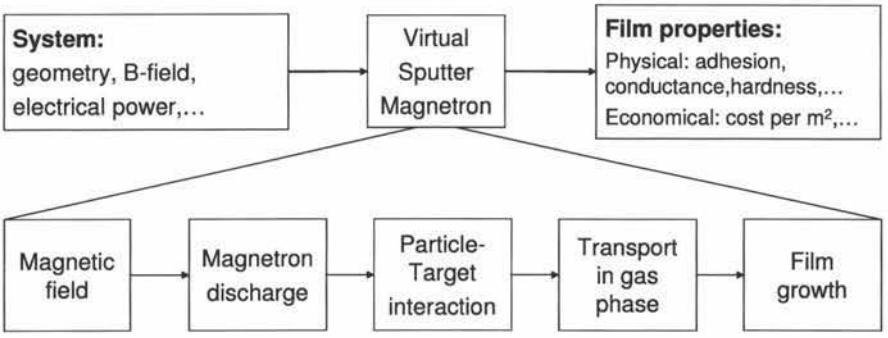

Fig. 2.1 Sketch of the "virtual sputter magnetron", a simulation tool that allows simulating the entire magnetron sputter deposition process. The basic parts needed in such a tool are also shown.

Now, we consider "the virtual sputter magnetron" of Fig. 1.1 in more detail. Basically, it consists of the following modules:

- magnetic field modelling
- magnetron discharge modelling
- ion bombardment of the target and characterisation of the sputtered particles
- transport of the sputtered particles through the gas phase
- deposition and film growth at the substrate

From a scientific view-point, these modules cover a wide range of disciplines (plasma physics, surface physics, materials science, ...). Some of the modules can be considered as known physics, others as challenging research topics. An example of the latter is the relation between the particles arriving at the substrate and the properties of the deposited film.

An accurate self-consistent virtual sputter magnetron that can operate over a wide range of parameters requires careful treatment of each of these modules. Like in a chain, the weakest link, will determine the total strength: however good the other modules, if there is one in the global model that is not accurate, the outcome of the whole model will be affected.

Now, the different parts are very briefly discussed and references to some relevant literature are given.

2.1.1 The magnetic field

Essential for a MD is the magnetic field: without it the discharge would be an ordinary diode discharge. Hence, it is necessary for any simulation to have accurate values for the magnetic field. This can be achieved for the most complex magnetic configurations with high accuracy by using finite element models that are available as commercial packages or as free- or shareware. Packages reported in literature regarding magnetron sputtering simulation are e.g. POISSON [Wendt88a, Shon98], OPERA [Shon99], FEMME [Kools04b]. A disadvantage of this method is that a high accuracy is only reached for a very dense mesh, which makes the magnetic field calculation time consuming. Very high accuracy is needed though: the length scale over which the electrons move during a time step when retracing their orbits is very

small, order of 0.1 mm or less. For an accurate simulation of the electron orbits, the magnetic field must vary smoothly over this scale length.

The magnetic field can also be calculated using an integral element method, as e.g. in the ELF/MAGIC code [Shidoji01a], which allows a fast calculation. Another possibility is to calculate the magnetic field analytically. This has the major advantage that the field strength can be determined practically instantaneously at any point in space, which guarantees the smooth variation of the magnetic field along an electron orbit. Drawback is that only relatively simple magnetic configurations can be modelled and that the effect of magnetic shunts or complex magnet shapes cannot be dealt with.

The last possibility is to start from a measured magnetic field and interpolating or fitting it by an analytical expression. This also leads to a smooth spatial variation of the magnetic field. Of course, in such an approach the principle of virtual coater is violated: it does not allow simulating different magnetic field configurations, unless they are built in reality and measured accurately.

2.1.2 The magnetron discharge

The simulation of the MD based on the magnetic field, the gas pressure and the electrical power input is the next step. The underlying basic physics is at microscopic level "only" the motion of charged particles in a region subjected to an electric and magnetic field. This, combined with the necessary cross sections and electron yields, is in principle sufficient to describe the MD. However, the emerging behaviour of the plasma as a whole can be very complicated and turns this module of the virtual coater into one of the most difficult hurdles to take.

Software packages exist to simulate plasmas in general. Basically they are two types: the ones based on a Particle-In-Cell Monte Carlo (PIC-MC) scheme and the ones based on fluid dynamics. Given the simple basic equations governing the magnetron discharge, these packages should be able to simulate magnetron discharges correctly. Unfortunately, the small time scales required for the electron motion (10^{-11}-10^{-12} s) combined with the large time scales required for reaching equilibrium (10^{-5} s) make the computational load extremely, and for certain configurations even unrealistically, high (see also section 2.3.4). For the fluid-based simulations, the difficulty is the assumption of local thermal equilibrium (section 2.2.4). Hence, there is a need for hybrid and simplified models. These, however, have their disadvantages too. As the MD is in principle the heart of the process, it is surprising that the more advanced simulation of the sputter process presented in [Pflug02] can completely bypass this and the previous module. Instead, the simulation starts with a profile characterising the sputtered particles.

This module of the virtual sputter magnetron is dealt with more extensively in section 2.2 where different methods and their specific (dis)advantages are discussed.

2.1.3 The particle-target interaction

The sputtering process is based on the removal of target atoms by ion bombardment. The simulation of ion bombardment on a solid is well developed. These packages do not only allow determination of the sputter yield, i.e. the average number of atoms removed per incoming ion, but are also able to reproduce the angular and energy distribution of the atoms that leave the surface. Very well-know are TRIM [Biersack80, Eckstein91], SRIM [Ziegler04] and packages based on these. These packages have as main shortcoming that they are not dynamical, i.e. changes in the solid because of the incoming ion flux are not taken into

account. Packages that take this into account are molecular dynamics based, e.g. TRIDYN [Möller88, Möller02] and KALYPSO [Karolewski05]. An illustration of a result obtained with the latter is Fig. 2.2: it shows the origin of the Cu-atoms sputtered by 3 keV Ar projectiles, which bombard the surface at (0,0). All the mentioned packages are numerical simulations, implying that the computational load is heavy. This is especially true for the molecular dynamics based ones.

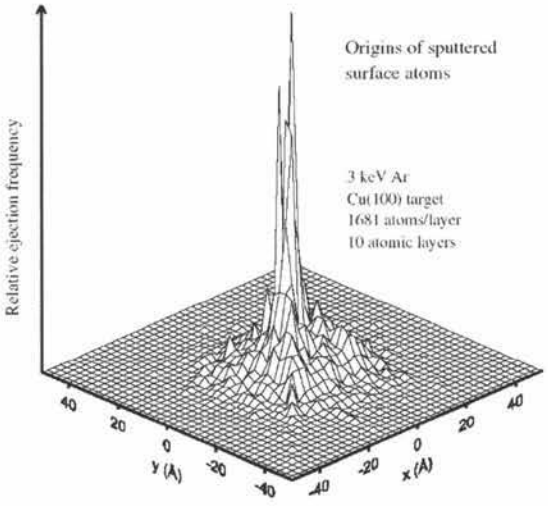

Fig. 2.2 Illustration of KALYPSO: plot showing the relative ejection frequency vs. lattice site position for Cu atoms sputtered from a Cu (100) crystallite by 3 keV Ar. Taken from [Karolewski03].

Hence, efforts are made to determine properties like the sputter yield and the angular and energy distributions of the sputtered particles by analytical expressions. These analytical expressions can be purely empirical or can be based on a simplified model. For the sputter yield, an example of the former is the well-known formula of Matsunami [Matsunami84], an example of the latter is the work reported in [Mahan97]. Also for the energy and angular distribution of the sputtered particles analytical models exist. A nice overview of this issue can be found in [Stepanova01].

2.1.4 Particle transport in the gas phase

Once the particles are sputtered from the target, they start spreading out through the vacuum chamber. The collision dynamics of these rather low energy (typically some tens of eV or below) particles is known. However, discussion exists about which interactomic potential is to be used [Kuwata03]. This is not an academic discussion as the choice of the interatomic potential influences the simulated energy and angular distribution of the sputtered particles at the substrate [Myers92]. As such, the exact potential is required for realistic thin film growth models. Ideally, the sputtered particle transport is described by combining a MC based model (for non-thermalised particles) and a diffusion model (for thermalised particles) [Nakano99].

Some examples of simulations are mentioned. In [Smy97] the transport is described by a MC approach (SIMSPUD) and by a diffusion approach. In [Macàk99] a MC model is described. Another package for the sputtered particle transport is e.g. ACAT [Yamamura95]. In [Mahieu05] the film thickness distribution is simulated using a MC model for different

target materials and for different target-substrate distances at different pressures. The results agree well with the experimental results, even for conditions where the ratio of the substrate and target diameter is large. Of course, also for this aspect of the magnetron sputter process simplified models have been developed, e.g. [Hong96].

2.1.5 Film growth on the substrate

For this part, the input consists of the energy and angular distribution of the particles arriving at the substrate and their arrival rate. With "particles" is not only meant the sputtered particles but also the electrons and discharge gas particles (neutrals and ions) as they also contribute to the energy deposition at the substrate. The relation between this input and the resulting film properties is one of the more difficult parts when modelling the magnetron sputter process.

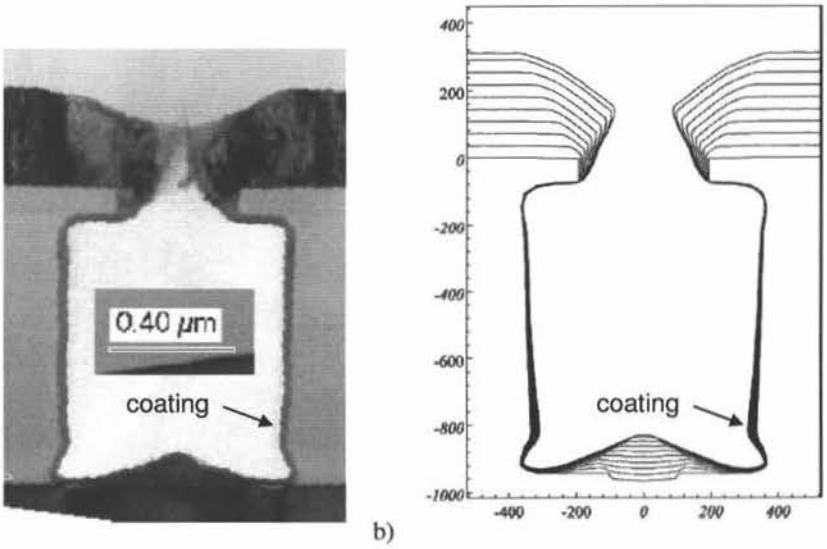

a) b)

Fig. 2.3 Example of the feature scale simulation of the deposited coating in a "bottled test structure" using a hollow cathode magnetron. Part (*a*) gives the SEM image, part (*b*) the corresponding simulation result. Taken from [Jacobs03].

A first step is the simulation of the film thickness distribution and/or its deposition rate as this follows rather straightforwardly from the information about the incoming particles and the sticking coefficients. In practice, in a lot of cases only this aspect is considered.

A more advanced form of this is "feature scale modelling". In microelectronics, the deposited coating might be required to fill structures like a thin trench or via. Feature modelling tries to simulate the exact coating thickness on all surfaces of such a feature [Graves03]. An illustration of the simulation of coating thickness on both the reactor and feature scale for ionised PVD using a hollow cathode magnetron is given in [Jacobs03], see Fig. 2.3. Similar work can be found in e.g. [Gilmer00, Cale00].

One step further is then to actually simulate the microstructure of the deposited material. The most accurate simulations are based on molecular dynamics but this is extremely computing intensive. Consequently, (empirical) approximations are needed. A sound discussion of this problem together with some examples of predicted structures can be

found in [Bilek02]. In [Hammerschmidt05] the deposition on grain boundaries is simulated for Ti (Fig. 2.4). Examples of the microstructural evolution during film growth (and the kinetic MC simulation thereof) can be found in [Petrov03]. Of course, also simplified models are developed, e.g. for the biaxial alignment in yttria stabilized zirconia layers [Mahieu04].

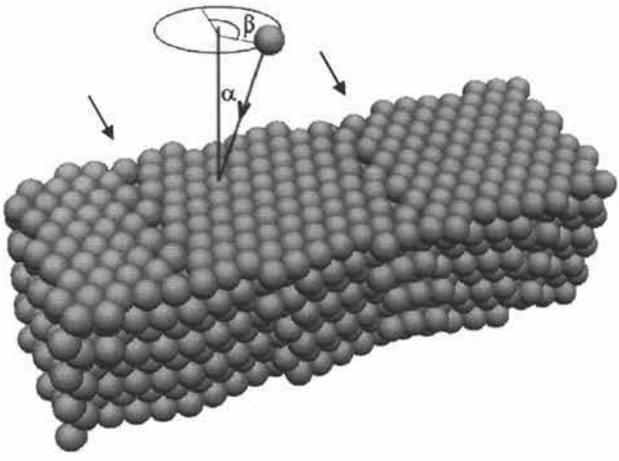

a)

b)

Fig. 2.4 Two relaxed grain boundaries (indicated by the arrows) in the (0001) plane (*a*). Part (*b*) shows the grain boundaries after deposition of five atomic layers. The depositing species arriving with $\alpha = 20°$ and $\beta = 0°$. The deposition on the grain boundaries results in amorphous regions. Taken from [Hammerschmidt05].

2.2 Magnetron discharge simulation models

With this module is meant the (self-consistent) modelling of the MD. This means a model that can relate the basic external parameters (gas pressure, magnetic field and electrical power input) with (some of) the properties of the resulting discharge. Numerous models were, and are still being, developed for this purpose. These range from models that have the potential to describe the MD very accurately (e.g. PIC-MC) to very elementary models (e.g. the Thornton formula for the discharge voltage, section 1.3.2). To count as a "simulation model", i.e. to be included in the list here, the model is required to reproduce certain MD characteristics with spatial resolution. For a cylindrical (or post) MD, this implies at least a one-dimensional model, for a planar magnetron a two-dimensional model is the minimum. The reason for this limitation is the conviction that this minimum number of dimensions is required for a model that wants to be quantitative, a logical demand for a simulation. Models that are less dimensional can of course also be very valuable as they can give insight into the MD but they can, at best, only be qualitative.

Several different models exist for MD simulation. An important property of a model is whether it is self-consistent or not. The most commonly encountered methods and their major (dis)advantages are discussed. For further reference, it is mentioned that relatively recently a review article with respect to magnetron discharge modelling has been published [Shon02].

2.2.1 Particle-In-Cell Monte Carlo method

One of the most encountered techniques in MD simulation is the "Particle-In-Cell Monte Carlo (PIC-MC)" method. This simulation method is not limited to MD but is frequently used in plasma simulation. It is a combination of the PIC and the MC technique. The latter technique is treated further (section 2.2.2). It is sometimes referred to as PIC-MCC, i.e. "Particle-In-Cell Monte Carlo Collisions", which stresses that the MC technique is used to handle the Collision events. The PIC technique is basically a method to describe the behaviour of a large number of charged particles. The space occupied by the particles is divided into cells. The particles are represented by a limited number of super-particles. Each super-particle has a weight factor that specifies the number of real particles it represents. By using the Poisson equation for the relation between the charge density and the electric field, this technique enables to calculate the electric fields generated by the charged particles and thus allows simulating their behaviour self-consistently. Combined with the MC technique for the charged particle collisions, this forms a powerful method to simulate plasmas in a self-consistent way.

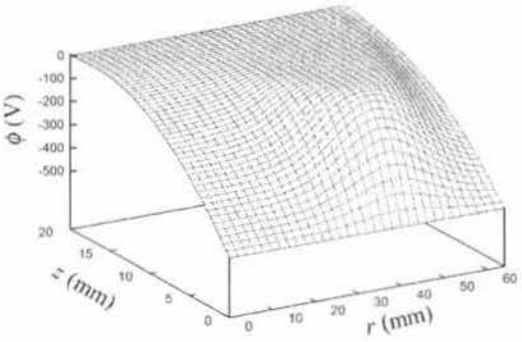

a)

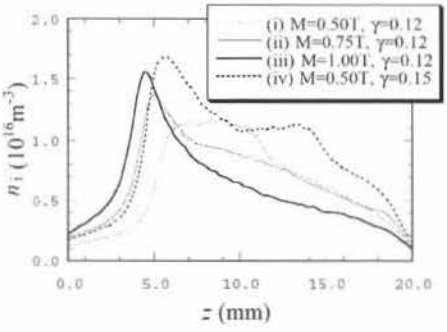

b)

Fig. 2.5 Example of some of the simulation PIC-MC results: the potential distribution for M =1.00 T and γ = 0.12 (*a*) and the ion density in the direction perpendicular to the target (*b*) for different SE yields γ and magnetic field strengths M (M = 1.00 T corresponds with $B_{max} \approx 650$ G). All shown results are obtained with the discharge voltage set to 500 V and the gas pressure equal to 5 mTorr. Taken from [Kondo99a].

The major advantage of the PIC-MC technique is that it is a truly self-consistent technique. It also results in a wealth of data, including the electron and ion density, their energy distribution, the potential distribution, the ionisation rate, ... Some of these are shown in Fig. 2.5. A major disadvantage is the required computational load. This can be overcome by running the program on a supercomputer or on a cluster. Nevertheless, in [Kondo99b] it is reported that running the PIC-MC simulation takes typically 150-200 hours on a Cray C916.

There is quite some literature describing the use of PIC-MC models for simulating the magnetron discharge. Van der Straaten et al. developed their own PIC-MC for the cylindrical MD [VanderStraaten98a,b]. In [Kudrna02] the cylindrical MD is simulated using the XPDC1-code from [Birdsall05]. For planar MD, the best known simulations are probably the work of Nanbu et al, see e.g. [Nanbu96, Nanbu97, Kondo99a, Kondo99b, Kondo01]. They used their own developed PIC-MC model. Also quite some work reports planar MD simulations using the OOPIC code [Shon98, Shon99, Kadlec04, Kools04b, Kwon05]. This OOPIC code was developed by Verboncoeur et al. [Verboncoeur95] and can be downloaded freely [Birdsall05]. Another software package that is used for MD is PEGASUS [Kusumoto04], the software itself is described in more detail in [Miyagawa03, Miyagawa05] and is based on NEPTUNE. The latter is used in [Yamazaki02] to simulate copper deposition by magnetron sputtering. More recently, Kolev and Bogaerts also developed a PIC-MC model for the magnetron discharge [Kolev04a].

In [Shon98] and in [Kwon05] it is reported that no steady state is found. Instead, the amount of particles increases. In both cases the time the plasma is simulated is very short (3 and 5 μsec, respectively). Following the discharge for a longer time period apparently leads to a steady state, e.g. [Nanbu97, Kondo99a, Kools04b], although [Kolev05] mentions that a reliable steady state, i.e. a steady state where the discharge evolves to the correct region of the current-voltage characteristic, can only be reached by including an external electric circuit. In the latter work, the required time for reaching convergence was "not less than 20 μsec". In [Kools04b], the results show that convergence was reached after roughly 10 μsec.

As mentioned, this type of magnetron discharge simulations produce a wealth of data. However, care has to be taken when interpreting the results. Here we mention some shortcomings of the results reported by the group of Nanbu et al [Nanbu97, Kondo99a, Kondo01]. First, the time step Δt used for the electron orbits is rather large: in [Kondo99a] it is mentioned that $\Delta t \approx 0.2$ ns. The examined magnetrons have B_{max} in the range of 325 to 650 G. With these B_{max} correspond Larmor frequencies of 6 to 11 GHz, which means that Δt varies from 0.18 to 0.36 times the inverse of the Larmor frequency. According to the results presented in Fig. 1.4 in section II.1.3.1.1, such large time steps result in an inaccurate orbit calculation and in a serious artificial electron energy loss. These inaccuracies compromise both the position and the amount of ionisation simulated, which seriously questions the reliability of the presented results. This might be the origin of the second shortcoming of these simulations: the simulated cathode sheath thicknesses are very large: in [Kondo99a] sheath thicknesses vary from 4.5 to 5.8 mm. In reality, sheath thickness of at most 3 mm are observed (section 1.3.3.5B). Third, the current densities are extremely low for magnetron discharges. From the sketch of the magnetron configuration in [Kondo99a] we can infer a race-track surface of roughly 24 cm^2 (race-track length ≈ 24 cm, race-track width ≈ 1cm). The total currents listed in the article are between 35 and 50 mA, which means current densities around 1.5 to 2.1 mA/cm^2. These values are at least a factor 10 lower as the current densities typically encountered in magnetron sputtering. The fourth remark concerns the simulated current-voltage characteristics: with increasing discharge voltage the discharge current and the electron density are found to decrease, the cathode sheath thickness is found to increase

[Kondo01]. These simulated dependences are opposite to experimental observations (see Chapter 1).

A very interesting result of these simulations is the magnetic field dependence: in [Kondo99a] the magnetic field strength B_{max} is varied from 325 to 650 G at constant discharge voltage (V_d = 500 V) and gas pressure (5 mTorr). The simulations show an increase in the plasma density and in the ionisation rate (Fig. 2.5b and Fig. 2.6). Moreover, the discharge intensifies and the cathode sheath thickness is found to decrease. This is in agreement with common sense: with increasing magnetic field strength, the MD intensifies and is better confined. This result seems to indicate that the anomalous electron transport is simulated, at least qualitatively, correctly (see also section 2.2.5).

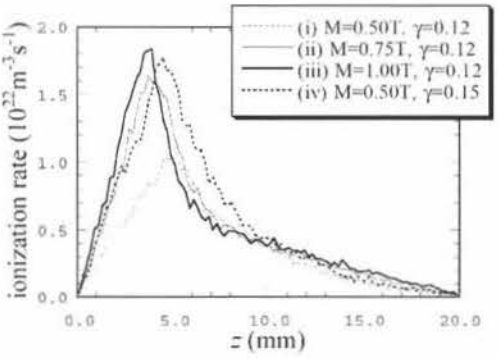

Fig. 2.6 Simulated influence of the magnetic field on the ionisation rate. Same settings as in Fig. 2.5. Taken from [Kondo99a].

In spite of the mentioned shortcomings, the PIC-MC technique is in principle a very viable method. Hence, one can easily agree with the conclusion of [Kolev04a] which states that PIC-MC is "*the most powerful tool to tackle the problem with the full description of the planar magnetrons at all operational conditions. The price for that is the very long computational time.*"

2.2.2 Monte Carlo method

In the Monte Carlo (MC) method, a test particle is followed in a fixed environment, i.e. the events generated by the test particle do not change its environment. This technique is also referred to as "Test Particle Monte Carlo method". An analysis of the foundation of the MC method in plasma simulations, including its physical meaning and relation with solving the Boltzmann equation can be found in [Bruno03].

The fixed environment is an input of the simulation and can be obtained from other models or from experiments. Note that "fixed" does not mean that the environment must be static, it can vary in the time during which the test particle is followed but the test particle cannot induce the changes. Consequently, the technique is not self-consistent, which is its major drawback.

To determine the events of the test particle, no deterministic algorithm is used. Instead, the events are determined stochastically using a set of random numbers. In reality, pseudo random numbers are used because these can be easily generated by computer algorithms. In principle each test particle that is followed will give a different result. A meaningful result can only be obtained when a large ensemble of test particles is used.

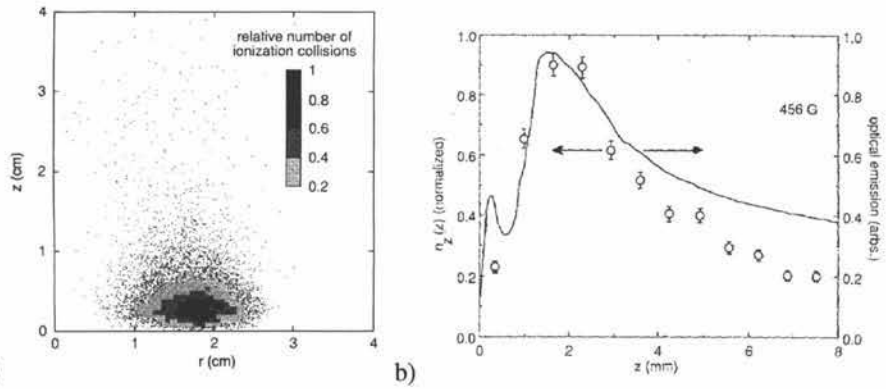

Fig. 2.7 Example of the simulated ionisation distribution for a cylindrical magnetron using the MC method (*a*). The *r*-axis is along the target, the *z*-axis is perpendicular to it. The results are for $V_d = 400$ V, gas pressure 1 Pa and $B_{max} = 245$ G. By integrating the ionisation distribution over the target, the obtained distribution can be compared with experimental measurements of the optical emission of the MD (*b*). Parts (*a*) and (*b*) are taken from [Sheridan90a] and [Miranda90], respectively.

This technique is most commonly encountered in numerical MD simulations when it comes to determining the ionisation distribution or the erosion profile on the target. The reason is the success of the work done by the group of Sheridan-Goree et al., e.g. [Miranda90, Sheridan90a, Goree91, Goeckner91] who were able to simulate the ionisation distribution using a two-dimensional MC model and compared it with optical emission measurements (Fig. 2.7). Also the erosion profile could be simulated. The basis of their model was a simple retracing of the high energy electron orbits by numerically integrating the Lorentz equation (eq. (1.1)) and combining this with a MC approach for the collision events. Similar work is reported in e.g. [Fan04, Ido93b]. The group Sheridan-Goree also simulated the ion motion [Goeckner91] and the influence of the magnetic field [Goree91] using the same Monte Carlo model.

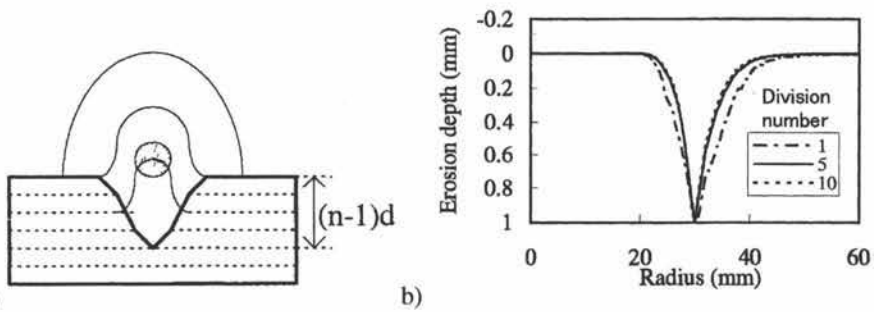

Fig. 2.8 Example of erosion profile simulation using the MC method. Part (*a*) shows how the formed erosion groove is taken into account. The target is split in *n* layers. Each time a layer is sputtered through, the simulation is restarted with the obtained erosion profile as input. Part (*b*) shows the simulated erosion profiles for $n = 1$, 5 and 10. In this case 5 divisions are sufficient. The agreement with the experimental erosion profile was excellent. Taken from [Ido98].

S. Ido et al. used a MC model to simulate the erosion profile in planar magnetrons. First, the erosion profile in a cylindrical and a rectangular magnetron were simulated for various pressures and magnetic field configurations [Ido93b, Ido96a, Ido96b]. Then, the erosion profile using ferromagnetic targets was simulated. They report how the eroded region

can be influenced by placing a ferromagnetic ring on top of the target [Kashiwagi99] and by the outer part of the yoke [Ido99]. For a ferromagnetic target, the eroded region strongly influences the magnetic field strength. In [Ido98] is reported how this effect is taken into account, which leads to a very accurate erosion profile simulation (Fig. 2.8).

The main advantages of the MC method are that it is easy to implement, it can handle the low gas pressures encountered in MD and it is much faster than self-consistent methods. Because of the latter, it can be used on (large) three-dimensional geometries, see e.g. [Shidoji94, Shidoji00, Lopp02, Fan03, Kubart04, Buyle05]. In all these references the MC model is basically used to investigate the cross corner effect. This term is used to denote the enhanced ionisation and erosion that occurs at opposite sides of a (long) rectangular target. It is due to a disturbed E×B drift of the electrons after they drifted trough the end region of the race-track [Buyle05]. Here, the MC method has an advantage over the PIC-MC method: in [Nanbu97] a three-dimensional magnetron was simulated but the variation of the ionisation along the race-track was too large to notice the cross corner effect. Although the PIC-MC method should undoubtedly be able to reproduce this effect, it would cost an enormous computational effort.

2.2.3 Kinetic model

The kinetic modelling of the MD is based on the solution of the Boltzmann kinetic equation for the electrons. To our knowledge, this technique has only been applied to cylindrical or post magnetrons. The discussion here is based on the work of Porokhova et al., see e.g. [Porokhova01, Porokhova03, Porokhova05a]. Their work is based on the spatially inhomogeneous Boltzmann equation [Porokhova01]:

$$\bar{v}\cdot\nabla_{\bar{r}}F-\frac{e}{m}\left(\bar{E}+\left[\bar{v}\times\bar{B}\right]\right)\cdot\nabla_{\bar{v}}F=C(F)$$

with $F(\bar{v},\bar{r})$ the electron distribution function. Note that the force term has already been replaced by the appropriate form containing the electric (E) and magnetic (B) field which also appears in the Lorentz equation (eq 1.1). The term $C(F)$ represents the various collision processes of the electrons.

To find a self-consistent solution for a given input of magnetic field strength, gas pressure and discharge current, the kinetic equation needs to be supplemented by some other requirements. In [Porokhova01], self-consistency is reached by adding an equation describing the ion motion in collisional regime (i.e. a fluid model for the ions) and Poisson's equation. In [Porokhova03] the radial distribution of the electric field is determined by fixing the discharge voltage to the experimentally measured one and by demanding that the radial potential distribution provides a radial electron density distribution that is similar to the experimentally measured one. This latter approach seems "less self-consistent" as both the discharge current and voltage are used as input parameter. In [Porokhova01] the model is one-dimensional, in [Porokhova03] the model is extended to two dimensions so that also the axial inhomogeneities generated by the shields at the ends of the cylindrical magnetron can be modelled. A major advantage of the method is the small computational load: a typical calculation requires about 2 to 10 minutes, depending on the number of grid points [Porokhova05b].

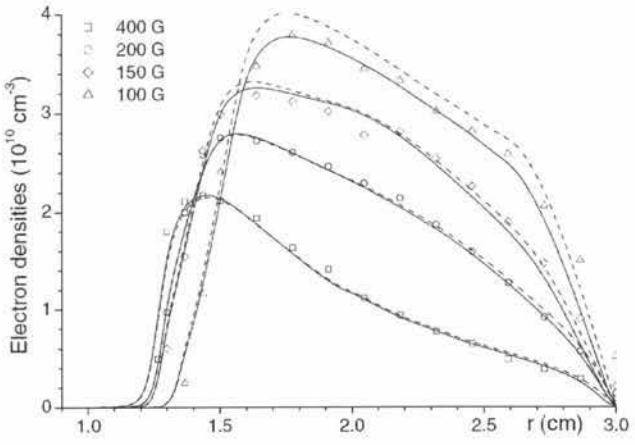

Fig. 2.9 Simulated (lines) and experimental (markers) results for the ionisation distribution in the radial direction in a cylindrical MD discharge for different magnetic field strengths. Taken from [Porokhova05a].

The presented results in the mentioned references show a very good agreement between the experiments and the simulations. However, the results are obtained for high gas pressures (minimum 3 Pa) and relatively weak magnetic field strengths (maximum 400 G). It would be interesting to see whether this modelling approach can deal with low pressures and strong magnetic fields as these are the working conditions were anomalous electron transport can be expected (see also section 1.3.6.2 and Chapter II.6). It is also not evident at all to adapt this technique to a two-dimensional model for the planar MD due to the non-uniform magnetic field [Porokhova05b].

2.2.4 Fluid model

The fluid model, or hydrodynamic model, is also based on the Boltzmann equation but it assumes that there is local thermal equilibrium, i.e. the electron energy distribution function (EEDF) is assumed to be Maxwellian in each point. What remains are the continuity, the momentum transfer and the mean energy transfer equations for both the ions and the electrons. Different fluid models differ in the approximations made to solve these equations. The model is made self-consistent by adding the Poisson equation.

Fluid models are not common to describe the MD. One-dimensional models are reported in [Bradley97, Cramer97, Rabiński98]. A two-dimensional fluid model for the planar MD was recently developed by Costin et al. [Costin05]. They reported simulation results (electron and ion densities, plasma potential distribution) for a circular magnetron (diameter 33 mm) with $B_{max} = 750$ G and $V_d = 550$ V (Fig. 2.10). For pressures varying form 30 to 5 mTorr they found cathode sheaths thicknesses from 3.0 to 7.5 mm for $V_d = 350$ V. These appear very unrealistic: typical measured values for these conditions are below 3 mm (section 1.3.3.5B).

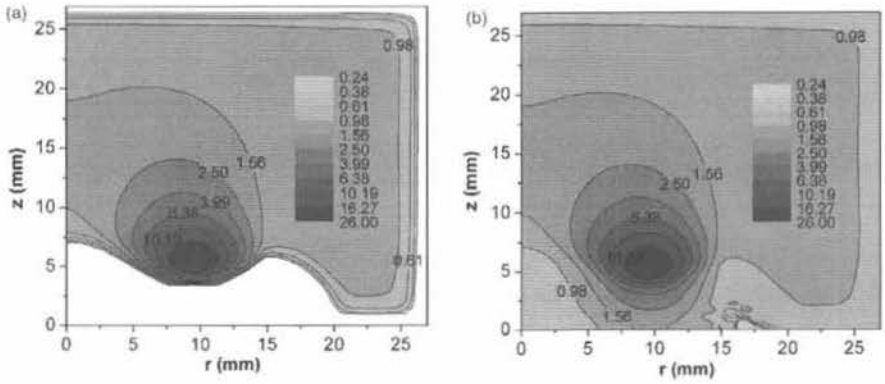

Fig. 2.10 Simulated electron (*a*) and ion (*b*) density using a 2D fluid model for B_{max} = 750 G, V_d = 550 V and p = 20 mTorr. Taken from [Costin05].

A major drawback of the model is that it is, in principle, not suitable for low gas pressures, i.e. when the mean free path length of the particles is of the same scale or larger than the dimensions of the space in which they are considered. For typical MD operation, this is always the case. This reasoning is often used to discredit the fluid model, e.g. [Kools04a, Kusumoto04]. However, according to [Costin05] this problem can be overcome because the electrons are magnetised. The result is that the effective distance between two collision events is much smaller than the device dimensions, implying that the fluid model can be used.

A more fundamental shortcoming of the model is that the collision frequencies are based on the Maxwellian EEDF, i.e. they rely on local thermal equilibrium. As mentioned in section 1.3.5.6, this is not the case: the EEDF have a high energy tail. The experimental reports about the existence of two electron groups, cold and hot ones, seems less cumbersome because the two groups of electrons are only observed outside the magnetic trap and there the ionisation is minimal. Because of the assumption of thermal equilibrium, one can conclude that "*strictly saying, the fluid approaches are unapplicable to magnetron plasma*" [Porokhova03].

2.2.5 Hybrid model

Strictly seen, a hybrid model could be a combination of any of two or more of the model types mentioned so far. However, here the term is used specifically to denote the type of model developed by Shidoji et al. [Shidoji99a] and by Kolev and Bogaerts [Kolev04a]. In both cases, the fast electrons, i.e. the electrons that generate ionisation, are treated by the MC technique. The slow electrons and the ions are described using the fluid model. Hence, this technique tries to use the advantage of the fluid model (relatively small computational load) without its questionable method to determine the ionisation generation by using the EEDF. Instead, the ionisation generation is handled using the MC technique, which is a particle approach. Self-consistency is obtained by adding the Poisson equation.

Using the hybrid model, Shidoji et al. were able to simulate the MD and its dependence on external parameters. We mention the influence of the gas pressure and the electrical power [Shidoji00] and of the magnetic field strength [Shidoji03]. Also the influence of balancing the magnetic field [Shidoji01b], of depositing an insulating layer [Shidoji99b] and of bipolar pulsed sputtering [Shidoji04] were investigated.

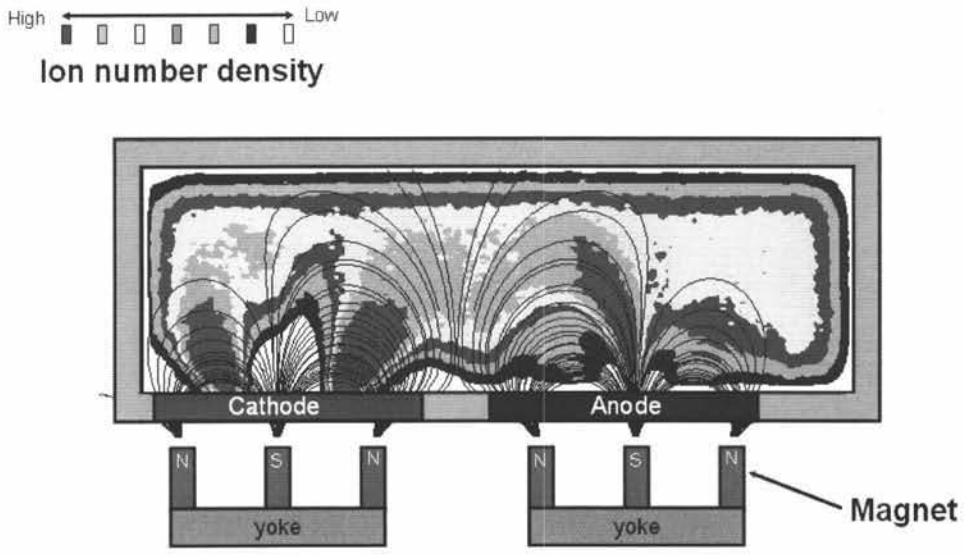

Fig. 2.11 Simulated ion density in the case of bipolar pulsed sputtering: the magnetron on the left acts as cathode, the one on the right as anode. The result is obtained using a hybrid model. Taken from [Shidoji04].

Kolev and Bogaerts report that the application of the hybrid model becomes problematic for strong magnetic fields and/or low gas pressures [Kolev04a]. They point out that in such cases the results appear unrealistic: a large amount of ionisations occurs at rather large distance from the cathode. The reason is that at high magnetic field strengths the electrons cannot diffuse across the magnetic field lines anymore when using the classical theory. Consequently, an electric field is formed between the sheath region and the anode. Because of this electric field, ionisations occur in that region. Also the simulation results reported in [Shidoji03] express this behaviour: the ionisation in the region from 10 to 40 mm above the target is stronger for a magnetic field strength of 360 G than for 180 G but the peak ionisation is lower. This is opposite to the behaviour reported in [Kondo99a]: there the simulated peak ionisation rate increases with increasing magnetic field. The latter result appears more realistic as the magnetic field is applied to the discharge to intensify the MD, not to spread it out.

The problem of the hybrid model to deal with strong magnetic fields is probably due to the fact that it does not account for the anomalous electron transport. Indeed, as mentioned, the slow electron transport is treated using the fluid model. This requires the electron diffusion coefficients for the transport perpendicular to the magnetic field lines. This coefficient is obtained using the classical theory, i.e.

$$D_{\perp} = \frac{D_{B=0}}{1+\frac{\omega^2}{\nu^2}}$$

with $D_{\perp}$ the diffusion coefficient in the direction perpendicular to the magnetic field lines and $D_{B=0}$ the one without magnetic field. However, according to experimental evidence, the diffusion across the magnetic field lines is larger as predicted by $D_{\perp}$ (section 1.3.6.2).

In conclusion, the main advantage of the hybrid model is that it is faster than PIC-MC models (a solution can be obtained in 2-3 days). The pay-off for this advantage is that assumptions need to be made about the slow electron motion in crossed electric and magnetic fields. Because of the latter, this technique seems to fail to describe the anomalous electron transport that occurs for strong magnetic fields and/or low gas pressures. A possibility could be to include this anomalous transport empirically like in Hall thruster modelling (section 1.3.6.2C).

2.2.6 Simplified models

Next to these simulation models, other (simplified) models have been presented for the planar MD. However, most of them are zero-dimensional or one-dimensional, e.g. [Rossnagel87b, Guimarães91, Pekker95, Bradley97, Miura00]. The advantage of these models is that they can be solved practically without computational cost. However, as mentioned before, these models cannot result in quantitative results because the planar MD is essentially two-dimensional.

The only model that, to our knowledge, does not require much computational effort but nevertheless is two-dimensional is the model from Wendt and Lieberman [Wendt88a, Wendt88b, Wendt90]. In this model, the discharge area is split up in arch-shaped areas, the shape of which is determined by the magnetic field lines (Fig. 2.12a). Using this model, Wendt et al. were able to relate the width of the erosion profile to the discharge current, discharge voltage and magnetic field strength through the Larmor radius (Fig. 2.12b). Using the same model, the light emission in a MD could be described [LanGu88].

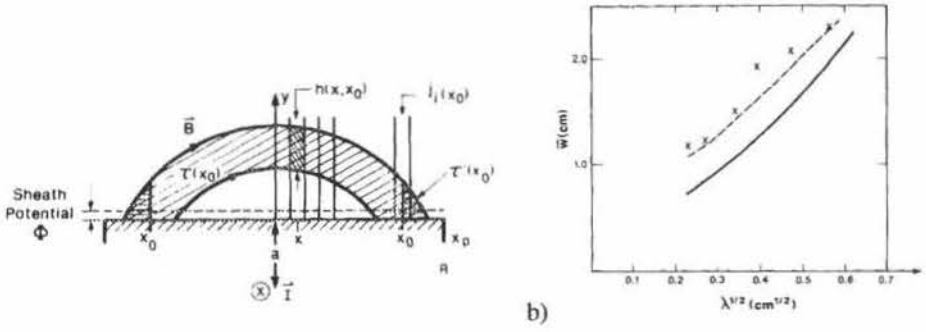

a) b)

Fig. 2.12 *a)* The simplified model developed by Wendt et al. is based on splitting up the discharge area in arch-shaped regions. *b)* Width of the current distribution vs. the square root of the electron Larmor radius. The points are experimental data, the dotted and solid line are obtained using the simplified model assuming a cylindrically symmetric and a rectangular model, respectively. Taken from [Wendt88a].

The arch-model from Wendt et al. is of course a strong approximation of the reality but the above examples highlight an important advantage of such a model: because it does not require much computational effort, it can be used to investigate the dependence of a certain characteristic on parameters like the gas pressure and the magnetic field strength. Unfortunately, this model is not self-consistent.

2.3 Challenges related to MD modelling

However sophisticated a simulation model, there are some limitations to what can be expected from the simulation results. The origin of this might be due to inadequate experimental input data or to the specific geometry or operating conditions of the process. As such, these situations can be called problem cases or, more positive, challenges related to MD modelling. Here, we give a list of the most important ones of these challenges.

2.3.1 SE yield

The SE yield γ gives the amount of SE electrons emitted per incoming ion. As mentioned in section 1.4.4 and as will be shown later (sections II.4.3.3 and II.6.4.3.5), the MD characteristics depend very strongly on the exact value of the SE yield. Unfortunately, these yields are extremely difficult to measure. Consequently, for most materials this yield is not accurately known (section 1.2.2.1).

This is probably the most fundamental factor limiting the output of MD simulations: whatever the model used for the MD simulation, it can only result in accurate results when the SE yield used is accurate. In Shidoji et al. it is mentioned that reducing the SE yield by 50% can decrease the currents with a factor four to five [Shidoji01a]. In [Kondo99a] the increase of the SE yield from 0.12 to 0.15 leads to a substantial increase in the plasma density (from 1.1 to $1.7\times10^{10}/cm^3$, see Fig. 2.5b) and in the discharge current (from 34.9 to 49.5 mA).

Given this situation, the values for the SE yield used in MD varies strongly. Usually, γ is taken independent of the discharge voltage (e.g. in [Nanbu97, Kondo99a]). On the other hand, Shidoji et al. use a SE yield that depends on the discharge voltage, e.g. in [Shidoji01a]. Sometimes, quite unrealistic values for the SE yield are used, e.g. in [Pflug03] where for certain conditions a SE yield of 5 is assumed for a metal surface. Also in [Kusumoto04] γ is used as a tuning parameter: the authors mention that it is set to 0.03 as "*a larger value sometimes leads to the unbounded increase of super particles*", i.e. the simulation does not reach a steady state but the plasma density continues to increase.

The challenge here is to make the MD simulations so reliable that, once the model is calibrated using a material with a relatively well-know SE yield, comparison of the experimental and simulation results can be used to determine the SE yield of the investigated target material.

2.3.2 Recapture

The orbit of a SE emitted from the target follows the magnetic field lines. When the electron does not interact with the discharge gas, this will lead to an electron-target interaction. This event is characterised by the reflection coefficient R, which gives the probability that the electron is reflected. If the electron is not reflected, it is recaptured by the target. This process is discussed extensively in Chapter II.1.

To simulate this effect accurately, the initial electron energy may not be neglected, the orbit calculation should be performed very accurately and the reflection coefficient R needs to be known. The required accuracy has important consequences as it can only be reached by reducing the time step used for retracing the electron orbits, which seriously increases the computational effort. In section II.1.3.1 it is shown that the time step needs to be at least a factor of two smaller then currently encountered in MD simulations. Second, experimental values of R, needed as input for the simulation, are very scarce as discussed in section 1.2.2.3.

This is highly inconvenient because the process of recapture is quite sensitive to this reflection coefficient (section II.1.3.3).

2.3.3 Electron mobility

The problem of the anomalous electron transport was already discussed in section 1.3.6.2. Briefly summarised: the electron transport in the direction perpendicular to the magnetic field lines is larger than expected from classical diffusion theory. The enhanced mobility is probably due to oscillations in the electric field.

This effect has its consequences for MD modelling. Obviously, all methods that rely on the classical theory are affected. This is especially valid for the models that rely on the fluid theory as this requires diffusion coefficients. For the hybrid model, this issue was already discussed (section 2.2.5).

In principle, the PIC-MC method should be able to deal with this problem as it uses no assumptions about the particles. However, a culprit here might be the time scale at which the phenomena occur. A broad range of oscillation frequencies have been observed in plasmas (section 1.3.6.2) but the typical frequency range is of the order of some 100 kHz, corresponding with a period of 10 µsec. Logically, it can be assumed that the discharge only reaches a steady regime after some oscillation periods. This means that the discharge should be followed during a time span of at least 50 µsec. Usually, PIC-MC simulations are not performed that long, implying they will not accurately describe the effect.

A possible way to model the enhanced electron mobility is by adding an extra type of collisions, the so-called Bohm diffusion collisions. This technique will be applied to the MD in section II.5.4.1 and II.6.2 for cylindrical and planar magnetrons, respectively. The contribution of Bohm diffusion can be tuned until the simulations correspond with the experimental measurements.

2.3.4 Modelling "industrially relevant" magnetron discharges

Of course, the magnetron discharges used for industrial sputter deposition are not fundamentally different from the ones used in laboratories. Nevertheless, there are some aspects that make them extremely challenging to simulate. Although including these in MD models is not a fundamental problem, it will make the simulations much more computing intensive. Given that the computational load is already high (order of several days for both the PIC-MC and hybrid model), it is clear that an industrially relevant "virtual sputter magnetron" is not for the immediate future, even taking into account Moore's law which states that the computation power doubles, on average, every 18 months [Ross03]. Some examples are given.

2.3.4.1 Geometry

Although it is not a fundamental limit, the geometry of the MD considered can make certain models useless. In the glass coating industry, magnetrons with cathodes up to 4 metres long are used. For such dimensions, the PIC-MC technique becomes useless because of the unrealistically high computational effort. Hence, less computational intensive methods are needed. An example is the simulation of the effect of the turnaround region on the uniformity. For this type of simulations the MC method is currently used (section 2.2.2). Although these have the disadvantage that the influence of the anode cannot be modelled self-consistently, they are preferred as the computational load of the PIC-MC is forbiddingly high.

2.3.4.2 (High power) pulsed sputtering

For industrial applications, pulsed sputtering is frequently used. The typical frequency range is in the order of 10 to 100 kHz. To simulate such processes, the MD needs to be followed for several periods, i.e. several times 100 to 10 µs. For the moment, this cannot be achieved by PIC-MC modelling. A good candidate for this type of problems is the hybrid model [Shidoji04].

Currently, high power pulsed sputtering is gaining interest because of its potential to deposit coatings with unique properties. In such discharges extremely high electrical powers are applied in short intervals. Because of the high plasma density, typical approximations made in MD modelling are not valid anymore. First, the magnetic field strength in the magnetic trap region changes because of the large Hall currents induced during the high power on-pulse [Bohlmark04]. In all simulation models known to us this influence is not accounted for. Second, because of the high ionisation degree in these high power discharges, it will not be possible anymore to neglect the interactions between charged particles (Coulomb collisions). Again, in all simulation models for the planar MD know to us, this type of interactions is neglected. Only in [Kudrna02] where a cylindrical MD is simulated using a PIC-MC model it is mentioned that the model takes into account electron-electron interactions, albeit in a simplified way. Third, the gas density reduction or gas rarefaction: in section 1.4.3.4A is discussed how the sputtered particles can heat the discharge gas, which leads to a gas density reduction. For standard operating conditions, this effect can be neglected. However, in high power pulsed sputtering this will not be the case. This effect is usually not accounted for in the MD models. To our knowledge, only the PIC-MC model developed by Kolev and Bogaerts is able to deal with this effect [Kolev04b].

2.3.4.3 Accuracy

The specifications for sputtered coatings can be very though. A typical example is the required coating uniformity. Even for large area coating of glass (with cathode lengths of almost 4 metres) the required uniformity is usually better than +/-2 %. It is not evident for a numerical technique to reach this level of accuracy. The only way to reach it when the technique is based on a MC technique is by following a sufficiently large amount of particles, i.e. the accuracy comes at the cost of computational load.

Apart from this, several other effects influence the accuracy at this scale. Some examples are the gas heating due to sputtered particles and the resulting gas density reduction, a non-uniform gas inlet, the influence of the erosion groove formation on the process, redeposition on the target, heating of the target, the influence of the sputtered particles,... Again, all of these examples form no fundamental problem, but they might seriously increase the computational effort.

Basically, the mentioned effects are all examples of "extended self-consistency". Usually, in MD modelling the term self-consistency is used with respect to the electric field. However, because of the on-going sputtering and deposition during the process, the environment of the MD changes. For a very accurate MD simulation, also these changes have to be taken self-consistently into account.

2.4 Conclusion: simplified model for the magnetron discharge

The main aim of the presented work is a fundamental understanding of the d.c. planar MD, which should be shown by the ability to simulate the MD behaviour. Hence, the question arises which of the presented methods for MD simulation is suited best for this purpose.

The discussed MD models range from very basic to extremely detailed. An important criterion to distinguish the models is self-consistency. Although non self-consistent models can be extremely valuable to assess certain aspects of the MD, they are by definition not suited to elucidate the whole process. Unfortunately, the overview of the methods showed that the self-consistent ones showed quite some shortcomings.

Moreover, none of the models has been tested to check whether they can reproduce the MD behaviour over the very wide range of electrical powers, gas pressures and magnetic field strengths encountered in magnetron discharges. A factor that plays definitely a role here is the required computational load. Such testing seems nevertheless absolutely necessary to be sure that the "right physics" is in the model.

This extensive testing can only be performed within a reasonable time when a simplified model is used. Another advantage is that a simplified model can be very instructive: *"Very often a simplified model throws more light on the real workings of nature than any number of ab initio calculations of individual situations, which, even where correct, often contain so much detail as to conceal rather than reveal reality. It can be a disadvantage rather than an advantage to be able to compute or measure too accurately, since often what one measures or computes is irrelevant in terms of mechanism. After all, the perfect computation simply reproduces Nature, it does not explain her."* [Anderson78].

In conclusion, given the limited computational effort and the potential "to explain", it was opted to develop a simplified model for the planar magnetron discharge. As mentioned before, developing a simplified model inevitably leads to discussion because of the reduced accuracy and because of the existence of personal simplified models (see Introduction).

PART II

1 RECAPTURE OF SECONDARY ELECTRONS

1.1 Introduction

In a magnetron discharge (MD) secondary electrons (SE) are emitted from the target, predominantly due to ion impact (section I.1.2.2.1). Once emitted, the collisionless SE movement is determined by the Lorentz equation. The result is a gyrating movement of the SE around the magnetic field lines, leading to arch-shaped orbits , see e.g. [Thornton78a, Thornton78b, Sheridan90a, Ido93a]. Fig. 1.1a shows a sketch of the orbits in the xz-plane indicating the typical SE movement under the assumption of $E_{init} = 0$ eV, with E_{init} the initial energy of the SE. In this case all z-values reached by the electron when passing through its orbit are greater than or equal to z_0, the initial z-value, i.e. the electrons do not interact with the target. This is due to the reflection of the SE just above the target because of the combined influence of the electrostatic sheath and the mirroring due to the magnetic field [Lieberman94]. If we choose E_{init} to be non-zero, the position and shape of the orbits are not significantly changed, suggesting that E_{init} is of small importance. However, in contrast to a zero E_{init}, the SE can now reach z-values which are smaller than z_0, i.e. the SE will interact with the target. This does not always happen when the electron returns to the vicinity of the target because a SE can, like in the case $E_{init} = 0$ eV, be reflected just above the target surface (Fig. 1.1b). The electron-target interaction, which leads to reflection or recapture of the electron, is characterised by the electron reflection coefficient R (section I.1.2.2.3).

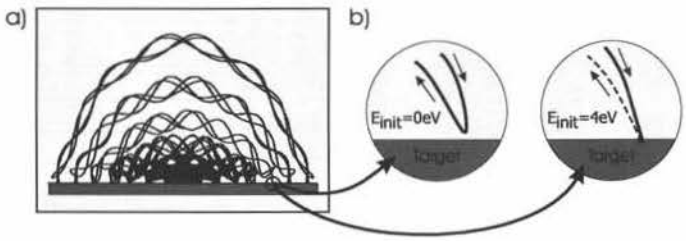

Fig. 1.1. *a*) Sketch of SE orbits showing clearly the arch-shaped orbits. *b*) Detail of the electron-target interaction: for E_{init} equal to 0 eV the electron is always reflected, for a non-zero initial energy electron-target interaction is possible and can lead to the recapture of the electron.

Van der Straaten et al. [VanderStraaten98a,b] implemented the possibility for a SE to be recaptured by the target in a one-dimensional PIC-MC model for a cylindrical post magnetron. Although according to this simulation the *"net secondary emission rate"* (secondary emission rate minus recapture rate) decreases by a factor four when the pressure drops from 10 to 1 mTorr, they concluded that for an electron reflection probability in the range of 0.5-0.9 *"the steady state to which the simulation evolved was found to be largely insensitive to the particular value [of the reflection coefficient] used"*.

For introducing the effect of electron recapture they refer back to [Thornton78a]. However, their conclusion is not in agreement with Thornton who, based on an expression for the discharge voltage (eq. (1.20) in section I.1.3.2), concluded that the discharge voltage has twice the value it would have if no recapture existed. Thus, in this case there is a very strong influence of recapture on the discharge. Thornton considered a cylindrical post magnetron with a typical magnetic field strength of 0.02 T and took a probability of 50% for a SE to be recaptured. Thornton based his suggestion for a 50% SE recapture probability on separate work done by Redhead and Jepson. Redhead [Redhead58] differentiated between the intrinsic

SE yield γ and the effective SE yield γ_{eff} as seen by the discharge and deduced the relationship:

$$\gamma_{eff} = \gamma\left[1 - e^{-\frac{s}{\lambda}}\right] \tag{1.1}$$

with s the average distance travelled by the electron before it is recaptured by the target and λ the mean free path of the electron. Redhead deduced this relation for an inverted-magnetron gauge, Jepsen [Jepsen61] deduced a similar relationship for a cylindrical magnetron. To quantify the process of recapture we introduce the *E*ffective *G*as *I*nteraction *P*robability (EGIP). This EGIP, which is represented by f, is defined as the probability that an emitted SE effectively interacts with the discharge gas and is not recaptured. Hence, the EGIP f is given by the factor between brackets in eq. (1.1), i.e.:

$$f = 1 - e^{-\frac{s}{\lambda}} \tag{1.2}$$

The influence of recapture of SE has been mentioned in discussions of the planar magnetron. An example is the mentioning by Rossnagel and Kaufman [Rossnagel86] that "*due to recapture of some fraction of the secondary electrons at the cathode surface (...), the secondary electron coefficient will effectively be lowered*". In [Lieberman94] the model of Thornton for determining the discharge voltage, including the assumption that half of the SE is recaptured, is applied to planar magnetrons. In [Debal98] it is mentioned that when the electrons are emitted where the magnetic field is maximum "*they immediately fall back onto the cathode*". In [Li95] a Monte Carlo technique is used to determine the ionisation in a magnetron-like model. It is reported that with increasing magnetic field (up to 0.15 T) the ionisation increases, but due to electron loss via *cathode absorption* it decreases when the magnetic field is further increased. In [Kubart04] it is concluded, based on MC simulation of the erosion profile, that the shape of the erosion profile is practically the same, whether recapture is accounted for or not. In [Kolev05] the influence of electron recapture on the MD is investigated using a PIC-MC model.

In this chapter, an analytical method for calculating the EGIP is developed. Furthermore, the model is verified by comparing its results with those from a Monte Carlo (MC) method for determining the EGIP. The analytical method is then applied to investigate the influence on the EGIP of different parameters, such as the initial energy E_{init} of the SE, the reflection coefficient R, the gas pressure, the electric field E and the magnetic field B.

1.2 Model

This part describes both the Monte Carlo (MC) and analytical model to calculate the EGIP f. First, four aspects common to both models are treated: the magnetron model (section 1.2.1), the initial starting conditions of the SE (section 1.2.2), solving of the Lorentz equation (section 0) and the electron interactions (section 1.2.4). Then, the MC model (section 1.2.5) and the analytical model (section 1.2.6) are discussed. Finally, the calculation of the average EGIP $\langle f \rangle$ is introduced (section 1.2.7).

1.2.1 Magnetron model

A sketch of the two-dimensional model used for the magnetron set-up is given in Fig. 1.2. The model represents the MD in the straight section of a rectangular planar magnetron. If we assume that the straight sections (y-direction) are sufficiently long, a two-dimensional model suffices for the cross section AB shown in Fig. 1.2a. Moreover, we

assume that the straight sections each have their own magnet array consisting of two magnets with opposite magnetisations and that the arrays are separated far enough from each other so that the magnetic field created by the array of side BC is not felt by the discharge of side AC. This implies we can limit ourselves to cross section AC. Since we only want to study the SE, the magnetron model shown in Fig. 1.2b is sufficient. The magnet system, which is balanced, is defined by the spacing d between the magnets, the side length s of the magnets and the magnet strength B_r. These parameters together with z_0, the height of the target surface (which is assumed flat) above the magnets, determine the strength and structure of the magnetic field in the discharge region. Given the symmetry of the model, it will be sufficient to limit ourselves to the positive side of the x-axis. The thickness d_E of the cathode sheath and the discharge voltage V_d are input parameters. These values of V_d and d_E, together with the assumption that the electric field varies linearly in the cathode sheath, defines the potential $V(z)$ as:

$$V(z)=\begin{cases}\dfrac{V_d}{d_E^2}\left[z-\left(z_0+d_E\right)\right]^2 & z_0+d_E\geq z\geq z_0\\ 0 & z>z_0+d_E\end{cases} \qquad (1.3)$$

The magnetic field B is calculated by introducing magnetic charges which allows analytical calculation on condition that the magnets are rectangular bars, the magnetisation is homogeneous and the magnetisation directions are parallel. This is discussed in detail in the Appendix.

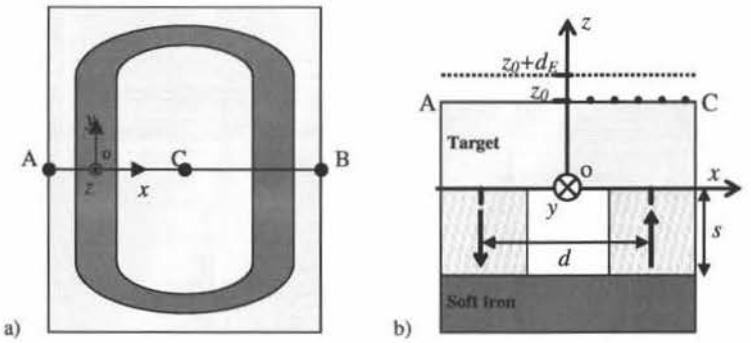

Fig. 1.2. *a)* Top view sketch of a rectangular magnetron system. The dark shaded area represents the most intense plasma region, i.e. the region that corresponds with the race-track area. The mid-plane of the magnetron, on which the model shown in Fig. 1.2b is based, is also shown. (*b*) Two-dimensional model for describing the SE behaviour: the magnets (strength B_r) of the array are placed on a soft iron plate and have a square cross section with side length s in the xz-plane and are infinitely long in the y-direction. The distance between the centres of the magnets is d. The plane of the target surface is given by z_0 which, in reality, is determined by the thickness of the target and the backing plate. The dots show examples for starting positions of secondary electrons. The dotted line at $z = z_0+d_E$ represents the end of the cathode sheath.

1.2.2 Initial starting conditions of the SE

The initial energy of the SE is typically in the range 2-6 eV [Chapman80, Baragiola94, Nishimura96, Shon02] and the angular distribution of the emitted electrons follows a three-dimensional (3D) cosine-law [Reimer85] (see also section I.1.2.2.1). This cosine-law can be approximated by taking for each x-position $2n+1$ different initial velocity vectors $\vec{v}_{init}$ in the xz-plane, each forming an angle θ_i with the z-axis (Fig. 1.3). The θ_i are given by $\theta_i = i\pi/2(n+1)$ ($i = -n,-n+1,...,n-1,n$). This two-dimensional approximation of the cosine-law is

sufficient to describe and compare both the analytical and Monte Carlo model. However, more accurate results are obtained when a 3D approximation is used (section 1.3.2). This is possible because the electron orbits are calculated in 3D. The 3D approximation is constructed by considering for each angle θ_i, except for $\theta_i = 0$, m angles $\varphi_j = j\pi/m$ ($j = 0,1,\ldots,m$-1) with φ the angle with the x-axis of the projection of $\bar{v}_{init}$ in the xy-plane (Fig. 1.3). This way $2mn$+1 initial velocity vectors are taken into account. The velocity vectors each have a weight factor $\cos(\theta_i)$ independent of φ.

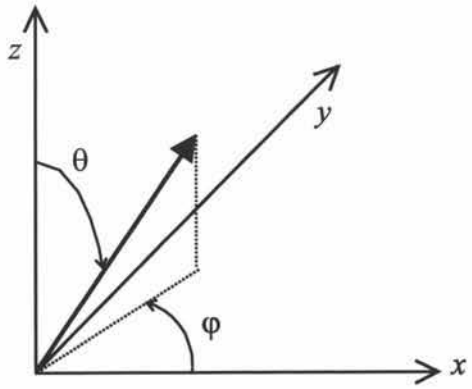

Fig. 1.3. Sketch showing how the angles θ and φ are defined in the *xyz*-coordinate system.

1.2.3 Solving the Lorentz equation

To solve the Lorentz equation (eq. (1.1) in section I.1.1) we apply the fourth order Runge-Kutta method. One can solve the Lorentz equation with a fixed or a variable time step Δt. The first one is the most simple. The time step can be determined from the Larmor frequency ω. The definition of ω was already given in section I.1.3.6.2 (eq. (1.49)) and is repeated here:

$$\omega = \frac{eB}{m} \tag{1.4}$$

Such a requirement is necessary: if Δt is chosen too large with respect to ω, the gyrating of the electron is not resolved completely. In general, this requirement is sufficient to determine the electron orbits. However, as we will show (section 1.3.1) the calculation of the EGIP requires a very high accuracy, which implies small time steps. Fortunately, these stringent requirements can be limited to certain areas. This means that using variable time steps is recommended to keep the computational load reasonable. To determine the variable time step three criteria are used.

First, as in the case of a fixed Δt, the time step Δt is required to be smaller than a fraction β_1 of the inverse of the Larmor frequency ω:

$$\Delta t < \frac{2\pi\beta_1}{\omega} \tag{1.5}$$

Second, a too large time step leads to an artificial decrease of the electron energy (section 1.3.1). Hence, the second criterion for determining Δt is that the energy loss E_{loss} per

time step should be smaller than a given maximum energy loss $E_{loss,max}$, which is chosen as fraction β_2 of the initial energy E_{init}.

For the third criterion, the spatial accuracy needed for calculating the recapture probabilities is considered. As already mentioned, when the initial energy of the SE is set to zero, the SE is always reflected above the target surface. The critical distance d_{crit} for calculating the recapture probabilities is the extra distance along the z-axis the SE can go lower because of E_{init}. Hence, d_{crit} is defined as:

$$E_{init} = d_{crit}\left|eE(z_0)\right| \tag{1.6}$$

with $E(z_0)$ the electrical field at the target surface and e the electron charge. Note that it is assumed that $E(z_0)$ is constant over d_{crit}. Given the definition of the electric field $E(z)$:

$$E(z) = -\left.\frac{dV}{dz}\right|_{z=z_0} \tag{1.7}$$

and eq. (1.3), it follows that $E(z_0)$ is given by:

$$E(z_0) = -2\frac{V_d}{d_E} \tag{1.8}$$

Hence, the distance d_{crit} is determined by:

$$d_{crit} = \frac{E_{init}}{2eV_d} d_E \tag{1.9}$$

To estimate the order of magnitude of d_{crit} we set $E_{init} = 4$ eV, $V_d = 300$ V and $d_E = 1.0$ mm. Eq. (1.8) gives $|E(z_0)| = 600$ V/mm, which results in $d_{crit} = 6.67$ µm. Given the small value of d_{crit}, the earlier assumption that $E(z)$ remains constant over that distance is justified.

To calculate the EGIP accurately, the distances Δs travelled per time step Δt in the vicinity of the target surface should be smaller than d_{crit}. Good accuracy is obtained for the requirement $\Delta s < 0.1 d_{crit}$. However, for practical reasons (computing time) it is highly favourable to restrict this requirement to a limited region above the target. The simulations show that in the region (relatively) far away from the target, the requirement for Δs does not have to be so stringent. Hence, we introduce the parameter β_3 (>1) which allows to specify the requirement $\Delta s < \beta_3 d_{crit}$. To prevent that this requirement interferes with the earlier one ($\Delta s < 0.1 d_{crit}$), it cannot be used in the region within $\beta_3 d_{crit}$ above the target surface. For safety it is only applied in the region $2\beta_3 d_{crit}$ above the target. It is obvious that a transition region is needed between the region with requirement $\Delta s < 0.1 d_{crit}$ and the region with requirement $\Delta s < \beta_3 d_{crit}$. Hence, we specify, according to the z-coordinate z_e of the SE position, the following upper limits for Δs :

$$\Delta s < \begin{cases} 0.1 d_{crit} & z_e < z_0 + 2d_{crit} \\ 0.1\beta_3 d_{crit} & z_0 + 2d_{crit} \le z_e < z_0 + 2\beta_3 d_{crit} \\ \beta_3 d_{crit} & z_0 + 2\beta_3 d_{crit} \le z_e \end{cases} \tag{1.10}$$

with z_0 the position of the target surface (Fig. 1.2).

In conclusion, to calculate the SE orbits accurately, three parameters (β_1, β_2 and β_3) are introduced that specify the upper limits of the step size when solving the Lorentz equation. Especially the third parameter is important as it guarantees that the accuracy is sufficient to retrieve recapture. The appropriate choice of the parameters β_1, β_2 and β_3 allows accurate calculation of the EGIP while keeping the required computing time reasonable (section 1.3.1).

1.2.4 Electron interactions

As already mentioned in the introduction, an emitted SE will interact either with the discharge gas or with the target. The latter process is characterised by the electron reflection coefficient R. This coefficient depends on the target material, the crystal orientation of the material and on the energy of the incoming electron, as discussed in section I.1.2.2.3.

The electron-gas interaction is characterised by the cross sections for the electron-argon interactions. The interactions taken into account are ionisations, excitations and elastic collisions, using the cross sections from [Bretagne86a] (Fig. 1.4 in section I.1.2.1.1). To calculate mean free path lengths $\lambda(E)$, which are needed for the analytical model, we apply the equation:

$$\lambda(E) = \frac{kT}{p\sigma(E)} \tag{1.11}$$

with k the Boltzmann constant, T the gas temperature (assumed to be 300 K), p the gas pressure and $\sigma(E)$ the sum of the appropriate cross sections.

1.2.5 MC model

In the MC method the trajectory of a SE, characterised by its starting position x and the angle θ of its velocity vector with the z-axis, is retraced using the method described above (section 1.2.2). Per time step Δt, it is first checked whether an electron-gas interaction occurs or not. Therefore, the cross section $\sigma(E)$ is calculated and a random number RN_1 is generated. An electron-gas interaction occurs when (section 2.5):

$$RN_1 \leq p_{coll} \tag{1.12}$$

with p_{coll} given by eq. (2.52). If this condition is fulfilled, it is determined by a second random number RN_2 if the collision is elastic or inelastic. If an inelastic interaction occurs the simulation is stopped because the electron cannot be recaptured anymore as the energy loss prevents the electron from returning to the target. If an elastic collision occurs, a third (RN_3) and fourth (RN_4) random number are generated to calculate the axial (χ) and azimuthal (ψ) scattering angles, which determine the new orientation of the electron velocity vector. This procedure is explained more elaborately in section 2.5, here it is only mentioned that for ψ a random distribution is implemented (eq. (2.56)) whereas for χ four different models have been implemented: forward scattering ($\chi = 0$), Okhrimovskyy-scattering (χ according to eq. (2.57)), Surendra-scattering (χ according to eq. (2.58)) and isotropic scattering (χ according to eq. (2.59)). The influence of the choice of χ-model on the results is treated in section 1.3.1. The small energy loss due the elastic collisions is neglected (see also section I.1.2.1.1A). After the calculation of the new velocity vector the retracing of the electron orbit is continued.

It is also checked per Δt if $z_e < z_0$ because this indicates an electron-target interaction. If this condition is fulfilled, a random number RN_5 is generated. The electron is reflected

when $RN_5<R$. The reflections are assumed to be elastic specular reflections because the probability of an inelastic reflection is very low for small energies of the impinging electron (section I.1.2.2.3). This is here the case as the maximum energy of the impinging electron is E_{init} (2-8 eV). If the electron is not reflected but recaptured, the electron trajectory is stopped.

This procedure for determining whether a SE is recaptured or interacts with the discharge gas is repeated N_e times for the same starting conditions x and θ and the number of gas interactions N_{gas} is recorded. As N_e is the number of emitted SE and N_{gas} the number of times the emitted SE interact with the discharge gas, the effective gas interaction probability $f(x, \theta)$ is then given by:

$$f(x,\theta)=\frac{N_{gas}}{N_e} \tag{1.13}$$

From the different θ-values the average $f(x)$ can be calculated using the equation:

$$f(x)=\frac{\sum_i f(x,\theta_i)\cos\theta_i}{\sum_i \cos\theta_i} \tag{1.14}$$

1.2.6 Analytical model

The basis of the analytical method is eq. (1.2). As mentioned in the introduction, the effective gas interaction probability or EGIP is referred to by f. The distance s depends on the start-position x of the SE but also on the orientation of its initial velocity vector. Assuming a 2D cosine-distribution for the velocity vectors, the EGIP becomes dependent on the spatial coordinate x and the angle θ:

$$f(x,\theta)=1-e^{-\frac{s(x,\theta)}{\lambda}} \tag{1.15}$$

The mean free path length λ is calculated using eq. (1.11). A difficulty is to choose which cross sections should be used. It is clear that the ionisation and excitation cross section should be included as recapture becomes impossible after such an interaction. However, although an elastic interaction does not reduce the electron energy relevantly, our simulations show that the recapture probability after such an interaction is low. To keep the analytical model simple, we assume that after an elastic collision the SE cannot be recaptured anymore. Hence, the elastic cross section is included in the total cross section used to calculate λ. This gives rise to a small systematic overestimation of the EGIP-values (see also section 1.3.1).

A simple estimation of the distance s in eq. (1.15) is obtained from the formula:

$$s=\frac{a}{1-R} \tag{1.16}$$

with a the distance travelled by the electron until the first electron-target interaction occurs. This distance a is determined by retracing the collisionless orbit until the first interaction with the target occurs. Although this is a very rough estimation of s, the results are relatively good (section 1.3.1). Nevertheless, an improved method to calculate the EGIP is used: instead of looking at the collisionless SE orbit until the first interaction with the target occurs, the

collisionless SE orbit is followed for several target interactions i. The distance travelled by the SE until interaction i occurs is referred to as s_i.

At the first interaction ($i = 1$), the probability that the electron is reflected is R. After n interactions, the probability that the electron is not recaptured yet is given by R^n. As the transmission probability T is equal to 1-R, the probability p_i that distance s_i occurs is given by:

$$p_i = TR^{i-1} \tag{1.17}$$

The probability $\mathcal{P}_1$ that a SE is recaptured after the first interaction is given by the product of the probability p_1 that distance s_1 occurs, times the probability that the SE did not interact with the discharge gas during s_1. As the latter probability is given by the expression $\exp(-s_1/\lambda)$ the probability $\mathcal{P}_1$ is given by:

$$\mathcal{P}_1 = p_1 e^{-\frac{s_1}{\lambda}} \tag{1.18}$$

Based on this, the total probability $\mathcal{P}_2$ that a SE is recaptured after two interactions with the target, taking into account that it cannot be recaptured anymore if an interaction with the discharge gas occurred, is given by:

$$\mathcal{P}_2 = p_1 e^{-\frac{s_1}{\lambda}} + p_2 e^{-\frac{s_2}{\lambda}} \tag{1.19}$$

Hence, the total probability $\mathcal{P}_i$ that a SE is recaptured after i interactions is given by:

$$\mathcal{P}_i = \sum_{j=1}^{i} p_j e^{-\frac{s_j}{\lambda}} \tag{1.20}$$

Given this equation, it follows that $f(x,\theta)$ is given by:

$$f(x,\theta) = 1 - \lim_{i\to\infty} \mathcal{P}_i \tag{1.21}$$

as for i going to infinity p_i approaches zero. In reality, the calculation of the SE orbits is stopped when p_i drops below 5 %. This leads to the following equation for the EGIP:

$$f(x,\theta) = (1-\mathcal{P}_{i_5})\frac{1}{\sum_{i=1}^{i_5} p_i} \tag{1.22}$$

with index i_5 indicating the interaction for which the condition

$$p_{i_5} < 0.05 < p_{i_5-1} \tag{1.23}$$

holds. The second factor on the right hand side of eq. (1.22) is a correction factor for stopping the calculation before p_i becomes infinitesimal small. However, as the distance needed to reach interaction i_5 can be extremely long for a given set of initial starting conditions, a maximum distance d_{max} during which the SE orbit is followed is introduced. This distance is set to three times the mean free path length of the SE at a pressure of 0.1 Pa. Thus, d_{max} represents the longest collisionless orbit length possible in realistic situations, as these require gas pressures above 0.1 Pa. If, after travelling the distance d_{max}, the electron did not undergo enough interactions to satisfy the condition $p_i < 0.05$, eq. (1.22) for the EGIP is replaced by the equation:

$$f(x,\theta) = (1 - \mathcal{P}_{i_l}) \tag{1.24}$$

with i_l the index of the last interaction of the SE with the target before d_{max} is reached. Once the $f(x,\theta)$-values are obtained, $f(x)$ can be derived from them in the same way as in the MC method (eq. (1.14)).

The extension of the model to the case where also the angles φ are considered (a 3D cosine-distribution) is straightforward: the s- and f-values become dependent on φ, i.e. $f = f(x,\theta,\varphi)$ and $s = s(x,\theta,\varphi)$. Eq. (1.14) to calculate the average f-value at position x needs to be replaced by

$$f(x) = \frac{\sum_{i,j} f(x,\theta_i,\varphi_j) w_{ij}}{\sum_{i,j} w_{ij}} \tag{1.25}$$

with $w_{ij} = \cos(\theta_i)$, the weight factor of $f(x,\theta_i,\varphi_j)$.

1.2.7 The average EGIP <f>

Given the rather irregular dependence of the individual EGIP-values on e.g. the starting position x of the SE (section 1.3.2), it is useful to introduce an average value based on the individual $f(x)$ that is representative for the MD. To calculate this average value <f> we took into account that in the discharge the emission of SE from the target is largely inhomogeneous: as the SE are emitted from the target due to ion bombardment, the incoming ion flux on the target determines the emission profile of the SE. This profile is approximated by a Gaussian distribution $G(x)$ with width σ_G, which means that the average EGIP <f> is given by the expression:

$$< f > = \int_x f(x) G(x) dx \tag{1.26}$$

1.3 Results and discussion

Unless mentioned otherwise, the simulation results presented here are for a magnetron geometry characterised by $B_r = 0.7$ T, $s = 12$ mm, $d = 36$ mm and $z_0 = 15$ mm (Fig. 1.2b). This configuration results in a maximum horizontal magnetic field component B_{max} at the target surface of 600 G. The previous settings are chosen such that the dimensions and magnetic field are typical values as they occur in the Von Ardenne magnetron that is commonly used at the lab (see also section 6.4.1).

The discharge voltage V_d was taken 300 V and the cathode sheath thickness d_E was set to 1 mm. The initial energy E_{init} of the SE is taken 4 eV, the electron reflection coefficient R is set to 0.5 and the gas pressure p is 0.5 Pa. SE are emitted from $x = -14.75$ mm to $x = -0.25$ mm per step of 0.5 mm. The calculation can be limited to one side of the x-axis because the geometry is symmetric (Fig. 1.2b). For the calculation of the average EGIP <f> the width σ_G of the emission profile was set to 4 mm. This choice is based on the simulation results for the FWHM of the erosion profiles (Fig. 6.7b in section 6.3.2.1) and on the relation $\sigma = 0.42$FWHM which is generally valid for Gaussian distributions. The angular distribution of the emitted SE is approximated by taking $n = 3$ and $m = 8$ (see section 1.2.2). These settings together with case II for defining the time step Δt (see further) is in this chapter

referred to as the "standard situation". For the MC method the number of retraced electrons N_e (eq. (1.13)) per x-position is equal to 1000.

1.3.1 Verifying the model

The calculation of the EGIP requires very accurate retracing of the electron orbits, both for the analytical and MC model. The main advantage of the analytical method over the MC method is that it demands much less computing time (roughly a factor 10). Moreover, for different gas pressures the calculation of the collisionless SE orbit, the most computation intensive part of the analytical model, does not need to be repeated. Consequently, all EGIP results shown in this thesis, except for this section, are obtained with the analytical method.

1.3.1.1 Required accuracy for the electron orbits

To check the required time step and to compare the analytical and MC model only SE emitted with an initial velocity vector in the xz-plane are considered ($n = 3$, $m = 1$). This is not a fundamental limitation but reduces the required calculation time significantly.

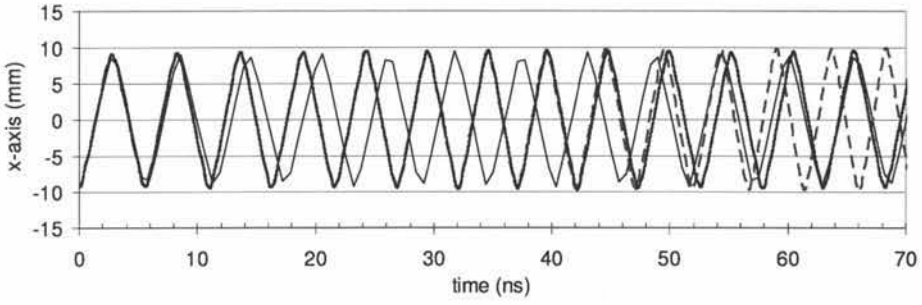

a)

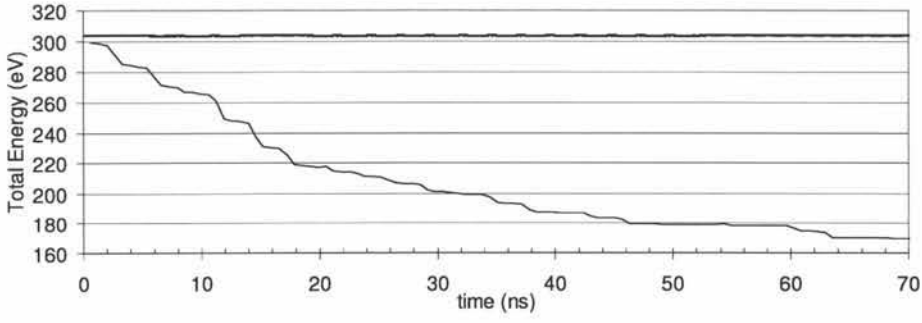

b)

Fig. 1.4. Influence of the time step Δt on the orbit of an electron emitted from the target at $x = -9.25$ with $E_{init} = 4$ eV. The figure shows the x-position (*a*) and the total energy (*b*) as a function of time. The results are obtained with $\beta_1 = 0.1$ (—), 0.01 (— —) and 0.001 (—). The parameters β_2 and β_3 are neutralised so that they have no influence on Δt.

First, the influence of the time step Δt on the orbit of an electron emitted at $x = -9.25$ with $E_{init} = 4$ eV (directed perpendicular to the target) was investigated by varying β_1 (see eq. (1.5)) from 0.1 to 0.001. The parameters β_2 and β_3 were neutralised so that they did not influence the time step. Fig. 1.4a shows the x-position of the electron as a function of time: For $\beta_1 = 0.1$ slight deviations from the *correct* orbit appear already after some nanoseconds. Setting β_1 to 0.01 is accurate up to approximately 40 ns for the orbit shown. A too large time

step also artificially reduces the total energy, the sum of the kinetic energy and potential energy in the cathode sheath, of the electron (Fig. 1.4b).

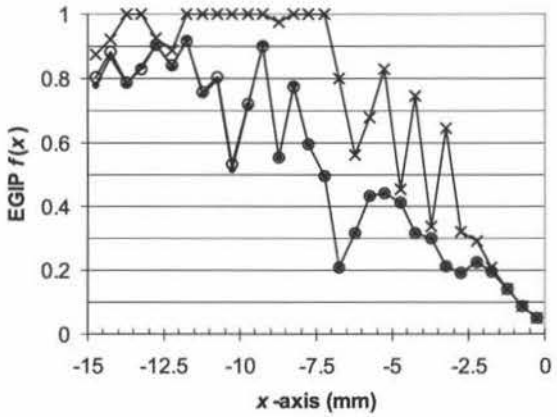

Fig. 1.5. Influence of the time step Δt, defined by β_1, β_2 and β_3, on the calculation of the EGIP: case I defined by $\beta_1 = 0.1$, $\beta_2 = 2\times10^{-6}$ and $\beta_3 = 10000$ (×), case II defined by $\beta_1 = 0.01$, $\beta_2 = 2\times10^{-7}$ and $\beta_3 = 100$ (O) and case III defined by $\beta_1 = 0.001$, $\beta_2 = 2\times10^{-8}$ and $\beta_3 = 20$ (•). It is clear that the settings of case I are not sufficient. Case II and III are practically identical, hence the choice for case II in the standard settings.

Then, the influence of the time step Δt on the EGIP was addressed by varying β_1, β_2 and β_3 when using the analytical method. Three cases are shown in Fig. 1.5: case I ($\beta_1 = 0.1$, $\beta_2 = 2\times10^{-6}$, $\beta_3 = 10000$), case II ($\beta_1 = 0.01$, $\beta_2 = 2\times10^{-7}$, $\beta_3 = 100$) and case III ($\beta_1 = 0.001$, $\beta_2 = 2\times10^{-8}$, $\beta_3 = 20$). In principle, the parameter β_1 alone enables to specify the required time step to obtain a sufficiently accurate electron orbit. However, this way a very small Δt would be required for the whole orbit. Use of the parameters β_1, β_2 and β_3 allows the same precision but with a larger average time step, and thus, less computing time. This is shown in Fig. 1.6 which shows the relative occurrence of the parameters β_1, β_2 and β_3 as limiting requirement for Δt. It can be seen that for large $|x|$, β_1 is dominating. However, for small $|x|$ the β_1-requirement (Δt smaller than 1/100 of the gyration period) is less strict than the β_3-requirement (distance travelled during Δt small compared to d_{crit}). The parameter β_2 is only very rarely the most stringent requirement.

Now, before further considering the accuracy, we look at the physical meaning of the results. Fig. 1.5 shows the EGIP f as a function of the distance x from the centre of the race-track. Towards the edge (large $|x|$), f is almost one. From Fig. 1.1 it follows that a SE emitted close to the edge travels a relatively large distance through the discharge area before it returns towards the target. Consequently, the distance s of eq. (1.15) is rather large, leading to an f-value close to one. Towards the centre of the race-track, this distance s becomes smaller (see again Fig. 1.1), leading to a smaller EGIP. The results of Fig. 1.5 show that in the middle of the race-track the EGIP drops to values below 0.1 for these settings. The fact that for these positions the vast majority of the SE is recaptured indicates the importance of the process.

It is difficult to explain what exactly causes the strong dip around $|x| = 7$ mm. As will be mentioned in the explanation for the results of Fig. 1.9 (see further), the exact EGIP is strongly dependent on the initial starting conditions of the electrons. In Fig. 1.9, the orientation of the initial velocity vector of the electron varies with respect to orientation of the magnetic field vector. For the results of Fig. 1.5, the orientation of the initial velocity vectors

is fixed but the orientation of the magnetic field vector changes with x-position. It is expected that the dip around $|x| = 7$ mm is due to the specific relative orientation of the magnetic field vector and the initial velocity vectors of the electron.

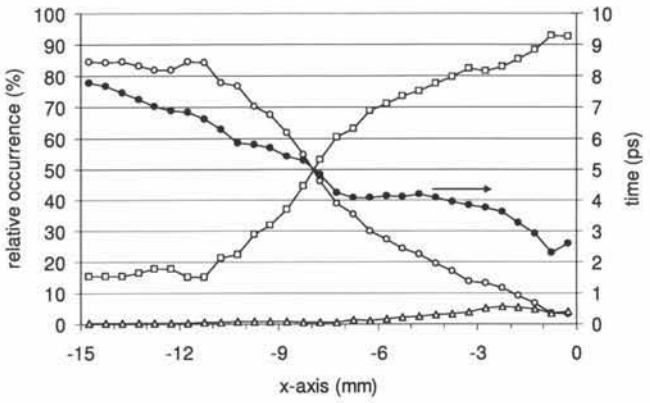

Fig. 1.6. The relative occurrence of β_1 (O), β_2 (△) and β_3 (□) as the limiting requirement for Δt for different electron starting positions along the x-axis. Also the average time step (•, right hand scale) is plotted. The results are obtained with the settings of case II.

From Fig. 1.5 it is clear that the most accurate results (cases II and III) are practically the same whereas the result of the least accurate case (I) is clearly different. Hence, except for the smallest $|x|$ (< 2 mm), the settings of case I are not sufficient to calculate the EGIP. For $7 < |x| < 12$ and for $13 < |x| < 14$ the EGIP becomes unity for case I which means that the effect of recapture is not retrieved at all in that region. The most accurate is case III. However, given the small difference between case II and III, case II is chosen for the standard situation. For case II, the average time step Δt varies from approximately 2.5 ps for the smallest $|x|$ to approximately 8 ps for the largest $|x|$ (Fig. 1.6). The average time step for case I varies from approximately 3 ps for the smallest $|x|$ to 60 ps for the largest $|x|$. These time steps explain why case I results in accurate results for small $|x|$ but not at all for large $|x|$ (Fig. 1.5). The time step of 60 ps is clearly too large, a maximum time steps of about 10 ps seem more appropriate. The typical time steps encountered in self-consistent MD simulations, e.g. 204.9 ps [Kondo99a], 75.9 ps [Nanbu97] and 20 ps [Shidoji01b], are too large for calculating the recapture probabilities accurately. Consequently, adding recapture simulation to these models would increase the computational load substantially.

1.3.1.2 Comparison of the analytical and MC model

The validity of the analytical method was evaluated by comparing its results with the MC method using Surendra-scattering. Fig. 1.7a shows the results for both methods: one can see that the analytical method slightly overestimates $\langle f \rangle$. The reason is the assumption in the analytical model that after an elastic collision no recapture can occur anymore (section 1.2.6). To prove this, a modified MC model was developed. The "modified" MC model includes the assumption of the analytical model, i.e. the impossibility for recapture to occur after an elastic collision. As shown in Fig. 1.7a the results of the modified MC model and the analytical model are practically identical. Hence, it is clear that the overestimation of $\langle f \rangle$ in the analytical model is indeed due to this assumption. The good agreement between the analytical solution $f_a(x)$ and the modified MC solution $f_{mod}(x)$ can also be deduced from Fig. 1.7b which shows the ratio $f_a(x)/f_{mod}(x)$. Also plotted in Fig. 1.7b is the ratio $f_{a,1}(x)/f_{mod}(x)$ with $f_{a,1}(x)$ the solution obtained by taking into account only one electron-target interaction. Considering

several electron-target interactions instead of one brings clearly the results of the analytical model more closely to those of the numerical model.

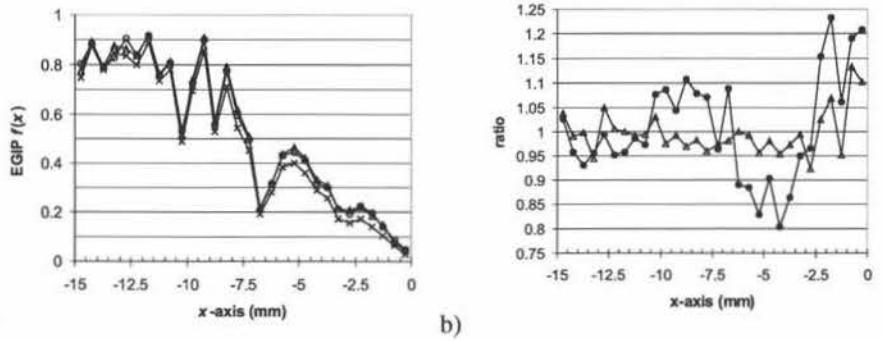

a) b)

Fig. 1.7. *a*) Comparison of the MC (×) and the analytical (O) model for the standard situation. When comparing with the result of the modified MC model (△) the origin of the slight overestimation of the analytical model becomes clear. *b*) Plot of $f_a(x)/f_{mod}(x)$ (△) and of $f_{a,1}(x)/f_{mod}(x)$ (•). The first ratio is clearly closer to unity as the second. Hence, the analytical model is improved by taking into account several electron-target interactions ($f_a(x)$) instead of one ($f_{a,1}(x)$).

1.3.1.3 Influence of the model for the scattering angle

As mentioned in the description of the model (section 1.2.5), the scattering angle χ was calculated using four different models. The results are shown in Fig. 1.8: although the difference between the two extremes (forward and isotropic scattering) is clearly visible, especially in the region $|x|<10$ mm, the difference between the results obtained with Surendra and Okhrimovskyy scattering are minimal. Hence, in this case the choice of the model for χ is not critical.

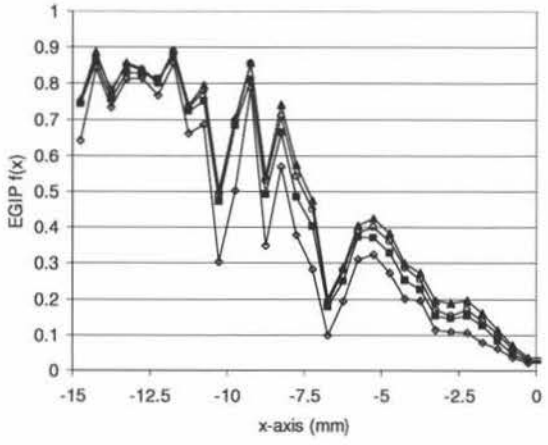

Fig. 1.8. Influence of the χ-model on the EGIP. The different results are obtained assuming forward scattering (◇), Surendra-scattering (O), Okhrimovskyy-scattering (■) and isotropic scattering (▲).

1.3.2 Influence of the initial starting conditions of the electron

The EGIP f(x) of an individual SE is strongly influenced by the emission angle. Therefore, it is necessary to average over several emission angles to obtain a relevant value for f(x). The influence of the initial energy of the SE on the EGIP is less critical and, as could be expected, f(x) decreases with increasing initial energy.

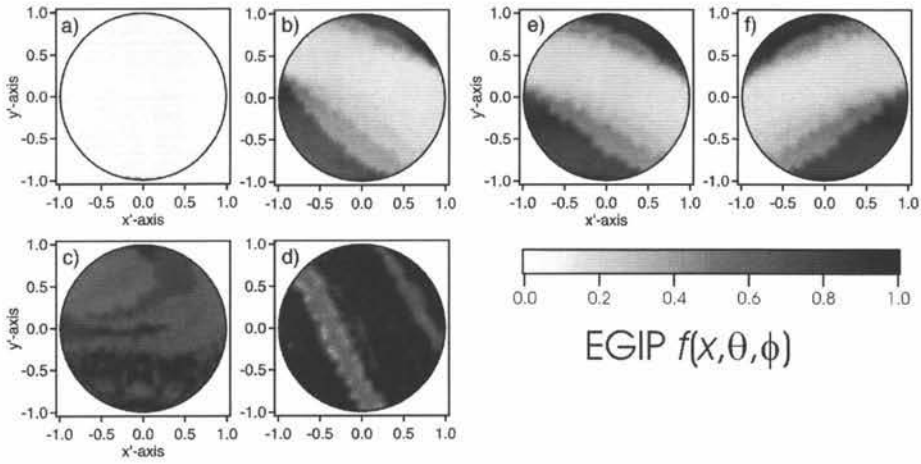

Fig. 1.9. The dependence of EGIP $f(x,\theta,\varphi)$ on θ and φ for $x = -0.25$ (a), $x = -4.25$ (b), $x = -8.25$ (*c*), $x = -12.25$ (*d*), $x = -6.25$ (*e*) and $x = 6.25$ (*f*). The plots illustrate the rather irregular dependence of the EGIP on the orientation of the initial velocity vector. Comparing parts *e* and *f* reveals the symmetry $f(x,\theta,\varphi) = f(-x,\theta,\pi-\varphi)$. Except for $m = 26$ and $n = 12$ the settings of the standard situation are used.

To show the influence of the orientation of the initial velocity vector, the EGIP $f(x,\theta,\varphi)$ is plotted as a function of θ and φ in Fig. 1.9. Each point in the unit circle corresponds to the projection of an initial velocity vector $\overline{v}_{init}$ in the xy-plane. The greyscale of a point is determined by its EGIP $f(x,\theta,\varphi)$. The x'- and y'-axis are defined as $(x-x_{SE})/|\overline{v}_{init}|$ and $(y-y_{SE})/|\overline{v}_{init}|$, respectively, with x_{SE} and y_{SE} the starting position of the SE. Given the 2D model, y_{SE} is always equal to zero. The standard settings are used to obtain the results, except that per x not 49 but 625 SE were retraced ($m = 26$, $n = 12$). Results are given for $x = x_{SE} = -0.25$, -4.25, -8.25 and -12.25 in parts *a* to *d* (Fig. 1.9) to illustrate the rather irregular dependence of the EGIP on θ and φ. Parts *e* and *f* of Fig. 1.9 show the result for $x = -6.25$ and $x = 6.25$. These two plots reveal the symmetry $f(x,\theta,\varphi) = f(-x,\theta,\pi-\varphi)$ which indicates the yz-plane as a symmetry plane for $f(x,\theta,\varphi)$. Hence, it is indeed justified to limit the emission of the SE to one side of the x-axis. Given the dependence of $f(x,\theta,\varphi)$ on the orientation of $\overline{v}_{init}$, it is necessary to average over different θ- and φ-values to obtain the EGIP $f(x)$.

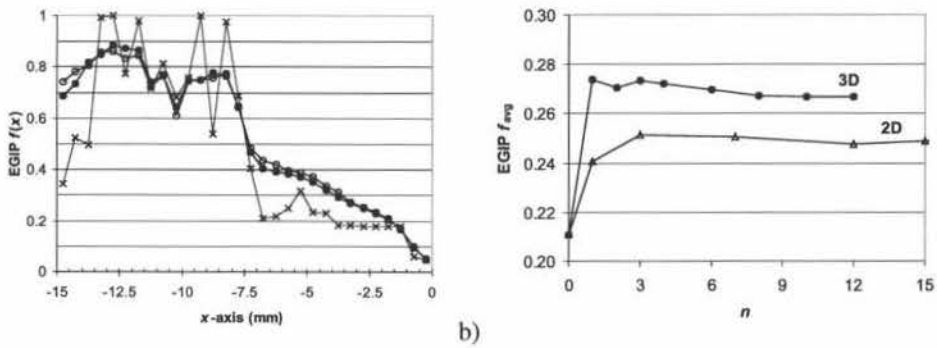

a) b)

Fig. 1.10. *a*) The influence of the amount of starting angles, which is given by $2mn+1$, on the EGIP $f(x)$ for $n = 0$ and $m = 1$ (×), $n = 3$ and $m = 8$ (O) and $n = 12$ and $m = 26$ (•). *b*) The average EGIP $\langle f \rangle$ as a function of n for a 2D ($m = 1$) and 3D ($m = 2(n+1)$) approximation of the cosine distribution. It is clear that a 2D approximation leads to an underestimation of $\langle f \rangle$. Except for the values of m and n, the settings of the standard situation are used for the calculations.

This is illustrated in Fig. 1.10a, which shows $f(x)$ for the case where 1 ($n = 0$, $m = 1$), 49 ($n = 3$ and $m = 8$, the standard situation) and 625 ($n = 12$ and $m = 26$) starting angles are taken into account. The curve obtained with 625 starting angles is smoother for $|x| > 10$ mm, which indicates that for the standard situation the fluctuating behaviour of $f(x)$ in that region is due to the (limited) number of starting angles considered. The influence of the number of starting angles in the 3D approximation is plotted in Fig. 1.10b, which gives $\langle f \rangle$ as a function of n (with $m = 2(n+1)$). Fig. 1.10b also shows $\langle f \rangle$ as a function of n for a two-dimensional (with $m = 1$) and three-dimensional (with $m = 2(n+1)$) approximation of the cosine distribution. The 2D approximation clearly underestimates the values of $\langle f \rangle$. For the standard situation, $n = 3$ and $m = 8$ are chosen as this gives accurate results without a too heavy computational load.

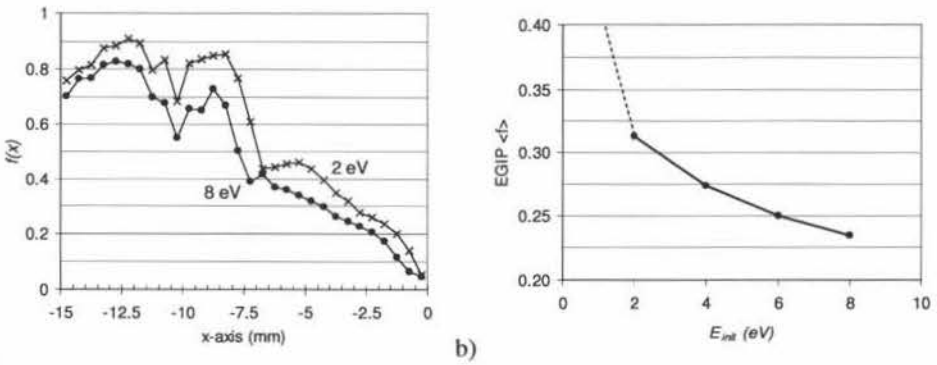

a) b)

Fig. 1.11. *a*) Result for the EGIP $f(x)$ for E_{init} equal to 2 eV and 8 eV. *b*) Dependence of $\langle f \rangle$ on E_{init}. Except for E_{init}, the settings of the standard situation are used for the calculation.

The influence of the initial energy E_{init} on the EGIP is plotted in Fig. 1.11a for 2 and 8 eV. The different curves express roughly the same features and it is clear that the higher E_{init}, the lower the EGIP. In order to present the dependence of the EGIP on E_{init} in a more clear way, the average EGIP $\langle f \rangle$ is calculated and plotted as a function of E_{init} (Fig. 1.11b). This shows the decrease of $\langle f \rangle$ with increasing E_{init}. At low initial energies the EGIP

increases steeply (indicated by the dotted line) because the EGIP has to become one for $E_{init} = 0$ eV.

1.3.3 Influence of the reflection coefficient R

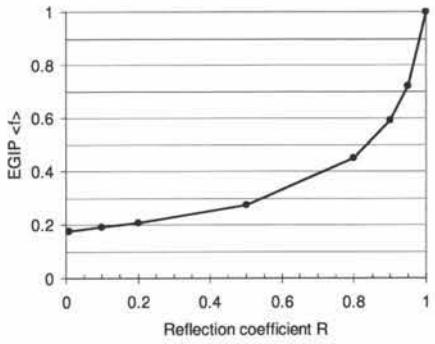

Fig. 1.12. The value <*f*> as a function of *R*. Except for the value of *R* the settings of the standard situation are used.

The influence of the value of *R* on <*f*> was investigated (Fig. 1.12). For *R* below 0.5 there is only a weak dependence of <*f*> on *R*. Hence, in this region the actual value used in the magnetron simulation will only have a limited influence on the simulation results. On the other hand, increasing *R* above 0.5 results in a strong increase of <*f*>. For *R* going to one also <*f*> goes to one because $R = 1$ means that no electrons can be recaptured (total reflection). For *R* going to zero <*f*> does not go to zero because even for $R = 0$ (total recapture) the emitted electrons have to travel a certain distance before they are recaptured and, hence, there remains a certain probability for them to interact with the discharge gas.

1.3.4 Influence of the gas pressure

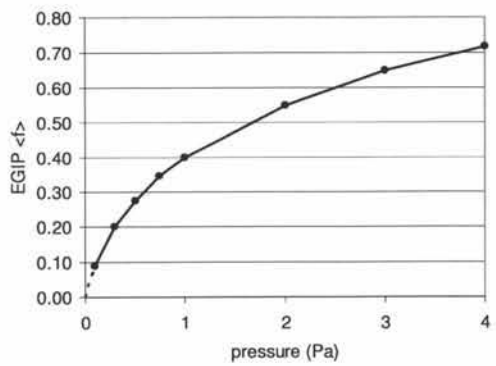

Fig. 1.13. The value <*f*> as a function of the gas pressure. Except for the gas pressure the settings of the standard situation are used.

The influence of the gas pressure *p* on <*f*> was investigated (Fig. 1.13). The figure clearly shows the decrease of <*f*> with decreasing pressure. For high pressures, the dependence tends to weaken. The reason is that at the highest pressures only the SE emitted close to the centre still have a chance to be recaptured. The lowest pressure calculated is

0.1 Pa. The curve can be extended to the point of zero pressure (indicated by the dotted line) where <*f*> is zero by definition. The strong dependence of <*f*> on the pressure is a major reason for the pressure dependence of the discharge (section 4.3.2).

1.3.5 Influence of the magnetic field

The EGIP <f> decreases with increasing magnetic field strength as could be expected. However, the dependence is not monotonous because of the rather complex relation between the magnetic field and the EGIP of the individual SE.

Fig. 1.14a shows <*f*> as a function of the magnetic field strength B_{max} for three different z_0-values: $z_0 = 10$ mm, $z_0 = 15$ mm and $z_0 = 20$ mm. For a given z_0-value the magnetic field strength is changed by varying the magnet strength B_r. The magnetic field is the strongest for the smallest z_0 because then the target surface is the closest to the magnets (Fig. 1.2). One would expect that with increasing magnetic field <*f*> decreases, because the Larmor radius decreases with increasing magnetic field. Hence, the distance travelled by the electrons before they interact with the target should decrease too, which results in a smaller <*f*>. The overall trend in Fig. 1.14a for a fixed z_0 is indeed a decrease in <*f*> with increasing B_{max} but the curve is not monotonous. Moreover, for a given B_{max}, the EGIP <*f*> is influenced by z_0. This indicates that not only the magnetic field strength but also its structure is important. Fig. 1.14b shows a detail of Fig. 1.14a, namely the dependence of <*f*> on B_{max} in the range 450 to 800 G for $z_0 = 15$ mm. In this figure also the EGIP for three different x-values ($|x| = 0.25$, 6.25, 12.25) is plotted. From these curves, it can be deduced that the reasoning that with increasing B_{max} the EGIP should decrease may only be applied to the electrons emitted close to the centre of the race-track ($|x| = 0.25$). For the SE emitted not in the centre of the race-track (e.g. $|x| = 6.25$, $|x| = 12.25$) the magnetic field dependence of their EGIP is much more complicated. It is this complex relationship that causes the non-monotonous behaviour shown in Fig. 1.14a.

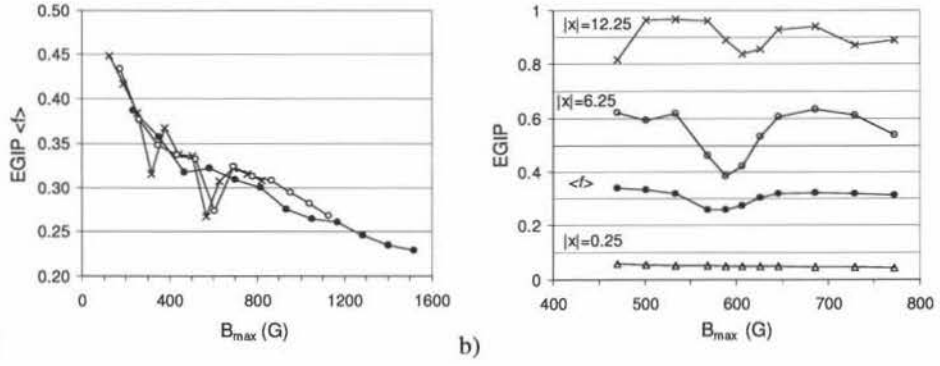

Fig. 1.14. *a*) The dependence of <*f*> on the magnetic field strength B_{max} for different positions z_0 of the target surface: $z_0 = 10$ (•), 15 (O) and 20 mm (×). *b*) The dependence of <*f*>, $f(|x| = 12.25)$, $f(|x| = 6.25)$ and $f(|x| = 0.25)$ on the magnetic field strength in the range $B_{max} = 450$ to 800 G. Except for the magnet strength B_r and the target position z_0, the settings of the standard situation are used.

Note that the influence of the magnetic field on <*f*> does not allow predictions about the dependence of the discharge voltage V_d on the magnetic field. From the combination of the Thornton relation for V_d (eq. (1.20) in section I.1.3.2) and the expression for γ_{eff} (eq. (I.1.21)), it follows that V_d is inversely proportional with the EGIP. As the magnetic field generally lowers the EGIP, one could reason that V_d will increase with increasing magnetic

field. However, this is not true because increasing the magnetic field will also lead to an increase in the multiplication factor m (see section 3.3.3).

1.3.6 Influence of the electric field

In general, the average EGIP <f> expresses a maximum as function of the electric field at constant discharge voltage and <f> increases with increasing discharge voltage at constant electric field. Similar as for the magnetic field dependence, there is an irregular component superposed upon the overall dependence of <f> on the electric field due to the complex dependence of the individual emitted SE on the electric field.

The electric field is determined by the discharge voltage V_d and the cathode sheath thickness d_E. In reality the values of V_d and d_E are interconnected and also depend on the gas pressure p. The values of V_d and d_E also influence the width of the erosion profile, and hence, the width σ_G of the emission profile of the SE. Nevertheless, the values of V_d and d_E are varied here independently of each other at constant σ_G (4 mm) and p (0.5 Pa), as this allows to investigate the direct influence of the electric field on the average EGIP $\langle f \rangle$. This influence is shown in Fig. 1.15a where $\langle f \rangle$ is plotted as a function of $E(z_0)$, the electric field at the target surface, for different discharge voltages V_d. Although the behaviour of the different curves is rather complex, three general trends can be distinguished: (i) $\langle f \rangle$ goes through a maximum as a function of $E(z_0)$, (ii) the value of $E(z_0)$ for which this maximum occurs increases with increasing discharge voltage and (iii) the value of $\langle f \rangle$ increases with increasing discharge voltage.

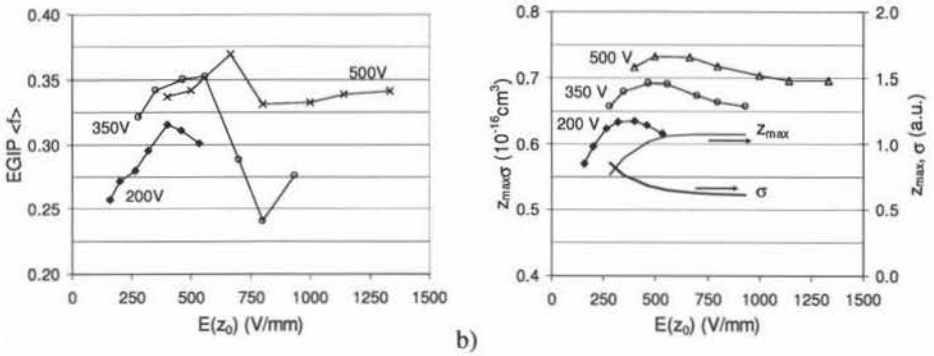

Fig. 1.15. *a*) The value of $\langle f \rangle$ as a function of $E(z_0)$, the electric field at the target surface, for different discharges voltages. The change in electric field for a given discharge voltage V_d was obtained by varying the cathode sheath thickness d_E from 0.75 to 2.5 mm. *b*) The dependence of the product $z_{max}\sigma$ on $E(z_0)$ for different discharge voltages with z_{max} the maximum height of the electrons before interaction with the discharge gas and σ the electron cross section. The same settings as in part *a* of the figure are used. The graph shows also the individual dependence of z_{max} and σ on $E(z_0)$ for V_d = 350 V. Except for the values of V_d and d_E the settings of the standard situation are used.

To understand this behaviour, we focus on the SE emitted close to the centre of the race-track ($|x| = 0.25$) because, as in the case of the magnetic field dependence, they demonstrate the general trend of $\langle f \rangle$. As $f(x)$ is small for these SE, the expression for $f(x)$ (eq. (1.3)) can be approximated:

$$f(x=0.25) = 1 - e^{-\frac{s}{\lambda}} \sim \frac{s}{\lambda} \qquad (1.27)$$

As the gas pressure p is constant, this expression in combination with eq. (1.11) results in:

$$f(x=0.25) \sim s\sigma \tag{1.28}$$

with σ the electron cross section for interaction with the discharge gas. As before, both the inelastic and elastic collisions are included in the electron cross section σ (section 2.3). This total cross section decreases monotonously with increasing energy above 20 eV (Fig. (1.4) in section I.1.2.1.1). The distance s travelled through the discharge by the SE emitted at $x = 0.25$ is proportional with the maximum height z_{max} they can reach above the target as they have a cycloidal motion because of the perpendicular electric and magnetic field [Thornton78a]. Hence, we can rewrite the expression (0.28) for $f(x)$:

$$f(x=0.25) \sim z_{max}\sigma \tag{1.29}$$

Fig. 1.15b shows this product $z_{max}\sigma$ as a function of $E(z_0)$ for different discharge voltages V_d. We see clearly the trends that were also present in the dependence of $<f>$ on $E(z_0)$. The figure shows also the individual dependence of z_{max} and σ on $E(z_0)$ for $V_d = 350$ V. The sharp increase of the EGIP at small $E(z_0)$ is due to the strong rise of z_{max}. For larger $E(z_0)$ the EGIP decreases again because z_{max} saturates while σ is continuously decreasing.

1.4 Conclusions

In this chapter the effective gas interaction probability (EGIP) of the secondary electrons (SE) emitted in a MD is discussed. For calculating this EGIP two different models were developed: a MC model and an analytical model. The latter has the advantage that it requires much less computing time. Both models require the numerical solution of the Lorentz equation. It appeared that for accurate calculation of the EGIP the time steps used to solve this equation need to be of the order of a few picoseconds.

For an individual SE the slightest change in its collisionless orbit can result in a very strong change in its EGIP. Hence, all the parameters influencing the electron orbit also influence the EGIP. These parameters include the initial starting conditions of the electron (position along the target, emission angle and initial energy), the gas pressure, the electric field and the magnetic field. The dependence of the EGIP of an individual electron on these parameters was found to be strong and rather complex.

As the EGIP of the discharge will be determined by the average behaviour of all the emitted SE, an average EGIP for the discharge, $<f>$, is introduced. The average value $<f>$ shows, in contrast with the individual EGIP of a SE, a general trend in the dependence on external parameters. It decreases, as expected, when the initial energy of the SE or the magnetic field strength increases. However, the dependence on the magnetic field strength is not monotonous. For a given discharge voltage, $<f>$ goes through a maximum as a function of the electric field at the target surface.

In general, the values for $<f>$ are rather low. Typical results presented here for a gas pressure of 0.5 Pa are in the range of 0.25 to 0.35. This means that the effective SE yield γ_{eff} as seen by the MD is a factor three to four smaller than the standard SE yield of the target material. Hence, calculation of the EGIP is necessary to accurately model and simulate the MD.

2 IONISATION MODEL

2.1 Introduction

In a magnetron discharge (MD), the sputter gas is ionised by electrons. The description of this ionisation is an important part of the MD simulation, regardless the kind of model used. This importance stems from the fact that the spatial and temporal spread of the ionisation determines to a large degree the MD properties. In general, the ionisation distribution is simulated using a Monte Carlo (MC) technique. This purely numerical technique has many advantages, one of them is that it is straightforward to implement (see section I.2.2.2). Its main disadvantage is the computational load. Because we want to obtain a MD model that allows investigating the influence of external parameters (see Chapters 3, 4 and 6), a method resulting in quick determination of the ionisation distribution is required. A MC approach is not considered an option for such a model. Instead, an *A*nalytical *I*onisation *M*odel (AIM) is developed. The MC technique is nevertheless implemented to verify the results obtained with the AIM.

The AIM allows determination of the ionisation faster than with the MC technique, but this inevitably leads to some restrictions. First, the model is not as exact as a numerical approach because certain approximations are needed. Second, the validity range of the analytical approach is smaller. To obtain the ionisation, it is explicitly assumed that the magnetron is balanced, that the magnetic field is sufficiently strong and that the pressure is low enough. Hence, it can for example not be used to investigate how the ionisation distribution is influenced by the transition from magnetron to diode sputtering.

The electrons in the MD can be divided into two groups: the ones that can cause ionisation, the so-called high energy electrons (HEE) with energy above the threshold energy E_{th}, and the bulk electrons (BE) that cannot, or very unlikely, perform ionisation. In the AIM only the HEE are taken into account. Given the splitting up of the electrons according to their ionisation ability, it appears logical to take E_{ion}, the first ionisation energy of argon (= 15.8 eV), as threshold energy. This choice is usually made. However, this approach can be questioned. Usually, when retracing HEE only the excitation, ionisation and elastic cross sections are taken into account. However, in section I.1.3.5.6 it was mentioned that at low electron energies (below 25 eV) the electron energy distribution function (EEDF) is (strongly) influenced by the Coulomb collisions, which means that at low energies the electrons also lose energy because of interactions with other electrons. This is not surprising as the probability for Coulomb collisions is high at low electron energies, e.g. at 20 eV and 1% ionisation degree the cross section for a collision with a small scattering angle (9 degrees or less) is approximately 5.3×10^{-15}cm^2, which is 80 times larger as the ionisation cross section ($\sigma_{ion} = 6.4\times10^{-17}$cm^2). Hence, at such energies, neglecting Coulomb collisions when retracing the electrons is doubtful. Therefore, the threshold energy E_{th} in this work is set equal to the effective ionisation energy W (=30 eV) and only the electrons with energy above this threshold are considered as HEE.

The energy used to define the HEE is not the kinetic energy of the electrons but their total energy. This total energy is the sum of the kinetic energy and the potential energy of the electron. At an arbitrary height z in the plasma, this potential energy is equal to $|eV(z)|$ with $V(z)$ the potential distribution in the plasma. In reality, this potential energy is only of importance in the cathode sheath. A concept that will be used frequently in the explanation of the model is the "lifetime in the discharge" of the HEE. This lifetime indicates the period between becoming a HEE due to acceleration into the discharge and stopping being a HEE

when its energy drops below the threshold energy E_{th} due to a collision. Hence, it denotes the period over which the potential energy drops from its maximum value to the threshold value.

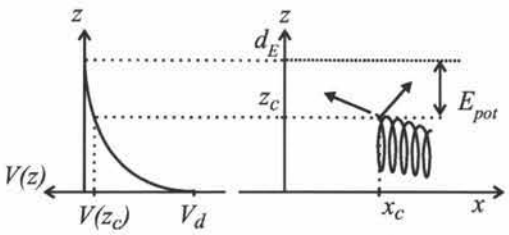

Fig. 2.1. The generation of an ion-electron pair at position (x_C, z_C) in the cathode sheath by an HEE is referred to as sheath ionisation (SI). The resulting ejected electron has a potential energy $|eV(z_C)|$. If this energy is larger than E_{th}, the ejected electron becomes a HEE^{SI}, "HEE due to SI".

The HEE in the MD originate from the target where they are released as secondary electrons (SE) or from the generation of an electron-ion pair in the cathode sheath. The HEE originating from the first process are referred to as "HEE due to the target", indicated with HEE^{ta}. The latter process is referred to as *S*heath *I*onisation (SI). This SI can produce a HEE if the ionisation occurs at a height z_C for which $|eV(z_C)|>E_{th}$ is valid (Fig. 2.1). The HEE due to this process are referred to as "HEE due to SI", indicated with HEE^{SI}. When SI happens, the original HEE^{ta} contributes an extra energy to the discharge equal to $|eV(z_C)|$. Generally, the emission of SE from the target is considered as the main source of HEE. However, in a typical MD, the magnetic field is strong enough such that also the HEE^{SI} need to be accounted for.

For a sufficiently strong magnetic field, the HEE move in arch-shaped orbits because of their gyrating around the magnetic field lines, see e.g. [Thornton78b, Sheridan90a, Ido93a]. Hence, the discharge can be considered as built up by arch-shaped regions [Wendt88a, Wendt88b]. This splitting up of the discharge area is one of the basic ideas on which the AIM is based.

This chapter discusses the determination of the ionisation distribution of the HEE based on such arch-shaped regions. First, the concepts of thin and thick sheath and of an individual sheath are introduced (section 2.2). The explanation of the AIM is divided in the explanation of the thin sheath ionisation model and the thick sheath ionisation model. The thin sheath *I*onisation *M*odel (thin sheath IM) concerns the situation where a thin sheath can be assumed for all SE (section 2.3). As this is the most simple case, it is used to introduce the different aspects of the analytical approach for the ionisation determination. However, for realistic results the model needs to be extended to thick sheaths (section 2.4). The resulting thick sheath IM is generally referred to in the text as *the* AIM. In section 2.5 a MC approach to determine the ionisation is discussed. This numerical approach, referred to as *MC I*onisation *M*odel (MIM), is needed for several reasons. First, it allows calculating some general quantities required for the AIM, e.g. the effective ionisation energy (section 2.6.1). After an illustration of the arches of the AIM (section 2.6.2), the AIM results for the sheath ionisation and for the ionisation distribution are verified by comparing it with the MIM results (section 2.6.3). Then, the influence of the scattering angle χ on the ionisation distribution (section 2.6.4) and the relation between the electron orbit and the spatial distribution of the excitations and ionisations (section 2.6.5) is addressed. The verification of the AIM is very important because the ionisation determination is a crucial step in the simplified self-consistent model (Chapter 3).

2.2 Concept of thin and thick sheath and individual sheath

As mentioned in the introduction, the AIM is based on the splitting of the discharge in arch-shaped regions. This concept was originally developed by Wendt et al. [Wendt88a, Wendt88b, Wendt90]. The cathode sheath thickness compared to the height of the arches is crucial in this approach. Therefore, they consider the cathode sheath thickness and the electron Larmor radius (eq. (1.2) in section I.1.1), which allows them to distinguish between "thin" and "thick" sheaths. The term thin sheath is used for the situation where the sheath thickness is small compared to the Larmor radius r_L of the HEE. The term thick sheath refers to the reverse situation, i.e. where the sheath thickness is large compared to the Larmor radius of the HEE. These terms are used for the complete discharge and are based on the behaviour of the SE in the middle of the race-track. However, whether an electron experiences a thin or thick sheath depends also on its starting position on the target. This is illustrated in Fig. 2.2: as the movement of the SE emitted at x_1 is confined to the cathode sheath, the discharge is considered as being a "thick sheath" case according to the definition because $z_{dE}>r_L$. However, for x_3 the HEE clearly do not see a thick sheath although the relation $z_{dE}>r_L$ still holds for the SE emitted at x_3. Therefore, we introduce the concept "*I*ndividual *S*heath" (IS). This IS can be for a given electron "thic*K*" (IS^K) or "thi*N*" (IS^N). To define these concepts we introduce $z_{SE,i}$, the maximum height a SE emitted at x_i can reach without interacting with the discharge gas, and $z_{MF,i}$, the maximum height above the target of the magnetic field line that intersects the target surface at x_i. We define now IS^K as $z_{SE,i}<z_{dE}$ and IS^N as $z_{MF,i}>z_{dE}$. This definition creates a *T*ransition zone (IS^T) for arches with $z_{SE,i}>z_{dE}$ and $z_{MF,i}<z_{dE}$. An example of such an arch is the one corresponding with x_2 in Fig. 2.2. The reason for the introduction of IS^K, IS^N and IS^T will become clear in section 2.4.1.

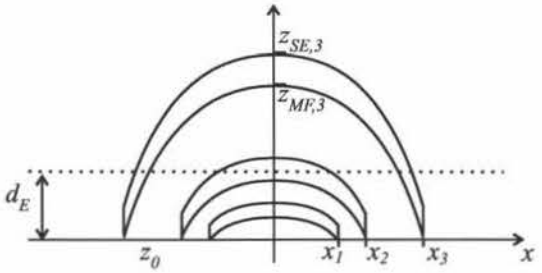

Fig. 2.2. The arch-shaped regions mark the area accessible to a SE emitted from the target without interactions with the discharge gas. The dotted line represents the end of the cathode sheath (thickness d_E). For the arch corresponding with x_3 the maximum height the SE can reach without interacting with the discharge gas ($z_{SE,3}$) and the maximum height of the magnetic field line ($z_{MF,3}$) are indicated. Given these positions, it is clear that whether a SE experiences a thin or thick sheath will depend on its starting position. Therefore the concept of individual sheath is introduced: x_1 has an individual thick sheath (IS^K), x_3 has an individual thin sheath (IS^N) and x_2 is in the transition region (IS^T).

In the case of an IS^N, the electron will only spend a very small fraction of its time in the cathode sheath. Hence, SI will hardly take place. If nevertheless SI occurs, the HEE^{SI} moves in practically the same area as the original SE. For an IS^K, SI is inevitable as the collisionless orbit of the original HEE^{ta} is entirely within the cathode sheath (x_1 in Fig. 2.2). Moreover, the region accessible to electrons due to SI can be substantially different from the one of the original SE. This is crucial as it implies that to model the IS^K the HEE^{SI} need a separate arch construction. This will make the analytical approach more complex. Therefore, the analytical model is first explained for the case with only individual thin sheaths (section 2.3). Then, the model is extended to thick sheaths (section 2.4).

2.3 Thin sheath ionisation model

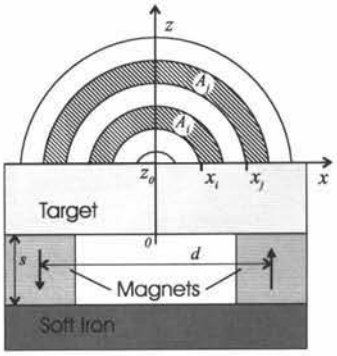

Fig. 2.3. Two-dimensional sketch of the magnetron model as before (see Fig. 1.2) but with semi-circles above the target, that show the idealised situation of how the discharge is built up by arch-shaped regions.

For a rectangular magnetron with two long straight sections that do not influence each other, the symmetric two-dimensional geometry shown in Fig. 1.2 (section 1.2.1) is sufficient for modelling the discharge in these straight sections. The discharge is considered as being built up by arches A_i, A_j,... that correspond with positions x_i, x_j,... at regular distances along the x-axis (Fig. 2.3). The idea for splitting up the discharge area becomes clear when comparing Fig. 1.1 with Fig. 2.3: the arches correspond with the area accessible to a SE that does not interact with the discharge gas. The arches are defined so that the probability to find a HEE during its lifetime in the surface area $\delta x \delta z$ at point (x,z) in arch A_i is given by $A_i(x,z)$. As mentioned before, in the thin sheath model, the HEE^{ta} and the HEE^{SI} practically move in the same area. Hence, no distinction between the two types of HEE has to be made and the high energy electrons can be referred to as HEE.

Fig. 2.3 represents an idealised situation because the arches are concentric circle segments, which is not the case for a realistic magnetic configuration. It is clear that this splitting up of the discharge region is only applicable in the case of a balanced magnetic field. Moreover, the magnetic field needs to be strong enough such that the confinement along the magnetic field lines is the dominating aspect of the electron movement.

By introducing the arches A_i the HEE distribution H of the discharge can be characterised by the occupation profile u that consists of a set of values u_i that give for each arch A_i its relative weight in the discharge:

$$H = \sum_i u_i A_i \tag{2.1}$$

The HEE distribution gives the relative amount of HEE per surface area $\delta x \delta z$ at point (x,z) of the discharge region.

In the following sections the thin sheath IM will be explained. A schematic overview of the model is given in Fig. 2.4. The input consists of the magnetic field, the electric field (defined by V_d and d_E) and the elements r_i of the SE emission profile. The electric field is assumed linear, based on experimental observations (see section I.1.3.3.5A). Consequently, it is defined by the discharge voltage V_d and cathode sheath thickness d_E. The first part of the model is the calculation of the arch-shaped regions A_i and the electron distribution within (section 2.3.1). Afterwards follows the deduction of the average transfer matrix T_{avg}, which describes the transfer of the HEE among the arches (section 2.3.2). Therefore, the effective

ionisation energy W, the ionisation energy E_{ion} and the fraction f_{ion} of ionising collisions in the total number of collisions are needed. Combining the electron distribution in the arches A_i with the electron collision cross sections allows estimating the contribution of SI for a given arch (h_i). This combined with T_{avg} allows deducing g_i, the weight factor for a SE emitted from the target that accounts for SI. From T_{avg}, g_i and r the occupation profile u can be deduced. The elements u_i of the occupation profile give for each arch the probability to find the HEE in that arch during the electron lifetime in the discharge. Combined with the A_i it determines the HEE-distribution H in the discharge. This deduction of H is discussed in section 2.3.3. From H the ionisation distribution I can be deduced (section 2.3.4), the output of the IM.

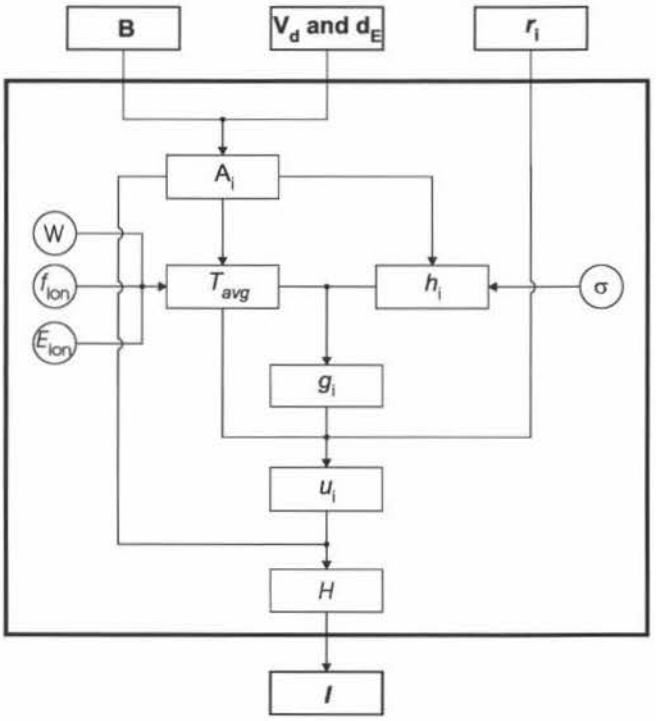

Fig. 2.4. Overview of the thin sheath IM showing how the ionisation distribution I is deduced from the magnetic field (B), the electric field (defined by V_d and d_E) and the elements r_i of the SE emission profile. The physical quantities needed are the electron cross sections (σ), the effective ionisation energy (W), the fraction of the total number of collisions that is ionising (f_{ion}) and the ionisation energy (E_{ion}). The meaning of the other symbols is explained in the text.

2.3.1 Determination of the arches A_i

To determine the arch A_i the corresponding collisionless SE orbit with starting position x_i is calculated using the Lorentz equation (eq. (1.1) in section I.1.1). As in the previous chapter B is calculated analytically, V_d and d_E are considered as input parameters and the electric field is assumed to vary linearly (section 1.2.1). The Lorentz equation is numerically solved using the fourth order Runge-Kutta method. As the accuracy is not so crucial here, a fixed time step Δt is chosen.

For a position x_i the maximum height $z_{SE,i}$ that the SE can reach is deduced from the collisionless SE orbit. By retracing the magnetic field line that intersects the target at that

position x_i the height $z_{MF,i}$ of the magnetic field line above the target at $x = 0$ is determined. The z-value z_i of the centre of arch A_i at $x = 0$ is defined as :

$$z_i = \frac{z_{SE,i} + z_{MF,i}}{2} \tag{2.2}$$

The centre line of the arch is defined by the magnetic field line going through z_i. The width of the arch is determined by the motion of the electron before it interacts with the discharge gas as indicated in Fig. 2.5. We assume a homogeneous spatial HEE distribution along this centre line. According to [Wendt88a] this is valid above the cathode sheath, within the sheath correction factors are needed (see next paragraph). This assumption is only valid for sufficiently low gas pressures. When the HEE move several times back and forth between $-x_i$ and x_i, their distribution will indeed be homogeneous. Hence, this assumption requires that the dimensions of the arch should be at maximum of the same order as the electron mean free path. The first is of the order of the width of the most intense part of the race-track (some centimetres), the latter can be deduced from the cross sections shown in Fig. I.1.4: for $\sigma = 5\times10^{-16}\text{cm}^2$ (at 100 eV) the mean free path length at 1 Pa is still 8 cm. Hence, for typical MD the criterion is fulfilled.

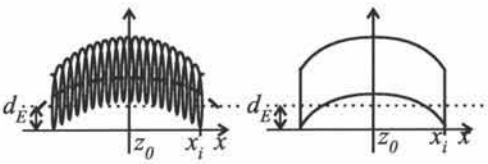

Fig. 2.5. Sketch showing how the arch-shaped regions are constructed: the arch corresponds with the area accessible to the SE emitted from the target before it interacts with the discharge gas.

For the HEE only the interactions with neutral discharge gas atoms are taken into account as they are by far the most important (section I.1.2.1). Due to these interactions, the arches A_i contain HEE with energies ranging from $|eV_d|$ (the maximum HEE energy) to E_{th}. Within this range, the energy distribution of the HEE, referred to as $D(E)$, can be considered homogeneous [Guimarães91]. Because of this energy distribution, the homogeneous spatial HEE distribution along the centre line of the arch needs to be corrected within the cathode sheath. Indeed, at a position z in the sheath a HEE has a potential energy equal to $|eV(z)|$. Hence, only the HEE with energy higher than $|eV(z)|$ can reach that height z. As $D(E)$ is homogeneous, the number $N(|eV(z)|)$ of HEE with energy higher than $|eV(z)|$ in the discharge is given by :

$$N(|eV(z)|) = \int_{|eV(z)|}^{|eV_d|} D(E)dE \sim |eV_d| - |eV(z)| \tag{2.3}$$

Similarly, the total number of HEE is $N(E_{th}) \approx |eV_d|$ because $|eV_d| >> E_{th}$ Hence, the correction factor at height z in the sheath is $|eV_d - eV(z)|/|eV_d|$. In this way, the normalised spatial HEE distribution along the centre line of each arch is determined.

2.3.2 Modelling of the transfer of HEE among arches

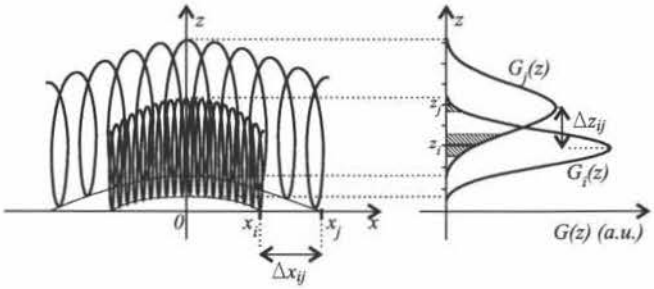

Fig. 2.6. For two positions x_i and x_j at the target surface, the position of the corresponding arches A_i and A_j are indicated by sketching the collisionless orbits of the SE emitted at these positions. The right hand part shows the Gaussian distributions attributed to the arches A_i and A_j. The transfer probability t_{ij} is proportional with the hatched surface under the Gaussian G_j at z_i. Similarly, t_{ji} is determined by $G_i(z_j)$.

The interaction of a HEE with the discharge gas can result in its transfer from one arch to another. In order to model these transfers, we consider the distribution of the HEE around the magnetic field line that forms the centre line of the arch. In general, the maximum distance a HEE can be away from the magnetic field line around which it gyrates is given by its Larmor radius r_L. This Larmor radius depends on the amplitude and orientation of the electron velocity vector since only the component perpendicular to the magnetic field line contributes to r_L. Because of the homogeneous energy distribution in the arches, the average energy E_{avg} of the HEE in an arch is half of the maximum energy: $E_{avg} = |eV_d|/2$. This average energy is used to determine the width of the distribution, i.e. $r_{L,avg}$ is defined as the Larmor radius corresponding with E_{avg} for a velocity vector perpendicular to the centre line. For the distribution of the electrons around the centre line of A_i we assume a Gaussian distribution $G_i(z)$ with width σ in the direction perpendicular to the centre line (Fig. 2.6). As the Gaussian distribution becomes practically zero at three times its width, σ is set equal to $r_{L,avg}/3$.

A change in the direction of the velocity vector of a HEE because of an interaction with the discharge gas can transfer it from one arch (A_j) to another (A_i). The probability t_{ij} that this transfer occurs is proportional with the value of G_j around z_i. This is shown in Fig. 2.6 by the hatched surface at z_i. Introducing δz_i as $(z_{i+1}-z_{i-1})/2$ and linearising G_j in the interval $[z_i-\delta z_i/2, z_i+\delta z_i/2]$ we find :

$$t_{ij} \sim \int_{z_i-\frac{\delta z_i}{2}}^{z_i+\frac{\delta z_i}{2}} G_j(z)dz \approx G_j(z_i)\delta z_i \qquad (2.4)$$

When deducing the transfer probabilities, it should be kept in mind that not always the whole arch contributes to the transfer. As an example, Fig. 2.6 shows the situation where only the fraction $|x_i|/|x_j|$ of the arch A_j overlaps with A_i. Such partial overlap only occurs if $\Delta z_{ij} \leq \Delta x_{ij}$ with $\Delta x_{ij} = |x_i|-|x_j|$ and $\Delta z_{ij} = |z_i-z_j|$. As this overlap reduces the transfer of HEE from A_j to A_i this interaction needs to be corrected with c_{ij} :

$$c_{ij} = \begin{cases} \dfrac{\Delta z_{ij}}{\Delta x_{ij}} + (1 - \dfrac{\Delta z_{ij}}{\Delta x_{ij}}) \left| \dfrac{x_i}{x_j} \right| & \dfrac{\Delta z_{ij}}{\Delta x_{ij}} \le 1 \\ 1 & \dfrac{\Delta z_{ij}}{\Delta x_{ij}} > 1 \end{cases} \tag{2.5}$$

Combining eqs. (2.4) and (2.5) we find :

$$t_{ij} \sim c_{ij} G_j(z_i) \delta z_i \tag{2.6}$$

from which the probabilities t_{ij} can be deduced by requiring :

$$\sum_j t_{ij} = 1 \tag{2.7}$$

All these probabilities t_{ij} define a square matrix T, which is referred to as the transfer matrix. In reality the HEE do not interact once but several times. The probability t^2_{ij} that the HEE transfers from A_j to A_i at the second interaction is given by :

$$t^2_{ij} = \sum_k t_{ik} t_{kj} \tag{2.8}$$

This is equal to element i,j of the matrix $T^2 = T*T$. Hence, the element that gives the probability that a HEE that started in A_j is transferred to A_i at interaction m is element i,j of T^m. This way a transfer matrix can be constructed for each interaction of the HEE. The problem arises to determine the average total number of interactions n of the HEE. First, we look at the average number of ionisations per HEE, which is given by:

$$n_{ion} = \frac{|eV_d| - E_{ion}}{W} \tag{2.9}$$

with E_{ion} the ionisation energy and W the effective ionisation energy. We define f_{ion} as the fraction of ionisations in the average total number of interactions :

$$f_{ion} = \frac{n_{ion}}{n} \tag{2.10}$$

Hence, n is determined by:

$$n = \frac{1}{f_{ion}} \frac{|eV_d| - E_{ion}}{W} \tag{2.11}$$

The values of W and f_{ion} depend on the maximum electron energy and thus, they vary in principle according to the discharge conditions. However, in the considered energy range, the dependence is weak and as a good approximation average values of W and f_{ion} can be used as will be shown in section 2.6.1.

We also introduce the average transfer matrix T_{avg}, defined as:

$$T_{avg} = \frac{1}{n} \sum_{m=0}^{n-1} T^m \tag{2.12}$$

The reason for introducing T_{avg} will become clear in the next section.

2.3.3 Deduction of the HEE-density *H*

To characterise the emission of SE from the target, the emission profile r is introduced. This profile r is a set of values r_i each of which corresponds with the number of SE emitted at position x_i on the target. If only one SE is emitted, e.g. at x_0, r is given by:

$$r_i = \begin{cases} 0 & |x_i| \neq x_0 \\ 1 & |x_i| = x_0 \end{cases} \tag{2.13}$$

To characterise the HEE-density H because of the emitted SE both the arches A_i and the elements u_i of the occupation profile need to be known (see eq. (2.1)). The A_i were determined in the previous section, in this section the relation between the emission profile r and the occupation profile u is deduced.

First, when SI happens, there is an extra energy input to the discharge equal to $|eV(z_C)|$ (Fig. 2.1). This extra energy input by an ionisation at height z_C can be described by giving the HEE^{ta}, the original HEE due to the target, a weight factor:

$$1 + \frac{|eV(z_C)|}{|eV_d|} \tag{2.14}$$

The energy of the ejected electron does not need to be considered in the extra energy contribution because it comes from the original HEE. So it is only a redistribution of the energy of the original HEE^{ta}. We introduce the arch $\mathfrak{A}_{i,z_C}$, the part of arch A_i at height z_C, which is defined as:

$$\mathfrak{A}_{i,z_C} = \sum_x A_i(x, z_C) \tag{2.15}$$

For an arch A_i the correction factor h_i is given by the weighted average of the individual weight factors :

$$h_i = 1 + \frac{1}{|eV_d|} \frac{\sum_{z_C} \frac{\sigma_{ion}(|eV(z_C)|)}{\sigma_{tot}(|eV(z_C)|)} |eV(z_C)| \mathfrak{A}_{i,z_C}}{\sum_{z_C} \mathfrak{A}_{i,z_C}} \tag{2.16}$$

The ratio of the ionisation and total cross section is needed because only that fraction of the collisions will be ionising. As deduced in the previous section a SE emitted in arch A_i has a probability T^k_{ji} to transfer to A_j at interaction k. Hence, due to SI, a SE emitted at position x_i needs a weight factor g_i given by:

$$g_i = \prod_{k=1}^{n} \left(\sum_j \min(h_i, h_j) T^k_{ji} \right) \tag{2.17}$$

with k ranging from 1 to n with n defined as in eq. (2.11). The minimum of h_i and h_j is taken in eq. (2.17). At first sight it might seem logical to take h_j, the value corresponding with the arch to which the HEE transfers. However, if h_j is larger than h_i this would mean that after the HEE interaction the electron will be relatively more in the cathode sheath. This is highly unlikely because the interactions of the electrons with the discharge gas and the accompanied change in their velocity vector "push" them out of the sheath (see also section 2.6.4). This

reasoning justifies the choice for the minimum of h_i and h_j. By taking into account ionisation in the sheath the emission profile r is transformed into the adapted emission profile r' according to the relation:

$$r_i' = r_i \, g_i \tag{2.18}$$

Second, we need to take into account that because of the interactions with the sputter gas, the electron will be scattered over the different arches. Therefore, we consider again the electron emitted at the target at x_0. As long as it does not undergo an interaction with the sputter gas, it remains in its original arch. Translated into the formalism of the model it means that the r_i and u_i are equal. We introduce u^0_i to indicate the occupation profile after zero interactions (i.e. before any interaction actually happened) and find then :

$$u_i^0 = \sum_k T_{ik}^0 r_k \tag{2.19}$$

with T_{ik}^0 element i,k from the unit matrix T^0. After one interaction of the electron with the sputter gas and neglecting the effect of SI we find for u^1_i:

$$u_i^1 = \sum_k T_{i,k}^1 r_k \tag{2.20}$$

with $T_{i,k}^1$ equal to $T_{i,k}$ (the superscript "1" is only added for similarity with $T_{i,k}^0$ and $T_{i,k}^m$). If the HEE would reach the threshold value after two interactions, the occupation profile would be the average of u_0 and u_1. Now, the HEE do not interact once but n times because after the n-th interaction the HEE is no longer a HEE by definition. Consequently, the average occupation profile u is given by the average of u_0 to u_{n-1} :

$$u_i = \frac{1}{n} \sum_{m=0}^{n-1} u_i^m \tag{2.21}$$

with u^m_i the occupation profile after m interactions defined as :

$$u_i^m = \sum_k T_{i,k}^m r_k \tag{2.22}$$

Alternatively, eq. (2.21) can also be rewritten as :

$$u_i = \frac{1}{n} \sum_{m=0}^{n-1} u_i^m = \frac{1}{n} \sum_{m=0}^{n-1} \left(\sum_k T_{i,k}^m r_k \right) = \sum_k \left(\frac{1}{n} \sum_{m=0}^{n-1} T_{i,k}^m \right) r_k = \sum_k \left(T_{avg} \right)_{i,k} r_k \tag{2.23}$$

using the average transfer matrix T_{avg} as introduced in the previous section (eq. (2.12)). It describes the transfer of HEE among the arches averaged over the energy interval [leV_dl, E_{th}]. Eq. (2.23) does not take into account SI. This effect is expressed by eq. (2.18). Combining the two equations results in :

$$u_i = \sum_k \left(T_{avg} \right)_{i,k} g_k r_k \tag{2.24}$$

Given eq. (2.1) these u_i characterise the HEE distribution H of the discharge.

2.3.4 Deduction of the ionisation distribution

In this part of the model, the ionisation distribution I is deduced from a known HEE distribution H. In order to deduce the ionisation caused by this H we would, in principle, need to calculate the probability $P(E)$ for an ionising collision during a certain time interval ε_t for each electron energy E:

$$I = P(E)H \tag{2.25}$$

The ionisation distribution is thus defined as the relative amount of ionisation per time interval and per surface area $\delta x \delta z$ at point (x,z) in the discharge area. Hence, the term "ionisation distribution I" stands for "the relative spatial distribution of the ionisation rate". The ionisation probability $P(E)$ is given by:

$$P(E) = 1 - e^{-\frac{\varepsilon_t v}{\lambda_{ion}(E)}} = 1 - e^{-\frac{\varepsilon_t}{\lambda_{ion}(E)}\sqrt{\frac{2E}{m}}} \tag{2.26}$$

with $\lambda_{ion}(E)$ the electron mean free path for ionisation and v the electron velocity. For E above approximately 100 eV, $\lambda_{ion}(E)$ has an energy dependence close to $\sqrt{E}$ (Fig. 1.4 in section I.1.2.1.1). Therefore, we consider $P(E)$ as independent of E. Combining eq. (2.25) and eq. (2.26) leads to:

$$I \sim H \tag{2.27}$$

i.e. the ionisation distribution is to a good approximation proportional with the HEE distribution.

2.4 Thick sheath ionisation model

In this section the thin sheath IM is adapted so that individual thick sheaths can be modelled. As mentioned in the introduction, the thick sheath IM is in general referred to as *A*nalytical *I*onisation *M*odel (AIM) in this work. However, in this section the term "thick sheath IM" is preferred to contrast with the thin sheath IM.

In the thin sheath IM we deduced the occupation profile u from the emission profile r (eq. (2.24)). This relation combined with eq. (2.1) allows determining the HEE-density H (see also Fig. 2.4). In the thick sheath IM, the distinction needs to be made between the two types of HEE: the HEE^{ta}, the accelerated secondary electrons from the target, and the HEE^{SI}, the accelerated electrons from electron-ion pairs generated in the cathode sheath. In the thin sheath IM, the HEE^{SI} were also accounted for but their behaviour was assumed identical to the behaviour of the original HEE. In the thick sheath IM this assumption is no longer valid because the HEE^{ta} and the HEE^{SI} behave fundamentally different.

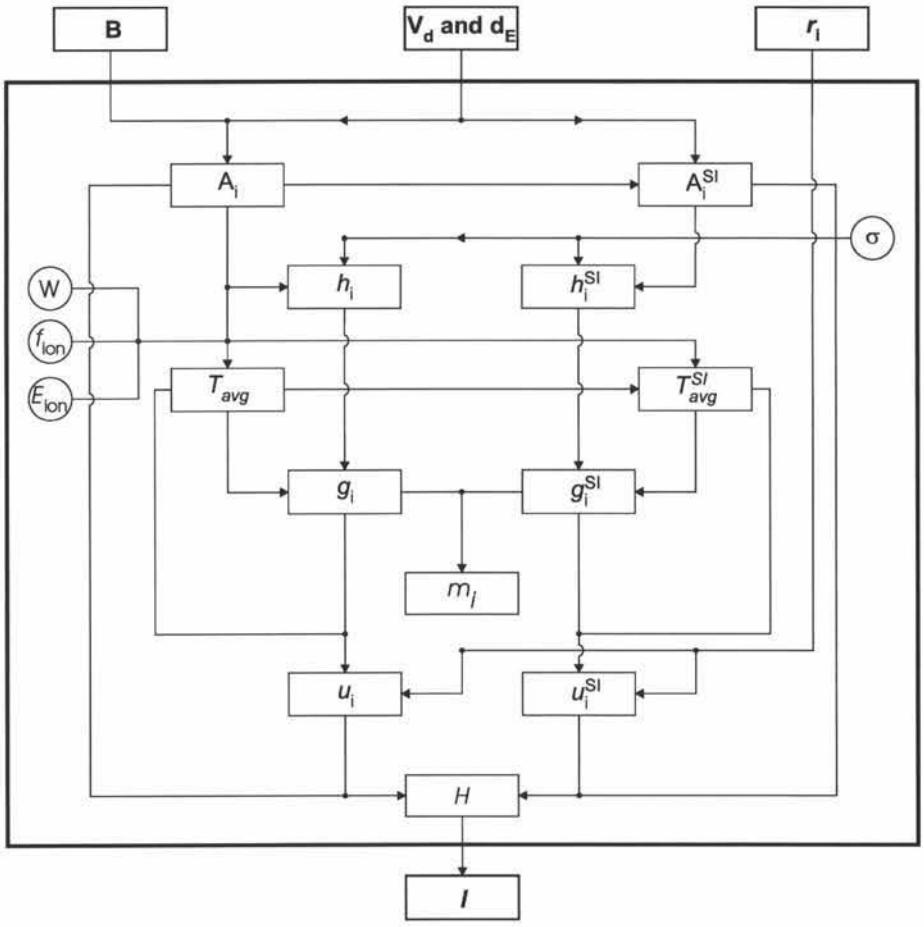

Fig. 2.7. Overview of the thick sheath IM showing how the ionisation distribution I is deduced from the magnetic field, the electric field and the emission profile of the SE. The different aspects of the model need two versions: one for the HEE^{ta} as in the thin sheath IM and an extra "SI-version" for the HEE^{SI}. The meaning of the symbols is explained in Fig. 2.4 and in the text.

Hence, for the different aspects of the thin sheath IM an "SI-version" needs to be introduced (Fig. 2.7). In the thick sheath IM, both types of HEE have their own arch-shaped regions: A_i for the HEE^{ta}, A^{SI}_i for the HEE^{SI}. Consequently, eq. (2.1) needs to be replaced by:

$$H = \sum_i \left(u_i A_i + u_i^{SI} A_i^{SI} \right) \tag{2.28}$$

Next to the arch-construction, two more of the basic parts of the thin sheath IM, the transfer of HEE and the deduction of the HEE-density, need to be reconsidered. The construction of the arches A_i and A^{SI}_i is discussed first (section 2.4.1). Because of the two types of HEE, two transfer matrices T and T^{SI} are needed (section 2.4.2). Finally, the elements u_i and u^{SI}_i of the occupation profiles are deduced (section 2.4.3), which allows determining H. Only the ionisation determination remains the same as in the thin sheath IM and does not need reconsidering.

2.4.1 Determination of the arches

In the thin sheath IM the procedure to deduce the arches is for all starting positions x_i the same. In the thick sheath IM this is no longer the case because the type of arch will depend on the kind of individual sheath the emitted SE experience (see section 2.2). When the type of the arch needs to be specified, a subscript is added: "N" for individual thin sheath, "K" for individual thick sheath and "T" for the transition region. Furthermore, the thick sheath IM requires arches specifically constructed for the HEE^{SI}. These arches are denoted by the superscript "SI". An overview of the different notations is given in Table 2.5. For example the notation $A^{SI}_{K,i}$ stands for the arch of a HEE^{SI} generated by a SE emitted at x_i in the case of an individual thick sheath.

	Notation	HEE^{ta}	HEE^{SI}
Thin individual sheath	IS^N	$A_{N,i}$	$A^{SI}_{N,i}$
Transition sheath	IS^T	$A_{T,i}$	$A^{SI}_{T,i}$
Thick individual sheath	IS^K	$A_{K,i}$	$A^{SI}_{K,i}$

Table 2.5. Overview of the different notations used in the thick sheath IM to denote the kind of individual sheath, the arches of the HEE^{ta} and of the HEE^{SI}.

2.4.1.1 Arch-construction for the original HEE $\boxed{A_i}$

A. Individual thin sheath $\boxed{A_{N,i}}$

This is the case where a SE emitted at the target position x_i experiences an individual thin sheath. The (construction of the) arch is the same as in the thin sheath IM. Hence, these arches $A_{N,i}$ are the same as the A_i (section 2.3.1).

B. Individual thick sheath $\boxed{A_{K,i}}$

This is the case where a SE emitted at target position x_i experiences a thick sheath. The construction as used for an arch $A_{N,i}$ is no longer valid in this case. An arch $A_{N,i}$ represents the area where a HEE ionises in the discharge, from its maximum energy $|eV_d|$ down to the threshold energy E_{th}. The principle of the construction of the arches $A_{N,i}$ is shown again in Fig. 2.8a. Using this method for a thick individual sheath, the region that corresponds with the

dashed area in Fig. 2.8b is obtained for a SE emitted at x_1. This is the region accessible to the electron without interactions with the discharge gas. An electron in the cathode sheath at height z has a potential energy equal to $|eV(z)|$. Hence, a HEE at the end of its lifetime in the discharge should have a z-value for which $|eV(z)| < E_{th}$. This has an important consequence because the minimum potential of an electron in the hatched area of Fig. 2.8b is $|eV(z_{SE,i})|$. If this energy is larger than E_{th}, the area is not accessible for all HEE. Hence, the arch has to be extended to the edge of the cathode sheath as indicated by the thick solid line in the right hand side part of Fig. 2.8b.

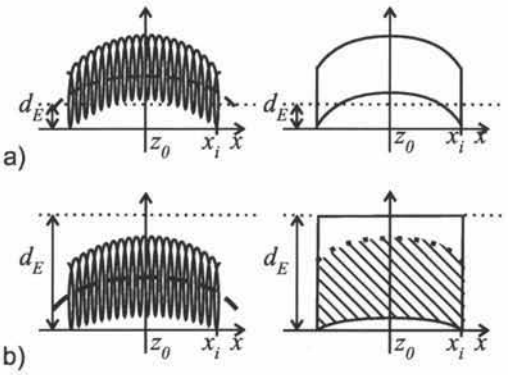

Fig. 2.8. Sketch showing how the arch-shaped regions are constructed for a thin (*a*) and a thick individual sheath (*b*), denoted with $A_{N,i}$ and $A_{K,i}$ respectively. The major difference is that the $A_{K,i}$ have to be extended to the cathode sheath edge. This sheath edge is indicated by the dotted line at height d_E above the target surface.

This solves the problem but introduces a complication since it implies that the HEE will shift their position within the arch-shaped region during their lifetime. Before, in an arch $A_{N,i}$, the probability to find a HEE at a certain position in the arch (above the cathode sheath) did not depend on its energy. This is no longer true in the area depicted in Fig. 2.8b, e.g. a HEE with energy $|eV_d|$ can be in the hatched area, an electron with energy smaller than $|eV(z_{SE,i})|$ has to be in the blank area close to the sheath edge. This problem relates to the electron transport in the direction perpendicular to the magnetic field lines, which is a complex topic (section I.1.3.6.2). Hence, the exact spatial distribution of the electron in the arch during its lifetime is very difficult to obtain. To circumvent this, the same weighing as in the case of the $A_{N,i}$ is used in the cathode sheath (end of section 2.3.1). This approach gives good results but because of its crudity, adjustments will have to be made when deducing the transfer matrices (see section 2.4.2).

C. Transition region of the individual sheath $\boxed{A_{T,i}}$

This is the case where a SE emitted at target position x_i experiences neither a thick nor thin sheath (x_2 in Fig. 2.2). The reason which forces to use $A_{K,i}$ does not apply here as the SE can reach out above the cathode sheath. Hence, for the construction of the $A_{T,i}$, the procedure of a thin sheath can be applied. Hence, for the original HEE it is not necessary to introduce the transition region. It will be, however, for the arches of the HEE^{SI}.

2.4.1.2 Arch-construction for HEE due to sheath ionisation $\boxed{A_i^{SI}}$

In the thick sheath IM, the HEE^{SI} need separate arches, referred to as A_i^{SI}. Again, the distinction is made between individual thin sheaths, the transition region and individual thick sheaths.

A. Individual thin sheath $\boxed{A_{N,i}^{SI}}$

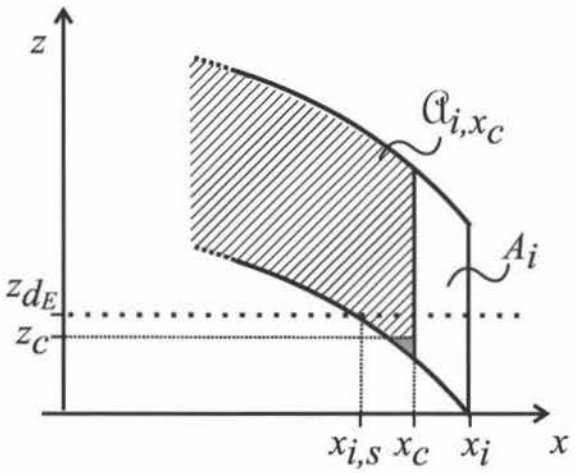

Fig. 2.9. Sketch showing the sheath region of A_i in the thin sheath case with a sheath ionisation at (x_C, z_C). The area accessible for the ejected electron is estimated by $\mathcal{A}_{i,x_C}$. The grey area is inaccessible for the new HEE but as it represents only a small fraction of $\mathcal{A}_{i,x_C}$, it is neglected.

In this case the portion of the arch in the cathode sheath is very small. If a HEE^{SI} is formed, it will follow an orbit very similar to the one of the original HEE^{ta}. The difference is that an electron generated at position (x_C, z_C) cannot reach positions with $z<z_C$ or $|x|>|x_C|$ because of energy conservation reasons (Fig. 2.9). As it concerns here thin sheaths, i.e. the thickness of the sheath is much smaller than the arch dimensions, the limitation along the z-axis is neglected. Hence, a HEE^{SI} generated at x_C is limited to the part of A_i that fulfils the condition $|x|<|x_C|$. This is equivalent with saying that this electron is in an arch $\mathcal{A}_{i,x_C}$, defined as:

$$\mathcal{A}_{i,x_C} = \sum_{x=-x_C}^{x_C} \sum_{z} A_i(x,z) \qquad (2.29)$$

This arch is indicated in Fig. 2.9. The grey part of $\mathcal{A}_{i,x_C}$ is actually not accessible to the HEE^{SI} generated at (x_C, z_C). However, given the small fraction of $\mathcal{A}_{i,x_C}$ that the grey area represents, it does not matter whether it is included in $\mathcal{A}_{i,x_C}$ or not.

Another problem is that an arch A_i represents the area where a HEE^{ta} performs ionisation during its lifetime in the discharge. For the A^{SI}, the same principle is applied but the HEE^{SI} are generated at different positions (x_C, z_C). Hence, the arch $A_{N,i}^{SI}$ is the weighted average over the different $\mathcal{A}_{i,x_C}$:

$$A_{N,i}^{SI} = \frac{\sum_{x_C=x_{i,S}}^{x_i} \mathcal{A}_{i,x_C} w_i(x_C)}{\sum_{x_C=x_{i,S}}^{x_i} w_i(x_C)} \qquad (2.30)$$

The summing over x_C is restricted to those x-positions where SI is possible, i.e. it is limited between x_i and $x_{i,s}$, with $x_{i,s}$ as shown in Fig. 2.9. The weights $w_i(x_C)$ are defined as:

$$w_i(x_C) = \sum_{z=0}^{z_{d_E}} A_i(x_C, z) \frac{|eV(z)|}{|eV_d|} \tag{2.31}$$

When in the above equations the positions x_0, x_i, $x_{i,S}$ and x_C are used, they are assumed positive. This poses no fundamental limitation but simplifies the notations.

B. Individual thick sheath $\boxed{A_{K,i}^{SI}}$

In this case, SI will be very important because a substantial amount of the ionisations caused by the original SE occurs in the sheath. The HEE^{SI} have, in general, a lower energy than the original HEE. Because of this lower energy and because in this case the HEE^{SI} spend their entire lifetime in the cathode sheath, the $A_{K,i}^{SI}$ are structurally different from the A_i. As in the case of an IS^N, the HEE^{SI} are generated at different positions (x_C, z_C). This time the limitation along the z-axis cannot be neglected anymore as the cathode sheath thickness is of the same order as the arch dimensions. Hence, instead of $\mathfrak{A}_{i,x_C}$ we introduce $\mathfrak{A}_{i,x_C z_C}$. The construction of this arch $\mathfrak{A}_{i,x_C z_C}$ is more complicated and is discussed in the next paragraphs.

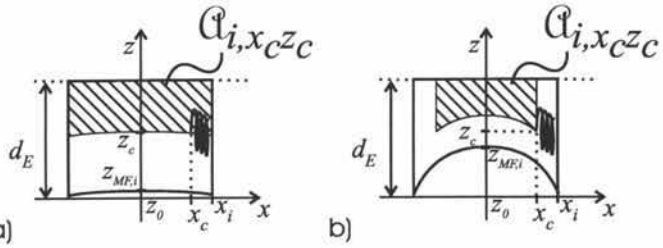

Fig. 2.10. Sketch showing the restriction along the x-axis of the HEE^{SI} generated at (x_C, z_C) for small ξ_i (*a*) and for large ξ_i (*b*), with ξ_i the curvature of the magnetic field lines (see text). The orbit of the original HEE^{ta} is sketched by the spiralling line. The hatched area represents the region accessible to the generated HEE^{SI}. In the first case, the ejected electron is limited to $|x| < x_i$, in the latter case to $|x| < x_C$.

Consider an ionisation in the cathode sheath that occurs at point (x_C, z_C) (Fig. 2.10). The point is chosen close enough to the target surface so that the newly ejected electron becomes a HEE^{SI}. The area where this HEE^{SI} performs ionisation is different from the one of the HEE^{ta}. Hence, a new procedure to determine the arch corresponding with the HEE^{SI} is needed. We distinguish the two cases depicted in Fig. 2.10. The first case (Fig. 2.10a) is the situation where the magnetic field lines are practically horizontal. If an ionisation occurs at (x_C, z_C), the region below z_C is inaccessible for the electron because of energy conservation. In spite of this, the ejected electron can reach the full length of the arch. Hence, there is no restriction along the x-axis. The second case concerns curved magnetic field lines (Fig. 2.10b). In this case, the electron will be bounded in its motion along the x-axis, similar to the situation sketched in Fig. 2.9. Therefore we introduce the boundary x-value x_B which defines the boundary of the electron along the x-axis. Hence, $x_B = x_i$ for the situation shown in Fig. 2.10a, whereas $x_B = x_C$ for the situation shown in Fig. 2.10b. To distinguish between the cases *a* and *b* we introduce the curvature of the magnetic field ξ_i, defined as $\xi_i = z_{MF,i} - z_0$, and propose the following criterion to determine x_B :

$$x_B = \begin{cases} x_C & \xi_i \geq r_{L,avg} \\ (1-\alpha)\,x_C + \alpha x_i & \frac{r_{L,avg}}{2} < \xi_i < r_{L,avg} \\ x_i & \xi_i \leq \frac{r_{L,avg}}{2} \end{cases} \tag{2.32}$$

with $r_{L,avg}$ the average Larmor radius (section 2.3.2) and the weight factor α defined as:

$$\alpha = 2 - \frac{\xi_i}{\frac{1}{2} r_{L,avg}} \tag{2.33}$$

As in the case of an arch A_i, the arch $\mathfrak{A}_{i,x_C z_C}$ has to represent the spatial distribution of the HEE^{SI} during their lifetime in the discharge. Therefore, the hatched areas in Fig. 2.10 cannot be filled homogeneously but have to be weighted similar to the part of the standard arches A_i in the cathode sheath. This was done using a weight factor $|eV_d\text{-}eV(z)|/|eV_d|$ at height z in the sheath (section 2.3.1). However, for $\mathfrak{A}_{i,x_C z_C}$ the argument z used in this expression has to be replaced by z' defined as:

$$z' = \frac{(z - z_C)\, z_{d_E}}{z_{d_E} - z_C} \tag{2.34}$$

because the weight factor has to be zero at height z_C as the electron cannot reach points below z_C. The arch $\mathfrak{A}_{i,x_C z_C}$ constructed in this way is the arch for the HEE^{SI} created at (x_C, z_C) by a HEE^{ta} emitted from the target at position x_i with a thick individual sheath :

$$\mathfrak{A}_{i,x_C z_C} = \sum_{x=-x_B}^{x_B} \sum_{z=z_C}^{z_{d_E}} F(x,z) \frac{\left|eV_d - eV(z')\right|}{\left|eV_d\right|} \tag{2.35}$$

with

$$F(x,y) = \begin{cases} 1 & A_i(x,z) \neq 0 \\ 0 & A_i(x,z) = 0 \end{cases} \tag{2.36}$$

For each position (x_C, z_C) where SI can occur, the appropriate arch $\mathfrak{A}_{i,x_C z_C}$ has to be constructed. Then, the $A_{K,i}^{SI}$ is given by the average over these arches :

$$A_{K,i}^{SI} = \frac{\sum_{x_C} \sum_{z_C=0}^{z_{d_E}} \mathfrak{A}_{i,(x_C,z_C)} w_i(x_C, z_C)}{\sum_{x_C} \sum_{z_C=0}^{z_{d_E}} w_i(x_C, z_C)} \tag{2.37}$$

with $w_i(x_C, z_C)$ the weight factor of each $\mathfrak{A}_{i,x_C z_C}$. This weight factor is determined by $A_i(x_C, z_C)$ and by $|eV(z_C)|$, the potential energy of the ejected electron and is thus defined as :

$$w_i(x_C, z_C) = A_i(x_C, z_C)\frac{|eV(z_C)|}{|eV_d|} \tag{2.38}$$

C. Transition region $\boxed{A_{T,i}^{SI}}$

For the transition region, there is no obvious way to construct the arch-shaped regions. Given the difference between the A_N^{SI} and A_K^{SI}, a smooth transition from the one case to the other is demanded. A means to achieve this transition is by considering the fraction f of the arch that is in the cathode sheath at $x = 0$ (Fig. 2.8). Given the definitions of the individual thin and thick sheath (section 2.2), f is zero for IS^N and one for IS^K. Consequently, the arches $A_{T,i}$ have an f-value between zero and one and the corresponding arches $A_{T,i}^{SI}$ can be constructed as follows:

$$A_{T,i}^{SI} = (1-f)\,A_{N,i}^{SI} + fA_{K,i}^{SI} \tag{2.39}$$

However, there is a complication because this equation implies that the A_N^{SI} and A_K^{SI} are used for the IS^T region, a region for which they are originally not intended to be. For the $A_{N,i}^{SI}$ this poses no problems but it does for the $A_{K,i}^{SI}$: for these arches the electrons did not reach out above the sheath, thus, the arches were limited within the cathode sheath (Fig. 2.11a). This is not valid for the $A_{T,i}^{SI}$: here the HEE^{ta} reach out above the cathode sheath. Hence, also the HEE^{SI} can reach out above the cathode sheath (Fig. 2.11b) and the maximum height is no longer given by z_{dE} but it is not given by $z_{SE,i}$ (the maximum height of the HEE^{ta}) either. To solve this problem, the maximum height is estimated by z_C+r_L with r_L the Larmor radius corresponding to the initial energy of the HEE^{SI}. This means that z_{dE} in eq. (2.35) needs to be replaced by z_C+r_L. However, if z_C+r_L is smaller than z_{dE}, z_{dE} remains. The arches constructed in this way are still referred to as $A_{K,i}^{SI}$ as it is only an extension of the arch-construction which does not change the results for the IS^N ($z_{SE,i}<z_{dE}$).

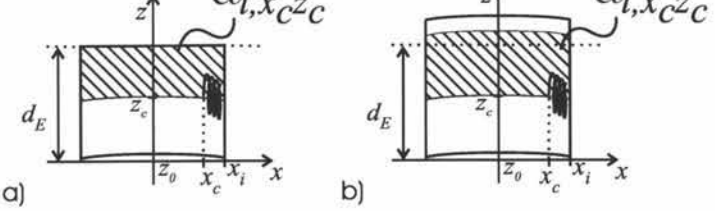

Fig. 2.11. This sketch shows the result of applying the procedure for determining the $A_{K,i}^{SI}$ in the case of IS^K (*a*) and in the case of IS^T (*b*).

2.4.2 Modelling of the transfer of HEE among arches

To model the effect of the HEE interactions with the discharge gas, the transfer matrix T was developed (section 2.3.2). As this matrix depends on the arches A_i, the arches A_i^{SI} need their own transfer matrix T^{SI}. However, given the introduction of the $A_{T,i}$ and $A_{K,i}$ also T needs to be adapted. Afterwards, the construction of T^{SI} and T_{avg}^{SI} is explained.

2.4.2.1 Adaptation of transfer matrix T

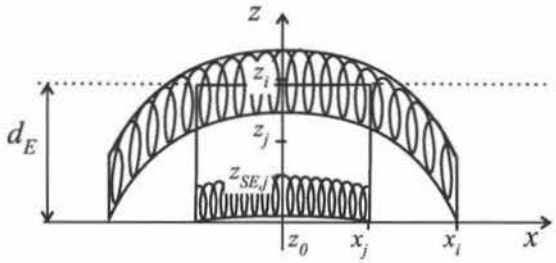

Fig. 2.12. Sketch showing arches A_i and A_j, their centres z_i and z_j and the collisionless orbit (spiralling line) for a SE emitted at x_i and x_j. For A_i, the centre of the arch is also the centre of the collisionless orbit at $x = 0$. However, for A_j this is not the case. Hence, to calculate the transfer from A_j to the other arches, z_j needs to be replaced in certain cases (see text) by $z_{SE,j}$, the maximum height of the collisionless orbit.

Each element t_{ij} from T represents the probability that an electron hops from arch j to arch i at the first interaction of the electron with the discharge gas. In other words, for a SE emitted at x_j in arch A_j, the probability to transfer to arch i at the first interaction is given by t_{ij}. Because of the introduction of the $A_{T,i}$ and $A_{K,i}$ a modification to the construction of T is necessary. This modification regards the value z_i, the average height of the arch at $x = 0$ (see eq. 2.2). For an IS^N or an IS^T, the centre z_i of arch A_i is relevant for all the electrons in the arch. Hence, as sketched in Fig. 2.12 for an IS^T, this is also true for the ones that did not interact with the discharge gas yet. For an IS^K, this is not valid: the orbit of the electrons before interacting with the discharge gas can be well below the centre of the arch. This is shown in Fig. 2.12 for arch $A_{K,j}$. It is clear that the Gaussian distribution G_j with centre at z_j is not representative for the HEE at the beginning of their lifetime in the discharge. The origin of the problem is the extension of the arches to the cathode sheath as this implies that the HEE will "shift" their position in the arches during their lifetime. Using nevertheless the Gaussian G_j around z_j to determine t_{ij} (eq. (2.7)) results in an artificially high transfer probability. To overcome this problem, the centre z_j of G_j for interaction from A_j to A_i is replaced by $z_{SE,j}$ when $z_j > z_{SE,j}$ and $z_i < z_{SE,i}$. This is the situation for transfer from A_j to A_i with A_j and A_i as shown in Fig. 2.12. Except for this adaptation, the calculation of the t_{ij}, and hence of T remains the same. The calculation of T_{avg} (eq. (2.12)) remains also the same.

Another complication is that the z_i can be very close to each other. This implies that the value δz_i (section 2.3.2, eq. (2.4)) becomes very small. To understand the physical meaning of this we introduce d_i, defined as:

$$d_i = \frac{1}{\delta z_i} \tag{2.40}$$

Hence, the value d_i expresses that there is one arch in the interval with length δz_i. In other words, d_i represents a "density of arches": it gives the number of arches per unit length along the z-axis. Now, if two or more arches are very close to each other, d_i will become very large. As a consequence, the element t_{ij} will be artificially small because, based on the high density, the model assumes far more arches than there exist in reality. To prevent this, a maximum density d_{max} is calculated. It is defined as the number of arches in an interval of 2σ around the centre of the arch. In cases where $1/\delta z_i$ is larger than d_{max}, δz_i is replaced by $1/d_{max}$ in eq. (2.6).

2.4.2.2 Construction of T^{SI} and T^{SI}_{avg}

Before starting the deduction of T^{SI}, an important remark needs to be made. The transfer matrix T for the standard arches A_i describes how the HEE transfer among the arches because of the interactions with the discharge gas. Hence, logically, one could expect T^{SI} to be the matrix describing how the HEE^{SI} transfer among the A_i^{SI}. This is not the case. Instead, the matrix T^{SI} describes the probabilities that SI occurs during the transfer of the HEE among the arches A_i. The transfer of the HEE^{SI} among the arches A_i^{SI} is neglected in the model. The reason is that the majority of the HEE^{SI} will be formed rather close to the edge of the cathode sheath. Consequently, they have a rather low maximum energy and they scatter much less than the original HEE.

Given the limited scattering of the HEE^{SI}, their spatial distribution is mainly determined by the position where they are generated. This requires determining which transfers A_j to A_i have a high probability to result in SI. Therefore, we define the element t_{ij}^{SI}, element i,j of matrix T^{SI}, as the probability for SI when a HEE transfers from A_j to A_i. This probability is given by:

$$t_{ij}^{SI} = p_i t_{ij} \tag{2.41}$$

with p_i the fraction of the arch A_i in the cathode sheath and t_{ij} element i,j of T.

Another difference concerns the calculation of the average T^{SI}_{avg}. T^{SI} describes, as mentioned, how the HEE^{SI} are distributed over the arches because of interactions of the HEE^{ta} with the discharge gas. Hence, it needs to be taken into account that the probability for SI depends on the energy of the HEE^{ta}. Therefore, T^{SI}_{avg} is defined as:

$$T_{avg}^{SI} = \frac{1}{n-1}\sum_{m=1}^{n-1} R_m \left(T^{SI}\right)^m \tag{2.42}$$

with R_m the fraction of the energy left after m interactions. Mark that, in contrast to T_{avg}, the unit matrix is not included in T^{SI}_{avg} because as long as the HEE^{ta} do not interact they cannot give rise to ionisation. The value of R_m is determined from the relation:

$$R_m = \frac{|eV_d - W'm|}{|eV_d|} \tag{2.43}$$

with W' the average energy loss per interaction, defined as:

$$W' = Wf_{ion} \tag{2.44}$$

and f_{ion} defined as in eq. (2.10) (section 2.3.2, see also section 2.6.1).

2.4.3 Deduction of the HEE-density *H*

As in section 2.3.3 we need to deduce the relation between the emission profile r and the occupation profile u. Assume a SE emitted at the target surface. If it does not cause any ionisation in the sheath, the energy contributed to the discharge is $|eV_d|$. However, if a HEE^{SI} is formed, e.g. at height z_C, the ejected electron contributes an energy $|eV(z_C)|$ to the discharge. Hence, the total energy contributed to the discharge because of the HEE^{ta} is equal to

$|eV_d|+|eV(z_C)|$. Of course, several ionisations in the sheath might be possible and the ejected electrons can in turn also cause SI. This total energy "delivered" to the discharge by a HEE[ta] is referred to as E_{tot}. In the thin sheath IM we introduced g_i such that $E_{tot} = g_i|eV_d|$, with g_i given by eq. (2.17). For thin sheaths it is highly improbable that the HEE[SI] also cause SI. On the other hand, for thick sheaths this effect becomes important because SI occurs frequently. This leads to the introduction of g_i^{SI}, the analogue of g_i for the HEE[SI]. Its calculation is similar to the one of g_i and will be dealt with in the next paragraph. Because of this new g_i^{SI}, the multiplication factor for a SE emitted at the target is no longer given by g_i but by m_i which is defined as :

$$m_i = 1+(g_i-1)g_i^{SI} \tag{2.45}$$

because the fraction due to SI (g_i-1) needs to be multiplied by g_i^{SI}. The expression for g_i (eq. (2.17)) remains valid since the procedure to calculate it from the A_i of the thin sheath IM is also valid for the $A_{N,i}$, $A_{K,i}$ and $A_{T,i}$ of the thick sheath IM. The multiplication factor m_i is an important parameter as it determines the actual energy contribution to the discharge by an SE emitted at the target (section 2.6.3).

Next, we discuss the calculation of g_i^{SI}. The calculation of the h_i^{SI} is similar to the one of h_i but, of course, the A_i need to be replaced by the A_i^{SI}:

$$h_i^{SI} = 1+\frac{1}{|eV_d|}\frac{\sum_{z_C}\frac{\sigma_{ion}(|eV(z_C)|)}{\sigma_{tot}(|eV(z_C)|)}|eV(z_C)|A_i^{SI}(z_C)}{\sum_z A_i^{SI}(z_C)} \tag{2.46}$$

Consequently, g_i^{SI} is given by :

$$g_i^{SI} = \prod_{k=1}^{n_i'-1}\left(\sum_j \min(h_i^{SI},h_j^{SI})\left(T^{SI}\right)_{ji}^k\right) \tag{2.47}$$

The only unknown in this equation is n_i', the maximum number of interactions of the HEE[SI]. To calculate g_i the total number of interactions n, corresponding with the maximum energy $|eV_d|$ was needed. In this case, n_i' is the total number of interactions corresponding with energy $E_{i,avg}^{SI}$, the average maximum energy of the HEE[SI]. The maximum energy is determined by the height z_C where SI occurs. The average of the positions z_C depends on the arch A_i. Hence, the average maximum energy depends on the starting position x_i, which explains the index i of $E_{i,avg}^{SI}$, and consequently, of n_i'. The energy $E_{i,avg}^{SI}$ is calculated from the A_i^{SI} as follows :

$$E_{i,avg}^{SI} = \frac{\sum_{z_C=0}^{z_{d_R}} \mathfrak{A}_{i,z_C}^{SI}|eV(z_C)|}{\sum_{z_C=0}^{z_{d_R}} \mathfrak{A}_{i,z_C}^{SI}} \tag{2.48}$$

with $\mathfrak{A}_{i,z_C}^{SI}$ the fraction of the arch A_i^{SI} at height z_C :

$$\mathfrak{A}_{i,z_C}^{SI} = \sum_x A_i^{SI}(x, z_C) \tag{2.49}$$

In the thin sheath IM, the knowledge of the transfer matrix T and of the sheath ionisation g_i allows deducing the occupation profile u from a given emission profile r (eq. (2.24)). A similar approach is followed for the thick sheath IM. Due to scattering the emission profile will be transformed into the occupation profile u according to the relation :

$$u_i = \sum_k \left(T_{avg}\right)_{i,k} r_k \tag{2.50}$$

However, the original HEE^{ta} will give rise to HEE^{SI}. Given the definition of the multiplication factor m (eq. (2.45)), the occupation profile of these HEE^{SI} is given by :

$$u_i^{SI} = \sum_k \left(T_{avg}^{SI}\right)_{i,k} (m_k - 1) r_k = \sum_k \left(T_{avg}^{SI}\right)_{i,k} (g_k - 1) g_k^{SI} r_k \tag{2.51}$$

These relations (2.50) and (2.51) together with eq. (2.28) allow determination of the HEE-density from a given emission profile. The deduction of the ionisation density I remains the same as for the thin sheath IM.

2.5 MC model

The basis of the MC model is the numerical integration of the Lorentz equation (eq. (I.1.1)), which was achieved using the Runge-Kutta method (4^{th} order) with a fixed time step Δt ($= 2 \times 10^{-11}$ s). The collision probability p_{coll} during that time step for an electron with energy E_0 is given by:

$$p_{coll} = 1 - \exp(-\Delta s n_g \sigma(E_0)) \tag{2.52}$$

with Δs the distance travelled in Δt, n_g the neutral gas particle density and $\sigma(E_0)$ the collision cross section. A random number RN_1 is generated and compared with p_{coll}. If $RN_1 > p_{coll}$ then no collision occurs and the electron simply continues its orbit. Otherwise, an interaction occurs. In the model, only interactions with argon atoms are considered, interactions with other species are neglected (see section I.1.2.1). This means that σ is defined as:

$$\sigma(E_0) = \sigma_{ion}(E_0) + \sigma_{exc}(E_0) + \sigma_{ela}(E_0) \tag{2.53}$$

The cross sections for the considered processes are plotted in Fig. I.1.4. To determine which type of interaction occurs, the fractional probabilities for the collisions are calculated. They are defined as: $p_{ion} = \sigma_{ion}/\sigma$, $p_{exc} = \sigma_{exc}/\sigma$ and $p_{ela} = \sigma_{ela}/\sigma$. The sum of these fractional probabilities is equal to one and the interval [0,1] is divided in intervals with lengths corresponding to the fractional probabilities. This is a typical procedure in MC modelling [Bogaerts96]. A second random number RN_2 is generated and the interval into which RN_2 falls, determines the type of interaction. In case of an interaction, the electron velocity vector needs to be adjusted.

First, its magnitude, i.e. the electron energy, is adjusted. In case of elastic collision the energy transfer is very small (see eq. (1.4) in section I.1.2.1.1) and can be neglected. For an excitation, the electron energy is reduced with 12 eV. For an ionisation, both the energies of the original electron and of the ejected electron need to be determined. The average energy E_{eject} of the ejected electrons is taken 10 eV (section I.1.2.1.2A). A Gaussian distribution with width $\sigma = 2$ eV was constructed around the average E_{eject}. A random number RN_3 is generated

to determine E_{eject}. Given the ionisation energy E_{ion} of an argon atom, the electron energy E after an ionisation is given by:

$$E = E_0 - E_{ion} - E_{eject} \tag{2.54}$$

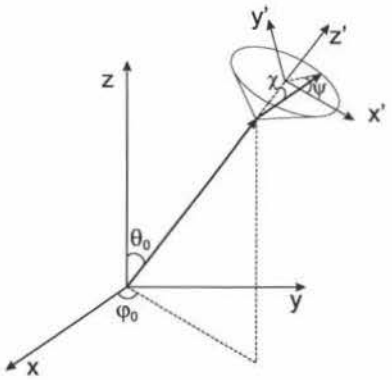

Fig. 2.13. Sketch defining the angles θ_0, the angle with the z-axis, and φ_0, the angle with the x-axis. Also the axial χ and azimuthal ψ scattering angles are indicated. To indicate all these angles both the laboratory frame of reference (xyz) and the particle scattering frame of reference ($x'y'z'$) are shown.

Second, the orientation of the velocity vector needs to be adjusted. Before interaction, this orientation is defined by θ_0, the angle with the z-axis, and φ_0, the angle with the x-axis in the xy-plane (Fig. 2.13). Because of the interaction, these angles are transformed into θ and φ. The relation between (θ_0, φ_0) and (θ, φ) is given by [Bogaerts96]:

$$\begin{bmatrix} \sin(\theta)\cos(\varphi) \\ \sin(\theta)\sin(\varphi) \\ \cos(\theta) \end{bmatrix} = \begin{bmatrix} \cos(\theta_0)\cos(\varphi_0) & -\sin(\varphi_0) & \sin(\theta_0)\cos(\varphi_0) \\ \cos(\theta_0)\sin(\varphi_0) & \cos(\varphi_0) & \sin(\theta_0)\sin(\varphi_0) \\ -\sin(\theta_0) & 0 & \cos(\theta_0) \end{bmatrix} \times \begin{bmatrix} \sin(\chi)\cos(\psi) \\ \sin(\chi)\sin(\psi) \\ \cos(\psi) \end{bmatrix} \tag{2.55}$$

with χ and ψ the axial and azimuthal angle of scattering, respectively (Fig. 2.13). To determine χ and ψ two new random numbers (RN_4 and RN_5) are generated. The azimuthal angle ψ is given by:

$$\psi = 2\pi RN_4 \tag{2.56}$$

For the axial scattering angle χ, different models can be found in magnetron simulations. We implemented the expression proposed by Okhrimovskyy (eq. (1.6) in section I.1.2.1.1A):

$$\chi = \arccos\left[1 - \frac{2RN_5}{1 + 8\varepsilon(1 - RN_5)}\right] \tag{2.57}$$

with $\varepsilon = E_0/E_u$ with E_u the atomic unit of energy ($E_u = 27.21$ eV). This is referred to as Okhrimovskyy scattering. As mentioned in section I.1.2.1.1A, this should be the most accurate model. However, to investigate the influence of the model for the scattering angle on the simulation results, three other models have also been investigated. Surendra scattering (eq. (1.5) in section I.1.2.1.1A), although physically incorrect according to [Okhrimovskyy02], was implemented as it is commonly used in MD simulations. In this case χ is given by [Surendra90]:

$$\chi = 2\arcsin\sqrt{\frac{\exp[RN_5 \ln(1+E_0)]-1}{E_0}} \tag{2.58}$$

In Fig. 2.14 the scattering angle χ is plotted as a function of the random number for E_0 = 100, 200 and 400 eV. Although both models clearly exhibit the same trend, eq. (2.58) gives consistently higher values for χ. Furthermore, also forward scattering and isotropic scattering were implemented. For the first $\chi = 0$ by definition, in the latter χ is determined by:

$$\chi = \arccos[1-2RN_5] \tag{2.59}$$

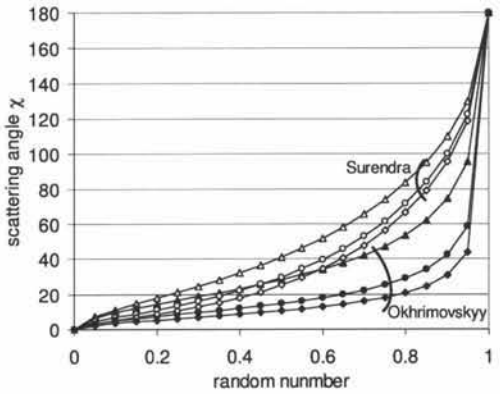

Fig. 2.14. The scattering angle χ as a function of the random number for Okhrimovskyy (closed symbols) and Surendra scattering (open symbols) at three different electron energies: 100 (triangles), 200 (circles) and 400 eV (diamonds).

After the calculation of the new velocity vector, the retracing of the electron orbit is continued. The electrons were followed during 2 μs or until their energy dropped below E_{th}, whichever occurred first. During the simulation the position of the orbit, the ionisations, the excitations and the elastic collisions are stored. Moreover, when SI occurred, the position and energy of the ejected electron were retained. When the calculation for the original electron was finished, the calculation started for the first retained electron. The magnitude of its initial velocity vector is determined by E_{eject} (see above), the orientation of it was chosen randomly. Again, the ionisations, excitations, elastic collisions and electron orbits were recorded together with the ionisations in the cathode sheath. For all the electrons generated in the cathode sheath (and the electrons generated in the cathode sheath of those electrons and so on) the ionisation was determined. This way, the total number of ions $n_{ion,tot}$ generated by a single SE emitted at the target can be deduced. From this, the multiplication factor m (eq. (2.45)) can be calculated :

$$m = \frac{n_{ion,tot}}{n_{ion}} \tag{2.60}$$

with n_{ion} defined by eq. (2.9). Hence, this allows verifying eq. (2.17) (section 2.3.3) which gives the extra energy contribution because of SI. The comparison of the results obtained with the MC model and the analytical model for both the multiplication factor m and for the ionisation distribution is discussed in section 2.6.3.

2.6 Results and discussion

For the results presented here the magnetron configuration as described in the beginning of section 1.3 is used. Unless mentioned otherwise, the discharge voltage V_d was taken 440 V and the cathode sheath thickness d_E 1.6 mm. The initial energy E_{init} of the SE is set to 0 eV, as we are not concerned with the recapture of the emitted SE in this section. For the *A*nalytical *I*onisation *M*odel (AIM), SE are emitted from $x = -14.75$ mm to $x = -0.25$ mm per 0.5 mm. For the *MC I*onisation *M*odel (MIM), only $x = -12.25, -9.25, \ldots, -0.25$ mm per 3.0 mm are considered because emission from all x-positions would require a too long calculation time. From each of these start positions 1000 electrons are emitted. The time step Δt for solving the Lorentz equation was set to 20 ps. Also the generated HEE^{SI} are included. The calculation can be limited to one side of the x-axis because the geometry is symmetric (Fig. 1.2b). These settings, together with Okhrimovskyy scattering for the MIM, are referred to as the "*standard settings*".

2.6.1 Determination of W and f_{ion}

	n_{MC}	f_{ion}(%)	f_{exc}(%)	f_{ela}(%)	W (eV)	n	n_{MC}/n
reference situation	48.2	29.7	7.9	62.4	30.7	47.1	1.02
influence of discharge voltage (standard V_d=440V)							
V_d=320V	37.2	27.6	7.9	64.5	31.2	33.8	1.10
V_d=560V	58.9	31.0	8.0	61.0	30.7	60.4	0.97
influence of the magnetic field (standard B_{max}=600G)							
B_{max}=400G	47.8	30.5	7.8	61.7	30.2	47.1	1.01
B_{max}=800G	48.0	28.6	7.7	63.7	32.1	47.1	1.02
influence of gas pressure (standard p=0.5Pa)							
p=0.1Pa	45.4	29.4	7.9	62.8	33.0	47.1	0.96
p=2Pa	48.7	29.9	7.8	62.3	30.3	47.1	1.03
influence of cathode sheath (standard d_E=1.6mm)							
d_E=0.8mm	42.8	30.3	7.9	61.8	33.9	47.1	0.91
d_E=2.4mm	51.6	28.0	7.7	64.2	30.5	47.1	1.09

Table 2.1 Overview of the results obtained with the MIM for different situations. Listed are the total number of interactions obtained from the MC calculation (n_{MC}), the relative number of ionisations (f_{ion}), excitations (f_{exc}) and elastic collisions (f_{ela}), the ratio n_{ion}/n and the effective ionisation energy W. The last two columns give the n-values obtained from eq. (2.11) and the ratios n_{MC}/n.

For the AIM the average total number of interactions n of the HEE^{ta} is needed to determine the average transfer matrix T_{avg} (section 2.3.2). This n is given by eq. (2.11), which requires the effective ionisation energy W and the fraction of ionisations f_{ion} in the total number of interactions. To determine W and f_{ion} the MIM can be used but, given the definition of n, only the contribution of the original HEE^{ta} needs to be considered. The gas pressure p is chosen 0.5 Pa. The result obtained at this pressure using the standard settings (except for the number of retraced SE which is 500 instead of 1000) is referred to as the *reference situation* in this section. W and f_{ion} are determined for different discharge voltages, pressures, magnetic field strengths and cathode sheath thicknesses. The results are listed in Table 2.1. First of all, the average total number of interactions n_{MC} is listed. This average number represents the same physical quantity as n defined in eq. (2.11) but the index MC is used to indicate that the value is calculated using the MIM. The table lists also the relative share of the ionisations f_{ion}, excitations f_{exc} and elastic collisions f_{ela} together with the effective ionisation energy W. As only ionisations and excitations are taken into account as energy dissipating collisions, W is determined from:

$$W = \frac{NV_d}{n_{ion,MC}} \tag{2.61}$$

with N the total number of electrons emitted from the target and $n_{ion,MC}$ the total number of ions generated by those electrons. The results for W agree very well with the typical value of 30 eV [Lieberman94, Thornton78a]. Given the results listed in the table, we set $W = 30$ eV and $f_{ion} = 0.30$. Using these values, n is calculated using eq. (2.11). The resulting n-value is also listed in the table, together with n_{MC}/n. Although the actual values of both W and f_{ion} vary for the different conditions, the fixed values chosen for them allow calculating n within an accuracy of 10% which is considered sufficient for the AIM.

2.6.2 AIM: example of the different arch types

In this part, examples of the arches and of the average transfer matrices obtained with the AIM using the standard settings (as defined in the beginning of section 2.6) are shown. Fig. 2.15 shows the different types of arches that can occur. The left column shows arches corresponding with the original HEE^{ta}: parts *a* through *c* are examples of an $A_{K,i}$ (thick individual sheath), $A_{T,i}$ (transition region) and $A_{N,i}$ (thin individual sheath), respectively. The right column shows arches corresponding with HEE^{SI}: parts *d* through *f* are examples of an $A^{SI}_{K,i}$ (thick individual sheath), $A^{SI}_{T,i}$ (transition region) and $A^{SI}_{N,i}$ (thin individual sheath), respectively. For each arch, the values $A_i(x, z)$ are rescaled such that the maximum value is equal to one.

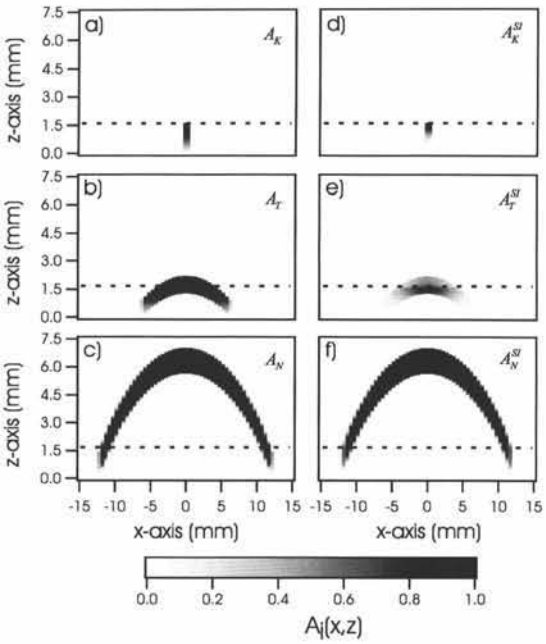

Fig. 2.15. Example of the different arch types occurring in the AIM. The left column shows the arches for the HEE^{ta} starting at x = -0.25 (*a*) , -6.25 (*b*) and -12.25 (*c*). The right column shows the arches for the HEE^{SI} for x = -0.25 (*d*), -6.25 (*e*) and -12.25 (*f*). The arches illustrate the situation of an individual thick sheath (*a* and *d*) , a transition region (*b* and *e*) and an individual thin sheath (*c* and *f*). The dashed line indicates the cathode sheath edge.

The average transfer matrices T_{avg} and T^{SI}_{avg} are shown in Fig. 2.16. The sum of each column of T_{avg} (and of T^{SI}_{avg}) is per definition equal to one. For T_{avg}, the concentration along the two diagonals is clearly visible for arches at the edge of the race-track ($|x|>8$). This is due

to the element $G_j(z_i)$, which reaches its maximum value when i and j fulfil the condition $|x_i| = |x_j|$ (the absolute x-values are needed because of the symmetry). This means that HEE in arches at the edge of the race-track tend to remain close to the original arch in spite of the interaction with the discharge gas. This does not hold for HEE in arches close to the centre of the race-track ($|x|<5$). In this case the HEE are transferred to arches with larger $|x|$, around $|x| = 6$.

The average matrix T_{avg}^{SI} gives the probability that SI occurs when a HEE interacts with the discharge gas. For arches at the edge of the race-track, this probability is the highest for an electron staying in the arch or for an electron transferring to a neighbouring arch. For arches at the centre of the race-track, this probability is especially high for transfer to arches around $|x| = 6$. Note that the elements of T_{avg}^{SI} only give an indication of the probability for SI to occur but not the energy contribution of such an SI. The latter is expressed by the multiplication factor m.

In principle, one could calculate the ionisation distribution with the MIM and "overlay" the result with the arch-shaped regions to see in which arches the ionisation distribution occurs. Such a comparison of the average transfer matrix obtained with the AIM and with the MIM could allow improving the AIM. However, this option was not followed in this work.

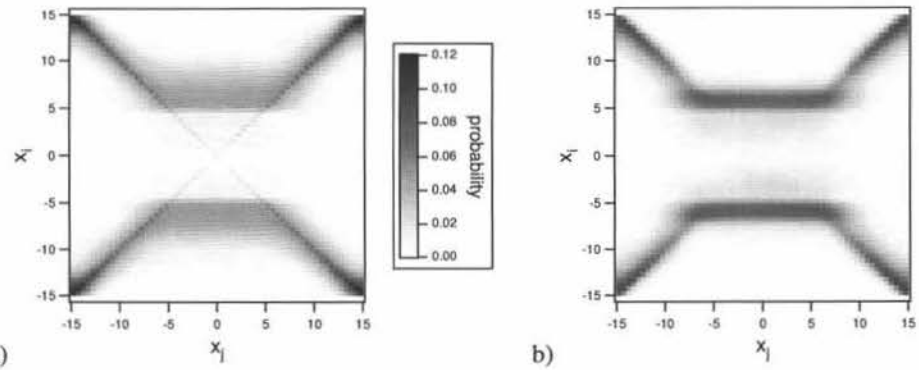

Fig. 2.16. The average transfer matrices T_{avg} (*a*) and T_{avg}^{SI} (*b*) calculated using the standard settings. The element at row i and column j corresponds with a transfer from arch A_j to A_i.

2.6.3 Multiplication factor *m* and ionisation distribution *I*

In this section the multiplication factor m and the relative ionisation distribution I is discussed for typical MD conditions. This is done for individual electrons, i.e. one electron is emitted at a certain position x_i along the x-axis and m and I are calculated. In the AIM, m is calculated from eq. (2.45), in the MIM from eq. (2.60). In the MIM the relative ionisation distribution along the x- and z-axis is directly obtained as all the ionisation events are recorded. In the AIM, I is obtained from H, which is determined using eq. (2.28). Solving the equation requires the transfer matrices T_{avg} and T_{avg}^{SI}, the arches A_i and A_i^{SI}, and the emission profile r. Since we discuss the ionisation by an individual SE, r_k is a Dirac pulse :

$$r_k = \begin{cases} 0 & k \neq i \\ 1 & k = i \end{cases} \qquad (2.62)$$

with i the index along the x-axis of the starting position of the SE under investigation.

Using the standard settings at 2 Pa, the ionisation distribution I (section 2.6.3.1) and the importance of SI (section 2.6.3.2) are discussed. Then, the influence of the gas pressure (section 2.6.3.3), the magnetic field (section 2.6.3.4) and the combination of the discharge voltage and the sheath thickness (section 2.6.3.5) on both m and I is treated.

2.6.3.1 Ionisation distribution

In the AIM the ionisation distribution is based on the occupation profile u of the HEE^{ta} and u^{SI} of the HEE^{SI}. For $x_0 = -6.25$ these occupation profiles are shown in Fig. 2.17. As long as the HEE do not interact, u^0 is equal to the emission profile (eq. (2.19)), which is a Dirac pulse in this case (eq. (2.62)). $u^{0,SI}$ is identical to zero before the first interaction as no SI occurred yet. After the first interaction, the occupation profile u^1 (eq. (2.20)) is strongly peaked around $|x_0|$. As the geometry is symmetric, the arches corresponding with -6.25 and 6.25 are identical, and thus, also the probabilities to find the HEE in them are the same. Because of the interaction with the discharge gas, SI can occur and $u^{1,SI}$ is no longer zero. The occupation profiles, obtained taking into account all interactions, are also shown. Compared with u, the profile of u^{SI} is more concentrated around $|x| = 6$.

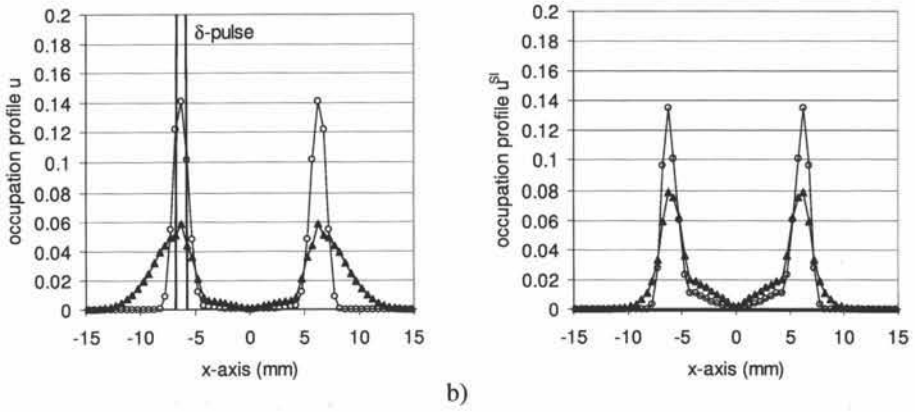

Fig. 2.17. Evolution of the occupation profiles u of the HEE^{ta} (a) and u^{SI} of the HEE^{SI} (b) before interaction with the discharge gas (—), after the first interaction (○) and averaged over all interactions (▲).

The occupation profiles combined with the arches allow determining the HEE (eq. (2.28)) and consequently also the ionisation distribution. The results for the relative ionisation distribution I along both the z-axis and the x-axis for $x = -6.25$ is shown in Fig. 2.18. Also the results for $x = -0.25$ and -12.25 are plotted. For all situations shown, the agreement between the AIM and MIM along the z-axis is excellent. Along the x-axis the AIM does not reproduce the sharp peak of the SE emitted at $x = -0.25$ completely. For an SE emitted from $|x| = -12.25$ I is practically constant in the region $|x|<10$.

Interestingly, compared with the ionisation distribution from $x = -12.25$, the ionisation distributions from $x = -0.25$ and -6.25 are quite similar. The main difference between the latter two is the stronger peak along the x-axis for $x = -0.25$. The distribution of $x = -3.75$ (not shown) is only for $|x|<1$ mm different from the one of $x = -0.25$. It follows that the ionisation distribution is rather independent of x for small $|x|$ (<4 mm). This explains why MC simulations that neglect recapture can nevertheless reproduce realistic relative erosion profiles, as discussed in section 3.3.2.

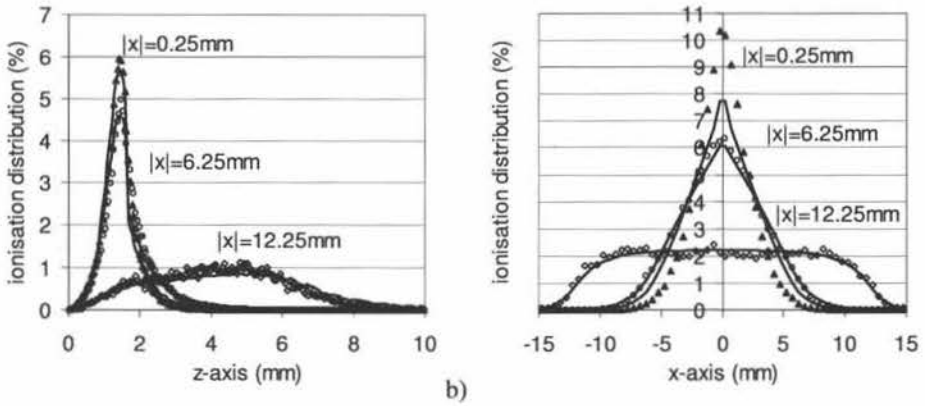

Fig. 2.18. Relative ionisation distribution along the z-axis (*a*) and the x-axis (*b*) for an SE emitted at x = -0.25 (▲), x = -6.25 (○) and x = -12.25 (◇) for the standard settings. The solid lines represent the AIM results, the markers represent the MIM results.

2.6.3.2 Importance of sheath ionisation

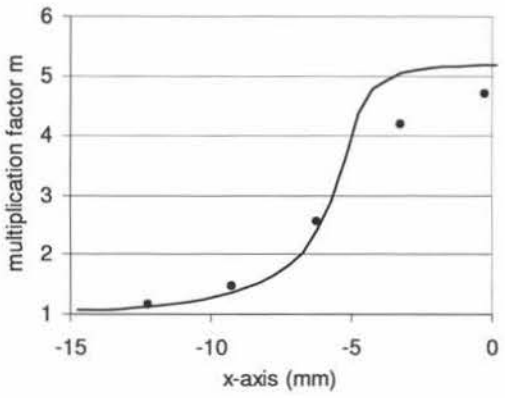

Fig. 2.19. The multiplication factor m along the x-axis: the solid line is the AIM result, the dots the MIM results. The AIM overestimates m-values for $|x| < 5$ mm, especially around $|x| = 3$ mm. The standard settings were used at 2 Pa.

In Fig. 2.19 the results obtained for the multiplication factor m are shown: the full line represents the AIM, the markers the MIM results. For large $|x|$, m is close to one as the SE emitted at such positions (e.g. x_3 in Fig. 2.2) have an individual thin sheath and thus a very low probability to generate an electron-ion pair in the cathode sheath. The smaller $|x|$, the larger m becomes. It reaches a value of 4.7 at $|x| = 0.25$. The high m-value could be expected for these x-values as this corresponds with the situation of x_1 in Fig. 2.2. Hence, an electron emitted at the centre of the race-track contributes an energy to the discharge that is more than four times as high as its maximum energy $|eV_d|$. Comparison of the AIM and MIM results indicates that the AIM overestimates m for $|x| < 5$ mm, especially in the region around $|x| = 3$.

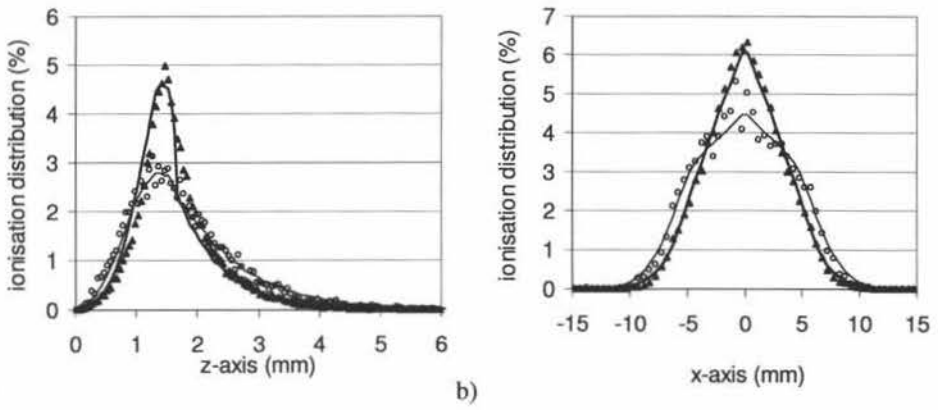

Fig. 2.20. Influence of sheath ionisation (SI) on the relative ionisation distribution for x = -6.25 mm. The ionisation distribution shown along the z-axis (*a*) and x-axis (*b*) is obtained without (○) and with (▲) taking into account SI in the MIM and without (—) and with (▬) SI in the AIM. Except for accounting for SI or not, the standard settings are used at 2 Pa.

The results for the relative ionisation distribution I along both the z-axis and the x-axis for x = -6.25 are plotted in Fig. 2.20. Both the results with and without taking into account the HEE^{SI} are plotted. With the contribution of these HEE^{SI}, I is much more peaked around z_{dE} in the direction along the z-axis. Along the x-axis, I is more peaked around $x = 0$. This could be expected as the HEE^{SI} are generated mostly close to the edge of the cathode sheath and they scatter much less than the original HEE.

2.6.3.3 Influence of the gas pressure

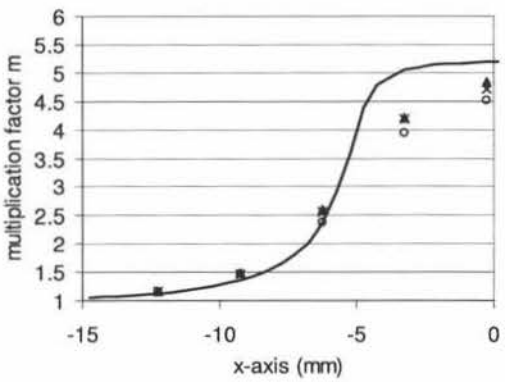

Fig. 2.21. The multiplication factor m along the x-axis obtained with the MIM at different pressures: 0.5 Pa (○), 2 Pa (×) and 4 Pa (▲). The result from the AIM is also shown (solid line). The standard settings were used.

An interesting difference between the AIM and the MIM is the role of the gas pressure p. For the MIM, the introduction of the gas pressure is obligatory: without gas pressure it is impossible to determine the collision probabilities p_{coll}. In the AIM, m is based on the transfer matrices and on the arches (see eqs. (2.16) and (2.17)). As the construction of both does not depend on the pressure, the values calculated for m are pressure independent. Similarly, the ionisation distribution I is calculated without the need for the gas pressure in the AIM. To check whether this is realistic, the MIM was run using the standard settings at different

pressures. The results (Fig. 2.21 and Fig. 2.22) show that m and I are indeed practically identical, regardless whether the pressure is 0.5, 2 or 4 Pa.

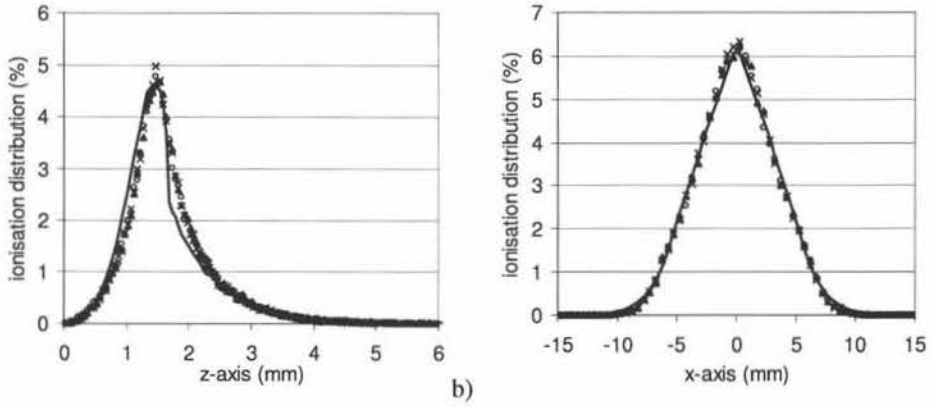

Fig. 2.22. The relative ionisation distribution I along the z-axis (a) and the x-axis (b) for an SE emitted at x = -6.25 mm obtained with the MIM at different pressures: 0.5Pa (○), 2Pa (×) and 4Pa (▲). The result from the AIM is also shown (solid line). The standard settings were used.

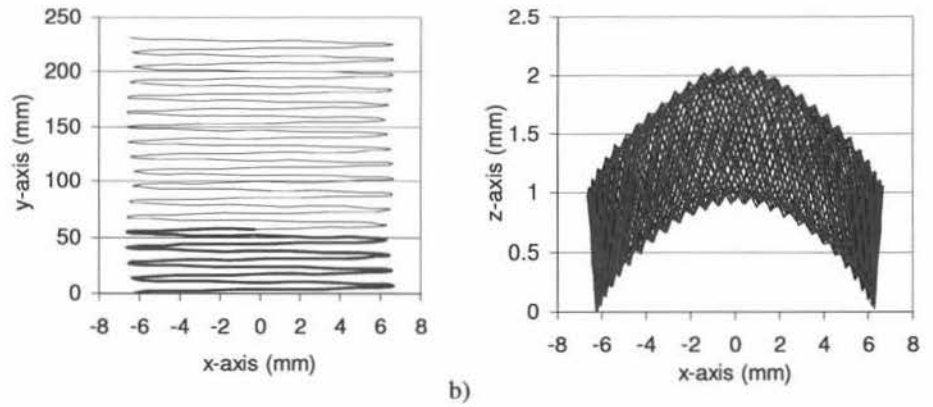

Fig. 2.23. Projection in the xy-plane (a) and xz-plane (b) of the collisionless orbit of a HEE emitted at x = -6.25 mm. The electron orbit is retraced during 1.5×10^{-8} s (▬) and 6×10^{-8} s (—). In both cases, the area occupied by the orbit in the xz-plane is practically the same. The standard settings are used.

To understand this insensitivity to the gas pressure, we consider Fig. 2.23 where an electron orbit is retraced up to 1.5×10^{-8} s and 6×10^{-8} s. We assume that these time intervals represent the time until the first interaction with the discharge gas occurs at 2.0 and 0.5 Pa, respectively. From the projection in the xy-plane, it follows that the electron drifted much further in the y-direction at the lower pressure. However, in the xz-plane, the situation is different. The electron moves back and forth along the magnetic field. Hence, the area to which its orbit is confined is practically the same after both time intervals. This explains why the ionisation distributions along the x- and z-axis are pressure independent.

Because of the pressure independence, a pressure of 2 Pa can be chosen for the MIM: although this is from practical viewpoint a very high pressure, it allows much faster

calculation than a more realistic pressure like 0.5 Pa. The cause of the pressure behaviour of the MD will be discussed in section 4.3.2.

2.6.3.4 Influence of the magnetic field

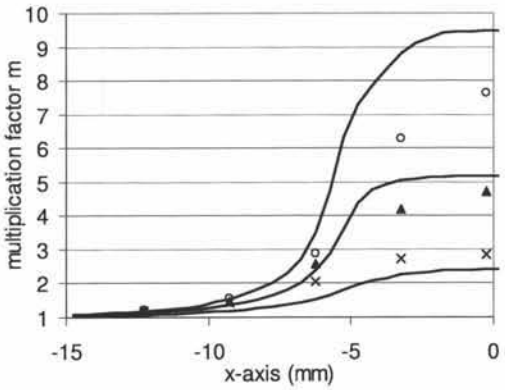

Fig. 2.24. The multiplication factor m along the x-axis obtained with the MIM for different magnetic field strengths: 800 G (○), 600 G (▲) and 400 G (×). The corresponding result from the AIM is each time indicated by the solid line. Except for the magnetic field strength, the standard settings are used at 2 Pa.

Fig. 2.24 and Fig. 2.25 show the influence of the magnetic field on the multiplication factor m and on the ionisation distribution I, respectively. Except for the magnetic field strength, the standard settings are applied at 2 Pa. By adjusting the magnet strength, the maximum horizontal magnetic field strength B_{max} at the target was varied from 400 to 800 G. The stronger the magnetic field, the stronger the electrons are bound to the magnetic field lines. Consequently, the ionisation is more localised. The multiplication factor m increases with increasing magnetic field as relatively more ionisation takes place within the cathode sheath.

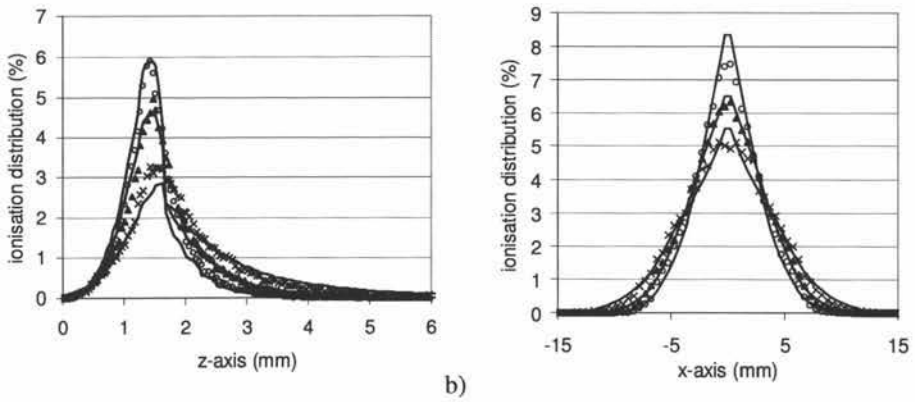

Fig. 2.25. The relative ionisation distribution I along the z-axis (a) and the x-axis (b) for a SE emitted at x=-6.25 mm obtained with the MIM for different magnetic field strengths: 800 G (○), 600 G (▲) and 400 G (×). The corresponding result from the AIM is each time indicated by the solid line. Except for the magnetic field strength, the standard settings are used at 2 Pa.

For the strongest magnetic field, the AIM clearly overestimates the peak in m for small |x|. For I the agreement between the AIM and MIM is good, both along the z- and x-axis.

However, for the weakest magnetic field the distribution along the z-axis starts to deviate. This is no surprise as one of the assumptions needed for the AIM is a sufficiently strong magnetic field.

2.6.3.5 Influence of the discharge voltage and the cathode sheath thickness

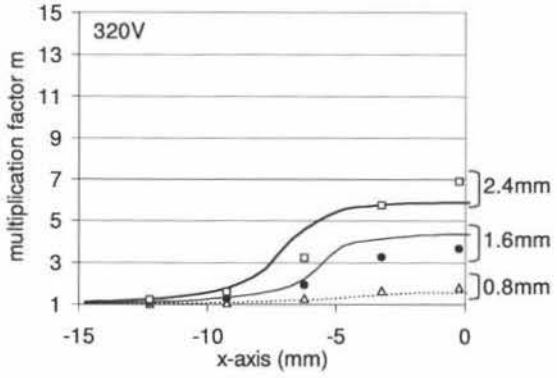

a)

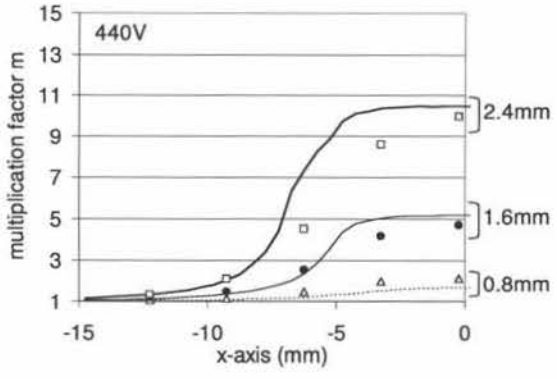

b)

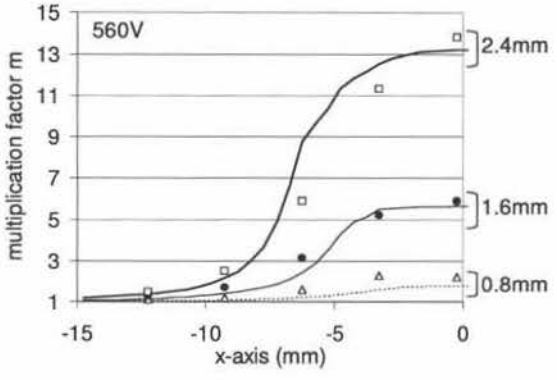

c)

Fig. 2.26. Results for m for different combinations of the cathode sheath thickness and the discharge voltage. The latter is taken equal to 320 (*a*), 440 (*b*) and 560 V (*c*). MIM results are represented with markers, the AIM results are represented with lines. The cathode sheath thickness corresponding with the different curves is indicated on the figure. Except for the values of V_d and d_E, the standard settings are used at 2 Pa.

In this part, the influence of the discharge voltage V_d and the cathode sheath thickness d_E is investigated: the results for m obtained for different d_E (0.8, 1.6 and 2.4 mm) are plotted in Fig. 2.26 for V_d equal to 320 (*a*), 440 (*b*) and 560 V (*c*). The strongest trend in these results is caused by the sheath thickness: the larger d_E, the larger m. The results clearly show that the AIM is able of reproducing the dependence of m on V_d and d_E.

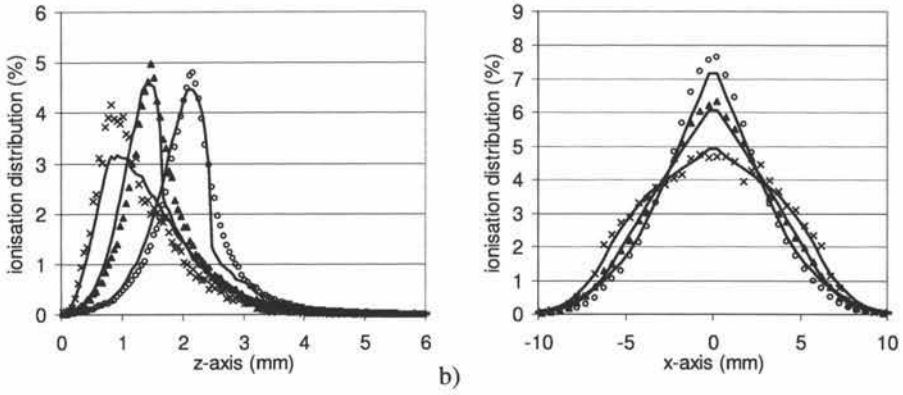

Fig. 2.27. The relative ionisation distribution along the *z*-axis (*a*) and the *x*-axis (*b*) for an SE emitted at x = -6.25 mm obtained with the MIM for d_E = 2.4 mm and V_d = 560 V (○), d_E = 1.6 mm and V_d = 440 V (▲) and d_E = 0.8 mm and V_d = 320 V (×). The corresponding result from the AIM is each time indicated by the solid line. Except for the values for V_d and d_E, the standard settings are used at 2 Pa.

The relative ionisation distribution along the *z*-axis peaks at the end of the sheath edge, regardless the value of d_E (Fig. 2.27), in agreement with the results from other self-consistent magnetron simulations (Table I.1.2 in section I.1.3.3.5B). For the situation d_E = 0.8 mm and V_d = 320 V the AIM does not reproduce this peak very well. As this shortcoming also occurs at other discharge voltages for small d_E, this must be inherent to the model. Hence, the AIM will not perform very well for situations with d_E below 0.8 mm.

2.6.4 MIM: Influence of the scattering angle

When an electron interacts with the discharge gas, its velocity vector needs to be adapted. For inelastic collisions, its energy must be reduced. Regardless the type of interaction, the direction of its velocity vector needs to be adjusted based on the scattering angles χ and ψ (section 2.5). In this part, the influence of the model for the axial scattering angle χ on the MIM results for the multiplication factor m and on the ionisation distribution I is investigated. Although according to [Okhrimovskyy02] the only correct expression is eq. (2.57), the influence of the scattering angle is investigated as in MD simulations different models are used: Surendra scattering is used most often (e.g. in [Nanbu97, Kondo99a, Kondo01, Shidoji99a]) but also isotropic scattering is sometimes assumed (e.g. in [Shidoji00]).

The results shown here are obtained with a gas pressure of 2 Pa and, except for the choice of the χ-model, the standard settings as defined at the beginning of section 2.6. The results for m are shown in Fig. 2.28. Keeping in mind that the scattering angle is consistently larger for Surendra scattering compared with Okhrimovskyy scattering (Fig. 2.14), there is a clear trend: the larger the scattering angle, the smaller m. Hence, as the energy loss is in all four cases the same, the larger the scattering angle, the less interactions occur in the cathode sheath. To illustrate this, the ionisation distribution for an SE emitted at x = -0.25 mm is

shown along the z-axis (Fig. 2.29a). For forward scattering practically all ionisation occurs in the cathode sheath, which explains the high m. In this case the driving force for pushing the electron out of the cathode sheath is purely energetic. Because of the energy loss, the electron cannot penetrate completely in the sheath anymore and the electron should be at the end of the cathode sheath when its energy is close to the ionisation threshold energy.

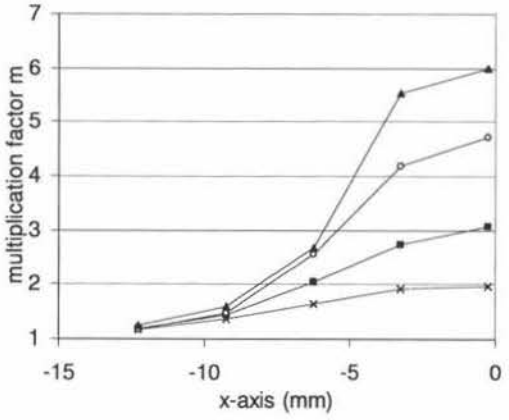

Fig. 2.28. The multiplication factor m along the x-axis showing the influence of the model to determine the scattering angle χ. The results correspond with χ determined assuming forward scattering (▲), Okhrimovskyy scattering (○), Surendra scattering (■) and isotropic scattering (×).

The results show that if the scattering angle is not by definition equal to zero, it contributes to push the electrons out of the cathode sheath because m, i.e. the fraction of the ionisation in the cathode sheath, decreases with increasing average scattering angle. Also the distribution along the x-axis is influenced by the model for the scattering angle (Fig. 2.29b): the smaller the average χ, the narrower and sharper the distribution.

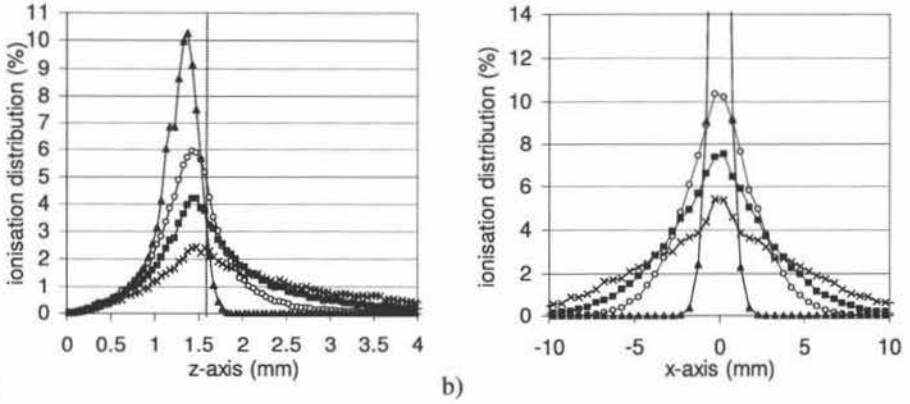

Fig. 2.29. Ionisation distribution I along the z-axis (a) and the x-axis (b) for an SE emitted at $x = -0.25$ mm showing the influence of the scattering angle χ: forward scattering (▲), Okhrimovskyy scattering (○), Surendra scattering (■) and isotropic scattering (×). The dashed line in part a indicates the end of the cathode sheath. The distribution along the x-axis reaches a peak of nearly 40% for forward scattering.

2.6.5 MIM: Comparison of relative ionisation and excitation distribution

In this part, the relative distribution of the ionisation and excitation are compared using the MIM for the standard settings at 2 Pa. The results are shown in Fig. 2.30: the excitation and ionisation distributions are very similar but the excitation profile is slightly more peaked, both along the z- and x-axis. Also the spatial distribution of the electron positions during orbit is shown: along the x-axis this distribution is practically identical to the excitation distribution, along the z-axis this distribution peaks closer to the target. This indicates that the assumption that the HEE and ionisation distribution are proportional in the AIM is not completely correct. However, as the AIM is an approximative model, this small difference can be neglected.

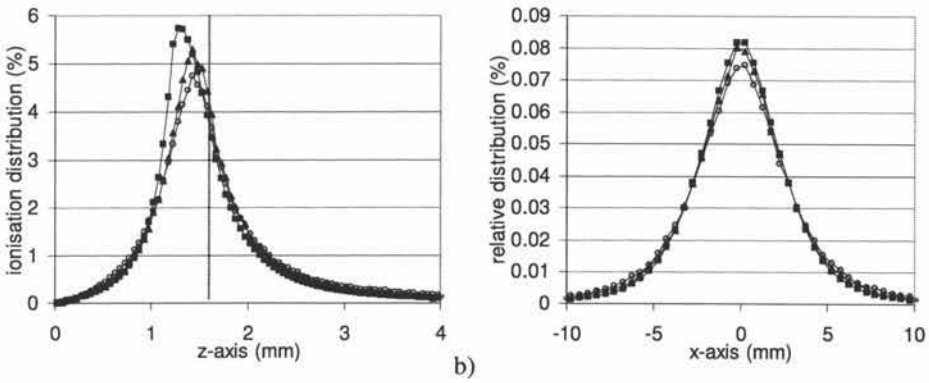

Fig. 2.30. Distribution of the ionisations (○) and excitations (▲) along the z-axis (*a*) and the x-axis (*b*). These relative distributions are very similar but the excitation profile is slightly more peaked, both along the z- and x-axis. Also the distribution of the electron positions is shown (■). This latter distribution is slightly more peaked and the maximum is closer to the target.

2.7 Conclusions

In this chapter the analytical ionisation model (AIM) for the determination of the ionisation in a d.c. magnetron discharge is explained. The model is limited to a two-dimensional geometry and only considers the high energy electrons (HEE), the ones that can cause ionisation. The AIM is based on splitting the discharge area in arch-shaped regions, which are mainly determined by the magnetic field lines. The HEE interactions with the discharge gas are modelled by considering the probabilities for the HEE to transfer from one arch to another. Sheath ionisation (SI), the generation of an ion-electron pair in the cathode sheath, is incorporated in the AIM as the ejected electron also adds to the ionisation in the discharge when SI occurs close enough to the target. The extra energy contribution to the discharge because of SI is characterised by the multiplication factor m.

The AIM was applied to simulate the ionisation distribution and the multiplication factor m of individual secondary electrons emitted from the target. These results were also obtained using a numerical Monte Carlo ionisation model (MIM) in order to verify the AIM. Comparing the results obtained with the AIM and the MIM, show that the AIM gives good results and can replace the MIM within its validity range. Moreover, these results help to understand the electron behaviour in the magnetron discharge.

First, we found that the relative ionisation distributions of electrons emitted close to the centre of target are quite similar, regardless of their exact starting position. This implies

that for a fairly accurate simulation of the relative ionisation distribution or erosion profile, the exact emission profile of the SE at the target is not crucial.

Second, the values for the multiplication factors were calculated: in the centre of the race-track m almost equal to 5 is found for typical MD conditions. Because of SI, the energy contribution of a secondary electron to the discharge is not $|eV_d|$ but $m|eV_d|$. Given the values of m, it is clear that the difference is relevant and that SI cannot be neglected in magnetron discharges, in spite of the narrow cathode sheath.

Third, the AIM did not require the gas pressure to determine the ionisation distribution or the multiplication factor. This was confirmed by the fact that the pressure had practically no influence on the ionisation distribution in the MIM. Hence, the pressure does not directly influence the ionisation distribution.

Fourth, the correct model for the scattering angle χ is obligatory as χ influences the ionisation distribution: the larger χ, the more spread out the ionisation. As such, χ has a strong influence on the multiplication factor m. This shows the need to use Okhrimovskyy scattering.

In the next chapter, the above gained insights will help to develop a self-consistent model for the magnetron discharge. Given the good agreement between the AIM and the MIM, the AIM will be used in the next chapter to simulate the ionisation distribution in that model. This has the main advantage that the model will be much faster as when a purely numerical approach (e.g. a Monte Carlo method) is used to determine the ionisation distribution

3 SELF-CONSISTENT MODEL

3.1 Introduction

In the previous chapter, the necessary concepts and equations were deduced to determine the ionisation caused by a single secondary electron (SE) emitted from the target. Thereto, it was assumed that the potential distribution, characterised by the discharge voltage V_d and the cathode sheath thickness d_E were known. Of course, in reality d_E is unknown: it is determined by the charge distribution in the discharge. This in turn is the result of the interplay between externally applied parameters (e.g. gas pressure, electrical power, magnetic field, ...) and the magnetron geometry (e.g. anode position, target size,...). In a self-consistent plasma simulation, the charge distribution is explicitly obtained from the simulation results. Unfortunately, its determination is a very time consuming part of plasma simulations in general, and thus, also of magnetron discharge (MD) simulations. Therefore, the charge distribution, i.e. the potential distribution, in the plasma is often assumed to be known a priori. In this case the charge distribution is not influenced by the simulation results and the simulation is not self-consistent. Whether a simulation is self-consistent or not is an important criterion to categorise different simulation approaches (section I.2.2).

In MD modelling, the term self-consistent is used in the sense described above, i.e. the electric field is determined from the charge distribution. Strictly seen, this is only one part, albeit an important one, from a true self-consistent model. Other aspects are e.g. the influence of the plasma on the magnetic field strength because of the electron E×B drift, the influence of target erosion or the influence of the sputtered particles on the discharge. The latter can lead to gas density reduction (section I.1.4.3.4) and to a change in the effective ionisation energy W. Although these influences can become important, especially at higher power inputs and/or high gas pressures, these effects are not (yet) included in self-consistent MD models (see also section I.2.3.4.3).

In this chapter, the analytical ionisation model (AIM) from Chapter 2 for the ionisation by a single SE is transformed into a self-consistent model for the MD. The term "self-consistent" is limited to the potential distribution and does not take into account the other effects mentioned in the previous paragraph. The next section (section 3.2) deals with the transformation of the AIM into a self-consistent model (SCM). In section 2.6 the results obtained with the SCM are discussed, showing its unique capabilities to gain insight into the MD.

3.2 Model

The ions generated in the MD bombard the target. This ion bombardment gives rise to the emission of sputtered particles and of SE. These SE become high energy electrons (HEE) and generate in turn ions, giving rise to further ion bombardment. This way the MD is maintained (see also section I.1.1). The challenge is to put this fairly simple maintaining mechanism into a self-consistent model.

The basic principle of the SCM is shown in Fig. 3.1. The symbol B represents the magnetic field in the area above the target, not just one specific magnetic field strength. Hence, the necessary information about the magnetron geometry is included in this B. As here, and in the subsequent chapters, the same magnetron geometry is used and only the strength of the magnets is changed, it is sufficient to give one specific magnetic field strength to characterise the whole magnetic field. This magnetic field strength is conventionally the

maximum value of the magnetic field component parallel to the target at the target surface. It is referred to in this text as B_{max} (see also section I.1.1).

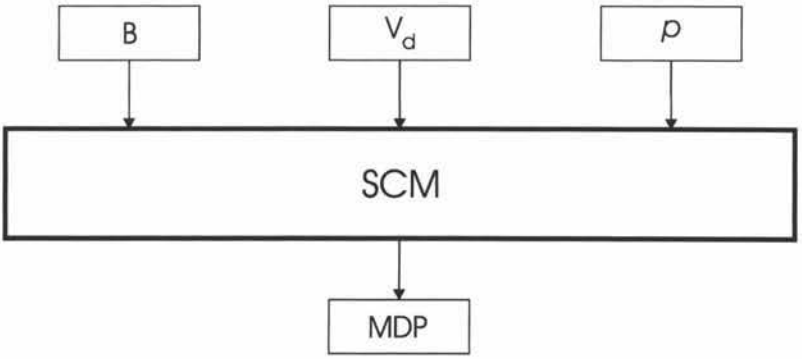

Fig. 3.1 Principle of the self-consistent model (SCM): using the magnetic field B (and system geometry), the discharge voltage V_d and the gas pressure p as input, the SCM should result in the magnetron discharge properties (MDP).

The input of the model consists of the most relevant external parameters, i.e. the magnetic field B, the discharge voltage and the gas pressure. The output of the model should give the magnetron discharge properties (MDP), e.g. the cathode sheath thickness, ionisation distribution or the erosion profile. An important part of the SCM is the determination of the ionisation caused by the HEE, for which the AIM is used. The transformation of the AIM into the SCM is given below, step by step.

The first step is to deduce from a given ionisation distribution I the ion bombardment on the target and the resulting SE emission (section 3.2.1). The second step is to combine the SE emission with the AIM, which allows determination of the steady state emission profile r_{SS} (section 3.2.2). Third, the procedure for r_{SS} is extended to include the effect of recapture of SE (section 3.2.3). Fourth, self-consistency with respect to the potential distribution is introduced (section 3.2.4). At this point, a valid model is obtained. However, from a practical view-point (meaning from the view-point of computational effort), it is more convenient to replace the gas pressure as input parameter by the cathode sheath thickness (section 3.2.5).

3.2.1 Ion bombardment of the target

The ionisation distribution I gives rise to ion bombardment of the target as the electric field ensures the acceleration of the ions towards the target. Given the typical cathode sheath thickness, gas pressure and argon ion cross section, it can be assumed that the ions reach the target without undergoing any collisions (section I.1.3.3.5). As the electric field is perpendicular to the target, the ions reach the target at the same x-value as where they were generated. This way, it is straightforward to deduce the ion bombardment $\mathcal{B}$ on the target, which at position x_i is given by:

$$\mathcal{B}_i = \sum_j I(x_i, z_j) \tag{3.1}$$

Similarly, the relative number $Y_{SP,i}$ of sputtered target atoms at position x_i can be calculated :

$$Y_{SP,i} = \sum_j I(x_i, z_j)\, y(|eV_d - eV(z_j)|) \tag{3.2}$$

with $y(E)$ the ion energy dependent sputter yield (section I.1.2.2.2). From this the erosion profile w can be determined. If we neglect the influence of the erosion groove formation on $Y_{SP,i}$, it follows that $w_i = -Y_{SP,i}$. The data for argon sputtering of aluminium mentioned in [Rossnagel99] were used for y(E).

In the MD, the SE yield γ is independent of the ion energy as for these low ion energies potential SE emission is dominating (section I.2.2.1). Unless otherwise mentioned, γ was set to 0.1. Given γ, the elements r_i of the emission profile are given by :

$$r_i = \sum_j I(x_i, z_j)\gamma = \gamma \mathcal{B}_i \tag{3.3}$$

3.2.2 Deduction of the steady state emission profile r_{SS}

The AIM leads to the relative ionisation distribution I of a SE emitted from the target surface. In the AIM, no electron-electron interactions are considered for the description of the electron motion, i.e. the electrons do not influence each other. Hence, there is no restriction that only one SE should be emitted. Consequently, the AIM allows to determine the ionisation I caused by a random SE emission profile r_0. Using eq. (3.3) a new emission profile r_1 can be obtained from I. In the AIM the emission profile r is considered as an input parameter (Fig.2.7 in section 2.4). However, as can be seen in that figure, the elements r_i of the SE emission profile are not needed to deduce the core parts (i.e. the arches, the transfer matrices and weight factors like h_i and g_i). Hence, another way to look at this is that the r_i *together with* the AIM result in the ionisation distribution I. This view is expressed in Fig. 3.2.

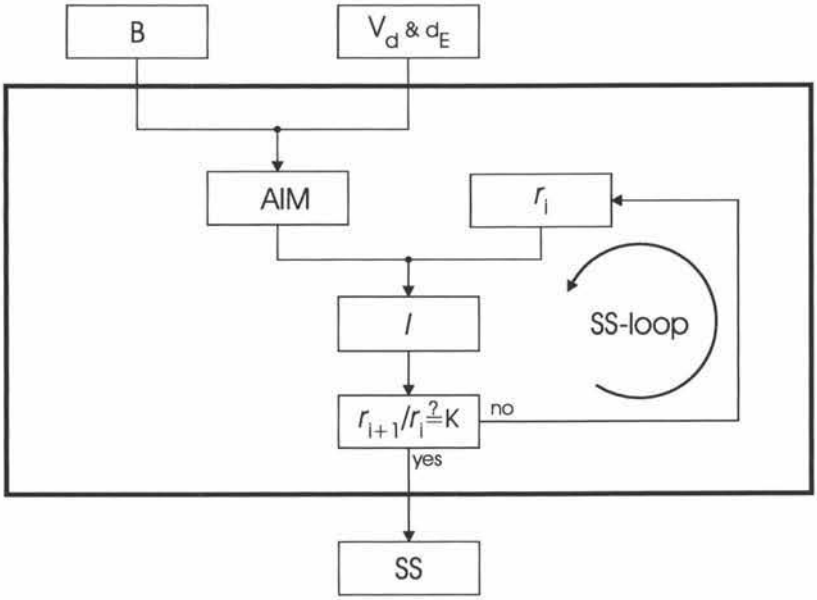

Fig. 3.2 Sketch of the preliminary SCM showing the SS-loop. Iterating through this loop enables to find the steady-state (SS) emission profile.

It is clear that in steady state (SS) the emission profiles r_0 and r_1 should be the same; this profile is referred to as r_{SS}. To find this r_{SS} the procedure that leads from r_0 to r_1 is repeated, each time redefining r_1 as the new r_0. This forms an iteration loop in the model, referred to as the "SS-loop" (Fig. 3.2). Through iteration, this SS-loop allows to find a SE

emission profile for which the ratio r_1/r_0 ($= K$) is constant for a given magnet system, discharge voltage V_d, cathode sheath thickness d_E and pressure p. The number of iterations for this loop is referred to as l_1. Iterating through this SS-loop only leads to a constant value of r_1/r_0 but does not lead to this ratio being unity for the considered input parameters. The solution to this problem will be dealt with later on (section 3.2.4); first the incorporation of recapture in the model is discussed.

3.2.3 Steady state emission profile taking into account recapture

An important and perhaps somewhat surprising result of Chapter 2 is the pressure independence of the AIM. This is reflected in the preliminary SCM that we developed so far as there is no pressure input (Fig. 3.2). However, in reality the MD properties do vary with the gas pressure. The solution to this paradox is the recapture of SE, which depends strongly on p (section 1.3.4). Up to now, it was assumed in the AIM that a SE emitted from the target resulted in ionisation of the discharge gas. However, only the fraction $f(x)$ of the SE emitted at x does effectively interact with the discharge gas, the rest is recaptured by the target. To include this in the SCM, the model needs the gas pressure as input parameter as shown in Fig. 3.3. This extends the SS-loop but does not alter it fundamentally as iterating through the new SS-loop allows only finding a constant ratio for r_1/r_0 but still does not allow making this ratio equal to one.

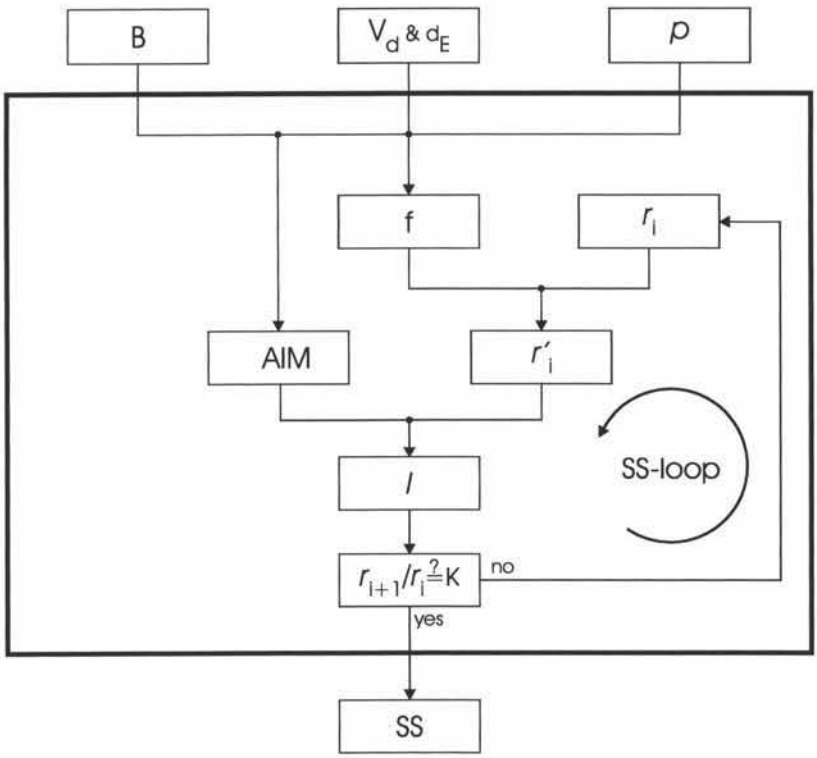

Fig. 3.3 Sketch of the preliminary SCM as in Fig. 3.2 but with taking into account the recapture of SE. This has no fundamental impact on the SS-loop.

3.2.4 Principle of the self-consistent model

When considering the input of the model of the previous section, it becomes clear why no solution is obtained. The input consists of the magnetic field, the gas pressure, the discharge voltage and the cathode sheath thickness. In reality, we only control the first three of these parameters as the cathode sheath thickness depends on the other three parameters. Hence, for the given four input parameters, a solution can only be found if the cathode sheath thickness that is used as input "fits" accidentally the other three input parameters. For a realistic model, the cathode sheath can no longer be considered as input but should become part of the output. We argue now that this corresponds with making the model self-consistent, with "self-consistent" referring to the fact that the potential distribution is obtained from the simulation results (section 3.1).

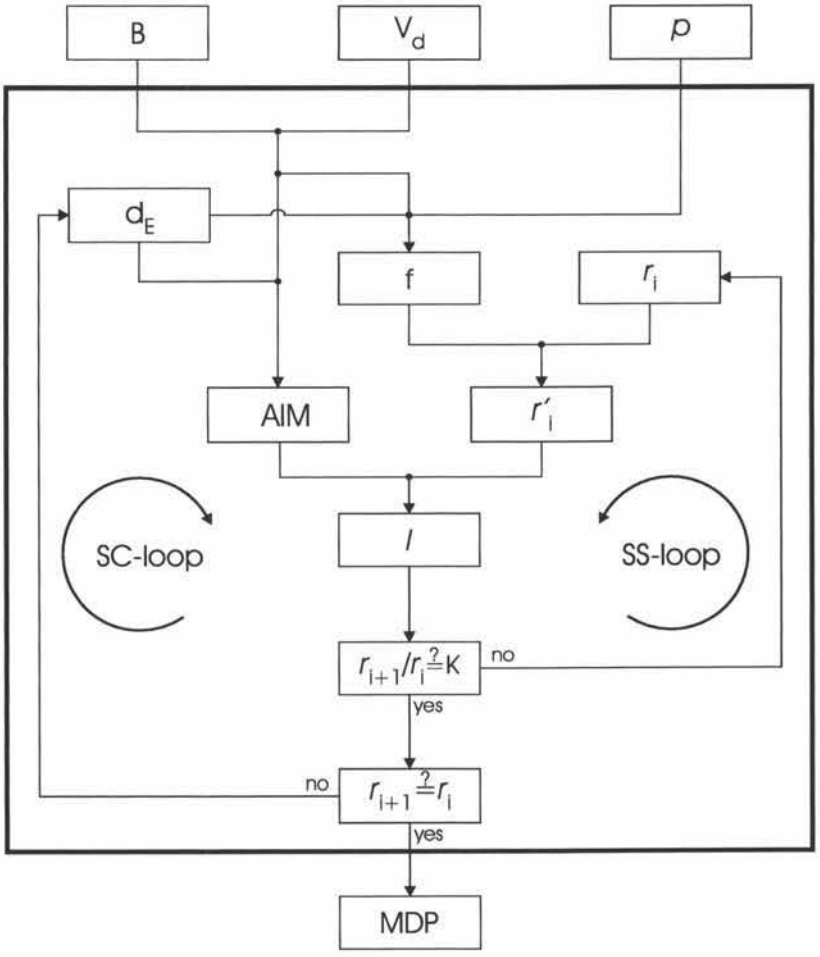

Fig. 3.4 Sketch of the SCM. Note that the AIM is part of the SC-loop.

In the model that is discussed here, the problem of determining the potential distribution from the simulation results is strongly simplified. First, it is assumed that the electric field can be limited to the cathode sheath. This is valid as the small electric field in the presheath will hardly influence the motion of the HEE. Second, the cathode sheath is considered uniform along the cathode. Third, the electric field in the cathode sheath is considered linear (see section I.1.3.3.5). Hence, the potential $V(z)$ is defined by eq. (1.3) in section 1.2.1, i.e. for a given V_d it is defined by the cathode sheath thickness d_E. This shows that to obtain a self-consistent model, d_E should no longer be considered as an input parameter.

The integration of d_E into the model is shown in Fig. 3.4. As it is no longer known a priori, d_E has to be given an initial value, $d_{E,0}$ to start a simulation. This solves the previously problem encountered (section 3.2.2) about the impossibility to reach the condition $r_i = r_{i+1}$. When the condition $r_{i+1}/r_i = K$ is reached, the value of d_E can be adjusted. When K is larger than one, there is too much ionisation. This amount of ionisation can be reduced by decreasing d_E as this leads to less sheath ionisation (a smaller m), lowering the effective SE yield. In the opposite case ($K < 1$), d_E has to be increased. This creates an extra iteration loop, referred to as "SC-loop". The number of iterations through this loop is indicated by l_2. After adjusting d_E the SS-loop is repeated. When SS is reached, d_E is adjusted again and so on until $K = 1$ is obtained. As this determines the potential distribution in the discharge, the addition of the extra iteration loop for d_E leads to the self-consistent model.

3.2.5 Practical self-consistent model

In the previous section the concept of the SCM was built up. However, when applying the model, it appears not so practical. For iteration through the SS-loop, the AIM does not have to be adapted, meaning that this loop does not require a lot of computational effort. However, running through the SC-loop requires the adaptation of the AIM, i.e. the recalculation of the arches, the average transfer matrices and the weight factors g_i and $g^{SI}{}_i$ (see section 2.4). This makes it, compared to the SS-loop, a computation intensive loop (running through it requires some minutes). To speed up the simulation, an alternative approach is needed in which the AIM is not included in the SC-loop. This can be obtained by replacing the gas pressure p as input parameter by the cathode sheath thickness d_E, which implies that p is determined by iterating through the SC-loop (Fig. 3.5). Although this approach is not the most practical from an application view-point, it can be used very well for the investigation of the MD conducted here. As it is much faster, this implementation of the simplified model is used for the results presented in this and the following chapters. In the remaining part of this text, this implementation of the model is referred to as "*the SCM*".

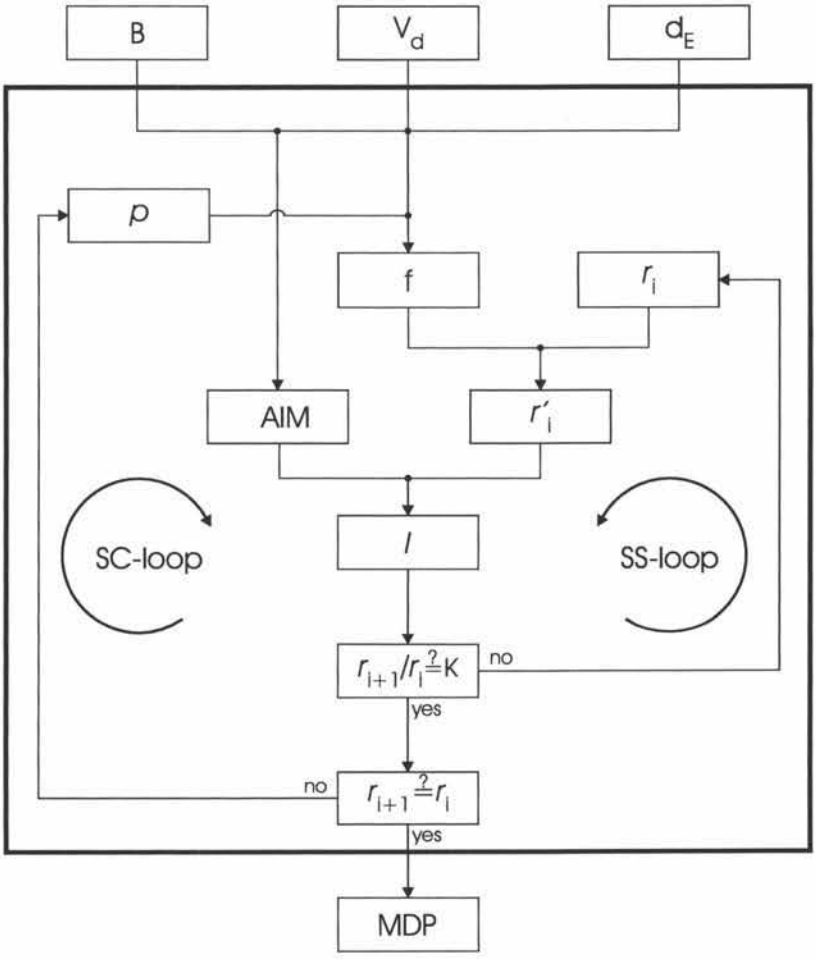

Fig. 3.5 Sketch of the actual form of the SCM that is implemented. Compared with the model shown in Fig. 3.4, this approach has the main advantage that iteration through the SC-loop does not require to adapt the AIM, which makes the model much faster.

3.3 Results and discussion

3.3.1 Verifying independence of initial conditions

For the results presented here the magnetron configuration as described in the beginning of section 1.3 is used. Unless mentioned otherwise, the discharge voltage V_d, the cathode sheath thickness d_E and the initial energy E_{init} was taken 440 V, 1.6 mm and 4 eV, respectively. To calculate the EGIP f the settings of case II were used (see section 1.3.1.1) and 7 initial velocity vectors (m =1, n = 3, see section 1.2.2) were considered. This limited number of velocity vectors was chosen as a compromise between accuracy and computational load. For the analytical model arches were constructed for x = -14.75 mm to -0.25 mm per step of 0.5 mm. These settings are referred to as the "*standard settings*". An initial emission profile r_{init} and an initial gas pressure p_{init} need to be chosen.

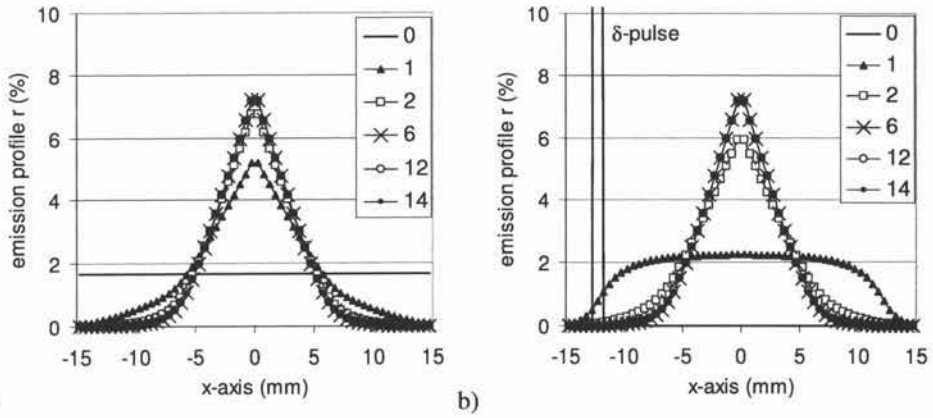

Fig. 3.6 Influence of the initial emission profile r_{init} on the final emission profile r_{sc}: in (*a*) r_{init} is homogenous, in (*b*) r_{init} is defined by the Dirac pulse $\delta(x+12.25)$. The iteration-number shown in the legend is defined as l_1+l_2.

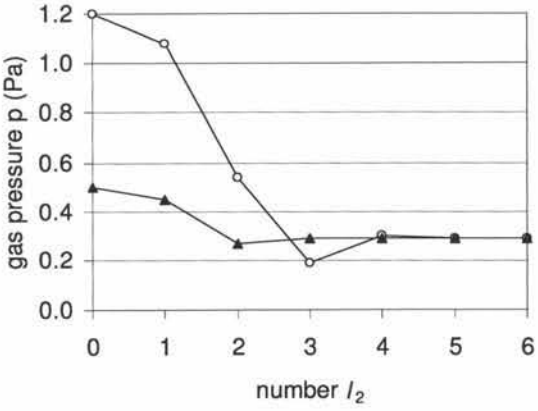

Fig. 3.7 The way the self-consistent pressure p_{sc} is reached for p_{init} = 0.5 Pa (O) and p_{init} = 2 Pa (▲): it is clear that p_{init} does not influence the end result.

First, $p_{init} = 0.5$ Pa and a uniform r_{init} were chosen. The evolution of the emission profile r is shown in Fig. 3.6a: r evolves from r_{init} to r_{sc}, the self-consistent emission profile, within approximately 10 iterations. The iteration number of the different profiles is given by l_1+l_2, with l_1 and l_2 defined as in section 3.2.2 and 3.2.4, respectively. In Fig. 3.7 the pressure evolution is shown as a function of l_2. For this particular case $p_{sc} = 0.29$ Pa is found.

If the model is realistic, the results for r_{sc} and p_{sc} should be independent of r_{init} and p_{init}. To verify this, two more initial starting conditions are considered. The first is characterised by $p_{init} = 0.5$ Pa but for the initial emission profile a Dirac pulse is chosen: $r_{init} = \delta(x+12.25)$. The latter means that one electron is emitted from $x = -12.25$, no electrons are emitted from the other positions. The evolution of the emission profile in this case is shown in Fig. 3.6b. Comparison of parts *a* and *b* of the figure shows that r_{sc} is indeed independent from r_{init}. Also the self-consistent pressure is not influenced by the choice of r_{init}: in both cases p_{sc} is 0.29 Pa. Second, the self-consistent solution was retrieved for a homogenous r_{init} but for $p_{init} = 1.2$ Pa. As can be seen in Fig. 3.7 this does not influence the final value for p_{sc}. Another investigated parameter is the influence of the resolution along the x-axis. For the standard settings, arches are constructed for $x = -14.75$ mm to $x = -0.25$ mm with step $\Delta x = 0.5$ mm. The simulation was also performed for $x = -14.875$ mm to $x = -0.125$ mm ($\Delta x = 0.25$ mm) and for $x = -14.5$ mm to $x = -0.5$ mm ($\Delta x = 1.0$ mm). The self-consistent emission profiles r are practically independent of Δx as shown in Fig. 3.8. For p_{sc} a limited influence of Δx was found, namely 0.26, 0.29 and 0.29 Pa for $\Delta x = 1.0$, 0.5 and 0.25, respectively.

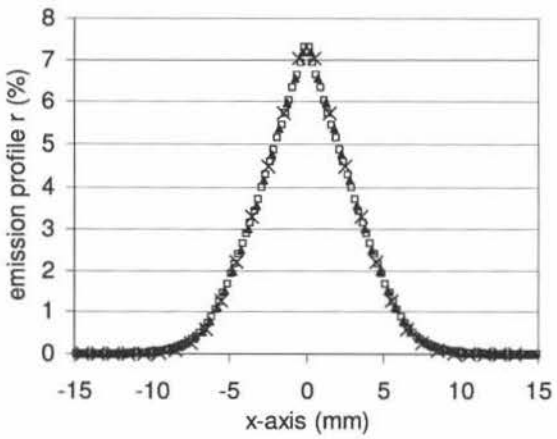

Fig. 3.8 Dependence of the self-consistent emission profile on the spacing of the arches Δx. The results for $\Delta x = 0.25$ (□), $\Delta x = 0.5$ (▲) and $\Delta x = 1.0$ (×) are practically identical.

Given these results, we conclude that the SCM is "self-consistent" in the sense that the results are independent of the choice of the initial conditions or the spacing of the arches along the x-axis.

3.3.2 Discharge properties for a given configuration

In this part, the results obtained with the SCM for the standard settings are discussed (see previous section). The self-consistent pressure p_{sc} was found to be 0.29 Pa. The ionisation distribution I is given in Fig. 3.9 : typical for the MD is the strong concentration of ionisation close to the target. As mentioned in section 2.3.4, this ionisation distribution represents the

relative ionisation rate and can be compared with results from numerical models, see e.g. [Shidoji01a]. A limitation of the SCM is that only a relative result is obtained for the ionisation distribution. A main advantage is that calculating the MDP requires only around 15 minutes on a now standard pc (Intel Pentium 3 GHz, 512 Mb RAM) using Microsoft Visual Basic 5.0 as programming language whereas a numerical model requires easily up to several days (section I.2.2).

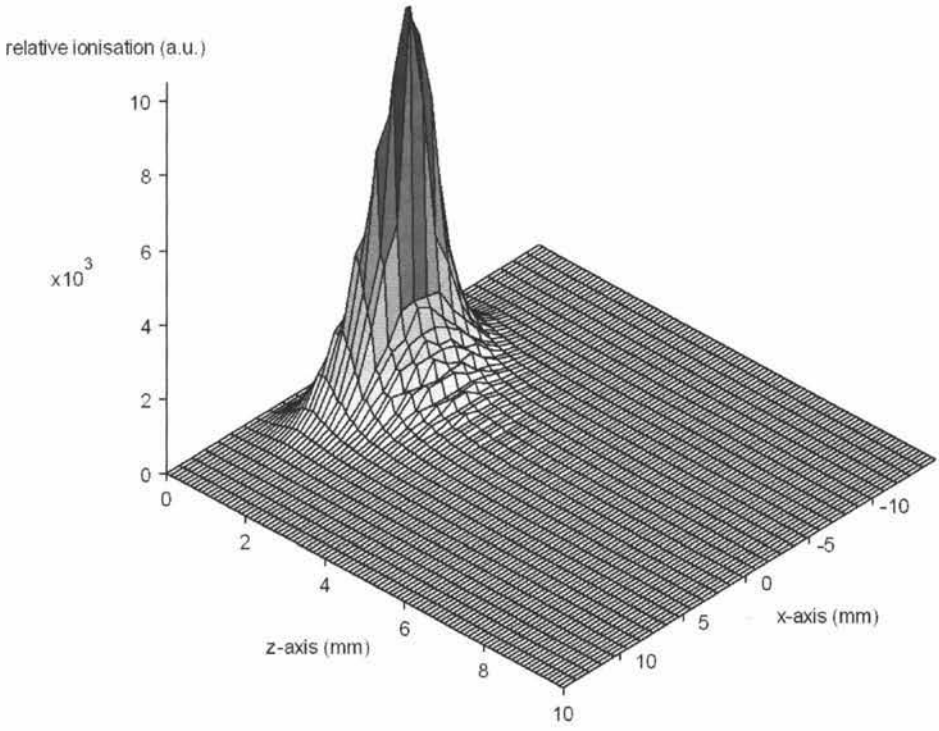

Fig. 3.9 The relative ionisation distribution $I(x,z)$ obtained for the standard settings.

Another advantage of the SCM is that we can probe into the different processes that occur in the discharge and estimate their importance. In Fig. 3.10a the self-consistent solution for $\mathcal{B}$, the ion bombardment distribution along the x-axis is shown. As the SE yield γ is taken constant this curve also represents the relative SE emission profile r (eq. (3.3)). The relative erosion profile w, determined using eq. (3.3), is also shown. As it is very similar to $\mathcal{B}$, we conclude that taking into account the energy dependence of the sputter yield y is of minor importance.

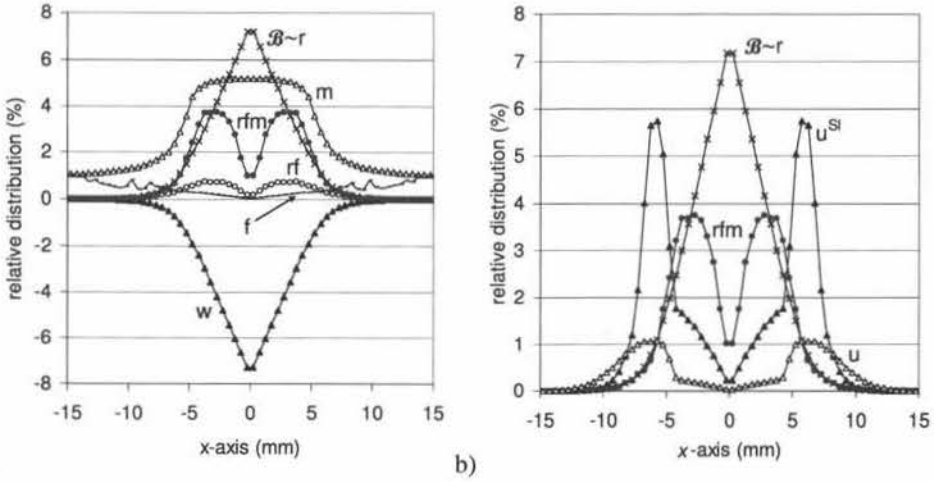

Fig. 3.10 The figure gives an overview of the self-consistent solution obtained with the standard settings. Part *a* shows $\mathcal{B}$, the distribution along the *x*-axis of the ions bombarding the target (×). Given the constant SE yield γ, this profile is proportional to the SE emission profile *r*. Furthermore, the erosion profile *w* (▲), the EGIP *f* (▪), the multiplication factor *m* (△), the emission profile corrected for recapture *rf* (O) and the effective SE emission profile *rfm* (●) are shown. Part *b* repeats the original and effective emission profiles but shows also the occupation profiles *u* (△) and u^{SI} (▲). Note that the emission profile *r* is scaled such that the sum of all r_i is equal to one. Also the occupation profiles are scaled such that the sum of all u_i and u^{SI}_i together equals one.

Fig. 3.10a shows also the EGIP *f* and the multiplication factor *m*. Interestingly, the resulting net SE emission profile *rf* has its maximum no longer at $x = 0$. Taking into account the multiplication factor *m* leads to the effective SE emission profile *rfm*. Also this profile does not peak around $x = 0$ but around $|x| = 3.0$ mm. We conclude that the SE emitted slightly off-centre contribute most to the ionisation although most SE are emitted at the centre of the target. This does not strongly influence the ionisation distribution or the resulting erosion profile. Indeed, as mentioned in section 2.6.3.1, for small $|x|$ the ionisation distribution is hardly dependent on *x*. Consequently, the shape of the relative erosion profile will hardly be influenced whether recapture of the SE is accounted for or not. This explains why MC simulations that neglect recapture can nevertheless reproduce realistic relative erosion profiles, see e.g. [Kubart04].

Fig. 3.10b shows again *rfm* together with the occupation profiles u_i of the HEE^{ta} and u^{SI}_i of the HEE^{SI}. The elements of the occupation profiles are scaled so that the total sum over all u_i and u^{SI}_i equals one. For $|x|>8$ mm the contribution of the HEE^{ta} dominates but for smaller $|x|$ there are more HEE^{SI}, indicating that SI is indeed very important. Both occupation profiles peak at large r $|x|$ (≈ 6 mm) than *rfm*. This could be expected as the interactions of the HEE push them out of the cathode sheath into arches that correspond with larger $|x|$ values.

Fig. 3.11 shows the same distributions as Fig. 3.10 but for d_E equal to 0.8 mm instead of 1.6 mm. In this case, the value for the self-consistent pressure p_{sc} is 1.66 Pa. The higher pressure is needed because the reduction of the cathode sheath thickness leads to a smaller *m*, which in turn reduces the effective SE yield. The reduction of *m* leads also to a reduced contribution of the HEE^{SI}: the occupation profile *u* dominates for $|x| > 5$ mm and *u* and u^{SI} are close to each other for smaller $|x|$, although u^{SI} is slightly larger.

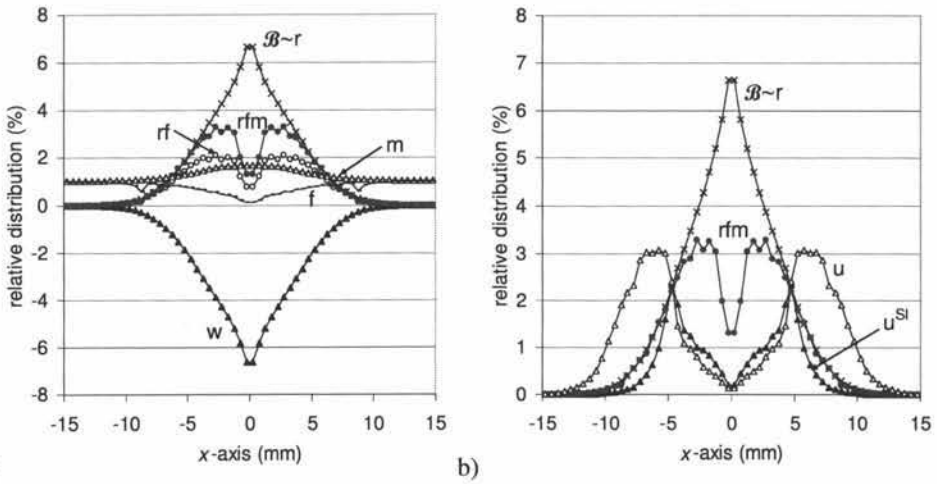

a) b)

Fig. 3.11 The figure gives the same results as Fig. 3.10 but the results are obtained for d_E equal to 0.8 mm instead of 1.6 mm. The symbols have the same meaning as in Fig. 3.10.

It is also interesting to consider the occupation profiles for both the HEE^{ta} and HEE^{SI} in Fig. 3.10b and Fig. 3.11b. In both cases the occupation profiles are practically zero at the edges of the race-track. This indicates that virtually no HEE escape of out of the discharge area. Also for the other situations of the "basic result" (see section 3.3.4), the occupation profiles were investigated. The fraction of escaping HEE increases with increasing V_d, decreasing d_E and decreasing magnetic field but even the largest fraction ($d_E = 0.8$ mm, $V_d = 560$ V, $B_{max} = 400$ G) was only around 1%. This confirms that for a typical MD, the fraction of lost HEE can be neglected.

3.3.3 Extended Thornton relation for the discharge voltage

For a given set of input parameters V_d, d_E and B, the iteration procedure for obtaining a self-consistent result leads only for a particular pressure p_{sc} to a solution (section 3.2.5). We now discuss in more detail the physical meaning of this pressure p_{sc}.

Thornton deduced a relation for determining the *minimum* discharge voltage $V_{d,min}$ in a MD [Thornton78a]. This relation is basically an expression of energy conservation: the energy input into the discharge has to be equal to the energy consumed by the discharge for excitations and ionisations. Assuming $\varepsilon_i = \varepsilon_e = 1$, this relation becomes (see eq. (1.20) in section I.1.3.2):

$$V_{d,\min} = \frac{W}{\gamma_{eff}} \tag{3.4}$$

with γ_{eff} the effective SE yield as seen by the discharge. Thornton assumed a constant value for γ_{eff}: it is taken equal to the product of the SE yield γ and a factor characterising the SE loss because of recapture. As said, the discharge voltage resulting from this expression is unique and is referred to as "the minimum discharge voltage $V_{d,min}$".

The SE emission profile is transferred into the effective SE emission profile by taking into account recapture and sheath ionisation. Hence, a position x_i has an effective SE yield $\gamma_{eff,i}$ given by:

$$\gamma_{eff,i} = \gamma f_i m_i \tag{3.5}$$

The effective SE yield as seen by the discharge is then the average of $\gamma_{eff,i}$ using the effective SE emission profile as weight factor:

$$\gamma_{eff} = \frac{\sum_i \gamma_{eff,i} r_i}{\sum_i r_i} = \gamma \frac{\sum_i f_i m_i r_i}{\sum_i r_i} = \gamma < fm > \tag{3.6}$$

with <*fm*> the average of the product *fm*. For the self-consistent solution obtained with the standard settings this leads to $\gamma_{eff} = 0.068$. This value of γ_{eff} could be predicted from eq. (3.4) as it equals W/V_d. Hence, the pressure p_{sc} found through the iteration procedure is the pressure for which the effective SE yield becomes equal to W/V_d. For a given B, d_E and V_d (the input parameters of the SCM), the multiplication factor m is fixed as it is pressure independent. Hence, γ_{eff} can only be influenced by varying the EGIP f (see eq. (3.6)), which is pressure controlled. Consequently, through the SC-loop (Fig. 3.5) the pressure is found for which eq. (3.4) is satisfied.

This elucidates the physical meaning of the SCM: it is basically equivalent to the equation proposed by Thornton for determining the discharge voltage based on the principle of energy conservation. However, the Thornton model includes only specific information about the discharge gas used (through W) and the target material (through γ_{eff}). It does not include any information about the magnetron configuration (geometry and magnetic field strength). In other words, it is a zero-dimensional model. The SCM extends the Thornton model by including the specific magnetron configuration.

Moreover, the original Thornton relation is able to reproduce only one specific discharge voltage, which is referred to as "the minimum discharge voltage $V_{d,min}$". Hence, the expression does not take into account the influence of the electrical power delivered to the discharge. By introducing f and m, this power dependence is also included. When the power is increased, the energy input is larger than the energy needed to generate the number of ions to maintain the discharge. Increasing the power decreases the cathode sheath thickness (section I.1.4.3.3), which reduces m. Moreover, the decrease in the cathode sheath thickness and the increase of the discharge voltage will influence the EGIP f. Because f and m are influenced, the effective SE yield changes. Consequently, for a different γ_{eff}, a different discharge voltage is found.

In conclusion, the SCM enables calculation of the effective SE yield γ_{eff} as seen by the MD. Using this γ_{eff}, one can extend the Thornton relation for the energy balance in the discharge. Indeed, the combination of the original Thornton relation (eq. (1.20) in section I.1.3.2) with the expression for the effective SE yield (eq. (3.6)) gives the "extended Thornton relation":

$$V_d = \frac{W}{\gamma < fm > \varepsilon_e \varepsilon_i} \tag{3.7}$$

This way, it becomes possible to relate the MDP to the (two-dimensional) geometry of the system, the electrical power input, the magnetic field strength and the gas pressure. Hence, the SCM can be used to determine the influence of these parameters on the MD and the extended Thornton relation can be used to give a better understanding of the processes that lead to that influence.

3.3.4 Basic result for simulating dependences

In the previous section, the result for one specific case of the input parameters B, V_d and d_E was presented and discussed. Given the rather short computation time needed for such a result, the SCM allows to investigate the influence of the different input parameters on the self-consistent result. A typical set of results is shown in Fig. 3.12 where the discharge voltage is varied from 260 to 560 V per step of 60 V and the cathode sheath thickness is varied from 0.8 to 2.4 mm per step of 0.2 mm. Except for V_d and d_E the standard settings are used. The results for the self-consistent pressure p_{sc} vary from approximately 0.1 to 5.3 Pa, which is a realistic range. The minimum p_{sc} is obtained for $d_E = 2.4$ mm and $V_d = 560$ V. For each couple (V_d, d_E) not only the self-consistent pressure is retrieved but also the relative ionisation distribution I in the xz-plane and the width w of the erosion profile.

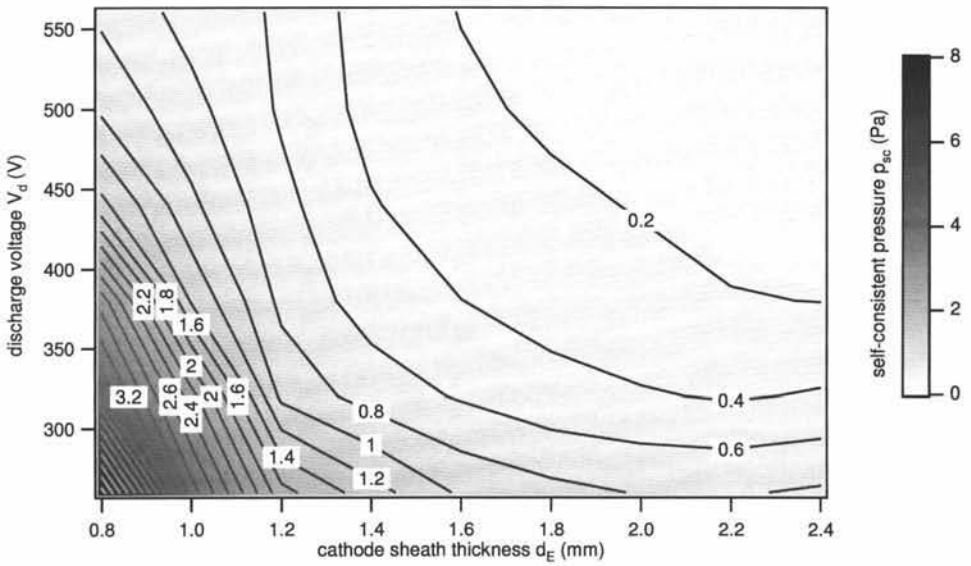

Fig. 3.12 The dependence of the self-consistent pressure p_{sc} on the discharge voltage V_d and the cathode sheath thickness d_E. The plot is based on the results obtained for $V_d = 260$ to 560 V per 60 V and for $d_E = 0.8$ to 2.4 mm per 0.2 mm. The labels indicate the gas pressure in Pa.

The isobars on the graph represent the relation between the discharge voltage and the cathode sheath thickness at constant pressure. For a given pressure, larger discharge voltages correspond with smaller cathode sheath thicknesses, which is in agreement with experimental measurements (see section I.1.4.3.3). According to the experiments in [Rossnagel87b], the isobars should also shift to lower cathode sheath thicknesses with increasing pressure. Also this characteristic is retrieved by the SCM. A major limitation to the interpretation of the results is the fact that the discharge current is not calculated. This aspect is discussed in the next chapter.

The graph also gives an idea of the accuracy of the simulation results: as can be seen the isobars do sometimes show an irregular behaviour, e.g. the kink in the one of 1.0 Pa. This is related to the calculation of the EGIP f, which behaves rather irregular as a function of e.g. the electric field (Fig. 1.15a). As mentioned in section 1.3.2, a more accurate calculation of f can be obtained by averaging over a larger number of initial starting conditions for the electrons. However, this seriously increases the required computational load.

On itself, such a matrix of results might look of little practical use. However, from these results, one can e.g. deduce (V_d, d_E)-combinations for which the self-consistent pressure is constant. Feeding these couples into the SCM allows investigating the discharge properties at constant pressure in a computation time efficient way. Hence, a matrix of results as shown in Fig. 3.12 forms the basis for the dependences presented in the next sections and in Chapters 4 and 6. Consequently, this matrix is referred to as the "basic result".

3.3.5 Influence of γ and R on the self-consistent gas pressure

The influence of the SE yield γ and the reflection coefficient R for electron-target interaction on the MD is investigated. This influence occurs through the effective SE yield γ_{eff} (eq. (3.6)). The reflection coefficient R influences γ_{eff} because it is crucial for the calculation of the EGIP f (see section 1.2.6). The aim is to show that γ_{eff} needs to be known very accurately for a realistic self-consistent MD simulation. From eq. (3.6) follows that also m is needed. However, m is not an input parameter like γ and R but is calculated within the model. Note that, although there are several ways of how the target material can influence the MD (section I.1.4.4), the major effect of the target material is through the effective SE yield because of γ and R.

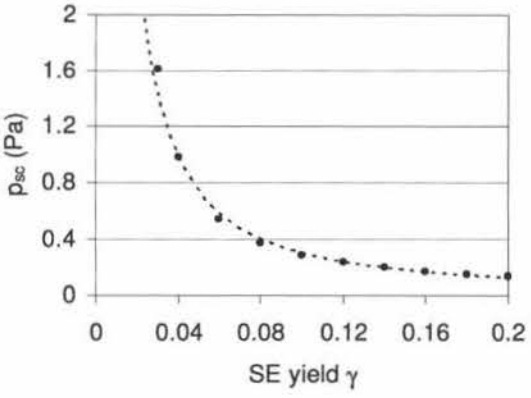

Fig. 3.13 The dependence of the self-consistent pressure p_{sc} on the SE yield γ for $V_d = 440$ V and $d_E = 1.6$ mm. The graph shows that p_{sc} depends strongly on γ, especially at low yields. Except for the values of γ, the standard settings are used. The dashed line is meant as a guide for the eye.

The influence of γ on the self-consistent pressure is shown in Fig. 3.13 for constant V_d (440 V) and d_E (1.6 mm). For the typical γ-values of metals (around 0.1) there is a strong dependence on the SE yield as p_{sc} obtained for $\gamma = 0.08$ is almost double of p_{sc} for $\gamma = 0.12$. This indicates that for an accurate self-consistent result, the value of γ is crucial. From the view-point of MD simulations, this is problematic as it is very difficult to find reliable experimental values for γ. Moreover, γ is very sensitive to the surface condition of the target (section I.1.2.2.1).

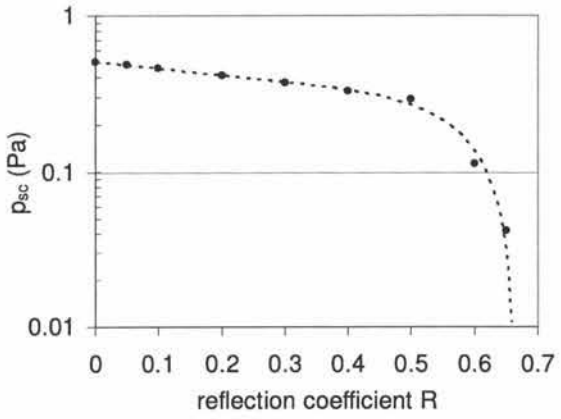

Fig. 3.14 The dependence of the self-consistent pressure p_{sc} on the electron reflection coefficient R for electron-target interaction for $V_d = 440$ V and $d_E = 1.6$ mm. The graph shows that for $R>0.65$ no realistic pressures are obtained. Except for the values of R, the standard settings are used. The dashed line is meant as a guide for the eye.

Fig. 3.14 shows the dependence of p_{sc} on the electron reflection coefficient R. Below $R = 0.5$, the dependence on R is practically linear and p_{sc} varies from 0.29 Pa ($R = 0.5$) to 0.50 Pa ($R = 0$). Most striking is the fact that no result can be obtained for R-values larger than 0.65 as in these cases the self-consistent pressure becomes unrealistically low ($p_{sc}<0.01$ Pa). This means that no solution is found when recapture is neglected ($R = 1$). The reason is that given the values for V_d and d_E, the multiplication factor m is quite high ($\langle m \rangle \approx 4$). As a result, per emitted SE the number of generated ions is much larger as required for maintaining the discharge, i.e. the number of electrons in the discharge area keeps increasing. The way to overcome this is by reducing the pressure. However, given the large R, even setting the pressure to unrealistically low values does not result in steady state.

In order to find a situation where a self-consistent solution is possible without recapture ($R = 1$), we consider the situation with the smallest d_E and V_d (0.8 mm and 260 V, respectively) of the basic result (previous section) as this situation has the smallest m. For $\gamma = 0.1$ no solution was found for $R = 1$ or $R = 0.95$; for $R = 0.9$, p_{sc} was found to be 0.048 Pa, which is unrealistically low for a discharge voltage of 260 V. We tried to find a self-consistent solution for these d_E and V_d and $R = 0.95$ by adjusting the SE yield γ. For $\gamma = 0.08$ the solution $p_{sc} = 0.87$ Pa was found. However, the dependence on γ was extreme: for $\gamma>0.085$ no solution was found ($p_{sc}<0.01$ Pa), for $\gamma = 0.07$ the self-consistent pressure was already more than 10 Pa.

These simulation results confirm that for a self-consistent solution including recapture is required. Given the dependence on R and γ and the difficulty to find accurate experimental values for these two parameters, the expectations for the accuracy of self-consistent simulations need to be moderate because even a slight error in one of the two can alter the discharge properties strongly.

3.4 Conclusions

In this chapter, a self-consistent model for the MD was developed. The term self-consistency refers to the determination of the electric field in the discharge area, as is common in MD simulation. The model is self-consistent in a simplified way because the electric field is assumed to be linear and limited to the cathode sheath. Moreover, it is considered uniform along the target.

The model can in principle be used to determine the MDP for an input consisting of the magnetic field geometry, the discharge voltage and the gas pressure. From computational view-point it is much more convenient to use the cathode sheath thickness as input parameter instead of the gas pressure, which then becomes part of the output.

To find the steady state self-consistent solution, the model considers the energy balance of the discharge, i.e. some key discharge properties are adjusted such that the number of electrons generated at the target per incoming ion is equal to the number of ions generated in the gas phase per emitted electron. As such, the model can be considered as an extended version of the relation proposed by Thornton for estimating the minimum discharge voltage to maintain the MD. By taking into account the gas pressure, recapture of SE and sheath ionisation, the model is no longer limited to the minimum discharge voltage but can express the required equilibrium for different conditions.

Although the model does not include the calculation of the discharge current yet (this is the topic of the next chapter), it already allows simulating some important characteristics of the MD. First, practically no high energy electrons escaping the magnetic trap are found. Second, although most electrons are emitted from the centre of the race-track, the positions slightly off-centre contribute the most to the MD because there the EGIP is larger. Third, to obtain a reliable self-consistent solution, the effective SE yield γ_{eff} is crucial. This requires accurate calculation of the sheath ionisation and of recapture. The latter demands accurate input values for the SE yield γ and for the electron reflection coefficient R.

4 DISCHARGE CURRENT CALCULATION

4.1 Introduction

In the previous chapter, a self-consistent model (SCM) for the magnetron discharge (MD) was developed. The focus there was on reaching self-consistency. This means that the electric field in the discharge is not assumed to be known but is calculated, albeit in a simplified form as it was limited to the cathode sheath and was taken linear. In this chapter we develop another -at first sight perhaps trivial- aspect of the model: the calculation of the discharge current I_d.

In principle, this problem is straightforward. In a self-consistent model, the potential distribution, and thus the electric field, in the MD are known. From this, the electron and ion motion can be calculated, which results in the charged particle flux to the electrodes per time unit, i.e. the discharge current. However, for determining the potential distribution, an accurate description of the charged particle distribution is needed. This poses a problem given the anomalous electron transport in the direction perpendicular to the magnetic field lines (section I.1.3.6.2).

The aim here is to develop a model for the discharge current which does not require the (bulk) electron motion. In the next section (section 3.2), the model will be discussed in detail. Then, it will be used to simulate and explain several aspects of the MD, including the current-voltage characteristic and how it is influenced by the pressure and the magnetic field (section 2.6).

4.2 Model

In this part, the model for the discharge current I_d is explained. First, the choice for calculating I_d based on the ion flux to the cathode is motivated (section 4.2.1). Second, the individual ion motion is considered (section 4.2.2). Finally, a method to determine I_d based on an extension of the Child-Langmuir law is introduced (section 4.2.3).

4.2.1 Discharge current based on the ion flux at the target

To determine the discharge current I_d, one can look at the charged particles arriving at the anode or at the cathode. At the anode, the current is carried by electrons (Fig. 3.1). In a typical magnetron, the magnetic field prevents the high energy electrons (HEE) from leaving the discharge. Consequently, the current is carried by bulk electrons (BE). The problem with determining the current from these electrons is that the electron diffusion in the direction perpendicularly to the magnetic field lines is not well understood, resulting in the so-called anomalous electron transport. This is most likely caused by oscillations in the electric field. Indeed, such oscillations have been observed in a broad frequency range (section I.1.3.6.2).

For self-consistent MD simulations the two most common approaches are the PIC-MC and hybrid model (section I.2.2). In the latter, the problem of the anomalous electron transport comes down to the choice of the correct diffusion coefficients. As discussed in section I.2.3.5, this choice is based on the classical theory. This questions the results for the potential distribution, and related discharge properties, obtained with the hybrid model in the region where the anomalous transport is important (strong magnetic field and/or low pressure).

The PIC-MC model is, in principle, able to reproduce the correct solution. However, to correctly simulate the mentioned oscillations the simulation should follow the discharge during several oscillation cycles. This means for an oscillation frequency of 100 kHz (10 kHz)

several tens (hundreds) of microseconds. This is much longer than the typical time the discharge is followed in a PIC-MC simulation (order of a few microseconds), which questions the validity of the obtained simulation results.

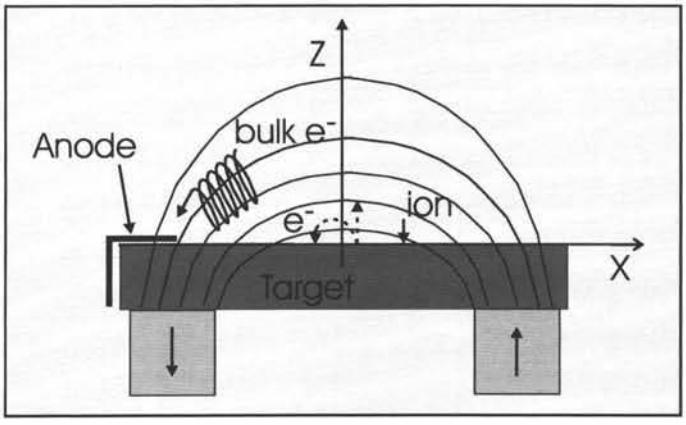

Fig. 4.1 Sketch showing the particle fluxes to and from the electrodes. At the cathode, there is an incoming flux of ions and an outgoing flux of electrons. Part of these electrons are recaptured and hence, do not contribute to the discharge current. At the anode, bulk electrons leave the discharge. Ideally, no high energy electrons can leave the discharge at that side.

The other option, which we prefer, is to calculate the discharge current based on the charged particle flux towards the cathode. Here, the current is predominantly carried by the ions. However, as the ions bombard the target, they cause the emission of secondary electrons (SE). As these electrons are accelerated away from the cathode, they also carry a part of the discharge current. The relation between the total discharge current I_d and the parts I_i and I_e, carried by the ions and electrons respectively, is given in I.1.3.4.3, eq. (1.40). As γ is typically around 0.1, about 10 % of the discharge current is carried by the electrons. However, one has to keep in mind the recapture of the SE (see Chapter 1). Hence, the SE yield γ needs to be corrected for this effect. Given the rather high recapture probabilities, the contribution of the electrons to the discharge current I_d at the cathode side will be well below 10 %, so that this contribution can be neglected. This neglecting is not fundamental and the electron contribution could be included if needed. In conclusion, to calculate the discharge current I_d we have to tackle the ion motion towards the target.

4.2.2 Individual ion motion

The SCM as developed in the previous chapter results in the normalised ionisation distribution I in the discharge area. To determine the ion flux at the cathode, the time it takes for an ion to reach the target is needed. Once the electric field E is known, this time can be calculated readily using the Lorentz equation (eq. (1.1) in section I.1.1). As the effect of the magnetic field on the ions can be neglected, this equation reduces to:

$$F = qE \tag{4.1}$$

The argon atoms in the discharge are assumed to be at room temperature. Hence, their initial velocity corresponds with the thermal drift. As this thermal drift is much smaller than the velocity gain due to the electric field, the initial ion velocity can be neglected. For the ions generated within the cathode sheath eq. (4.1) can be solved easily. However, there is a problem for the ions generated above the cathode sheath as, up to now, no electric field was

assumed in that region. This was not necessary because the motion of the HEE in the discharge is hardly influenced by the small electric field of the presheath. However, for the ions, this field is crucial: the electric field is small and the time an ion needs to reach the cathode is predominantly the time needed to reach the beginning of the cathode sheath.

In section I.1.3.3.1 the presheath was discussed for different plasma sheaths. To estimate the electric field E in the presheath, we assume that it is constant. The presheath length is of the order of the ion mean free path. The latter was estimated to be around 7 mm at 0.5 Pa (section I.1.2.1.1). Hence, the presheath is roughly of the order of a centimetre. Here, we use the concept of the virtual anode (section I.1.4.6) to determine the potential in the presheath. The principle is shown in Fig. 4.2: the presheath is defined as the region between the cathode sheath and the virtual anode. Hence, its thickness varies along the target surface.

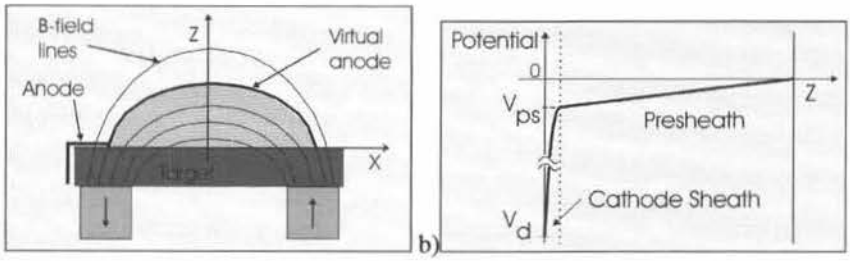

Fig. 4.2 Sketch of the position of the virtual anode (*a*) and the potential distribution at $x = 0$, the centre of the race-track (*b*).

In conclusion, to calculate the ion motion, the electric field in the region above the cathode sheath is needed. Therefore, we use the concept of the virtual anode and the knowledge that the energy equivalent of the potential drop over the presheath is typically half the electron temperature kT_e (section I.1.3.3.1).

4.2.3 Model for discharge current

In this part, a model for the MD current is deduced. For this purpose j_m, the magnetron line current density is introduced (section 4.2.3.1). The basis for this j_m is the Child-Langmuir law. After a more detailed discussion of this law (section 4.2.3.2), it will be extended for the typical situation encountered in MD (sections 4.2.3.3 to 4.2.3.5).

4.2.3.1 The magnetron discharge line current density j_m

To determine the discharge current of a diode discharge, one can use the Child-Langmuir law (CL law). This law gives the "current density" j_d as a function of the discharge voltage and the cathode sheath thickness. The quotation marks are used to indicate that what is generally referred to as "current density" is more precisely a "surface current density" as j_d has A/m^2 as dimensions. The fact that j_d is "per surface area" is usually omitted as it is by far the most commonly used current density. However, here we will mention explicitly that it is a surface current density to differentiate it from the line current density.

Similar to the diode discharge, we want to define for the MD a characteristic current density. In the diode discharge, the characteristic current is the surface current density because the current through a surface S on the cathode is the same, regardless the position of the surface (Fig. 4.3a). Hence, the first option is to see whether this surface current density is a good option for the MD.

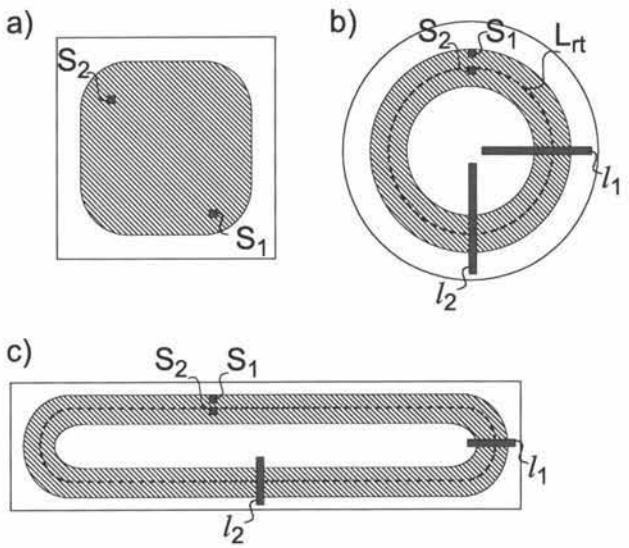

Fig. 4.3 For a diode discharge (*a*) the characteristic current is a surface current density as the current through two surfaces S_1 and S_2 with the same area is the same, regardless of the position of the surfaces within the discharge. For a magnetron discharge, this is not true: two surfaces S_1 and S_2 located within the race-track do not necessarily carry the same amount of current (*b+c*). Instead, the characteristic current is a line current density: the current through l_1 and l_2 is equal, regardless their position along the race-track. The *x*-axis as referred to in the text is along the length of l_1 and l_2.

This is not the case: the current through S_1 (at the edge of the race-track) and S_2 (at the centre of the race-track) is not the same because the current density varies along the cross section of the race-track (Fig. 4.3b and c). However, if we consider a race-track slice like l_1, then the total current through such a line is constant along the race-track for a planar circular magnetron. For a rectangular magnetron, this is a simplification as along the race-track the current to the target surface can vary, especially in the regions just behind the turnaround region (see e.g. [Fan03, Buyle05]). However, these effects will not be considered here.

We conclude that for a MD, instead of a current density per surface area, a current density per unit race-track length is needed so that:

$$I_d = j_m L_{rt} \tag{4.2}$$

with L_{rt} the length of the race-track (Fig. 4.3). Hence, the task of calculating I_d is reduced to finding the line current density j_m.

The first step in the deduction of j_m, is the integration of current density as obtained from the CL law over the width of the race-track:

$$j_m = \int j_d'(x)dx \tag{4.3}$$

Note that in the above equation, the surface current density is denoted with j_d'. The prime is used to indicate that it is obtained from the *extended* CL law (see further). The relation between j_d and j_d' is given by:

$$j_d'(x) = j_d K(x) \tag{4.4}$$

with $K(x)$ a factor that will be discussed in section 4.2.3.5. The surface current density j_d is constant because the cathode sheath thickness is taken constant along the x-axis in the SCM. This has to be kept in mind when determining $K(x)$.

4.2.3.2 Child-Langmuir law (CL law)

For a diode discharge, the surface current density j_d can be determined using the CL law (see also eq. (1.26) in section I.1.3.3.2):

$$j = \frac{4}{9}\varepsilon_0 \left(\frac{2e}{M}\right)^{1/2} \frac{V_w^{3/2}}{d_E^2} \tag{4.5}$$

The only difference with the expression shown in section I.1.3.3.2 is that we have replaced the cathode sheath thickness d_{CL} by d_E as here no distinction is made for the cathode sheath thicknesses obtained using different models.

The CL law is based on the idea of a space charge limited current [Chapman80]. This is generally valid for calculating the current from an emitter of charged particles to an electrode that attracts these particles (Fig. 4.4). Important assumptions to deduce this law are that the charged particles move collisionless in the sheath and that no other charge carriers are present within the sheath. Moreover, as mentioned in [Chapman80] when deducing the law, "*space charge limitation applies only in the absence of a more stringent limitation such as the supply of charge carriers*".

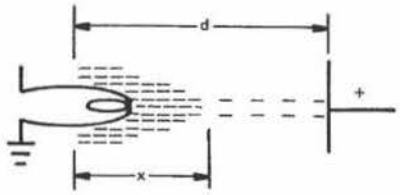

Fig. 4.4 Sketch of the situation for which the CL law can be applied. At the left side, there is a source of charge carriers (a filament emitting electrons). The charge carriers are attracted to an electrode at a certain distance d. In front of this electrode a sheath is formed. Among other requirements, the CL law can only be applied when (i) enough charge carriers are supplied, (ii) all charge carriers enter the sheath at the same position and (iii) only one type of charge carrier exists in the sheath [Chapman80].

If the law is applied to a filament emitting electrons, this requirement of charge supply poses no problem as the charge carriers are generated abundantly "at the right time" and "at the right position". Hence, the requirement is fulfilled "in time" and "in space". If the CL law is applied to a glow or magnetron discharge the charged particles are the ions and the attracting electrode acts as cathode. The latter is important because it implies that the (cathode) sheath has to maintain the discharge. Hence, the requirement "supply of charge carriers" is not trivial. To further explain the principle of this charge supply requirement, we consider how the diode discharge is maintained.

The maintaining of a diode discharge is similar to the one of a MD. A SE is emitted from the target and accelerated over the cathode sheath into the discharge. There, it generates electron-ion pairs. The positive ions are attracted by the cathode and the resulting bombardment leads to the emission of a new SE. A more detailed description of this mechanism can be found in [Chapman80].

Now, we look at the requirement of charge supply in time. Be τ_i the time needed by the ions to cross the sheath and τ_e the time needed by a SE emitted from the cathode to evolve from a HEE to a BE (*b*ulk *e*lectron). The latter corresponds with the lifetime of the electron in the discharge, i.e. the time during which it generates ion-electron pairs (section 2.1). For the requirement of a sufficient ion supply, τ_e should be much smaller than τ_i. Diode discharges operate typically at a pressure of 50 Pa ($n_g \approx 1.3\times10^{16}/cm^3$) or more and a discharge voltage around 900 V. Given that the cross section for electron impact ionisation is around $1\text{-}3\times10^{-16}cm^2$ in the energy range 100-900 eV (Fig. 1.4 in section I.1.2.1.1) the time scale to generate one electron-ion pair is of the order of 0.6 ns at 50 Pa. Given an effective ionisation energy W of 30 eV (section 2.6.1), this means that an electron generates all its ionisations within roughly 18 ns, i.e. $\tau_e \approx 18$ ns. On the other hand, the time τ_i for an ion to cross a sheath of 900 V and a typical thickness of 2 mm [Bogaerts96], is around 150 ns. This is about ten times larger than τ_e, which means that for a typical diode discharge the requirement of a sufficient charge carrier supply in time is fulfilled.

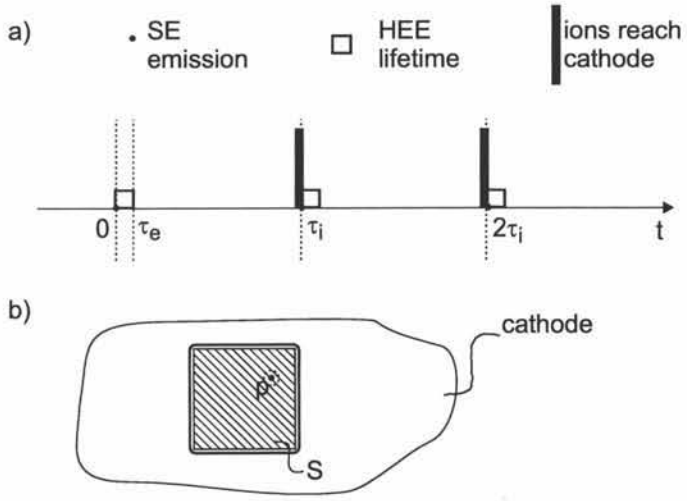

Fig. 4.5 Schematic representation of the charge supply requirement in time (*a*) and space (*b*). In part *a* the different events relevant for maintaining the discharge are indicated on a timeline: the emission of a SE (•), the time τ_e during which it generates ions (□) and the point in time when the ions strike the cathode (▮). The small width of this bar symbolises the spread of the latter event. A time τ_i after the emission of the SE the ions strike the cathode and a new cycle starts. In part *b*, the ions generated by an SE emitted at position *p* bombard the cathode in the area denoted by the dotted circle. Consequently, the ions generated by the SE emitted from the macroscopic area *S* bombard the cathode in the area within the thick dark line, which is practically identical to *S*.

The maintaining cycle -the events of SE emission, ion generation and ions reaching the cathode- is sketched on a time line in Fig. 4.5a. Once an electron is emitted, it generates ions during τ_e. The majority of the ions is generated at the end of the cathode sheath. As τ_e is much smaller (roughly a factor 10) than τ_i, the latter is hardly influenced by τ_e. However, there is a certain spread on τ_i. This spread originates from the spread in heights above the target where the ions are generated and from ion interactions with the discharge gas. In Fig. 4.5a the spread of τ_i is sketched by the thickness of the black vertical line that indicates τ_i. A new maintaining cycle starts once the cathode surface is bombarded with the required number of ions to emit, on average, a new SE. The time scale at which the maintaining cycle repeats itself is τ_i (Fig. 4.5a). This corresponds with the time the ions need to cross the sheath to which the CL law is applied.

Next, we look at the requirement of charge supply in space. Consider again a diode discharge with surface current density j_d for a given surface S. Assume that S is a "macroscopic" surface area, i.e. its dimensions are much larger than the typical mean free path length $\lambda_{e,i}$ for electron impact ionisation (for a typical diode discharge at 50 Pa: $\lambda_{e,i} \approx 5$ mm). Consider an electron emitted at point p. It is accelerated perpendicular to the cathode and generates ions. Because of its interactions with the discharge gas, its velocity vector is scattered. Hence, the ions are not generated exactly above p but in an area with radius r around it. We now try to get an estimate of r.

For a SE yield of 0.1, ten ions should strike the cathode per emitted SE to maintain the discharge. The maximum distance the electron can drift in the direction parallel to the cathode in-between two ionisations is given by the mean free path length $\lambda_{e,i}$. However, this is only valid when the electron velocity is parallel with the cathode plane. Given the scattering of the electrons with the discharge gas, this an upper limit. A more realistic estimate is half this length. Thus, using the theory of random walk which states that the average distance from the starting point is proportional with the square root of the number of steps [Wikipedia05], we find for r:

$$r \approx \sqrt{10}\frac{\lambda_{e,i}}{2} \tag{4.6}$$

which results in $r \approx 8$ mm. The average position of the ions hitting the target will be centred around the initial emission point p. The ions generated by electrons emitted in S, bombard the cathode in practically the same area and ensure the emission of a new electron from within S. This means that the requirement of charge supply in space is fulfilled for a macroscopic surface.

In conclusion, in a diode discharge the requirements of charge supply per individual maintaining cycle is fulfilled, both in time and space. As will be shown, this is not the case for an individual maintaining cycle in the MD. Hence, to ensure nevertheless this requirement, several maintaining cycles have to run in parallel in time and in space. Of course, in a diode discharge also several electrons are in parallel in the discharge. The essential difference is that the maintaining cycle can be represented by considering an individual electron.

4.2.3.3 Extension of CL law to maintaining cycles running parallel in time

In a magnetron discharge, the gas pressure is typically 0.5 Pa, the discharge voltage 300 V, the presheath potential drop -5 V and the cathode sheath thickness 2 mm. We first check whether the requirement of charge supply in time is met. The average time to generate an ion-electron pair is around 60 ns. One electron can generate roughly ten electron-ion pairs ($W = 30$ eV), leading to $\tau_e \approx 600$ ns. Now we need to determine τ_i, the time required by the ions to reach the cathode.

Define φ as the fraction of the ions generated in the cathode sheath (1-φ as the fraction generated above the cathode sheath), see Fig. 4.6a. The time needed to reach the cathode depends on the height where the ions are generated. It was calculated that ions generated at e.g. 2.5 and 5 mm above the target (at $x = 0$), require up to 0.75 and 1.8 µs, respectively, to reach the cathode (for the above mentioned conditions). For simplicity, we group all ions generated above the sheath together and say they reach the target after time τ_a, with τ_a the weighted average of the actual times of these ions. As this time is much larger than τ_e, the requirement of charge supply in time is, at first sight, fulfilled.

However, this is not correct. As mentioned before, when applying the CL law to a cathode sheath, the time constant required for the maintaining cycle is τ_i, the time an ion generated at the end of the cathode sheath needs to cross it. Given the typical values for the MD, we find $\tau_i \approx 300$ ns. This is smaller than τ_e, and thus, the charge supply requirement is not fulfilled. These values for τ_e and τ_i indicate that, contrary to the diode discharge, the CL law cannot be applied directly here to describe the current through the cathode sheath. Indeed, applying the CL law requires that all ions enter the sheath at the same position and have the same transit time through the sheath. However, this is clearly not the case here: ions are also generated within the cathode sheath and these reach the target quickly because of the strong electric field. Hence, the question arises how to describe the relation between the cathode sheath thickness and the surface current density.

A first possibility is to consider the "whole" cathode sheath, i.e. both the ion sheath (electron-free) and the Debye sheath (transition region). Expressions relating the sheath thickness and the plasma parameters for this case can be found in literature, e.g. [Kono04] (see also section I.1.3.3.2) but no expression for the surface current density was found. A second possibility, which is chosen here, is to find a way to extend the CL law so that it can deal with the non-neglectable fraction φ of ions generated within the sheath.

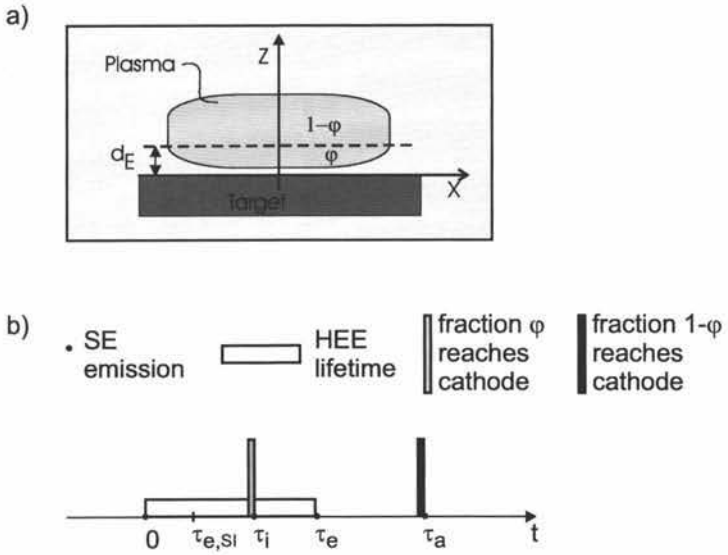

Fig. 4.6 *a*) Sketch of the MD area with the indication where the fractions φ and 1-φ are generated. The first fraction reaches the cathode within τ_i, the latter (on average) within τ_a. *b*) Timeline indicating the most important events of the maintaining cycle.

Consider the three characteristic time scales in the MD and find $\tau_i<\tau_e<\tau_a$ as shown in Fig. 4.6b. For simplicity, we assume that all the ions generated in the cathode sheath reach the cathode at τ_i. Assume now $\tau_e<<\tau_a$. This way, the exact time at which an ion is generated above the cathode sheath will practically have no influence on τ_a, the time needed to reach the target. As said, the charge supply requirement for fraction 1-φ of the ions generated above the cathode sheath is fulfilled. Now, we look at the fraction φ generated within the sheath. As mentioned in section 2.6.4, the HEE are pushed out of the sheath due to interactions with the discharge gas. This implies that sheath ionisation occurs relatively early in the electron lifetime in the discharge. Hence, the time $\tau_{e,SI}$ after which the ion generation in the sheath

stops, is considerably smaller than τ_e. On the other hand, τ_i is of the same order as τ_e. Consequently, we can simplify the situation by assuming that $\tau_{e,SI}$ is smaller than τ_i. This means that also for the fraction φ generated in the sheath, the required charge supply is fulfilled.

We stress that the foregoing reasoning is a simplification as in reality the time the ions need to reach the cathode will vary. Nevertheless, Monte Carlo simulations performed by Goeckner et al. to determine the ion transit times support this approach [Goeckner91]. They calculated the ion lifetime in the discharge and found a group "born in sheath" (fraction φ) reaching the cathode after approximately 200 ns and a group "born in presheath" (fraction 1-φ) reaching the cathode after some microseconds (Fig. 4.7). Hence, splitting up the original group of ions in two fractions (φ in the sheath and 1-φ above the sheath) is supported by these simulation results. Moreover, our assumptions have the major advantage that they simplify the situation as the requirement of the charge supply in time is fulfilled for both groups separately. Hence, we should be able to apply the CL law.

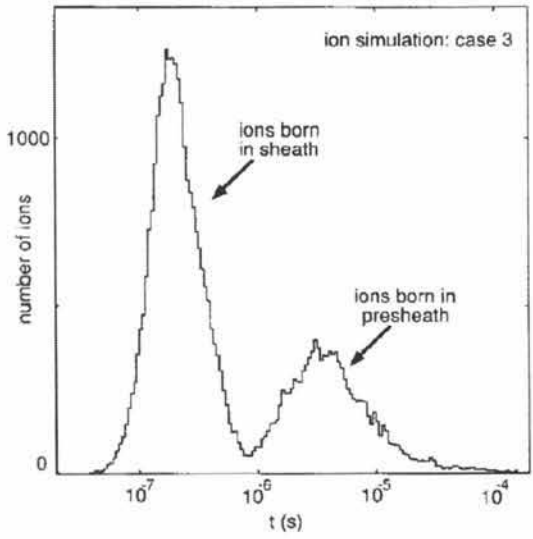

Fig. 4.7 Histogram of ion lifetime based on Monte Carlo simulations. Two groups of ions can be identified: the ones born in the sheath and the ones born in presheath. The latter take approximately ten times as long as the first to reach the cathode. Figure taken from [Goeckner91].

Therefore, we look at the consequences of having two groups of charge carriers with different time scales for maintaining the discharge. As an example, we consider the case where $\varphi = 1/3$ and $\tau_a/\tau_i = 3$. Consider an electron e_1 emitted from the target at $t = 0$ (Fig. 4.8). Given our earlier assumptions, it already generated after time $\tau_{e,SI}$ the fraction φ of the ions, which reach the cathode at τ_i. The electron then continues to cause ionisation and after τ_e it is no longer a HEE but becomes a BE, which means it stops generating ions. The fraction 1-φ reaches the cathode at time τ_a.

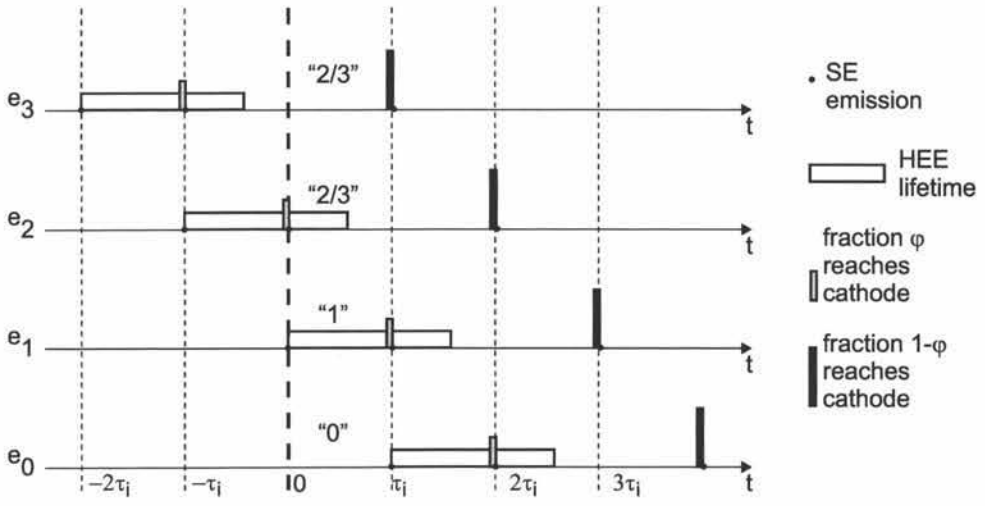

Fig. 4.8 Example illustrating $A_{//,t}$ with $\varphi = 1/3$ and $\tau_a/\tau_i = 3$. The numbers between quotation marks indicate for how much "the electron is in the discharge" (see text) for time interval $[0, \tau_i]$.

In a MD the type of SE emission is predominantly potential emission (section I.1.2.2.1). Hence, the SE yield can be considered independent of the impinging ion energy. This means that all ions bombarding the target have the same probability to emit a SE, whether they are generated in or above the cathode sheath. To maintain a steady state, the total number of ions generated by an electron emitted from the target needs to lead to the emission of, on average, one new SE. Therefore, the fraction φ of the ions generated in the sheath will have a probability φ to emit a SE from the cathode. However, this φ is well below one. Hence, after τ_i the probability φ to emit a SE is too low to guarantee that the discharge is maintained. As illustrated in Fig. 4.8, the remaining fraction $1-\varphi$ reaches the cathode at $\tau = \tau_a = 3\tau_i$. This is too late as applying the CL law requires a new maintaining cycle per τ_i.

The only way to satisfy this requirement is that in parallel with e_1 one or more other electrons are participating in the maintaining cycle and they should ensure that after time τ_i the remaining fraction $1-\varphi$ of bombarding ions is supplied. Consider electron e_2 emitted at $t = -\tau_i$: its fraction φ already reached the target at $t = 0$ but its fraction $1-\varphi$ will only reach the cathode at $t = 2\tau_i$. Hence, we have to look one electron "further back" and consider electron e_3, emitted at $t = -2\tau_i$. The fraction $1-\varphi$ of this electron reaches the target at $t = \tau_i$. Hence, together with the fraction φ of e_1, enough ions bombard the target at τ_i to ensure the emission of a new SE. However, this has an important implication for the number of electrons needed to maintain the discharge. For a diode discharge, at a given moment in time, one electron per maintaining cycle is sufficient (Fig. 4.5a). Note that the expression "an electron is in the discharge" is used to indicate that not all its ions reached the cathode yet. Because of the two ion groups with different transit times τ_i and τ_a one electron per maintaining cycle is not enough. Between the time interval 0 and τ_i, electron e_1 is "completely" in the discharge, i.e. no ions it generated reached the cathode yet. Hence, it counts as one. For electron e_2, only the fraction φ reached the anode, so it still is in the discharge for $1-\varphi$ (2/3 in the example). The same holds for electron e_3. Consequently, in the considered time interval $[0,\tau_i]$ there are 1+2/3+2/3=7/3 electrons required for the maintaining cycle. This number is referred to as $A_{//,t}$. It is clear that in general:

$$A_{//,t} = \varphi + (1-\varphi)\frac{\tau_a}{\tau_i} \tag{4.7}$$

For the example we choose $\tau_a/\tau_i = 3$ and $\varphi = 1/3$ so that indeed $A_{//,t} = 1/3+3\times2/3 = 7/3$. Consequently, to apply the CL law in the case of two ion groups we need to multiply the expression for the surface current density j_d with $A_{//,t}$, leading to a current density $j_{d,t}$:

$$j_{d,t} = j_d A_{//,t} \tag{4.8}$$

In conclusion, the time the ions need to travel trough the cathode sheath sets a reference time for the discharge. Within this time, the charge supply requirement set by the CL law has to be met. This requirement cannot be fulfilled if there is only one electron per maintaining cycle as the electron takes too long to generate the required number of ions. Instead, a certain number $A_{//,t}$ of electrons are needed per maintaining cycle. This number depends on the characteristic times the two ion groups need to reach the target and on the fraction of ions that is generated within the cathode sheath.

4.2.3.4 Extension of CL law to maintaining cycles running parallel in space

Because of the crossed electric and magnetic fields in the race-track, the electrons experience an E×B drift (section I.1.3.6.1). This drift, like sheath ionisation, complicates the use of the CL law as it implies taking into account that more than one electron per maintaining cycle might be required. This required number is referred to as $A_{//,s}$.

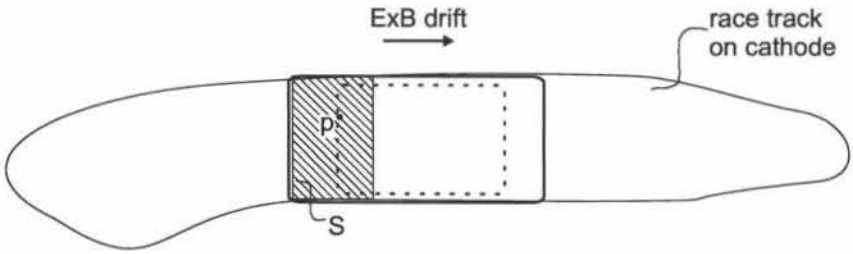

Fig. 4.9 Sketch of the problem of the electron E×B drift on the charge supply requirement: the ions generated by a SE emitted at position p bombard the target within the dotted rectangle. Consequently, the ions generated by SE emitted from a macroscopic area S do not bombard the target within S but within the much larger area indicated by the thick rectangle.

Consider again the situation sketched in Fig. 4.5b for a diode discharge: the ions generated by an SE emitted at p strike the cathode in an area centred around p. It follows that the new SE will be emitted from approximately the same position p. In a MD, the situation is dramatically different. For an electron emitted at position p in the race-track, the ion distribution is spread over the area within the dotted rectangle (Fig. 4.9). Hence, the ions generated by the SE emitted at point p do not contribute to the emission of a new SE in that area. However, if we want to apply the CL law, the requirement of charge supply should be met, i.e. a new SE should be emitted from the area around S within τ_i. This means that in parallel with the electron emitted at p, SE further downstream the race-track (in the sense of the drift direction of the electrons) should be emitted so that these electrons generate the necessary ions above S. Hence, we have again a requirement that several electrons per maintaining cycle should run in parallel. The characteristic that determines this number $A_{//,s}$ is the length $l_{E\times B}$ the electrons drift along the race-track in time τ_i. The number of electrons needed in parallel is equal to $\delta l/l_{E\times B}$, with δl the length of area S along the race-track. Consequently, for the current density per length unit, we find:

$$j_{d,s} = j_d A_{//,s} \tag{4.9}$$

with :

$$A_{//,s} = \frac{1}{l_{ExB}} \tag{4.10}$$

To calculate l_{ExB}, the drift velocity is required. This velocity is estimated by $v_{ExB,nc}/2$, with $v_{ExB,nc}$ the E×B drift velocity of an electron that does not undergo collisions with the discharge gas. Consequently, we find :

$$l_{ExB} = \frac{v_{ExB,nc}}{2}\tau_i \tag{4.11}$$

4.2.3.5 Deduction of the line current density j_m

In the SCM, the cathode sheath thickness is assumed constant. Hence, if the CL law is applied, we find a constant j_d along the x-axis, which is not realistic. For the x-dependence we look at the number of ions bombarding the cathode at x. Given the ionisation distribution $I(x,z)$ (section 2.3.4), the normalised number of ions bombarding the cathode at x is defined as:

$$\mathcal{B}_n(x) = \frac{\sum_{z_j} I(x, z_j)}{\sum_{z_j} I(0, z_j)} \tag{4.12}$$

Hence, this $\mathcal{B}_n(x)$ is normalised so that $\mathcal{B}_n(0) = 1$. This way, the x-dependent surface current density $j_{n\text{-}u}$, which takes into account the non-uniform ion density of the MD, is given by:

$$j_{n-u}(x) = j_d \mathcal{B}_n(x) \tag{4.13}$$

The aim is now to combine the expressions obtained for taking into account the specific MD conditions in order to define the relation between j_d and j_d', i.e. to determine $K(x)$ of eq. (4.4). To satisfy the requirement for charge supply in time and in space, the required numbers $A_{//,t}$ and $A_{//,s}$ need to be multiplied. This together with eq. (4.13) leads to :

$$j_d'(x) = j_d A_{//,t} A_{//,s} \mathcal{B}_n(x) \tag{4.14}$$

Thus the factor $K(x)$ is given by the product of $A_{//,t}$, $A_{//,s}$ and the normalised ion bombardment $\mathcal{B}_n(x)$. Combined with eq. (4.3) this leads to:

$$j_m = \int j_d A_{//,t} A_{//,s} \mathcal{B}_n(x) dx \tag{4.15}$$

As already mentioned, j_d is independent of x but we need to investigate a possible x-dependence of $A_{//,t}$ and $A_{//,s}$.

The number $A_{//,t}$ is determined by the time needed by the ions to reach the cathode and by the relative number of ions generated in the sheath. Of course, the ionisation distribution varies according to the initial position of the SE. However, the majority of the SE is emitted from a rather narrow interval along the x-axis (section 3.3.2). For this interval, the ionisation

distribution for the different start positions is rather similar (section 2.6.3.2) so that the x-dependence of $A_{//,t}$ can be neglected.

The situation for $A_{//,s}$ is different as the E×B drift, and consequently l_{ExB}, depends strongly on the SE initial position. However, it does not have a physical meaning to split up the maintaining cycle per x-position because the SE emitted at different x undoubtedly have a strong mutual interaction. Hence, we need one $A_{//,s}$ for all x-values together. To calculate this average value $\bar{A}_{//,s}$ we do need to take into account the x-dependence of the E×B drift. In the practical implementation of the model, the x-axis is split up in intervals. The average is then given by :

$$\bar{A}_{//,s} = \frac{\sum_i \left(A_{//,s}\right)_i r_i}{\sum_i r_i} \tag{4.16}$$

as the different $(A_{//,s})_i$, the number of electrons in parallel in space for a SE emitted at x_i, need to be weighted with the contribution of that position x_i in the SE emission. That contribution is given by element i of the emission profile r. Thus, we find for j_m :

$$j_m = j_d A_{//,t} \bar{A}_{//,s} \int \mathcal{B}_n(x) dx \tag{4.17}$$

or for the numerical implementation:

$$j_m = j_d A_{//,t} \bar{A}_{//,s} \sum_i \mathcal{B}_{i,n} \Delta x \tag{4.18}$$

From this expression the total discharge current I_d can be readily determined by multiplying with the race-track length L_{rt} (eq. (4.2)).

The above expressions for j_m still rely on the CL law to determine the surface current density j_d for a given discharge voltage and cathode sheath thickness. This means that we have to take into account the major limitations to apply the CL law to the MD as discussed in section I.1.3.3.5. The problem of the non-uniform current density and of the ion generation within the sheath is resolved. The other two limitations remain: ϕ_w (the ratio of V_d and kT_e) is rather small and the electron density in the sheath is non-zero. As most of the sheath ionisation takes places near the sheath edge (see e.g. Fig. 6.20 in section 6.4.3.3), this should not be critical. Nevertheless, it is important to keep in mind that the model for the line current density j_m is only a simplified representation of the actual physics.

4.2.3.6 Summary of extending the CL law

The Child-Langmuir law (CL law), which describes the space charge limited current between two electrodes, is encountered frequently in plasma physics [Luginsland02]. It is also used in diode (e.g. [Maniv82]) and magnetron discharges (e.g. [Westwood83, Rossnagel87b, LanGu88]). However, one should take into account that the CL law can only be applied when the charge supply requirement is fulfilled, which is a fundamental restriction for its use. As the discharge has to supply the charge carriers, this requirement cannot be taken for granted. We distinguish between the availability of charge carriers "in time" and "in space".

To check the requirement "in time", two time scales are critical: the time the ions need to reach the cathode and the time the electrons need to generate the ions. The charge supply requirement in time is only fulfilled if the latter occurs much faster as the first. In a diode

discharge this requirement is met. In a magnetron discharge it is not because the low gas pressures (factor 100 less than in diode discharges) increases the ion generation time.

The requirement "in space" basically means that the electrons need to generate the ions in such a region that, on average, the ions hit the cathode at the same spot as from where the electron was emitted. This requirement is met in diode discharges but not in magnetron discharges because, due to the E×B drift of the electrons, the ions are generated scattered over the race-track length.

Because of these requirements, the CL law cannot directly be applied to the magnetron discharge. Nevertheless, the CL law can still be used when taking into account that a certain number of electrons "running in parallel" is required to represent the maintaining cycle. Consequently, an expression for the line current density j_m in a MD could be developed. This extension of the CL law does not resolve the other limitations of its use to a MD like the non-zero electron density.

4.3 Results and discussion

For the results presented here the *standard settings* of section 3.3.1 are used, except for the fact that V_d and d_E are not fixed. The magnetic field line that intersects the target at $|x| = 16.25$ mm is taken as virtual anode. Instead of a "true" IV, i.e. discharge current I_d as a function of the discharge voltage V_d, the current line density j_m is plotted as a function of V_d. This is equivalent as j_m is proportional with I_d, see eq. (4.2). Consequently, we refer also to such a j_m vs. V_d plot as an "IV".

4.3.1 Understanding the IV characteristic

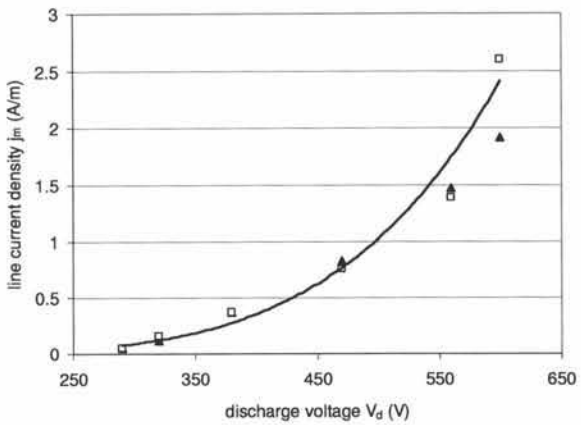

Fig. 4.10 IV at 0.5 Pa. The triangles represent the interpolated results, the squares the actually calculated results. There is good agreement between the interpolated and calculated points although there is a deviation at high currents. The full line is a fit using $I_d = kV_d^n$.

In order to obtain the IV at 0.5 Pa, we started from the basic result (Fig. 3.12 in section 3.3.4). Then, through linear interpolation, the combinations of V_d and d_E which correspond with 0.5 Pa were determined. The current at these points was also determined by linear interpolation. The result is shown in Fig. 4.10. To check the validity of the interpolation approach, the self-consistent pressure p_{sc} and the current line density j_m were directly calculated using the SCM with the interpolated V_d and d_E. The interpolated points (triangles)

agree well with the directly simulated ones (squares) (Fig. 4.10). The largest difference occurs at the highest discharge voltage. Also, the calculated p_{sc} were very close to 0.5 Pa (not shown). Hence, in what follows, the explicit recalculation of the interpolated points is not performed.

We now investigate the obtained IV. As mentioned, the experimentally obtained IVs are typically fitted using the expression $I_d = kV_d^n$ (eq. (1.34) in section I.1.3.4.1). The IV is then characterised by its n-value. For the simulated IV, $n = 4.7$ is found. This is within the typical range encountered for magnetron discharges, although it is on the lower side of the range. As mentioned, the equation used to fit the IV is purely empirical, i.e. there is no physical background to it. We will not try to explain the empirical relation but, using the simulation results, will try to understand why the IV in a MD becomes so steep at sufficiently high electrical power, i.e. why the current becomes practically independent of the discharge voltage above a certain discharge voltage.

Consider again eq. (4.17) for j_m on which the calculation of I_d is based. Basically, the dependence of j_m on V_d is caused by j_d, $\bar{A}_{//,s}$, $A_{//,t}$ and $\mathcal{B}_n(x)$. The latter can be characterised by the FWHM of the erosion profile w. At low V_d, w increases with increasing V_d but at high V_d w only increases slightly (Fig. 4.11a). Hence, it is of less importance to explain the strong increase in j_m. The dependence of the other three parameters on V_d is plotted in Fig. 4.11b. The dependence of j_d on V_d can be fitted by a power law: $j_d \sim V_d^q$. For the presented results we obtain $q = 3.6$, which is smaller than n, the value used to characterise the IV. Note that q is not equal to 3/2 as one might, at first, expect from the CL law (eq. (4.5)) because d_E also changes with V_d (Fig. 4.11a).

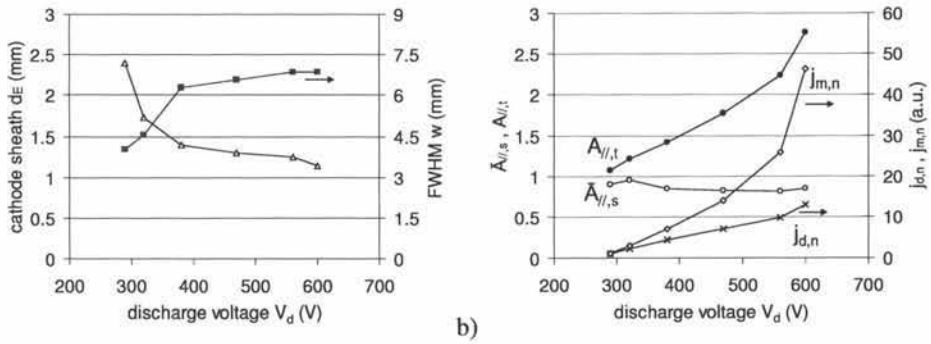

Fig. 4.11 *a*) The cathode sheath thickness d_E (△) and FWHM w (■) of the erosion profile as a function of V_d. *b*) The discharge voltage dependence of the current density j_d (×) and of the required number of electrons per maintaining cycle in space $\bar{A}_{//,s}$ (O) and in time $A_{//,t}$ (•). The strong increase in the latter at sufficiently high V_d explains how j_m (◇) can increase practically independent of the discharge voltage at large V_d. Note that j_d and j_m are normalised, i.e. they are plotted relative to the value they have at the lowest V_d considered (290 V).

From Fig. 4.11b it follows that the parameter $\bar{A}_{//,s}$ is practically independent of V_d. This is not surprising as it is predominantly determined by the E×B drift velocity of the electrons which is only weakly dependent on V_d. This factor basically represents the influence of the target area on the discharge current and can, as such, be interpreted as a scale factor. It does not have a fundamental influence on the typical shape of the IV but influences the absolute current values. This factor $\bar{A}_{//,s}$ helps to explain the pressure behaviour (section 4.3.2).

More interesting here is the behaviour of $A_{//,t}$, which increases strongly with increasing V_d. By considering this factor, we can understand how the discharge current can increase so

strongly at practically constant discharge voltage. At low electrical power, the discharge is basically only able to maintain itself. This means that there is only one electron per maintaining cycle ($A_{//,t}$ close to one). When the discharge voltage is increased, less sheath ionisation is required, enabling the cathode sheath to become thinner (Fig. 4.11a). This way, an increasing fraction of the ionisation occurs above the sheath (1-φ increases). This means that the ions will, on average, remain longer in the discharge as the acceleration towards the target occurs slower for ions generated above the cathode sheath.

At first sight, it might appear surprising that with increasing discharge current the ions need more time to reach the target but this is also observed experimentally: Sheridan and Goree report for a MD at 1.1 Pa and a target diameter of 4.25 inch that the average charged particle confinement time increases from 0.65 (lower end of IV) to 0.85 μs (higher end of IV) [Sheridan89a]. For the IV presented in Fig. 4.10 the average time the ions reside in the discharge varies from approximately 0.47 (lower end) to 0.70 μs (higher end), which indicates that the model reproduces quite accurately the charged particle confinement times and its increase with increasing electrical power.

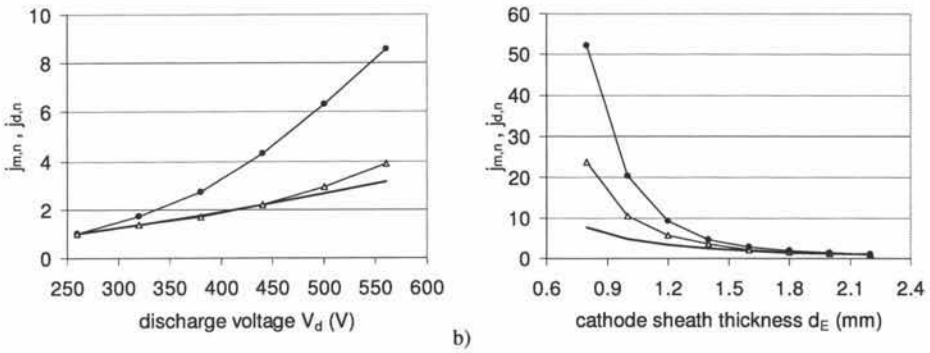

Fig. 4.12 Isolated influence of V_d (*a*) and d_E (*b*) on the normalised $j_{m,n}$ and $j_{d,n}$. The "normalised" refers to the fact that they are plotted relative to the value they have at the lowest j_m and j_d considered. In part *a* of the figure, the dependence on V_d is shown for $d_E = 0.8$ (•) and 2.2 mm (△). In part *b* the dependence on d_E is shown for $V_d = 220$ (△) and 560 V (•). In both graphs the current density $j_{d,n}$ as given by the CL law is also indicated (—). It is clear that this dependence is too weak.

Now, we single out the influence of the discharge voltage and the cathode sheath thickness on the current. First, consider the influence of the discharge voltage. Fig. 4.12a shows the normalised $j_{m,n}$ ($j_{m,n} = j_m/j_m(V_d = 260\text{ V})$) for $d_E = 0.8$ and 2.2 mm. Also the dependence according to the CL law is plotted. The latter clearly underestimates the dependence because it does not account for the changes in $A_{//,t}$, $\bar{A}_{//,s}$ and w. Fig. 4.12b shows the normalised $j_{m,n}$ ($j_{m,n} = j_m/j_m(d_E = 2.2\text{ mm})$) for $V_d = 260$ and $V_d = 560$ V together with the CL law, which again underestimates the dependence. The very strong variation of the current with d_E at small d_E is striking, e.g. at $V_d = 560$ V the current increases with a factor of more than 2.5 when the cathode sheath is reduced from 1.0 to 0.8 mm. This strong variation explains why the current in the MD can increase practically independently of the discharge voltage at high electrical power input.

The sensitivity of the current to the sheath thickness also indicates an extra difficulty for purely numerical self-consistent simulations. In literature, the reported resolution along the *z*-axis for this type of simulations is typically 0.1 mm, see e.g. [Kondo99a, Shidoji99a]. However, given the dependence of the current on the exact cathode sheath thickness, it is clear that the corresponding result cannot be very accurate.

When looking at the extended Thornton relation (eq. (3.7)), it is clear that the discharge voltage must influence the MD through f and/or m as γ is determined by the target material. Hence, it is interesting to consider the behaviour of $\langle f \rangle$, $\langle m \rangle$ and $\langle fm \rangle$ as a function of V_d (Fig. 4.13): $\langle m \rangle$ and $\langle fm \rangle$ clearly increase while $\langle f \rangle$ remains practically constant with decreasing V_d. The strong increase in $\langle m \rangle$ could be expected as also the sheath thickness d_E increases strongly (Fig. 4.11a). This reveals the behaviour of the MD at low electrical powers: the decrease in V_d is compensated by increasing $\langle fm \rangle$ as this enlarges the effective SE yield. As $\langle f \rangle$ is practically not influenced by V_d, $\langle m \rangle$ has to increase. This requires a widening of the cathode sheath. However, the need for a large multiplication factor leads to a reduced stability because the emission of a single SE from the target has a much larger contribution to the discharge. The processes of SE emission and sheath ionisation are statistical processes. Hence, both can vary strongly from electron to electron giving rise to instabilities, which are typical for MD run at very low electrical powers.

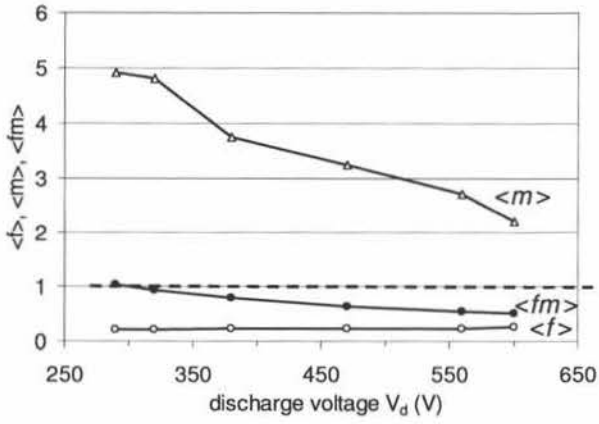

Fig. 4.13 Influence of V_d on the average EGIP $\langle f \rangle$, on the average multiplication factor $\langle m \rangle$ and on the product $\langle fm \rangle$ at constant pressure (0.5 Pa).

The last item related to the IV is the influence of the presheath. The presheath is characterised in our model by V_{ps}, the potential drop over the presheath, and by the position of the virtual anode. The latter is characterised by z_{VA}, the height of the virtual anode above the target at the centre of the race-track ($x = 0$). This parameter cannot be chosen independently but depends on the anode position. As mentioned, the standard setting for V_{ps} is -5 V. This value is chosen based on the fact that the voltage drop over the presheath is half the electron temperature (section I.1.3.3.1). Assuming an electron temperature of 10 eV might appear rather high but the electron temperature does increase towards the cathode (section I.1.3.5.6). The influence of V_{ps} on the IV is investigated: Fig. 3.6 shows the IV at 0.5 Pa obtained for V_{ps} equal to -3, -5 and -10 V. The trend is an increase in j_m with increasing $|V_{ps}|$. The reason is that increasing $|V_{ps}|$ decreases the time τ_i an ion generated at the end of the cathode sheath needs to reach the target. This leads to a higher $A_{//,s}$, see eqs. (4.10) and (4.11). In reality, V_{ps} depends on the external parameters and influences as such the IV, implying that for a true self-consistent model V_{ps} should be calculated based on the plasma properties. However, Fig. 3.6 shows that the influence of V_{ps} is rather small. Consequently, this dependence is not considered critical and will be neglected, i.e. in what follows V_{ps} will be taken -5 V.

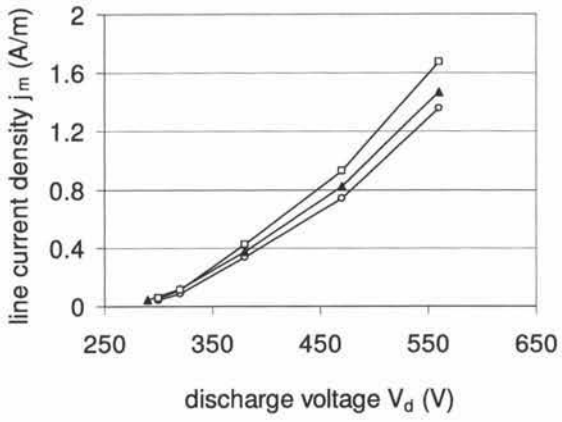

Fig. 4.14 Influence of V_{ps} on the IV: results shown are obtained for V_{ps} = -3 (O), -5 (▲) and -10 V (□). The line current density j_m is, except for small V_d, consistently slightly larger for higher $|V_{ps}|$.

4.3.2 Pressure dependence of the MD

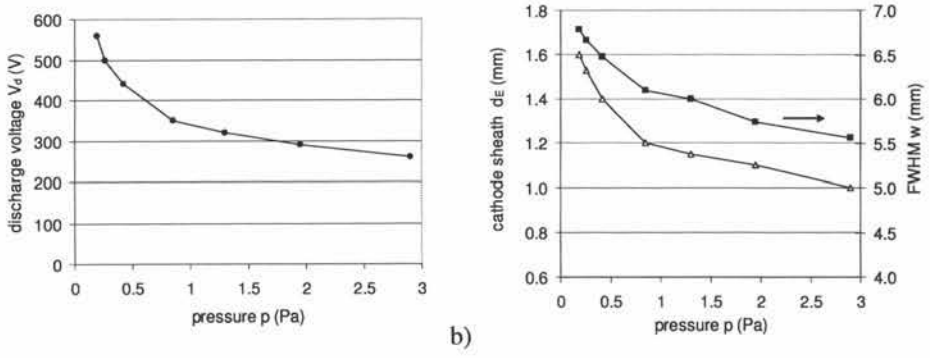

Fig. 4.15 Influence of pressure on the discharge voltage V_d (*a*), on the cathode sheath thickness d_E (△) and on the FWHM *w* of the erosion profile (■) (*b*) at constant j_m (0.5 A/m).

The SCM is applied to simulate the influence of the gas pressure on the MD. The settings are the same as in the previous section except that the basic results are interpolated in such a way that the discharge properties are obtained for a constant line current density (j_m = 0.5 A/m) while the pressure varies. This corresponds with experiments conducted at constant discharge current. The pressure dependence of the discharge voltage (Fig. 4.15a), of the cathode sheath thickness d_E and of the erosion profile *w* (Fig. 4.15b) is calculated. The typical pressure behaviour is reproduced: with decreasing pressure, the discharge voltage increases, the cathode sheath becomes thicker and the erosion profile widens. These pressure dependences are also measured experimentally and can be found in [Depla05a], [Gvozdev98, Rossnagel87b] and [Fukami87], respectively. In agreement with the experiments we find that at high pressures the dependence of the MD properties on the gas pressure is rather weak but the influence of the pressure increases with decreasing pressure.

Before explaining the observed behaviour, the pressure dependence of the diode discharge is considered. There, the emitted SE from the cathode are accelerated into the plasma. As there is no magnetic field, the only way the HEE can be prevented from escaping

the discharge is by interactions with the discharge. Hence, when the gas pressure is reduced, the HEE have an increased probability to leave the discharge. When considering the extended Thornton relation (eq. (3.7) in section 3.3.3), this means that with decreasing pressure, ε_e decreases. As a result V_d increases, which explains the typical diode response to a pressure reduction.

It is common to apply the same reasoning to explain the pressure dependence of the MD. This is not correct: as mentioned in section 2.6.3.3, the position where the HEE perform ionisation does not depend directly on the gas pressure. With increasing V_d the HEE become more energetic, and thus, undergo more interactions with the discharge gas. Consequently, the ionisation will be more spread out. However, practically no HEE leave the discharge area, even at the highest simulated discharge voltages (see also the end of section 3.3.2). This means that regardless the pressure, ε_e can be taken equal to one for the typical magnetic field strengths encountered in sputter magnetrons.

Sometimes, the pressure dependence is explained by mentioning that the HEE have higher energies at reduced pressure. These higher electron energies lead to less efficient ionisation as the ionisation cross section decreases for electron energies above 100 eV. However, also the other cross sections (for elastic collisions and excitations) decrease for increasing energy so that the effective ionisation energy W hardly increases for increasing V_d. Indeed, as shown in Table 2.1 in section 2.6.1, W is hardly influenced by V_d in the range 320 to 560 V. Hence, the pressure dependence cannot be explained by this change in W.

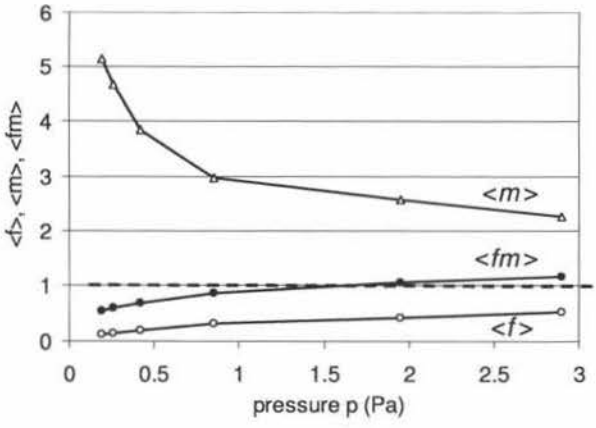

Fig. 4.16 Influence of the gas pressure p_{wc} on the average EGIP <*f*>, on the average multiplication factor <*m*> and on the product <*fm*> at a constant j_m (0.5 A/m).

When looking at the extended Thornton relation (eq. (3.7)), it is clear that the pressure must influence the MD through f and/or m as γ is determined by the target material. Fig. 4.16 shows <*f*>, <*m*> and <*fm*> as a function of the gas pressure. With decreasing pressure, <*f*> decreases because the electron mean free path length λ increases (eq. (1.15)). Because of this, fewer electrons effectively take part in the discharge. The equilibrium can be restored by either increasing V_d or by increasing the cathode sheath thickness as this increases the multiplication factor. As shown in Fig. 4.16, this is exactly what happens. The need for a large multiplication factor to maintain the discharge leads to a reduced stability, similar as in the case of low discharge voltages (see previous section). This explains the instabilities which are typical for MD run at very low gas pressures.

To explain the widening of the erosion profile, expressed by w, we have to look at the x-dependence of the EGIP f. As shown in e.g. Fig. 1.5, f is much smaller in the centre of the race-track ($x = 0$) than at the edges ($|x|>10$) because a SE emitted at the edge has a much larger s (see section 1.2.6) than the ones emitted at the centre. As a result, a change in λ has a much stronger effect on the EGIP in the centre of the race-track. Consequently, relatively more SE originate from larger x-values with decreasing pressure. As the ionisation distribution of these electrons is more spread along the x-axis (Fig. 2.18 in section 2.6.3.1), this leads to a wider erosion profile.

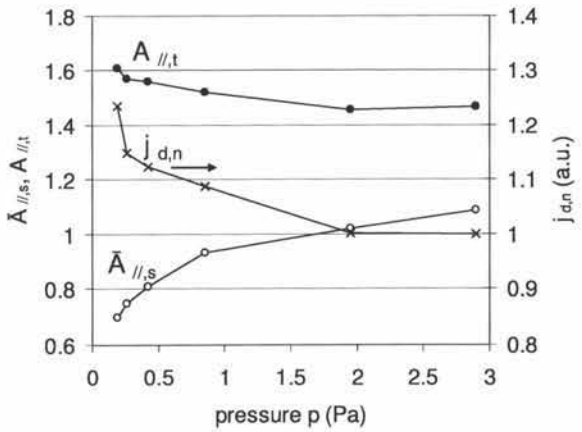

Fig. 4.17 The pressure dependence of the required number of electrons per maintaining cycle in space $\bar{A}_{//,s}$ (O) and in time $A_{//,t}$ (•). Also the surface current density $j_{d,n}$ is plotted (×).

Another point of interest is to investigate how the MD maintains the constant current in spite of the changing pressure. In Fig. 4.17 the pressure behaviour of j_d, $\bar{A}_{//,s}$ and $A_{//,t}$ is shown as they are the main parameters that determine j_m. It is clear that although j_m is kept constant, the three parameters do vary with pressure. With decreasing pressure both j_d and $A_{//,t}$ increase. Hence, to keep j_m constant $\bar{A}_{//,s}$ has to decrease. This is indeed the case: $\bar{A}_{//,s}$ decreases from approximately 1.1 (2.9 Pa) to 0.7 (0.2 Pa). This decrease is due to the increase in $l_{E\times B}$, which is inversely proportional with $\bar{A}_{//,s}$, see eq. (4.10). This increased $l_{E\times B}$ in turn is due to an increased V_d, involving an increase of the E×B drift velocity (eq. (4.11)).

4.3.3 Influence of γ and R on the IV characteristic

In the previous chapter (section 3.3.5) we already simulated the influence of the SE yield γ and of the electron reflection coefficient R on the self-consistent pressure p_{sc} at constant discharge voltage. Here, the influence of γ and R on the IV at 0.5 Pa is simulated.

Fig. 4.18 shows the influence of a variation of γ from 0.08 to 0.12. Although this is only a 50 % increase of γ, the values for j_m are a factor of two higher. This result is in agreement with other simulation results that also reveal the large influence of γ on the discharge current for a given V_d [Kondo99a, Shidoji01a]. Also experiments performed with different targets allow investigation of the influence of the SE yield on the IV. This will be discussed in more detail in section 6.4.3.5 but it is already mentioned here that the same qualitative trend is observed.

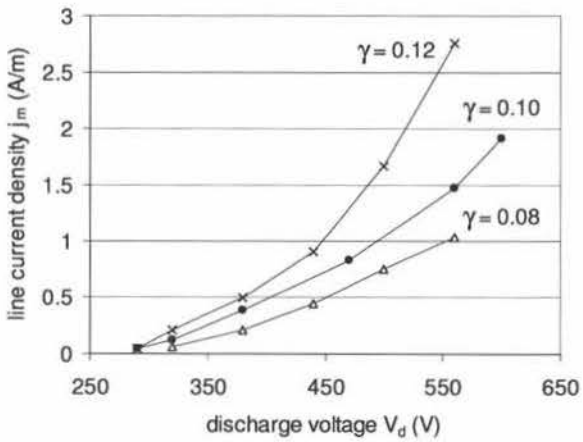

Fig. 4.18 Influence of the SE yield γ on the IV: results shown for γ equal to 0.08 (△), 0.10 (•) and 0.12 (×) at 0.5 Pa.

The effect of R on the IV is shown in Fig. 4.19. Around 500 V an increase in R from 0.3 to 0.5 has a small effect but a further increase to 0.7 leads to a six times higher current. Hence, the sensitivity of the IV to R is even larger as the sensitivity to γ.

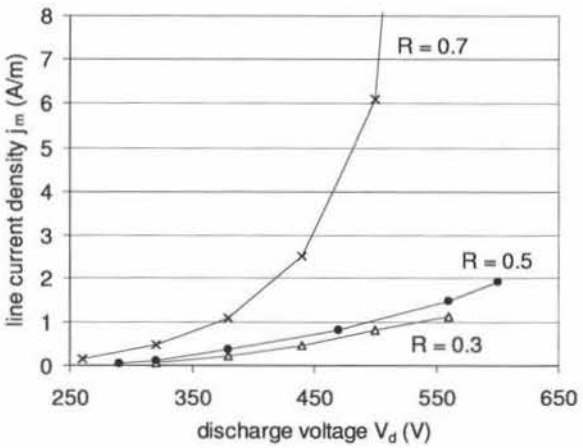

Fig. 4.19 Influence of the electron reflection coefficient R on the IV: results shown for R equal to 0.3 (△), 0.5 (•) and 0.7 (×) at 0.5 Pa.

This indicates that both the SE yield and the electron reflection coefficient have a very strong influence on the discharge current for a given discharge voltage. Given the typical spread on the experimental values for the SE yield and the very limited availability of experimental R-values, this implies that the accuracy of even the most precise self-consistent model is limited. A possible outcome would be to determine γ and/or R by comparing simulated and experimental IVs. However, this requires that all the other aspects of the MD should be very accurately modelled. Given the problem of the anomalous electron transport, this seems not (yet) possible.

4.3.4 Pressure dependence of the IV characteristic

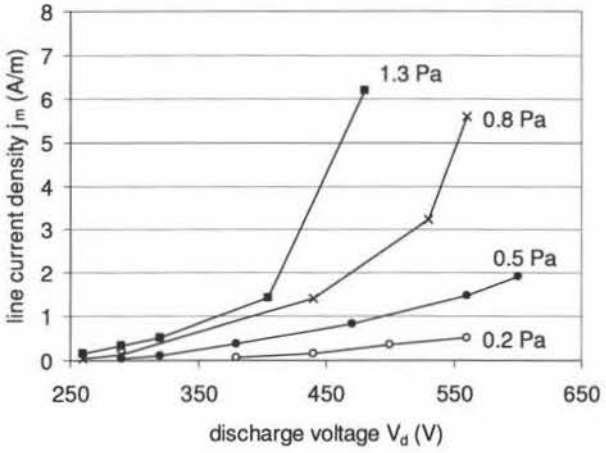

a)

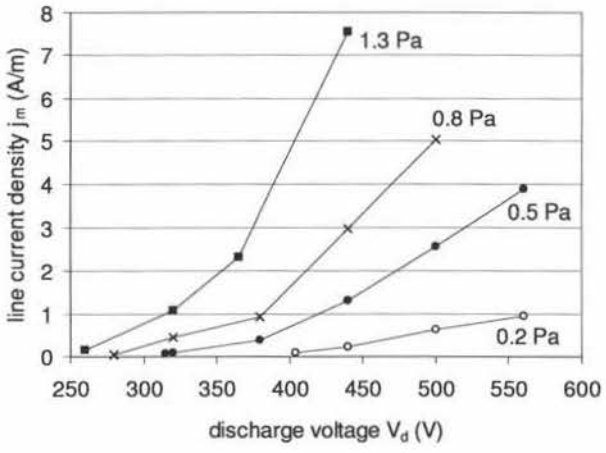

b)

Fig. 4.20 Influence of the gas pressure p_{sc} on the IV: results shown for 0.2 (O), 0.5 (•), 0.8 (×) and 1.3 Pa (■) for B_{max} = 600 (*a*) and 1200 G (*b*).

In this section the basic result is used again to deduce IVs at different pressures. The result at 0.5 Pa is shown together with the IV obtained at 0.2, 0.8 and 1.3 Pa (Fig. 4.20a). For the same pressures, the IV has also been calculated for B_{max} = 1200 G. For these simulated IVs the *n*-values are all between 4.5 and 7.5. Although these are realistic values, they are on the low side of the typical *n*-values encountered, especially for the strong magnetic field.

One clearly sees that the IVs fan out with increasing discharge voltage. This behaviour is observed experimentally as shown in Fig. 4.21a. This plot shows the IV obtained with a tantalum target (8.3 cm diameter) for B_{max} = 420 G for pressures from 0.3 to 5 Pa [Nyaiesh81]. A major difference with the simulated IVs is that the latter do not express the extreme steepness at large discharge voltages.

However, a different pressure dependence of the IV is also observed. In [Depla05a], the behaviour as mentioned above is observed for weak magnetic fields (<400 G). For

stronger magnetic fields the pressure behaviour is as shown in Fig. 4.21b: the shift to lower discharge voltages with increasing pressure is still observed but the IVs are practically parallel to each other. Hence, the pressure dependence of the IVs is influenced by the magnetic field strength. The pressure dependence of the IV was also simulated for $B_{max} = 1200$ G (Fig. 4.20b) but we found practically the same behaviour as for 600 G. Hence, a shortcoming of the simulations is that the pressure dependence of the IVs is the same regardless the magnetic field strength. Because of this relationship with the magnetic field, the magnetic field dependence of the model is first investigated before probing further into this problem.

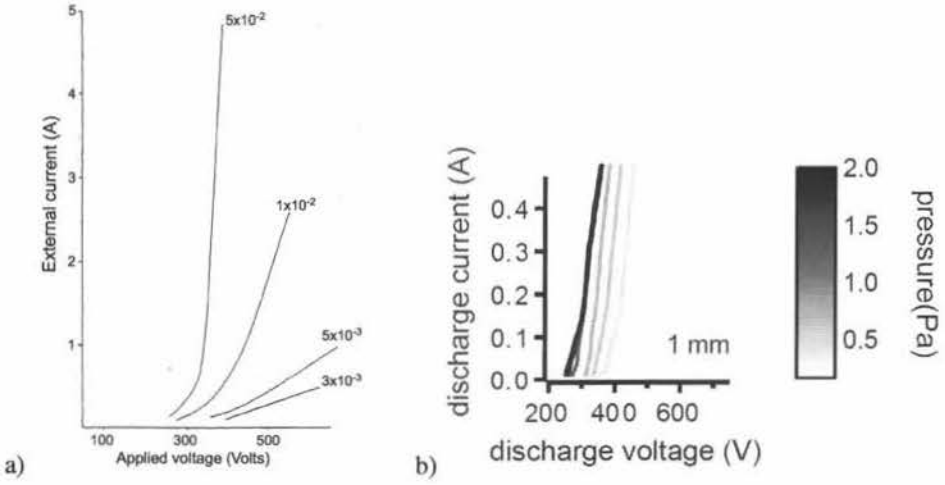

Fig. 4.21 Experimental measurements for the influence of the gas pressure p_{ac} on the IV. The pressure dependence of the IVs for a Ta target for $B_{max} = 420$ G is shown in part (*a*), taken from [Nyaiesh81]. In [Depla05a] the same behaviour is observed at low magnetic fields but at high magnetic fields the dependence as shown in part (*b*) is observed (the example shown is for a Cu target (2 inch diameter) for $B_{max} = 1100$ G).

4.3.5 Magnetic field dependence of the IV characteristic

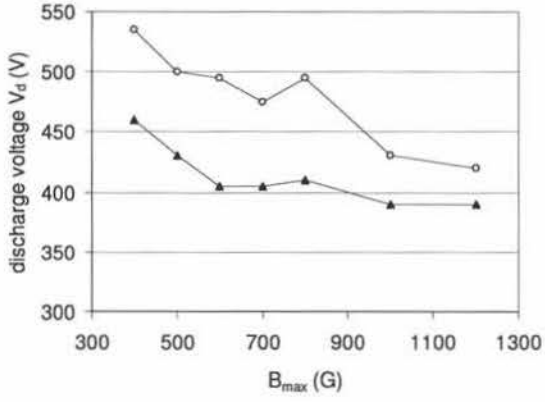

Fig. 4.22 Influence of the magnetic field strength B_{max} on the discharge voltage V_d at constant pressure (0.5 Pa) and constant line current density: $j_m = 0.5$ (▲) and 1.0 A/m (O).

In this section the basic results are calculated for magnetic field strengths B_{max} from 400 to 1200 G. Similar as in the standard case (600 G), interpolation is used to determine the necessary points for the curves. The aim is to see whether the model reproduces the typical magnetic field behaviour of the MD.

The discharge voltage is plotted as a function of B_{max} for $j_m = 0.5$ and 1.0 A/m (Fig. 4.22): V_d decreases with B_{max} in both cases. For 1.0 A/m there is an influence up to the strongest magnetic fields, for 0.5 A/m the influence of B_{max} above 600 G is weak. In [Goree91] it is argued that such an independence of the magnetic field should be expected as practically no high energy electrons escape from the magnetic trap for magnetic field strengths above 500 G (see also section I.1.4.1.2). However, experiments show a decrease with increasing B_{max} up to 1200 G (Fig. 4.23), although at lower pressures (<0.3 Pa) the discharge voltage is seen to level off above 600 G [Depla05a]. From Fig. 4.23 can be deduced that V_d should decrease with increasing B_{max} at constant current, the effect being stronger at high discharge currents. This is exactly what is shown in Fig. 4.22.

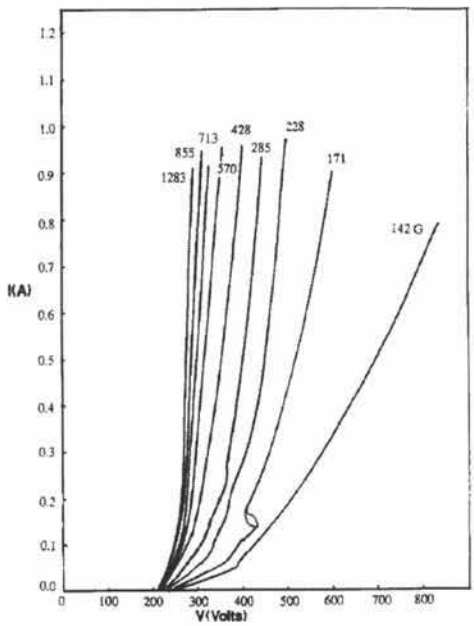

Fig. 4.23 Experimentally measured influence of the magnetic field strength B_{max} on the IV at 5 mTorr, taken from [Wendt90].

The influence of the magnetic field on the IVs is shown in Fig. 4.24: except for the IV at 800 G, the IVs become steeper with increasing B-field, as expected. The n-values increase from 4.6 (400 G) to 7.1 (1200 G). The latter n is rather low given the very strong magnetic field. The figure also shows that even at the strongest magnetic field simulated the IV is not so steep compared to the extreme steepness recorded in experiments (Fig. 4.21b and Fig. 4.23).

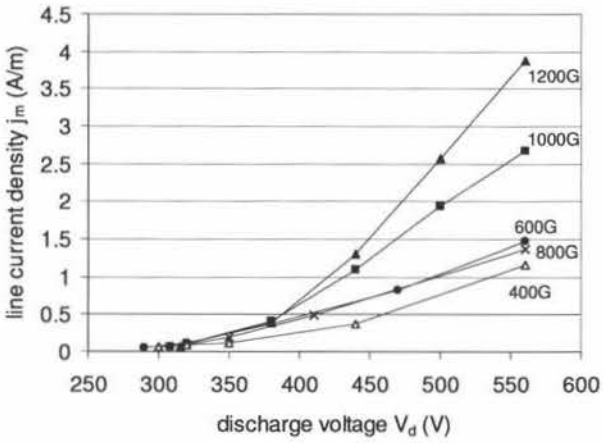

Fig. 4.24 Influence of the magnetic field strength B_{max} on the IV for B_{max} from 400 to 1200 G at 0.5 Pa.

In conclusion, for the magnetic field dependence the SCM simulation results exhibit the same trend as experimentally observed. However, the simulated dependence of the IVs appears weaker than expected. The extremely steep IVs experimentally observed at strong magnetic fields are not retrieved by the SCM.

4.4 Conclusions

In this chapter, the SCM was extended so that the discharge current could be modelled. This model is based on the extension of the Child-Langmuir law so that the typical situation of the MD is taken into account: for a diode discharge the characteristic current density is a surface current density, for a MD it is a line current density. Also the influence of the E×B electron drift and the fact that a large number of ions is generated within the sheath is accounted for.

The developed model allows simulating the current-voltage characteristic of the MD. The typical feature of these characteristics, the steepness at high discharge voltages, can be explained by the increasing number of maintaining cycles running in parallel in time. Also the pressure dependence of the discharge voltage, the cathode sheath and the erosion profile was simulated at constant current. This pressure dependence can be understood by considering its influence on recapture of SE and on sheath ionisation.

The behaviour of the IV under the influence of gas pressure and magnetic field strength was simulated with reasonably good agreement. However, the simulated magnetic field dependence is rather weak and the SCM fails to reproduce the extremely steep IVs that are experimentally reported at very strong magnetic fields. Furthermore, it was shown that the steepness of the IVs increases by increasing the secondary electron yield γ and/or the electron reflection coefficient R.

However, one should not forget that experimental evidence points to the existence of anomalous electron transport, i.e. the electron diffusion in the direction perpendicular to the magnetic field lines is larger than can be expected from classical electron diffusion. This effect is not included in the model here. The possible influence of this enhanced electron diffusion will be investigated in the following two chapters: in Chapter 5 we investigate the influence on the cylindrical MD, in Chapter 6 on the planar MD.

5 MAGNETIC FIELD DEPENDENCE OF THE CYLINDRICAL MAGNETRON DISCHARGE

5.1 Introduction

In this chapter, the magnetic field dependence of the cylindrical (or post) magnetron discharge is considered. In such a Cylindrical Magnetron Discharge (CMD), a cylinder serves as cathode. The cathode is usually axially limited by two discs, which are referred to as wings and they are also at cathode potential. The anode can be the surrounding vacuum chamber or can be constructed around (one or both of) the wings. The magnetic field can be generated by permanent magnets inside the cathode or by an electromagnet that is placed around the anode. The latter has the advantage that the generated magnetic field is very uniform and parallel to the cathode surface. Consequently, the emitted secondary electrons (SE) are subjected to electric and magnetic fields which are perpendicular to each other. This implies that recapture of SE is very important in the CMD. Indeed, especially in the middle of the race-track of a planar magnetron, where the electric and magnetic field are also perpendicular to each other, the EGIP f is very low, i.e. the recapture probability is very high (see e.g. Fig. 1.5 in section 1.3.1).

In general, increasing the magnetic field strength intensifies the discharge. This is the main reason for using magnetron discharges instead of standard diode discharges. However, given the decrease in EGIP with increasing magnetic field (section 1.3.5), it is expected that this effect might prevent further intensification at sufficiently high magnetic field strengths. If this is correct, increasing the magnetic field above a certain value should have a negative effect on the discharge. In planar magnetrons this reasoning does not necessarily hold because other SE starting positions (off-centre) are possible which prevent the EGIP from becoming very low.

The influence of the magnetic field B on the CMD has been reported in literature. Note that in this text the magnetic field strength of a cylindrical magnetron is indicated by B instead of B_{max} because the magnetic field is uniform. Yeom et al. [Yeom89] measured the influence of an increase of the magnetic field from 100 to 200 G and found V_d consistently smaller at the strongest magnetic field. Behnke et al. [Behnke00] also investigated the discharge dependence on the magnetic field strength for a cylindrical magnetron with a cathode diameter of 10 mm. The electron density was observed for $I_d = 125$ mA at 4 Pa: it *decreased* from $3.0\times10^{10}/m^3$ at 150 G to $0.25\times10^{10}/cm^3$ at 350 G. Unfortunately the corresponding discharge voltages are not mentioned. The radial position of the maximum electron density is about 4 to 6 mm above the cathode. Although the variation of the maxima with magnetic field strength is small, it can be seen that from 150 to 250 G the maximum moves towards the cathode whereas for higher magnetic fields it moves away from the cathode. Also in [Porokhova05a] the magnetic field dependence of a CMD is reported. The results are obtained for a cathode with diameter 18 mm at 7 Pa and $I_d = 200$ mA. Again the electron density is seen to decrease from 100 to 250 G but for higher magnetic fields (measured up to 400 G) it increases slightly. The maximum electron density shifts towards the target for increasing magnetic field over the whole range. The discharge voltage on the other hand decreases continuously with increasing magnetic field.

Another study regarding the influence of the magnetic field on the CMD has been performed by Van der Straaten et al. [Vanderstraaten98a,b]. They developed a PIC-MC program to simulate the CMD. The model predicted the transition to a negative space charge at high magnetic fields and low pressures (see also section I.1.3.6.2). However, their

Langmuir probe measurements found practically no influence of the magnetic field on the potential distribution in the plasma [Vanderstraaten98b]. Bilyk et al. mention MC simulations of the CMD which show that the electrons cannot reach the anode at lower pressures although for the same conditions the discharge could be maintained experimentally [Bilyk04]. They attribute the discrepancy to a lack of electron interactions, probably due to neglecting stochastic oscillations in the simulation.

In the next section (section 5.2) our experiments on the magnetic field dependence of the discharge voltage of a CMD are reported. Then, it is investigated whether recapture of SE can explain the observed magnetic field dependence of the CMD (section 5.3). It turns out that accounting for recapture is necessary but cannot explain the observed behaviour. Consequently, the model is extended for Bohm diffusion and Coulomb collisions (section 5.4). The effect of these extensions on the results is investigated, which leads to a possible explanation for the observed behaviour (section 5.5).

5.2 Experimental results

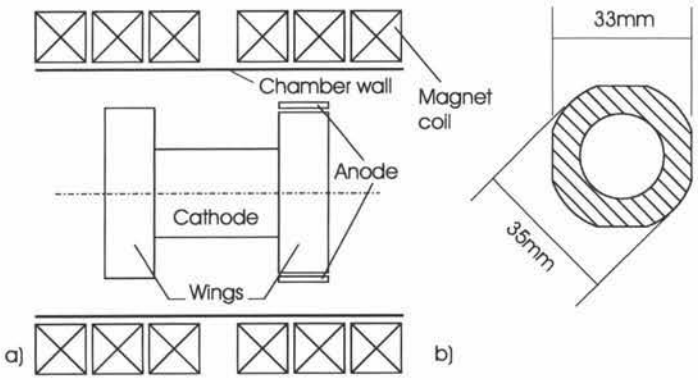

Fig. 5.1. *a*) Sketch of the cylindrical magnetron used in the discussed experiments. The magnetic field is generated by an electromagnet placed outside the vacuum chamber. *b*) Cross section of the flattened target tube (cathode).

For the experiments a slightly modified cylindrical magnetron Fig. 5.1a was used: the cylindrical part of the target is made of a tube with diameter 35 mm and length 50 mm but the tube is 'flattened' as depicted in Fig. 5.1b. The wings are on cathode potential and have a diameter of 68 mm and of 64 mm respectively. The smaller wing is surrounded by an anode to create a virtual anode (see section I.1.4.6). The magnetic field is generated by an electromagnet that consists of 6 separate coils (Fig. 5.1a). Over the length of the target tube the magnetic field is uniform within 2%. The values given for B are measured in the centre of the coil. The chamber pressure was measured using a capacitance gauge from Pfeiffer (CMR 264). The experiments were performed at constant power (100 W) and pressure while the magnetic field was varied. In Fig. 5.2 the magnetic field dependence of the discharge voltage is shown at 0.2 and 1.0 Pa.

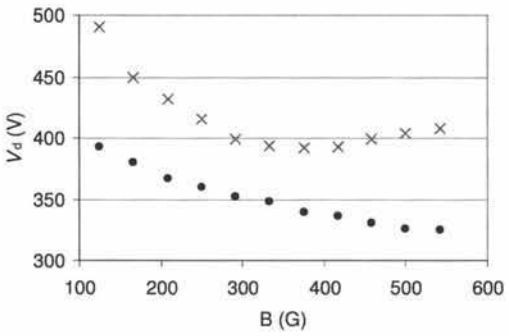

Fig. 5.2. Dependence of the discharge voltage V_d on the magnetic field strength B at 1.0 Pa (•) and 0.2 Pa (×).

5.3 Discussion: explanation by recapture?

One can clearly see in Fig. 5.2 that V_d displays a minimum as a function of B at 0.2 Pa but not at 1.0 Pa. Hence, the question arises which processes are responsible for this observed B-field behaviour. In a CMD the EGIP decreases strongly with increasing magnetic field. We want to investigate whether this decrease can explain the observed behaviour.

Different approaches can be followed to elucidate the observed behaviour. One option is to simulate fully self-consistently the CMD, see e.g. [Vanderstraaten98a, Kudrna02, Porokhova03]. However, such an approach is out of the scope of this thesis. Instead, the physical processes will be dealt with in a simplified way based on the extended Thornton relation (eq. (3.7) from section 3.3.4), which is repeated here:

$$V_d = \frac{W}{\gamma f m \varepsilon_e \varepsilon_i} \tag{5.1}$$

This equation describes basically the equilibrium between the generation of ions in the plasma phase and the emission of electrons from the cathode.

Consider the right hand side of the above equation. As before, we assume that ε_i and ε_e are equal to unity. The SE yield γ is set to 0.1. The EGIP f is determined using the analytical model described in section 1.2.6. The electron reflection coefficient R is taken 0.5 (see section I.1.2.2.3). The effective ionisation energy W and the multiplication factor m are calculated using the MC model described in section 2.5. Here, it can no longer be assumed that W is equal to 30 eV because the HEE energy is too low. At lower energies, the probability for excitation is relatively higher so that W increases. Hence, the quantities needed on the right hand side can be calculated, when a discharge voltage $V_{d,in}$ and a cathode sheath thickness d_E are provided as input parameters. The first is known from the experiments but the latter is not, so that an initial ad hoc value needs to be chosen. Once the factors of the right hand side are defined, it results in the simulated discharge voltage, which is referred to as $V_{d,sim}$ to differentiate it from the input discharge voltage $V_{d,in}$. For a realistic situation $V_{d,sim}$ should be equal to the input discharge voltage $V_{d,in}$. However, for a random d_E this is not the case. Hence, by iterating through this process we can determine d_E.

We use the experimental discharge voltages $V_{d,exp}$ as input voltage $V_{d,in}$ for the simulation. To start the simulation, an initial value for d_E is chosen. If $V_{d,sim}<V_{d,in}$ d_E needs to be decreased, in the opposite case d_E needs to be increased. Through this iteration process, d_E

is calculated. The iteration process is stopped when $|1-V_{d,sim}/V_{d,in}|<0.05$. This way, the accuracy of the presented simulations is of the order of 5%. Per iteration step 50 electrons are retraced. Note that, again, the MC simulations are performed at 2.0 Pa as the ionisation distribution, and consequently the multiplication factor m, does not explicitly depend on the gas pressure (section 2.6.3.3). The result for d_E is shown in Fig. 5.3 for 1.0 and 0.2 Pa.

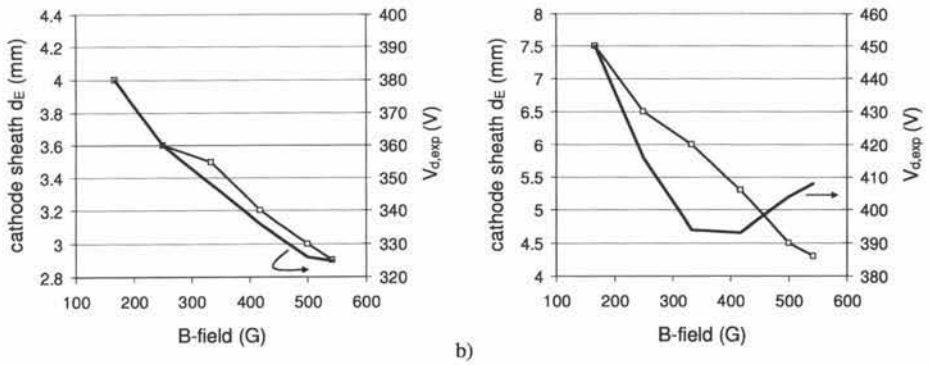

Fig. 5.3. The simulated dependence of the cathode sheath thickness d_E (□) on the magnetic field strength B at 1.0 Pa (*a*) and 0.2 Pa (*b*). Also the experimentally measured discharge voltage $V_{d,exp}$, which was used as $V_{d,in}$, is shown (—).

The question arises whether the calculated cathode sheath thicknesses are physically correct or not. From magnitude they seem rather realistic: at 1.0 Pa d_E decreases monotonously from 4 to 3 mm, which is a realistic range for the CMD. At 0.2 Pa larger d_E, in the range 4 to 7 mm, are found. These larger d_E-values could be expected as decreasing the pressure increases the cathode sheath thickness. At this low pressure, d_E is also found to decrease monotonously with increasing B. In the next paragraphs it will be discussed that this latter result is not physically correct by considering the magnetic field dependence of the derivative $\Delta V_d/\Delta B$ and of the cathode sheath thickness d_E.

It is clear that at 1.0 Pa $\Delta V_{d,exp}/\Delta B$ is always negative. This has a physical meaning. Assume a CMD in steady state. When the magnetic field B is abruptly increased, the equilibrium expressed by eq. (5.1) is disturbed. For the given situation, an increase in B will increase the ionisation in the sheath (larger m) and the EGIP will decrease (smaller f). The first effect tends to decrease, the latter to increase the discharge voltage. Apparently, the latter effect is in this case smaller so that the new steady state $V_{d,exp}$ is lower, i.e. $\Delta V_{d,exp}<0$. To simulate $\Delta V_{d,sim}/\Delta B$ we start from known discharge conditions, i.e. a magnetic field strength B_0 for which d_E is determined so that $V_{d,in} = V_{d,sim}$. Then the magnetic field is increased at constant d_E and $V_{d,in}$. Given the above reasoning, the new $V_{d,sim}$ should be smaller than $V_{d,in}$, which is indeed simulated.

At 0.2 Pa $\Delta V_{d,exp}/\Delta B$ is negative up to magnetic field strengths of approximately 400 G. Above this, it is clear from Fig. 5.2 that $\Delta V_{d,exp}/\Delta B$ should be positive. However, the model yields only positive values, i.e. it does not reproduce the change in sign of the derivative. When for example at 460 G the magnetic field is increased with 40 G the corresponding $V_{d,sim}$ is almost 80 V lower than $V_{d,sim}$ at 460 G. Hence, the model does not reproduce the change in $\Delta V_{d,sim}/\Delta B$ at high magnetic fields and low pressures. The fact that $V_{d,sim}$ increases with increasing B is only because it is enforced externally: we demand $V_{d,sim}$ to be equal to $V_{d,exp}$.

There is another indication that the simulated results are not correct. As said, above 400 G at 0.2 Pa, an increase in B disturbs the equilibrium expressed by eq. (5.1) so that per emitted SE more ions need to be generated. The discharge can restore the equilibrium by an increase in the discharge voltage. However, from the pressure dependence of the planar MD, we know that the discharge tries to restore the equilibrium not only by increasing the discharge voltage but also by increasing the cathode sheath thickness (section 4.3.2). Hence, it is expected that the transition from negative to positive $\Delta V_{d,exp}/\Delta B$ is accompanied by a similar change in $\Delta d_E/\Delta B$. However, the simulation results reveal a continuous decrease in d_E at both 0.2 and 1.0 Pa.

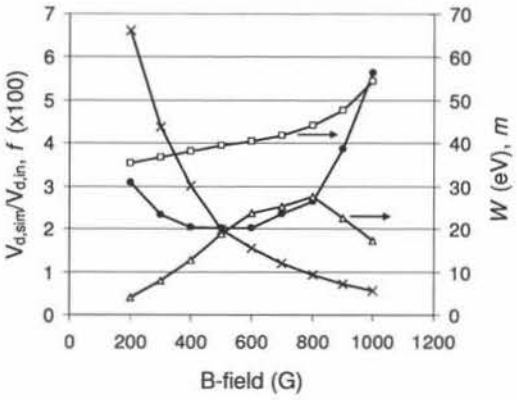

Fig. 5.4. The simulated dependence of the ratio $V_{d,sim}/V_{d,in}$ (•) on the magnetic field B at 0.2 Pa. Next to this ratio, also the EGIP f (×), the multiplication factor m (△) and the effective ionisation energy W (□) are shown. The latter two are plotted against the vertical axis on the right hand side. The values of f are multiplied by a factor 100. These results are obtained using the test settings (see text).

Hence, for a physically correct simulation, we need to find a situation where for given parameters, the simulation results indicate that $\Delta V_{d,sim}/\Delta B>0$. In order to find such a situation, we first check if this condition can be met with the model as it is. For this purpose, we introduce the *test settings*: $V_{d,in} = 300$ V, $d_E = 6.0$ mm, $p = 0.2$ Pa, $\gamma = 0.1$ and $R = 0.5$. Using these test settings, the ratio of $V_{d,sim}/V_{d,in}$ was calculated in the range of 200 to 1000 G (Fig. 5.4). These settings do not correspond with a physical consistent situation because this ratio is not equal to one. Nevertheless, from this kind of simulation in which only the magnetic field strength varies while all other parameters are kept constant the sign of $\Delta V_{d,sim}/\Delta B$ can be studied. In Fig. 5.4 $V_{d,in}$ is kept constant at 300 V. Consequently, the increasing ratio of $V_{d,sim}/V_{d,in}$ at large B indicates that in this case the condition $\Delta V_{d,sim}/\Delta B>0$ is fulfilled at large B. The reason is the rather low $V_{d,in}$ combined with a large d_E. When the magnetic field becomes stronger, the electrons emitted from the target can only reach a small height above the target so that their average energy is low. As a result the effective ionisation energy W increases significantly (Fig. 5.4). This combined with an m reaching a peak and the continuous decrease in the EGIP f (both also shown in Fig. 5.4) explains the simulated increase in the discharge voltage above 400 G. However, this correct B dependence is not found for a realistic simulation, which requires $V_{d,sim}/V_{d,in}$ equal to unity. For the experimental conditions, this effect might also occur but it will be at too high magnetic field strengths because there V_d is larger.

Consequently, the model as it is now cannot correctly explain the observed magnetic field dependence of the CMD at low pressure. Hence, we need to find another process that

can explain the experimental observation. If we think about the aspects we neglected in the simulation, then two possibilities appear: both the anomalous or Bohm diffusion and Coulomb collisions were neglected. Both aspects will now be incorporated in the MC model to find out whether they can explain the observed magnetic field dependence of the discharge voltage or not.

5.4 Extension of the MC model

In this part, we reconsider the MC model that was introduced in section 2.5 to determine the ionisation caused by a single electron. In a cylindrical discharge, the magnetic field can be assumed constant. This is a major simplification when applying the MC model to the CMD. The extension of the MC model to include Bohm diffusion (section 5.4.1) and Coulomb collisions (section 5.4.2) is now discussed.

5.4.1 Bohm diffusion

As mentioned before, it is expected that Bohm diffusion occurs in the MD (section I.1.3.6.2). In the same section, an empirical method (from [Smirnov04]) to include *B*ohm *D*iffusion *C*ollisions (BDC) in a MC model is mentioned. Here, we follow the same approach: it is assumed that when an electron undergoes an interaction with the electric field fluctuation, its velocity component perpendicular to the magnetic field scatters isotropically [Smirnov04]. The parallel velocity component is not changed. This implies that the guiding centre of the electron orbit gets a random shift in the plane perpendicular to the magnetic field. The frequency ν_B of the BDC is defined as [Smirnov04]:

$$\nu_B = \alpha\omega_L \tag{5.2}$$

with ω_L the Larmor frequency (eq. (1.49) in section I.1.3.6.2) and α a fitting parameter. The justification of this approach is given in Appendix 4 of [Ahedo03]. From the comparison of their simulation results with experiments, Smirnov et al. report that α should be close to 1/16 [Smirnov04]. Other simulation work related to Hall thrusters indicates α around 1/44 [Keidar01]. According to [Ahedo03] a more plausible value is around 1/100 as this is reported several times in Hall thruster simulations.

This approach for ν_B has a major consequence. Up to now, the ionisation distribution of a single electron was independent of the gas pressure (section 2.6.3.3). This enabled to simulate the ionisation distribution much faster because the simulations could be performed at higher gas pressures. However, if eq. (5.2) is used, this is no longer the case: ν_B does not depend on the pressure but the relative occurrence of the BDC does depend on it. Thus, the ionisation distribution is pressure dependent. Although this physical fact cannot be denied, we can define the Bohm collision frequency in a pressure independent way by using the empirical parameter F_B instead of α:

$$\nu_B = F_B \nu_{tot} \tag{5.3}$$

with ν_{tot} the sum of the collision frequencies for ionisations, excitations and elastic collisions for an electron energy of 100 eV. Hence, the parameter F_B gives the relative occurrence of the Bohm diffusion collisions compared to the other collision processes. In other words, F_B is defined such that the product of both F_B and ν_{tot} is pressure independent, although both individually are pressure dependent. This implies that the simulated ionisation distribution is again pressure independent. Of course, the magnetic field dependence remains, meaning that F_B is proportional with the magnetic field strength B.

5.4.2 Coulomb collisions

In a CMD, all SE that are emitted from the target experience a magnetic and an electric field that are perpendicular to each other. As a result, the SE remain much closer to the target surface as in a planar MD. In the latter they can gain height by following the magnetic field lines (see e.g. Fig. 1.1). Here, the maximum energy the SE can gain before undergoing an interaction with the discharge gas is determined by their Larmor radius r_L (eq. (1.2) in section I.1.1), which decreases when the B-field is increased. As already mentioned (section 5.3) this causes the effective ionisation energy to increase. For a sufficiently strong B-field and a relatively thick cathode sheath, the SE energy will be so small that neglecting Coulomb collisions (CC) becomes doubtful because the cross section for CC increases very strongly with decreasing electron velocity (Fig. 1.6 in section I.1.2.1.1D).

The full and exact treatment of CC in a CMD model is beyond the scope of this work. Instead, we want to indicate here that by taking into account CC the observed B-field behaviour of the CMD can be understood. Hence, CC will be modelled in a simplified way. As for the Bohm diffusion collisions, the two important aspects to determine are the scattering angle χ in the centre of mass system and the scattering cross section σ_χ. In the case of CC, both are related through eq. (1.9) in section I.1.2.1.1D). We used this equation together with eq. (1.8) for σ_{90} (in the same section) to deduce σ_χ. In reality, the scattering angle χ depends on the impact parameter. However, as will be shown (section 5.5.2), for small scattering angles, which are the most likely to occur, the exact choice of χ has a very small influence on our results. Therefore, the model was only implemented for a fixed scattering angle, referred to as χ_0, which is an input parameter of the simulation.

For CC also the density of the colliding species needs to be determined. This is fundamentally different from the other collision processes previously discussed as for those the colliding species are the neutral argon atoms, the density of which can be deduced from the gas pressure. For the electron density n_e, both the gas pressure and the ionisation degree (ID) of the discharge are needed. The latter is not known exactly but can be estimated based on the overview given in Table 1.3 and Fig. 1.18 (both in section I.1.3.5.3). Furthermore, we relate the ID to the cathode sheath thickness. Consider a given discharge with cathode sheath thickness $d_{E,0}$ and ionisation degree ID_0. It is assumed that for a given applied electrical power the total number of electrons in the cathode sheath is constant. Note that here it is explicitly demanded that there are electrons in the cathode sheath, which is justified given the strong B-fields and the rather large sheaths considered. Consequently, the ID is related to the volume within the cathode sheath. For a cylindrical magnetron with cathode diameter R_c, length L and sheath thickness d_E, this volume $\mathcal{V}$ is given by:

$$\mathcal{V} = \pi\left[\left(R_c + d_E\right)^2 - R_c^2\right]L \tag{5.4}$$

The ID is inversely proportional with this $\mathcal{V}$, which for a given magnetron geometry only depends on d_E. Consequently:

$$ID_0\mathcal{V}(d_{E,0}) = ID_1\mathcal{V}(d_{E,1}) \tag{5.5}$$

Hence, once the ID is chosen for a given d_E, the ID is also determined for all other d_E.

The assumption that the total number of electrons only depends on the applied electric power not only allows determining the ID for different d_E, it also fixes the ID for different gas pressures. Indeed, given this assumption, it follows immediately that:

$$ID_0 p_0 = ID_1 p_1 \tag{5.6}$$

with ID_0 (ID_1) the ionisation degree at p_0 (p_1). In conclusion, when working at constant electric power, once ID_0 is specified for a certain cathode sheath thickness $d_{E,0}$ and a certain pressure p_0, the ID can be determined for any d_E and p.

5.5 Results and discussion

5.5.1 General influence of Bohm diffusion

To retrieve the effect of Bohm diffusion collisions on the CMD, we redo the simulations for the B-field dependence of $V_{d,sim}$ for the test settings (section 5.3). To perform these simulations, we need to specify the frequency of the Bohm diffusion collisions by assigning a value to F_B (see eq. (5.3)). This empirical factor defining the Bohm collision frequency needs to be chosen at a specific magnetic field strength. We choose this factor equal to 0.3 at 500 G, i.e. $F_B(500) = F_{B,500} = 0.3$, which means that at 500 G roughly one in four of the electron interactions is a Bohm collision. The magnetic field dependence of F_B is given by:

$$F_B(B) = F_{B,500} \frac{B}{500} \tag{5.7}$$

with B given in Gauss. The reason for this choice of $F_{B,500}$ is that this results in a value of α (eq. (5.2)) of approximately 0.01, which is one of the more frequently encountered α-values in Hall thruster modelling [Ahedo03].

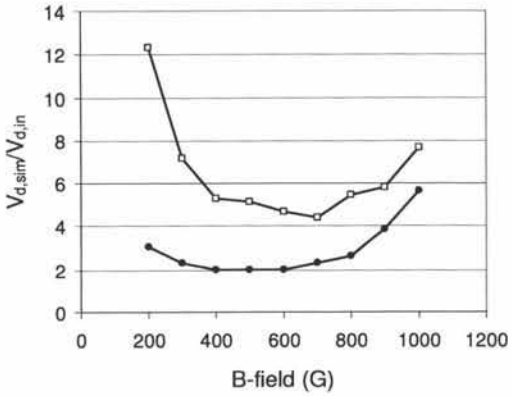

Fig. 5.5. The simulated dependence of the ratio $V_{d,sim}/V_{d,in}$ on the magnetic field B at 0.2 Pa. The ratio is obtained without (•) and with (□) taking into account Bohm diffusion collisions. In the latter case, $F_B(500)$ is set to 0.3. These results are obtained using the test settings (see section 5.3).

The results are shown in Fig. 5.5 for the ratio $V_{d,sim}/V_{d,in}$. Also the result obtained without Bohm diffusion is shown. By taking into account BDC, the magnetic field strength at which the minimal ratio occurs is shifted to stronger fields. This indicates that Bohm diffusion has the opposite effect as what was needed. This is logical: by including BDC, the mobility of the electrons in the direction perpendicular to the magnetic field lines is enhanced. This means that the electrons shift to relatively higher positions above the target, i.e. they gain more kinetic energy. Because of this the effective ionisation energy W is lowered. As the increase in

W caused the increase of the discharge voltage with increasing magnetic field strength (section 5.3), this means that here this increase will start at stronger magnetic fields. Consequently, taking into account Bohm diffusion does not explain the observed magnetic field dependence at low gas pressures.

5.5.2 General influence of Coulomb collisions

To assess the influence of CC, we determine the magnetic field dependence for the test settings. As the ID is not known, two different options were simulated: $ID_0 = 0.005$ and $ID_0 = 0.001$ with ID_0 the ionisation degree for $d_E = 10$ mm at 0.2 Pa. If not mentioned otherwise, the scattering angle χ_0 was taken 9° (see also section I.1.2.1.1D).

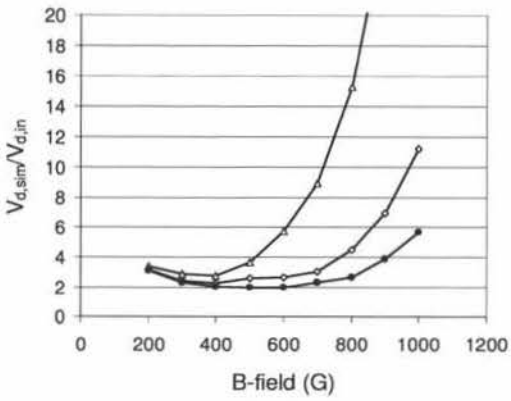

Fig. 5.6. The simulated dependence of the ratio $V_{d,sim}/V_{d,in}$ on the magnetic field B at 0.2 Pa. The ratio is obtained for $ID_0 = 0.005$ (△), $ID_0 = 0.001$ (◇) and for $ID_0 = 0$ (•). The latter means that CC are not accounted for. The scattering angle χ_0 was set to 9°. These results are obtained using the test settings (see section 5.3).

The results for the ratio $V_{d,sim}/V_{d,in}$ are shown in Fig. 5.6, together with the result obtained without CC (equivalent with $ID_0 = 0$). First of all, it is clear that the exact choice of the ID_0 has a strong influence on the results. At weak magnetic fields CC have a rather small influence but the influence grows with increasing magnetic fields. The reason is that by accounting for CC the increase in the multiplication factor m with increasing magnetic field is strongly reduced. Hence, because of CC the cathode sheath thickness should be much larger at strong B-fields. This corresponds with the effect that was needed to explain the experimental behaviour. In conclusion, it appears that redoing the simulation procedure of section 5.3 with CC included might result in the correct dependence.

Before doing so, the influence of the scattering angle χ_0 is investigated. Fig. 5.7 shows the ratio $V_{d,sim}/V_{d,in}$ for $ID_0 = 0.005$ and scattering angles χ_0 equal to 4.5, 9 and 18. In general, it can be seen that the effect of the CC becomes smaller for decreasing χ_0. However, it is clear that the influence of the exact choice of χ_0 is much smaller than the effect of including CC. As we already mentioned, the aim of the simulations is to outline which physical processes can explain the observed behaviour. For this aim, the rather small influence of χ_0 can be neglected.

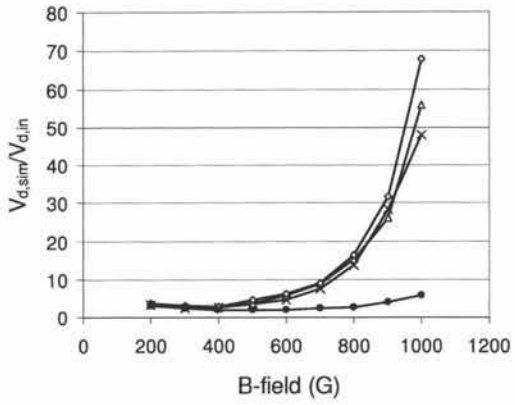

Fig. 5.7. The magnetic field dependence of the ratio $V_{d,sim}/V_{d,in}$ for different scattering angles χ_0 at 0.2 Pa. The ratio is obtained for $\chi_0 = 4.5$ (×), 9 (△) and 18 (◇) and $ID_0 = 0.005$. Also the result without taking into account CC ($ID_0 = 0$) is shown (•). These results are obtained using the test settings (see text).

5.5.3 Application to the experimental results

Now, we redo the simulations for reproducing $V_{d,exp}$ as described in section 5.3 but with CC included. For the reference ionisation degree ID_0 at 0.2 Pa we choose 0.002 and 0.005. All needed IDs can be deduced using eqs. (5.5) and (5.6). The radius R_c of the cathode is taken 34 mm, based on the physical dimensions of the cylindrical magnetron (see Fig. 5.1).

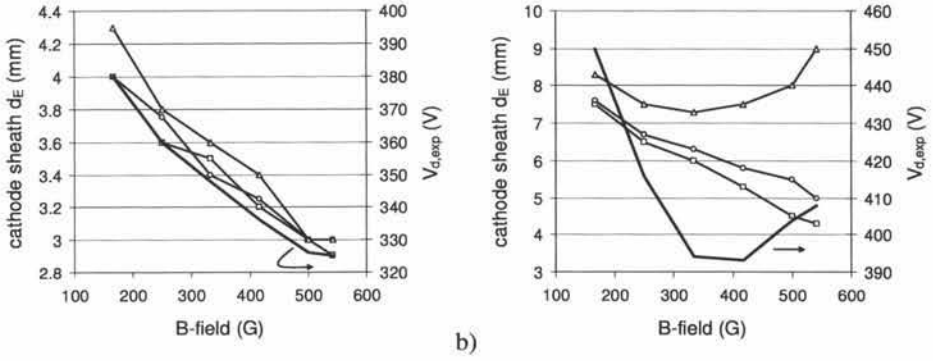

Fig. 5.8. The simulated magnetic field dependence of the cathode sheath thickness d_E at 1.0 Pa (*a*) and 0.2 Pa (*b*). The results for three different cases are shown: $ID_0 = 0.005$ (△), $ID_0 = 0.002$ (○) and $ID_0 = 0$ (□). Only the result obtained with $ID_0 = 0.005$ shows the expected increase in d_E at high magnetic fields at 0.2 Pa. Also the experimentally measured discharge voltage $V_{d,exp}$, which was used as $V_{d,in}$, is shown (—).

The results obtained for the cathode sheath d_E are presented in Fig. 5.8. Also the result without taking CC into account (from section 5.3) is repeated. At 1.0 Pa the influence of CC is very small. The reason is that at this pressure, the ID is five times smaller than at 0.2 Pa because the number of charged particles is considered independent of the gas pressure in agreement with experimental observations (section I.1.4.2.4). For $ID_0 = 0.005$ the values for d_E are slightly higher than for $ID_0 = 0.002$ and $ID_0 = 0$ (Fig. 5.8a). For the latter two cases, the figure shows that the difference is within the accuracy of the simulation (around 5% as

mentioned before) as the two curves for d_E are intertwined. According to these results, these low ID have a very limited influence on the MD.

At 0.2 Pa the curves for d_E are clearly different. We see that for $ID_0 = 0.002$ the cathode sheath has to remain larger at strong magnetic fields but d_E still continuously decreases. For $ID_0 = 0.005$ the overall d_E are larger and d_E increases at sufficiently high magnetic field strengths for the lowest pressure. The minimum of d_E occurs at slightly weaker B-fields as the minimum of $V_{d,exp}$. For the two minima to coincide ID_0 should be chosen slightly lower than 0.005.

Based on these results and the extended Thornton relation (eq. (5.1)), the following mechanism for the magnetic field dependence of the CMD is proposed. Assume a discharge without magnetic field. Initially, applying a small magnetic field will keep the electrons trapped close to the target surface. As a result no high energy electrons can leave the discharge ($\varepsilon_e = 1$) and the ions are generated close to the target so that all ions bombard the target ($\varepsilon_i = 1$). For standard magnetron discharges this requirement is fulfilled. Hence, further increasing the magnetic field has no effect on these parameters and the decrease in discharge voltage is not caused by a better electron confinement as might be intuitively expected. Instead, the reduced discharge voltages are due to the enhanced probability for sheath ionisation (multiplication factor m increases). Also the recapture of electrons becomes more important (EGIP f decreases). However, at not too high B-fields or sufficiently high pressures, the discharge voltage decreases which indicates that the increase in m has the strongest effect. However, due to the increasing magnetic field, the maximum energy the electrons can reach decreases. This leads to an increase in W and also to an enlarged probability for CC. Because of the latter, the electron mobility in the direction perpendicular to the magnetic field increases, which means that there is relatively less ionisation in the cathode sheath, i.e. m will tend to saturate with increasing magnetic field. These effects combined with the decrease in EGIP f are the reason that at sufficiently low pressures, the value of the right hand side of eq. (5.1) decreases with increasing B, i.e. an increase in the magnetic field leads to a decreased ion generation per emitted electron. The discharge will try to restore this equilibrium, which explains the experimentally observed increase in V_d. Most likely, this restoring of the equilibrium is enhanced by the widening of the cathode sheath.

5.6 Conclusions

In this chapter the magnetic field dependence of the CMD was studied. Experimental observations show that in the considered magnetic field range (150-550 G), the discharge voltage decreases monotonously at high pressure (1.0 Pa) with increasing magnetic field strength at constant power. At low pressure (0.2 Pa), the discharge voltage reaches a minimum around 400 G.

To explain this behaviour the extended Thornton relation is used in combination with the analytical model for the EGIP f and the Monte Carlo model for determining the effective ionisation energy W and the multiplication factor m. The simulation results obtained when only taking into account the standard electron-atom interactions (ionisations, excitations and elastic collisions) are unable to explain the observed increase in discharge voltage, although an increase in the discharge voltage can be simulated for a hypothetical situation.

To overcome this problem, the Monte Carlo model was extended to include Bohm diffusion and Coulomb collisions. When taking into account the latter type of collisions, the observed experimental behaviour could be simulated and explained.

The "usual" decrease in discharge voltage with increasing magnetic field is caused by an increased probability for sheath ionisation. However, at very high magnetic fields the electrons emitted from the target remain less energetic as they cannot reach out far above the target due to the small Larmor radius. Consequently, the effective ionisation energy increases and the electrons become more susceptible to Coulomb collisions. Moreover, at low pressures the recapture of electrons, which increases for stronger magnetic fields, is very important. As a consequence, increasing the magnetic field above a certain value at sufficiently low pressure actually reduces the amount of generated ions per emitted electron. The discharge counteracts this by increasing the discharge voltage and cathode sheath thickness.

6 INFLUENCE OF BOHM DIFFUSION AND VALIDATION OF THE MODEL

6.1 Introduction

As seen in the Chapter 4, the current-voltage characteristics (IVs) calculated with the SCM as described up to now do not really agree with the experimental observations, especially the steepness of the slope is not reproduced. Logically, one or more physical processes involved in the MD have so far not been included (correctly) in the simulation.

In the previous chapter a similar problem was discussed. There, accounting for Coulomb collisions and Bohm diffusion could help to explain the experimental behaviour. Here also, it is investigated whether the discrepancy between the experiments and the simulations can be explained by these processes.

Coulomb collisions can be ruled out immediately. In contrast to a cylindrical magnetron, the height that electrons emitted in a planar magnetron can reach is not strictly related to their Larmor radius because they follow the magnetic field lines. Consequently, even for strong magnetic fields, the electrons can gain a considerable amount of kinetic energy. As the Coulomb collision cross section drops dramatically with increasing electron velocity (see Fig. 1.6 in section I.1.2.1.1), this type of collisions can be neglected here. Hence, we have to focus on the Bohm diffusion collisions (BDC).

In the simulation of Hall thrusters, the anomalous electron drift also hampers the simulations. There, the problem is dealt with by introducing a phenomenological term describing BDC, see e.g. [Bareilles04, Smirnov04] (and section I.1.3.6.2). For the simulations presented in the previous chapter, we incorporated the effect of Bohm collisions in a similar way. This was possible because the ionisation distribution was determined using a MC method. Here, the ionisation distribution of the HEE is determined analytically. Hence, the challenge is to include Bohm diffusion into the SCM.

In the next section the SCM is adapted to account for Bohm diffusion (section 6.2). Afterwards, the adapted model is used to simulate the effect of Bohm diffusion on the MD properties (section 6.3). Finally, the simulation results are compared with experimental results (section 6.4).

6.2 Model

In the previous chapter, the BDC were assumed to occur at a frequency ν_B, defined by (section 5.4.1):

$$\nu_B = F_B \nu_{tot} \tag{6.1}$$

with F_B an empirical factor determining the relative occurrence of the BDC compared to the standard collisions, which occur with frequency ν_{tot}.

Hence, an artificial type of collisions, the Bohm diffusion collisions, is introduced. They represent the electron interaction with the electric field oscillations. These "collisions" occur in-between the standard collisions, i.e. excitations, ionisations and elastic collisions. Because of the extra number of collisions, the mobility of the HEE in the direction perpendicular to the magnetic field lines is enhanced.

Now, we want to introduce the effect of these Bohm diffusion collisions in the SCM. Therefore, we look back how the electron transport is modelled in the SCM. In section 2.3.2, it was explained that this is achieved by considering a Gaussian distribution around the magnetic field lines. The width of the Gaussian was related to the Larmor radius of the HEE. Hence, to increase the electron transport, there are two options.

First, the number of collisions can be increased. However, this would seriously complicate the model because the total number of interactions influences MD properties like the multiplication factor (section 2.4.3). Additionally, as Bohm diffusion collisions do not generate ions, they should not be included in this process. Hence, increasing the total number of interactions would require that a distinction is made between the "standard" total number of collisions and the total number of collisions including Bohm diffusion. This would further complicate the model.

A second possibility to increase the electron transport is by widening the Gaussian distribution. This is very straightforward to include in the model: it needs only an adaptation of the expression which defines the width of the Gaussian distribution σ (see section 2.3.2). This option was preferred as it is much more practical to implement. The newly introduced width of the Gaussian distribution σ_B is defined as:

$$\sigma_B = \sigma(1+F_B) \tag{6.2}$$

with F_B defined as before. This can be interpreted as follows. For determining the average transfer matrix, we only consider the standard number of interactions. The electron has some extra possibility to diffuse in the direction perpendicular to the magnetic field lines because of the Bohm diffusion collisions in-between the standard collisions. This extra mobility is introduced by multiplying the width of the Gaussian distribution with the factor $1+F_B$.

Note that due to the way F_B is included in the model, it can only be considered as the relative occurrence of Bohm diffusion collisions when, on average, the scattering angle of the standard collisions is the same as of the Bohm diffusion collisions. If this is not the case, the right hand side of eq. (6.2) should actually be $\sigma(1+cF_B)$ with the constant c a factor defining the effect of the different scattering angle. Whatever the actual value of c, it does not affect the results of the model, it only compromises the physical meaning of F_B as relative occurrence of Bohm diffusion collisions. Hence, whenever in the remaining part of the text F_B is referred to as the relative occurrence of Bohm diffusion collisions this is only valid under the assumption of equal scattering angles.

The factor F_B depends on the magnetic field, which can be deduced from eqs. (6.1) and (5.2), and on the gas pressure. The reason for the latter is that, even though ν_B does *not* depend on the gas pressure ν_{tot} does. Consequently, the relative occurrence of ν_B to ν_{tot} is pressure dependent. Taking into account this magnetic field and pressure dependence, F_B is defined by:

$$F_B(B_{max}, p) = F_{B,ref} \frac{B_{max}}{B_{max,ref}} \frac{p_{ref}}{p} \tag{6.3}$$

This implies that the effect of Bohm diffusion on the MD can be consistently simulated by choosing $F_{B,ref}$ for a specific magnetic field strength and a specific pressure. Once this choice is made, F_B is determined for all other B_{max} and p. To define $F_{B,ref}$ the same convention as in the previous chapter is followed, i.e. $B_{max,ref} = 500$ G and $p_{ref} = 0.2$ Pa.

In conclusion, to take into account the increased mobility of the HEE, the empirical Bohm diffusion factor F_B is introduced. Although this is an "artificial" way to include Bohm diffusion, F_B is defined in such a way that, once a choice is made, it consistently describes the influence of Bohm diffusion for different magnetic field strengths and gas pressures. Although the implementation is seemingly simple, the introduction of Bohm diffusion has a profound influence on the MD properties as will be shown in the next sections.

6.3 Influence of Bohm diffusion: results and discussion

In this section, the influence of taking into account Bohm diffusion in the SCM is treated. Its effect on different aspects, such as the IV, the pressure and magnetic field dependence, is investigated. Some parts of this discussion are quite similar to parts of section 4.3. However, there the results obtained without Bohm diffusion were presented. The reason to explicitly mention the results both with and without Bohm diffusion is to be able to compare them.

For the results presented here the settings described at the beginning of section 4.3 are used. As in Chapter 4, "IV" refers to both a plot of I_d vs. V_d and j_m vs. V_d. Of course, here the results are obtained taking into account BDC by specifying an $F_{B,ref}$.

6.3.1 Influence of the Bohm diffusion collision frequency

6.3.1.1 For a given current and pressure

In this section, we start from a given j_m (2 A/m) and a given gas pressure (0.5 Pa). It is simulated how different MD properties are influenced by an increasing contribution of Bohm collisions. The latter is achieved by increasing $F_{B,ref}$.

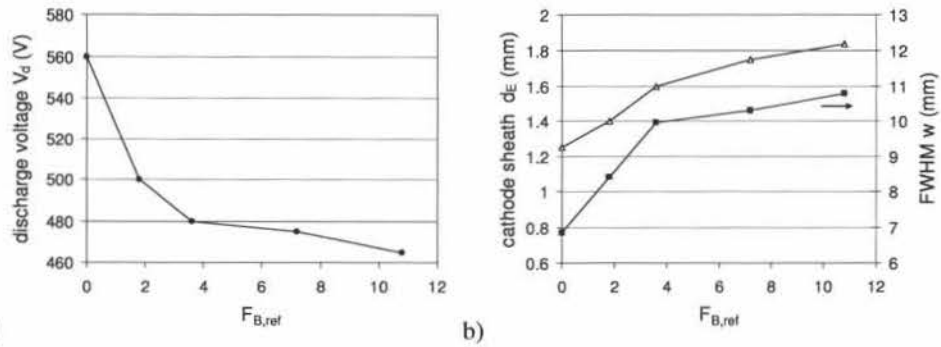

Fig. 6.1 Influence of $F_{B,ref}$ on the discharge voltage V_d (*a*), on the cathode sheath thickness d_E (△) and the FWHM w of the erosion profile (■) (*b*), at constant j_m (2 A/m) and pressure (0.5 Pa).

The discharge voltage V_d is plotted as a function of $F_{B,ref}$ in Fig. 6.1a: it is clear that with increasing $F_{B,ref}$ the required discharge voltage drops. For $F_{B,ref}$>4, the influence of increasing the contribution of Bohm diffusion is relatively small. Fig. 6.1*b* shows that also d_E and w are influenced by $F_{B,ref}$: both increase with increasing $F_{B,ref}$. The increase in w is obvious: because of the enhanced electron mobility, the ionisation distribution is more spread out. The increase of d_E and decrease of V_d are more difficult to understand.

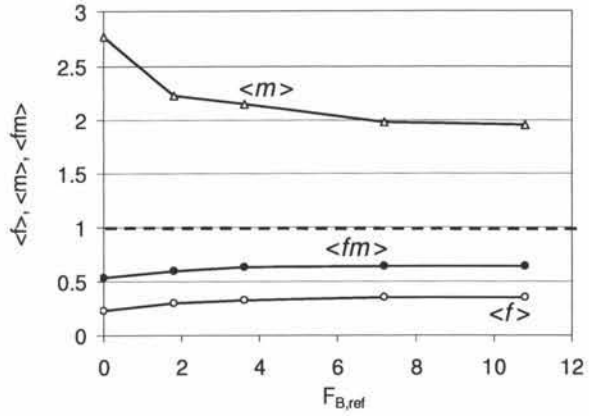

Fig. 6.2 Influence of $F_{B,ref}$ on the average EGIP $\langle f \rangle$, on the average multiplication factor $\langle m \rangle$ and on the product $\langle fm \rangle$ at constant j_m (2.0 A/m) and gas pressure (0.5 Pa).

To understand this, we first consider the behaviour of $\langle f \rangle$, $\langle m \rangle$ and $\langle fm \rangle$ as a function of $F_{B,ref}$ (Fig. 6.2). With increasing $F_{B,ref}$, the mobility of the electrons is raised. Consequently, the electrons pass the sheath faster, which decreases $\langle m \rangle$. To compensate this decrease, the cathode sheath thickness is increased. However, this can only partially compensate the effect because the net result is still a decrease in $\langle m \rangle$. This is only possible because of the wider erosion profile, which implies that the electron emission profile is wider. As this increases the EGIP f, the discharge is maintained in spite of the reduced $\langle m \rangle$. Apparently, the increase in $\langle f \rangle$ is so strong that also the discharge voltage can decrease.

Because of the enhanced electron mobility, the ions are generated on average further away from the target and less in the cathode sheath: indeed, the fraction φ decreases from approximately 50 % ($F_{B,ref} = 0$) to 40 % ($F_{B,ref} = 10.8$). This explains why $A_{//,t}$ increases with $F_{B,ref}$ as seen in Fig. 6.3. The figure also shows $j_{d,n}$ ($= j_d/j_d(F_{B,ref} = 0)$): it clearly decreases strongly because of the increase in d_E and decrease in V_d. The line current density j_m can nevertheless be kept constant because of the increase in w, $\bar{A}_{//,s}$ and $A_{//,t}$.

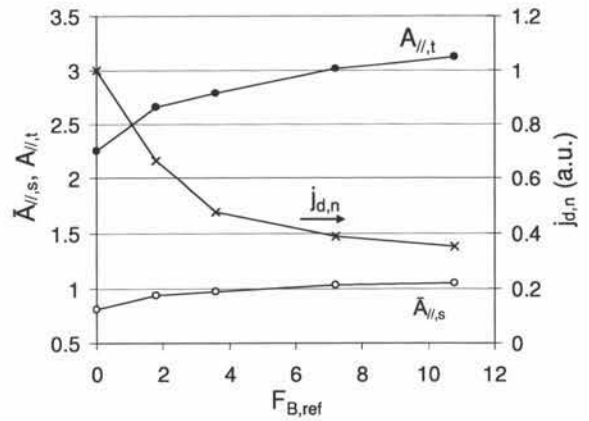

Fig. 6.3 Influence of $F_{B,ref}$ on the required amount of electrons per maintaining cycle in space $\bar{A}_{//,s}$ (O) and in time $A_{//,t}$ (•). Also the surface current density $j_{d,n}$ is plotted (×). The latter is j_d normalised the value for j_d at $F_{B,ref} = 0$.

As mentioned, F_B is a function of both the magnetic field and the gas pressure as expressed by eq. (6.3). For example, for the results shown in Fig. 6.1 to Fig. 6.3 the actual F_B is $F_{B,ref} \times (600/500) \times (0.2/0.5) = 0.48 F_{B,ref}$. Based on the comparison of the simulation and experimental results, $F_{B,ref} = 3.6$ was chosen (see section 6.4.3.1). A plot of F_B as a function of B_{max} and p is made to get a "feeling" for the relative occurrence of Bohm diffusion collisions for this choice (Fig. 6.4). This shows that at high pressures and/or low magnetic fields, Bohm diffusion plays a minor role, e.g. at 400 G and 1.2 Pa we find $F_B \approx 0.5$, meaning that only one Bohm diffusion collision occurs per two standard collisions. On the other hand, at 600 G and 0.1 Pa, we find $F_B \approx 8.6$, which implies more than eight Bohm diffusion collisions per standard collision.

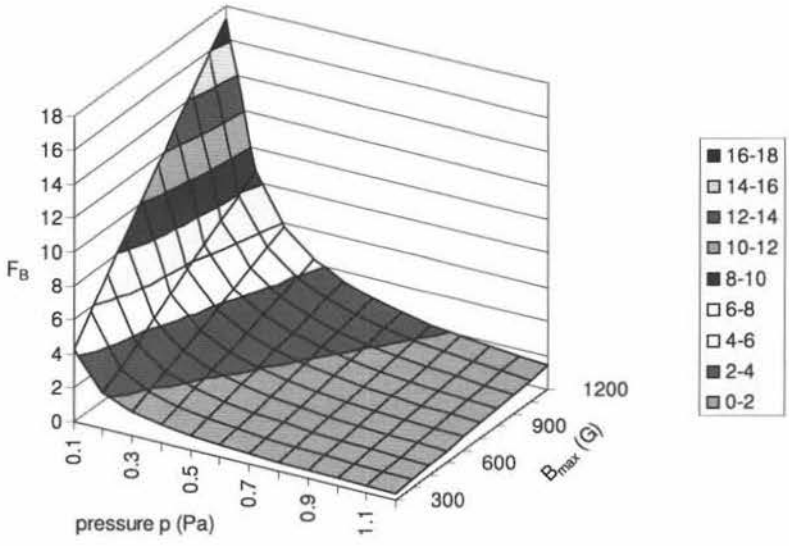

Fig. 6.4 The Bohm diffusion factor F_B as a function of p and B_{max} for $F_{B,ref} = 3.6$.

6.3.1.2 Influence of Bohm diffusion on the discharge structure

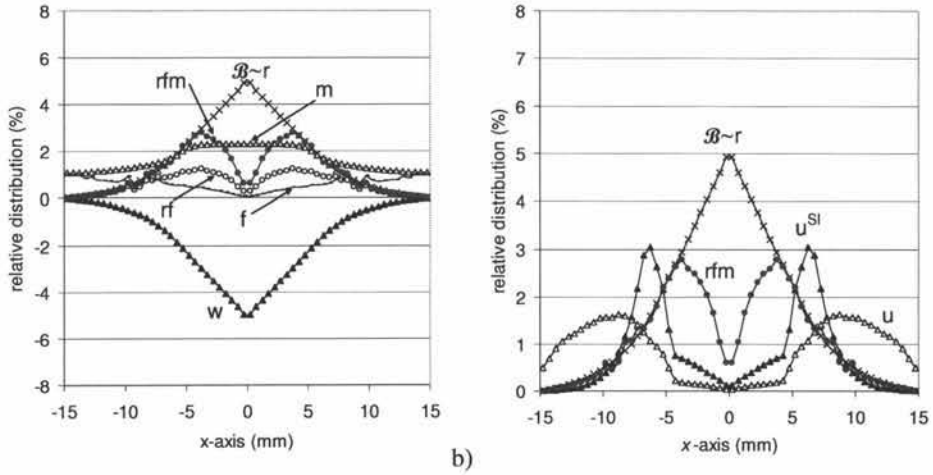

Fig. 6.5 The figure gives an overview of the self-consistent solution obtained for $V_d = 440$ V, $d_E = 1.6$ mm and $F_{B,ref} = 3.6$. Part *a* shows $\mathcal{B}$, the distribution along the *x*-axis of the ions bombarding the target (×). Given the constant SE yield γ, this profile corresponds with the SE emission profile *r*. Furthermore, the erosion profile *w* (▲), the EGIP *f* (▪), the multiplication factor *m* (△), the emission profile corrected for recapture *rf* (O) and the effective SE emission profile *rfm* (●) are shown. Part *b* repeats the original and effective emission profiles but shows also the occupation profiles *u* (△) and u^{SI} (▲). Note that the emission profile *r* is scaled such that the sum of all r_i is equal to one. Also the occupation profiles are scaled such that the sum of all u_i and u^{SI}_i together equals one. The boundaries of the vertical axes are taken the same as those of Fig. 3.10 to facilitate comparison of the figures.

In this section, the influence of accounting for Bohm diffusion on the MD structure is investigated. The term *structure* refers to the different profiles used in the SCM to characterise the MD, e.g. the emission profile *r* and the occupation profiles *u* and u^{SI}, as displayed in Fig. 3.10 (section 3.3.2). Here a similar plot is made for the same settings, i.e. for $V_d = 440$ V and $d_E = 1.6$ mm, but including BDC by setting $F_{B,ref} = 3.6$ (Fig. 6.5). Comparing the results obtained with and without Bohm diffusion confirms that the multiplication factor *m* is indeed much smaller with Bohm diffusion because of the enhanced electron mobility. As a result, the contribution of sheath ionisation is much smaller, which is reflected in the strongly decreased peak of u^{SI} shown in part *b* of the figure. Note that the peak position of u^{SI} did not change as this is determined by the sheath thickness which is kept the same in both cases. The arches towards the edge of the race-track are much more occupied as expressed by the wide maximum of *u*. This leads to a more spread out emission and erosion profile. Because of the reduced *m*, the effective SE yield is lower. As a consequence, the self-consistent pressure for these settings is 0.57 Pa, without Bohm diffusion it was 0.29 Pa.

6.3.1.3 Influence of Bohm diffusion on the current-voltage characteristic

In this section, the influence of Bohm diffusion on the IV is investigated. The results are presented in Fig. 6.6 at 0.5 Pa for $B_{max} = 600$ G: with increasing $F_{B,ref}$ the IV becomes steeper. This is also reflected in the *n*-values which increase from below 5 to around 7.5. This is a very encouraging result: in the introduction (section 6.1) it was mentioned that the IVs simulated without Bohm diffusion were not as steep as experimentally observed. Apparently including Bohm diffusion can overcome this shortcoming.

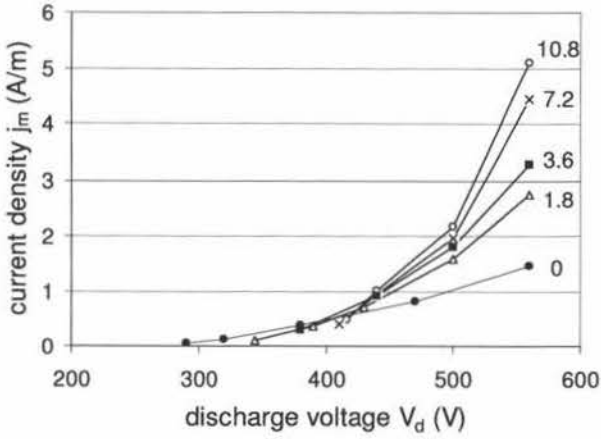

Fig. 6.6 Effect of $F_{B,ref}$ on the IV for B_{max} = 600 G at 0.5 Pa. The numbers at the right hand side of the curves indicate the corresponding $F_{B,ref}$–values.

6.3.2 Influence of Bohm diffusion on the pressure dependence of the MD

In this section, the pressure dependence of the MD as simulated including Bohm diffusion is investigated. In section 6.3.2.1 we look at the influence of the pressure at constant discharge current, in section 6.3.2.2 the influence on the IV is discussed.

6.3.2.1 Pressure dependence at constant current

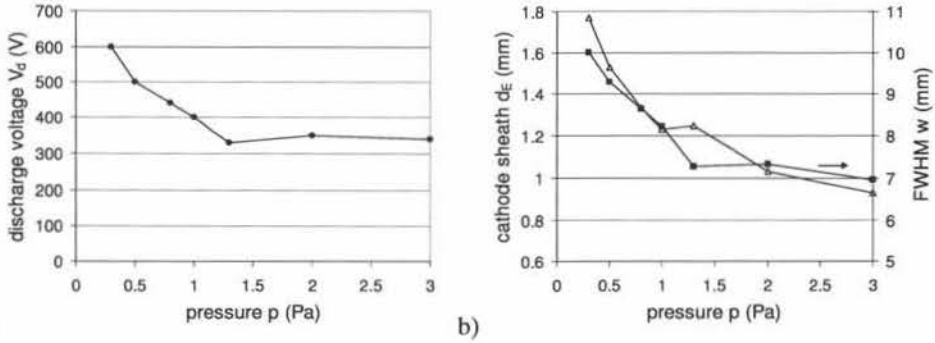

Fig. 6.7 Influence of the gas pressure on the discharge voltage V_d (*a*), on the cathode sheath thickness d_E (△) and on the FWHM *w* of the erosion profile (■) (*b*), at constant j_m (2.0 A/m) for $F_{B,ref}$ = 3.6 and B_{max} = 600 G.

This section discusses the influence of the pressure on the MD at constant line current density. Hence, it is similar to section 4.3.2 (Fig. 4.15). We start with the influence of the pressure on the discharge voltage (Fig. 4.15a), on the cathode sheath thickness and on the FWHM of the erosion profile (Fig. 4.15b). Note that here j_m is equal to 2.0 A/m, without Bohm diffusion it was equal to 0.5 A/m. Another interesting difference is the behaviour of V_d at high pressures: without Bohm diffusion, a small but persistent decrease was simulated. Here, the discharge voltage remains practically constant, with even a tendency to increase again. This can be explained as follows. With increasing pressure, the EGIP *f* increases. At high pressures, this increase is weak but, in the absence of Bohm diffusion, it is strong enough

to cause the small decrease in V_d as observed in Fig. 4.15a. When Bohm diffusion is included in the simulation, we have to take into account that with increasing pressure, the effect of Bohm diffusion decreases as can be seen in Fig. 6.8. This reduction of the actual F_B leads to an increase of V_d, as shown in Fig. 6.1a. Apparently, the latter effect is stronger than the increase in $\langle f \rangle$ for the conditions shown in Fig. 4.15a.

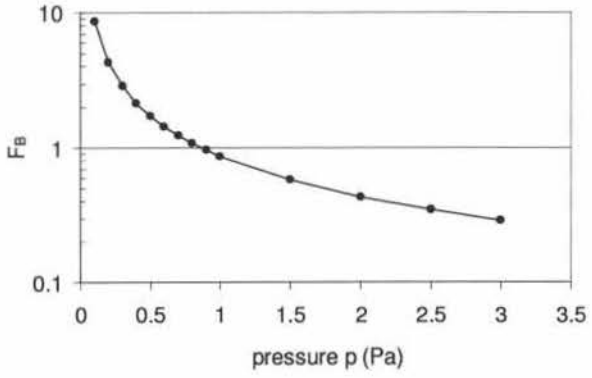

Fig. 6.8 Influence of pressure on the actual F_B for the results presented in Fig. 4.15.

For d_E and w we find a similar qualitative pressure dependence as without Bohm diffusion. However, the pressure dependence of w with Bohm diffusion is stronger: without Bohm diffusion it increases approximately 20% from the highest to the lowest pressure, with Bohm diffusion it increases more than 40%. The reduced contribution of Bohm diffusion with increasing pressure explains why the pressure dependence of w is stronger as due to this mechanism, the pressure exerts a direct influence on the electron mobility.

6.3.2.2 Pressure dependence of the IV at different magnetic field strengths

Fig. 6.9 shows the IVs simulated with $F_{B,ref} = 3.6$ at different gas pressures and magnetic field strengths. The maximum experimental discharge currents obtained with the magnetrons used for experimental verification (section 6.4.1) are around 1.0 A, which corresponds with $j_m \approx 10$ A/m. The IVs have been truncated accordingly. At 400 G (Fig. 6.9a) the typical pressure behaviour is reproduced, i.e. the fanning out of the curves at high discharge voltages. This behaviour is also retrieved experimentally (see Fig. 4.21a) and could also be simulated without Bohm diffusion (see Fig. 4.20a). However, by including Bohm diffusion, also the pressure dependence that is measured at stronger magnetic fields is reproduced (compare Fig. 4.21b and Fig. 6.9c). In this case, the IVs are practically parallel to each other.

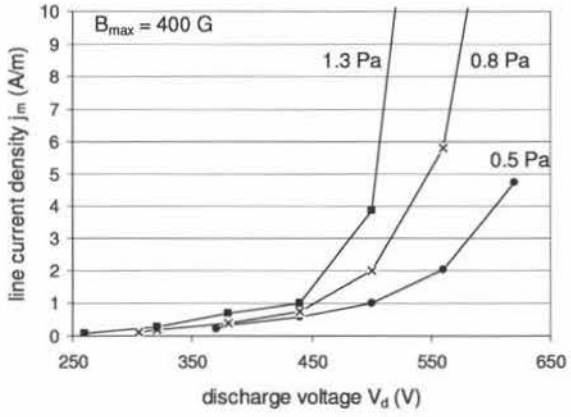

a)

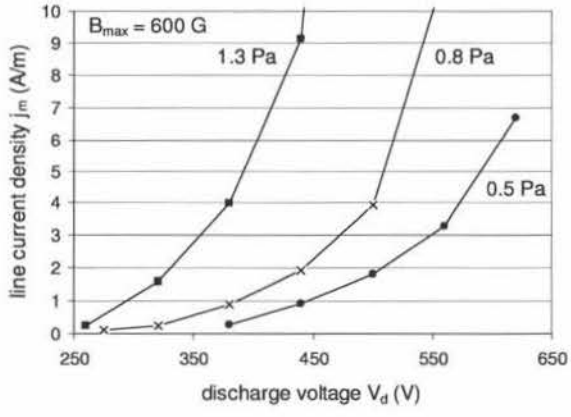

b)

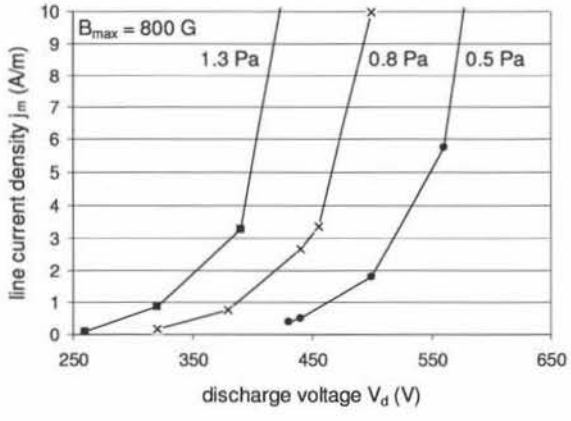

c)

Fig. 6.9 Influence of pressure on the IV for $B_{max} = 400$ (*a*), 600 (*b*) and 1200 G (*c*). The j_m-axis is limited to realistic values (see text).

From these results, it can be deduced that also the dependence of V_d on the magnetic field at a given discharge current and gas pressure is simulated correctly. This means that a plot like Fig. 4.22 can be obtained (not shown).

6.3.3 Conclusion

The relative occurrence of Bohm diffusion collisions is strongly dependent on both the magnetic field strength and the gas pressure. From the presented results, it follows that the increased electron mobility because of Bohm diffusion widens the erosion profile and leads to steeper IVs. By including Bohm diffusion it was also possible to simulate the influence of the magnetic field on the pressure dependence of the IVs.

6.4 Comparison of simulations with experiments

In this section the simulation and experimental results are compared. Before comparing, it is useful to consider what can be expected from the model (see also Introduction). Certain aspects of the MD are only in a very simplified form included in the SCM (e.g. the anode position, the presheath) while others are not included at all (e.g. the bulk electrons). Consequently, the SCM cannot be expected to reproduce peculiarities of the MD due to a specific magnetron configuration or operation, e.g. a specific anode arrangement, working at extreme high or low powers, ... Nevertheless, being convinced that the most important aspects and processes of the MD are represented correctly, the SCM should result in realistic, self-consistent values for the MD properties. Moreover, it should be able to produce the generic behaviour of the MD under the influence of the gas pressure, electrical power input and magnetic field strength.

First, the experimental conditions are discussed (section 6.4.1). Then follows an optimisation of the model (section 6.4.2). Finally, some results are compared and the agreement (or absence of it) with the experimental observations is discussed (section 6.4.3).

6.4.1 Experimental conditions

Most of the experimental data presented here are taken from [Depla05a]. This reference is dedicated to the importance of the discharge voltage to understand the MD. From the wealth of experimental results it reports, only the results regarding the influence of the gas pressure, the magnetic field, the electric power and the SE yield γ are considered. The influence of the latter was determined by measuring the discharge voltage using different target materials. The influence of the magnetic field strength is investigated by changing the target thickness. The description of the other experimental details is taken from [Depla05a]:

"The experiments were performed in a stainless steel chamber (approximately 0.025 m^3) which was evacuated down to a base pressure lower than 4×10^{-4} Pa with a turbomolecular pump backed up with a rotary pump. The base pressure was measured with a Penning gauge. The argon gas pressure during sputtering was measured using a capacitance gauge (Baratron MKS).
Two types of magnetrons were used. The first magnetron was built in the laboratory. We have used NdFeB magnets (Goudsmit Magnetic Supplies). The outer magnet has an outer diameter of 47 mm and an inner diameter of 34 mm. The inner magnet has a diameter of 20 mm. The second magnetron configuration was a commercially available magnetron (Von Ardenne, PPS 50). The latter one can be equipped with or without a plasma shield. This plasma shield is an extension of the anode ring around the magnetron.
Two-inch targets (Goodfellow/ SCI Engineering Materials, all targets were 99.99% pure, except for the Cu targets (99 %) used to study the influence of the magnetic field on the

discharge voltage) were mounted in the magnetrons and powered with a DC generator (Hüttinger 1500 DC). The discharge voltage was registered using a digital voltmeter. "

It should be mentioned that, for comparing the simulations with the experiments, the race-track length L_{rt} is required as it links the calculated line current density j_m with the actual discharge current I_d, see eq. (4.2). For the laboratory magnetron, L_{rt} is 8.2 cm, for the Von Ardenne magnetron it is 11.3 cm.

Next to these experiments, the simulations are also compared with own experiments. These were obtained using the same Von Ardenne magnetron, again without anode shield. This time an aluminium target was used.

The first set of experiments regards the measurement of the erosion profile. The central part of the target was masked such that the non-sputtered area could serve as the reference point for these measurements. The target thickness was 5.5 mm. An enlarged target diameter (58 mm) was preferred in order to visualise the outer edge of the race-track. The experiments were performed at constant current (0.43 A) at different pressures. In order to have a sufficiently deep erosion profile, each target was sputtered for 270 minutes. Then, the erosion profile was measured using a micrometer with needle-tip. Some erosion profiles were measured with an automated 3D measuring unit. In both cases, the vertical resolution was 0.01 mm.

During a second set of experiments, the MD was studied optically by measuring the light emission. For these experiments, the magnetron was mounted in a different vacuum chamber (approximately 50 *l*) and an aluminium target of thickness 4.5 mm was used. These measurements were performed at constant power (50 W) using a DC power supply (Advanced Energy MDX 20kW).

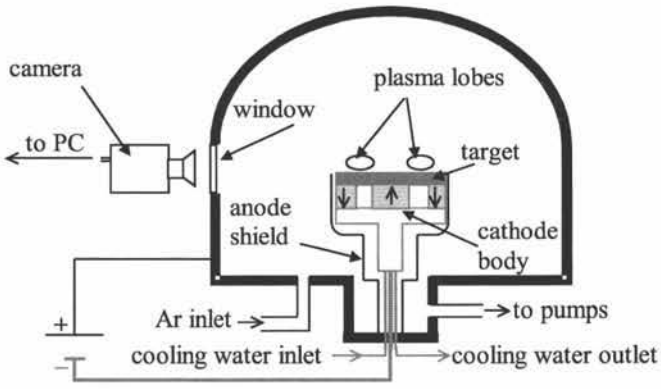

Fig. 6.10 Sketch of the configuration for the measurement of the plasma light emission.

A sketch of the set-up for measuring the plasma light emission is shown in Fig. 6.10: the anode cup of the magnetron was removed to allow the light to enter horizontally the analogue video camera (Panasonic S-VHS MS4). The black and white images were captured with a frame grabber (National Instruments NI-IMAQ-card) and 'translated' into grey scale values by Labview software (National Instruments). These values were used for plotting the intensity of the plasma light emission. The result is the light emission of the plasma (in grey scale values) in the direction perpendicular to the target. The length scale along the latter axis

was obtained in pixels. Through calibration it was determined that 1 pixel corresponds with 0.054 mm.

6.4.2 Optimising the accuracy of the model

For the simulation results presented here, the same settings as in section 6.3 were used. First, the basic result was obtained and the necessary points were determined through linear interpolation. When needed, some results outside the matrix result were obtained, e.g. because a larger discharge voltage or a smaller cathode sheath thickness were required. The former applies to weak magnetic fields and/or low pressures, the latter to strong magnetic fields and/or high pressures. To compare the SCM results with experiments, the accuracy of the model was increased by a more sophisticated calculation of the EGIP f and of the Hall drift velocity v_{ExB}.

In section 1.3.2 the influence of the initial starting conditions of the SE on the EGIP f was discussed: the accuracy improves by increasing the number of initial velocity vectors. This number is defined by m and n (see section 1.2.2). In Chapter 3 and 4, the average over 7 different initial velocity vectors in the xz-plane ($m = 0$, $n = 3$, see section 1.3.2) was taken for calculating f. This was a compromise between the required calculation time and the accuracy. Here, the average over 21 initial velocity vectors ($m = 5$, $n = 2$) is taken as this should give a more accurate value of the EGIP.

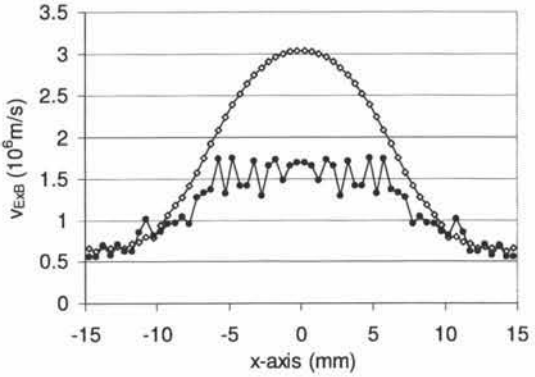

Fig. 6.11 Results for the Hall drift velocity v_{ExB} along the x-axis as estimated (◇) and as calculated using the MC technique (•). The results are obtained for $d_E = 1.6$ mm, $V_d = 440$ V at 2 Pa and $B_{max} = 600$ G.

Another adaptation to the model is the calculation of v_{ExB}, the Hall drift velocity of the electrons. This velocity is needed as it determines l_{ExB} which is required for calculating $A_{//,s}$, see eqs. (4.10) and (4.11) in section 4.2.3.4. There, v_{ExB} was estimated to be half of the drift velocity of an electron that does not undergo any collisions. Here, v_{ExB} is calculated by a MC method taking into account the electron interactions with the discharge gas. For a given starting position ten electrons were emitted and followed until their energy dropped below the threshold energy E_{th} (section 2.1). For each of these HEE the average drift velocity during their lifetime was calculated. The average of these values was taken for v_{ExB}. Fig. 6.11 shows both v_{ExB} as estimated and as calculated. For large $|x|$ (>5), the estimated v_{ExB} is quite accurate but around the centre there is almost a factor of two difference. For the general discussion of the magnetron behaviour this is of minor importance but it is crucial for obtaining quantitative results.

Both these changes do not have any fundamental influence on the results but they increase the accuracy of the model output. As usual, the trade-off is the required computation time, which is roughly twice as long.

6.4.3 Comparison of the simulation and experimental results

6.4.3.1 Choosing the input parameters

Two of the input parameters required by the SCM, the electron reflection coefficient R and the relative occurrence of Bohm diffusion collisions $F_{B,ref}$, are difficult to specify by lack of experimental data. Also the SE yield γ is not very accurately known for the different target materials. To avoid discussion about the exact value of the SE yield γ we took for both target materials that were used (copper and aluminium) the value of 0.1. This leaves two parameters, $F_{B,ref}$ and R, as "tuning parameters", i.e. they can be determined by comparing the simulations with the experimental results. Of course, we have to keep in mind the physical limitations. R is a material property and is not dependent of other external parameters. By lack of experimental data, R is taken the same for all target materials. The factor $F_{B,ref}$ is assumed to be independent of the type of magnetron (Von Ardenne or laboratory magnetron) used.

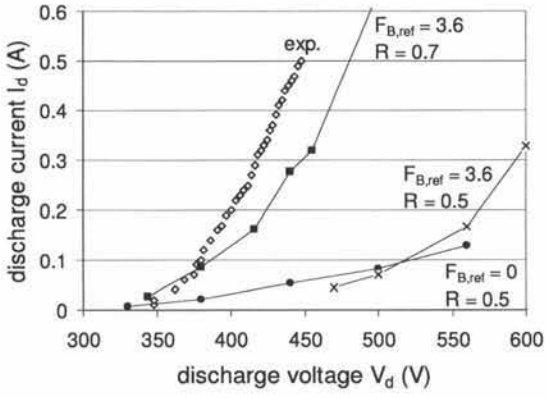

a)

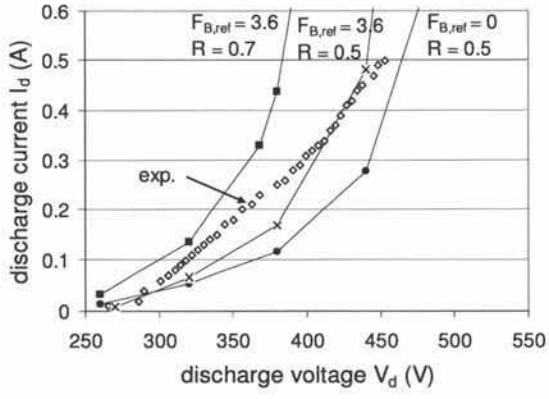

b)

Fig. 6.12 The experimental IV at 0.3 (*a*) and 1.0 Pa (*b*) for the laboratory magnetron with a 3 mm target together with the simulated IV using both standard and optimised settings (see text).

To find a value for these parameters, we compare the simulation results using the standard settings ($R = 0.5$, $F_{B,ref} = 0$) with the experimental results (Fig. 6.12). The IVs are obtained at 0.3 and 1.0 Pa for a target thickness of 3 mm using the laboratory magnetron ($B_{max} \approx 600$ G). At 1.0 Pa the agreement is quite good: the shape of the curves agrees rather well but the simulated IV has a stronger curvature. At 0.3 Pa there is no agreement at all. By setting $F_{B,ref}$ to 3.6 the situation at 1.0 Pa is not altered much but at 0.3 Pa there is a serious change: the IV is much steeper and the shape starts to look like the experimental one. However, the simulated discharge voltages are still too high. By setting $R = 0.7$ and keeping $F_{B,ref} = 3.6$ the simulated IV comes closer to the experimental one at 0.3 Pa. At 1.0 Pa the IV is for these settings already shifted to slightly too low discharge voltages and the increase in I_d at high V_d is stronger than experimentally observed. Nevertheless, with these settings the simulated and experimental IVs agree reasonably well at both pressures. Consequently, we refer to these settings for R and $F_{B,ref}$ as the "optimised settings". In principle, $F_{B,ref}$ and R could be further optimised by considering more IVs and using a mathematical method for their determination.

6.4.3.2 IV characteristics at different pressure and magnetic field strengths

The aim of the model is to reproduce the influence of the external parameters on the MD. The most important external parameters are the gas pressure p, the magnetic field strength characterised by B_{max} and the electrical power input (through I_d, V_d or directly through power regulation). The best way to assess all these parameters is to consider IVs at different pressures and magnetic field strengths. An example of such a series of measurements can be found in [Depla05a].

First, consider the IVs obtained using the Von Ardenne magnetron (without anode) with a copper target at two different pressures (0.4 and 1.2 Pa) and three different magnetic field strengths: $B_{max} = 400$, 600 and 800 G. Experimentally, these different magnetic field strengths were obtained by varying the target thickness. The results for 0.4 and 1.2 Pa are shown in Fig. 6.13 and Fig. 6.14, respectively. Part *a* gives the experimental results, part *b* the simulated IVs. The experimental IVs were measured up to 0.5 A, the simulated ones are shown up to 0.7 A. Given the assumptions made to deduce the SCM the agreement is considered very good, especially at 0.4 Pa. At 1.2 Pa the agreement is also good except for the weakest magnetic field: the IV for $B_{max} = 400$ G is steeper as the one for $B_{max} = 600$ G. Most likely, this is due to irregular behaviour of the EGIP f as a function of the magnetic field strength (see Fig. 1.14 in section 1.3.5).

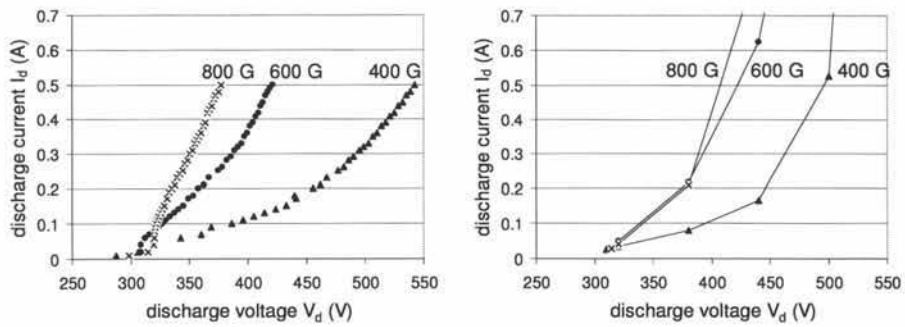

Fig. 6.13 The experimental IVs using the Von Ardenne magnetron (*a*) and the simulated ones (*b*) for $B_{max} = 400$ (▲), 600 (●) and 800 G (×) at 0.4 Pa.

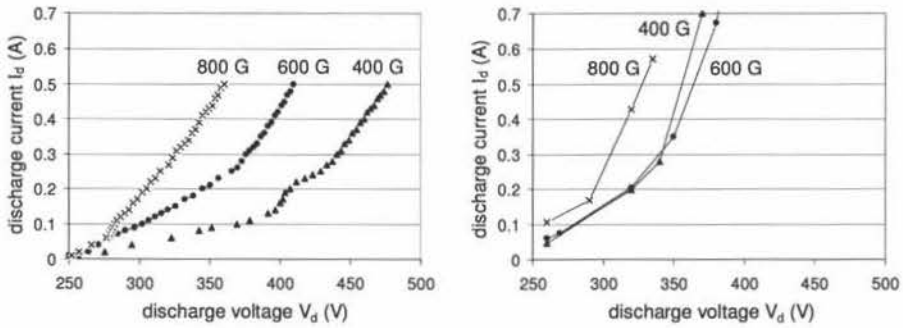

Fig. 6.14 The experimental IVs using the Von Ardenne magnetron (*a*) and the simulated ones (*b*) for $B_{x,max}$ = 400 (▲), 600 (•) and 800 G (×) at 1.2 Pa.

Second, we look at the IVs obtained using the laboratory magnetron for different magnetic field strengths and gas pressures. This time, the results are grouped per magnetic field strength. Fig. 6.15, Fig. 6.16 and Fig. 6.17 show the results obtained for 300, 600 and 1200 G, respectively. In each figure, the IV is shown for 0.2, 0.5 and 2.0 Pa. Part *a* of the figures give the experimental IVs, part *b* the simulated ones. The model is not able to reproduce the peculiarity in the shape of the IV for a specific condition. In most cases, there is a slight shift in the position of the IV along the V_d-axis. This is due to the extreme sensitivity of I_d on V_d. In spite of this, the main trends regarding the influence of the external parameters are reproduced, which was the intension of the model. Moreover, the simulation results apply to a very wide range of external parameters, e.g. B_{max} varies with a factor 4 (from 300 to 1200 G), the pressure even with a factor 10 (from 0.2 to 2.0 Pa). The electrical power varies from a few to more than 300 Watt.

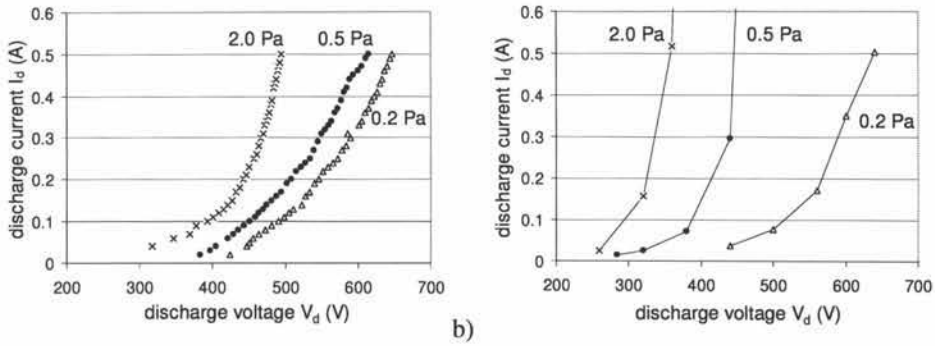

Fig. 6.15 The experimental IVs using the laboratory magnetron (*a*) and the simulated ones (*b*) at 0.2 (△), 0.5 (•) and 2.0 Pa (×) at for B_{max} = 300 G.

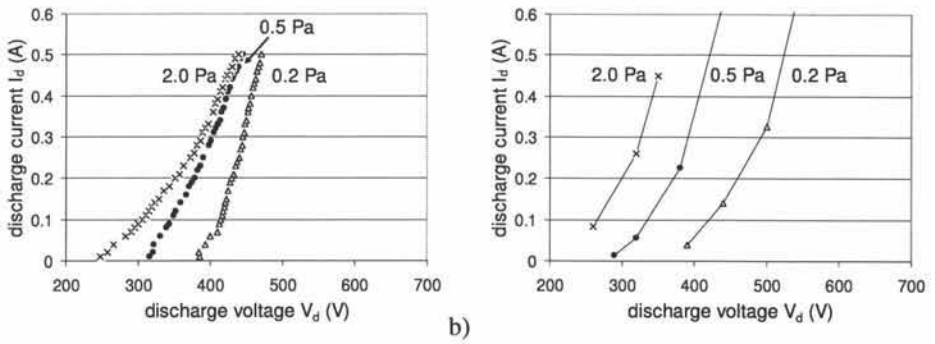

Fig. 6.16 The experimental IVs using the laboratory magnetron (*a*) and the simulated ones (*b*) at 0.2 (△), 0.5 (•) and 2.0 Pa (×) at for B_{max} = 600 G.

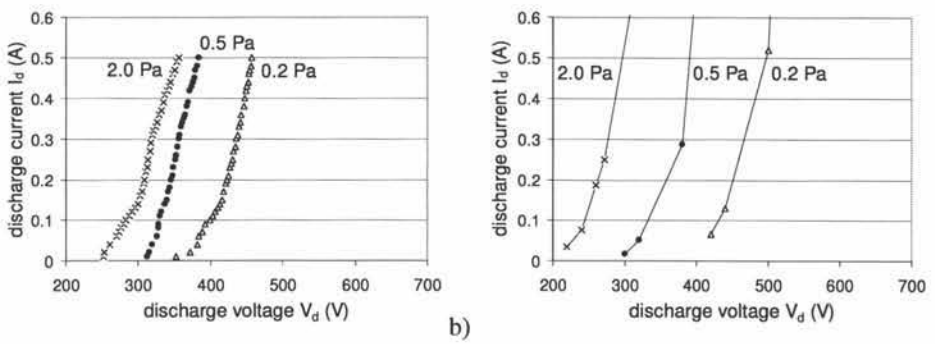

Fig. 6.17 The experimental IVs using the laboratory magnetron (*a*) and the simulated ones (*b*) at 0.2 (△), 0.5 (•) and 2.0 Pa (×) at for B_{max} = 1200 G.

In conclusion, even though the agreement between the experimental and simulated IVs is not perfect, the SCM is able to reproduce the dependence of the MD on the major three external parameters, i.e. the magnetic field, the gas pressure and the electrical power, over a wide range. Moreover, the test was performed using two different magnetrons. It is stressed

that, except for the three external parameters and the race-track length that were also varied experimentally, all other settings of the model were kept equal for all simulation results presented.

In the next sections, the variation of one parameter at the time is considered as this allows a more precise comparison of the experimental and simulation results.

6.4.3.3 Influence of the pressure on the magnetron discharge

In [Depla05a] the discharge voltage was measured as a function of the pressure at constant discharge current. The results were obtained using the laboratory magnetron with a copper target. These results, together with the simulated dependence are shown in Fig. 6.18. The agreement is very good. The two main differences are the slightly higher simulated discharge voltages at low pressures and the stronger voltage decrease at high pressures for higher current (I_d = 0.42 A).

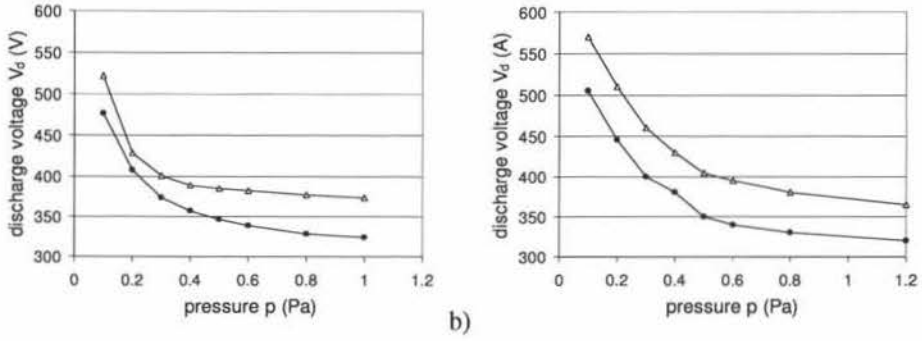

Fig. 6.18 The influence of the pressure on the discharge voltage V_d as experimentally measured (*a*) and as simulated (*b*). The results are shown for I_d = 0.16 (•) and 0.42 A (△) for B_{max} = 600 G. The experimental results are obtained using the laboratory magnetron.

As mentioned before, the pressure also influences the width of the erosion profile. The results are shown in Fig. 6.19a. The area under the mask (x'<2.7 mm) on the target surface coincides for all erosion profiles since there is no erosion or redeposition there. Consequently, the measurement in this area, corresponding to the point x' = 2.6 mm in Fig. 6.19a, served as a reference. The x'-axis represents the distance along the target surface, its origin is the centre of the target. Given the small absolute maximum depths of the erosion profiles (around 0.6 mm for each target), the differences in increase of magnetic field strength due to target erosion can be neglected. In order to compare the erosion profiles they were normalised by setting the maximum depth to minus one. It can be clearly seen that with decreasing pressure the width of the erosion profile increases in the considered pressure range.

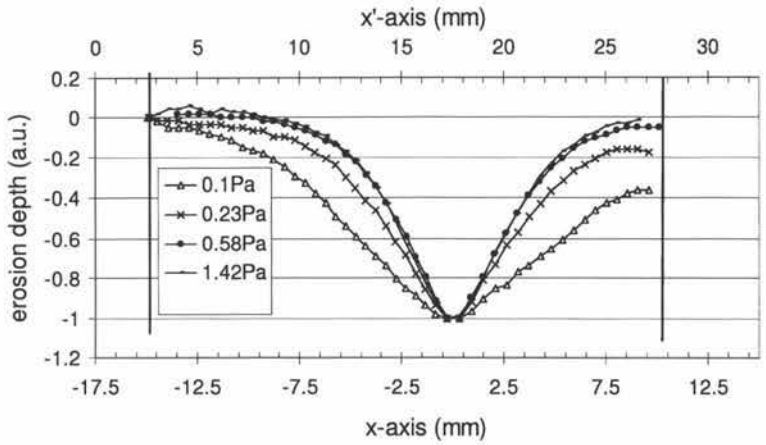

a)

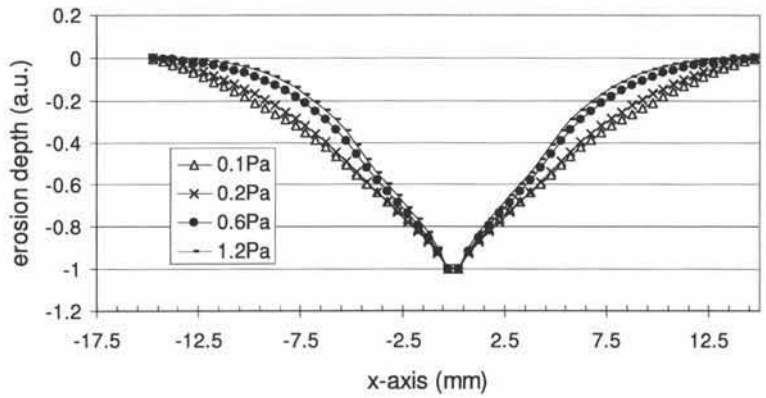

b)

Fig. 6.19 The influence of the pressure on the erosion profile as experimentally measured (*a*) and as simulated (*b*). The results are shown for $I_d = 0.43$ A. In part *a* of the figure the *x*'-axis gives the distances measured from the centre of the target. The *x*-axis gives in both cases the distances measured from the centre of the race-track. For the experimental results also the area covered by the mask (see text) is indicated (region on the left hand side of the left vertical line) together with the outer diameter of the target (right vertical line).

Fig. 6.19b shows the simulated erosion profiles using the optimised settings. It should be kept in mind that the intention of the comparison is *not* to show that the model can accurately reproduce the erosion profile for a given magnetron. This would require taking into account the specific magnet and cathode geometry, redeposition on the target, influence of the erosion groove forming, ... Moreover, the symmetric magnet geometry as shown in Fig. 1.2 was used. In the circular magnetron used for the experiments, the magnet configuration in a 2D cross section is asymmetric. Also the spacing *d* between the magnets (see Fig. 1.2) of the experimental and simulated configuration is not the same. Hence, the aim cannot be to reproduce the erosion profile. Instead, the aim is here to reproduce the influence of the gas pressure on the erosion profile. From Fig. 6.19 it can be deduced that the simulated erosion profiles do widen with decreasing pressure but the pressure dependence is weaker than the measured one. For the experimental results, the FWHM of the race-track increases

approximately with 50 % from the highest to the lowest pressure. For the simulated erosion profiles, the increase is only around 25 %.

Also the cathode sheath thickness was determined as a function of the pressure. Therefore, the plasma emission was recorded as a function of the distance in the direction perpendicular to the target (Fig. 6.20a). The results are very similar to what was measured by Lan Gu and Lieberman [LanGu88] (see also section I.1.3.3.5). Now, we briefly discuss the measured intensity profiles and the method that was used to deduce Δ, the height of the maximum of the plasma emission intensity above the target (as defined in section I.1.3.3.5).

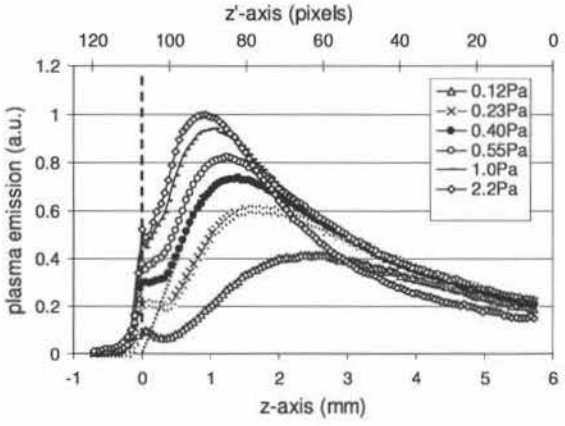

a)

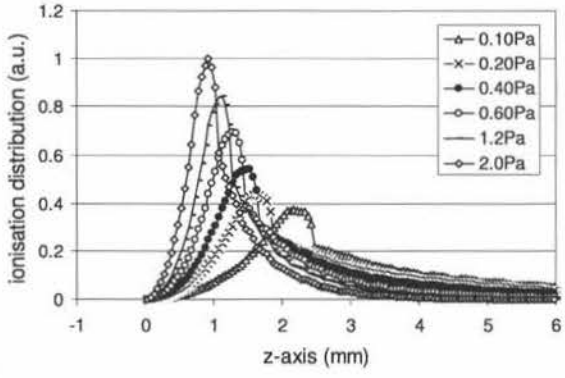

b)

Fig. 6.20 The influence of the gas pressure on the optical emission of the MD at 50 W, as measured (*a*) and as simulated (*b*). Note that the emission has been normalised to the maximum emission at 2.2 Pa (2.0 Pa) for the experiments (simulations). The dashed vertical line (part *a*) indicates the position of the target. The dotted line (part *a*) suggests the "true" emission, i.e. without target reflection for 0.40 Pa.

The z'-axis represents the distance along the direction perpendicular to the target and is expressed in pixels. The vertical line at $z' = 107$ indicates the position of a small peak that is due to the light that reaches the camera after reflection on the target. Although the exact position of the target surface is, according to [LanGu88], probably at slightly lower z'-values, this peak was chosen as first reference point for determining Δ because the peak is easily recognisable and hardly changes with pressure. Because of the measured reflected light, the

signal is troubled. Indeed, the "true" optical emission from the plasma is expected to drop to zero at $z = 0$. This true emission profile is sketched for 0.40 Pa (dotted line in Fig. 6.20a). The highest peak of each profile is the second reference point. The distance Δ is defined as the number of pixels between the two reference points. This number of pixels can be converted to millimetres (1 pixel = 0.054 mm).

In the model the light emission of the plasma is not simulated. However, as discussed in section 2.6.5 (see e.g. Fig. 2.30), the excitations and ionisations generated by the high energy electrons occur practically at the same positions. Hence, the ionisation rate distribution can be used for comparison with the experimentally measured emission intensity and is plotted in Fig. 6.20b. The shift of the peak and the decreased intensity with decreasing pressure are reproduced very well. The discontinuity in the simulated distribution that can be seen especially at lower pressures (e.g. around $z = 2.4$ mm at 0.1 Pa) is due to the ending of the cathode sheath and is an artefact of the simulation. The main difference between the experimental and simulated profiles is that the experimental ones decrease slower with increasing distance from the target. A similar comparison of the measured emission with the simulated ionisation distribution is reported by Miranda et al. [Miranda90] (see also Fig. 2.7b in section I.2.2.2). They tried to compare their MC results with the measured intensities of [LanGu88] and report a similar discrepancy. They argue that the higher experimental emission further away from the target is due to emission from the sputtered metal particles. This reasoning applies here too.

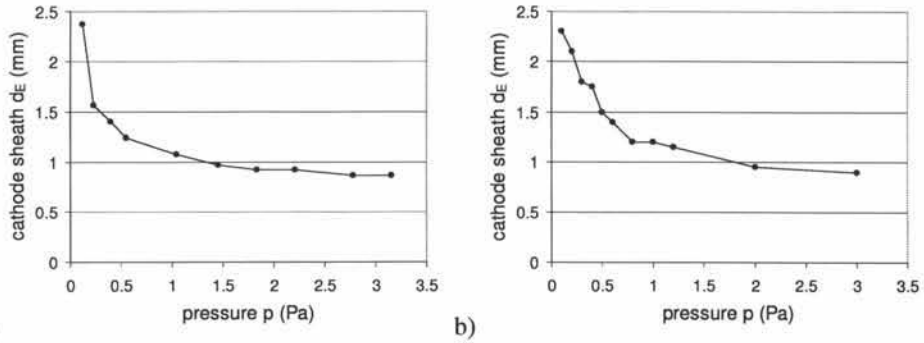

Fig. 6.21 The influence of the pressure on the cathode sheath thickness at 50 W as measured (*a*) and as simulated (*b*).

Based on the results shown in Fig. 6.20, a plot of the pressure dependence of Δ is made (Fig. 6.21): for pressures above 1.5 Pa, Δ is nearly constant with pressure, between 0.5 and 1.5 Pa there is only a small change and below 0.5 Pa the increase in Δ with decreasing pressure is strong. The agreement between the experimental and simulation results is very good.

6.4.3.4 Influence of the magnetic field at constant current and gas pressure

In [Depla05a], the influence of the magnetic field on the MD is investigated by changing the target thickness. This procedure was performed for both the laboratory and the Von Ardenne magnetron. By measuring B_{max} for each target thickness for the two magnetrons, a plot showing V_d versus B_{max} can be made. The result is shown in Fig. 6.22a for $I_d = 0.3$ A at 2.0 Pa.

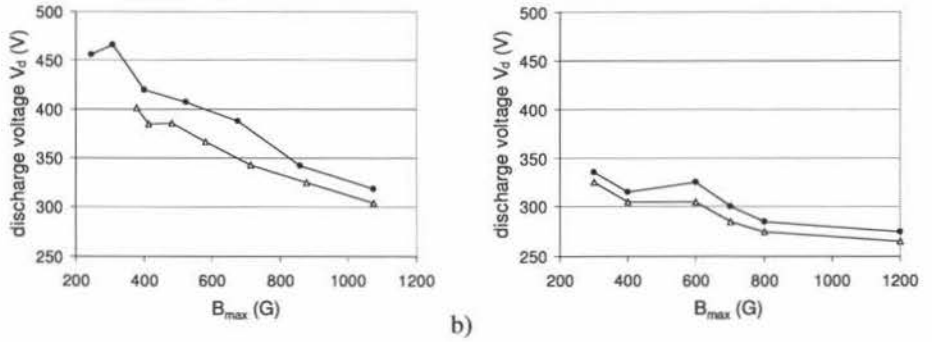

Fig. 6.22 The influence of the magnetic field strength B_{max} on the discharge voltage V_d as experimentally measured (*a*) and as simulated (*b*). The results are shown for $I_d = 0.3$ A at 2.0 Pa. The results presented are for the laboratory (•) and the Von Ardenne (△) magnetron.

In the simulation, the magnetic field variation is not obtained by changing the target thickness. Instead, the strength of the magnets is varied because it is much more simple. This way, possible changes in the structure of the magnetic field due to a target thickness variation are not taken into account. However, these influences are expected to be of minor importance. The simulation results are shown in Fig. 6.22b. The discharge voltage decreases as measured experimentally but the simulated magnetic field influence is substantially weaker. Overall, the simulated discharge voltages are smaller as the experimental ones. Note that the consistently lower discharge voltages measured for the Von Ardenne magnetron are reproduced. These low voltages are due to the larger race-track length (L_{rt}) of the Von Ardenne magnetron: I_d is calculated as the product of j_m and L_{rt} (eq. (4.2) in section 4.2.3.1). Hence, to obtain a given I_d a longer L_{rt} requires a smaller j_m and, consequently, a smaller V_d.

6.4.3.5 Influence of the SE yield on the discharge voltage

As an application, the discharge voltage is calculated as a function of the SE yield γ at constant pressure (0.3 Pa) and discharge current (0.16 A). For the experiments the laboratory magnetron was used. The variation in γ was experimentally achieved by using different target materials under otherwise identical experimental conditions. Fig. 6.23 shows that the increasing steepness of the IV with increasing γ is reproduced nicely. The relative spacing between the curves is also reproduced very well for $\gamma = 0.06$ through 0.14. For $\gamma = 0.18$ the experimental curve lays much closer to $\gamma = 0.14$ as the simulated one. The choice of yttrium (Y) as material for obtaining the experimental curve corresponding with $\gamma = 0.18$, is based on the relations (1.10), (1.11) and (1.12) for γ (see section I.1.2.2.1) and not on experimental data [Depla05a]. This, together with the comparison of the simulated and experimental IVs suggests that very likely the SE yield of yttrium is in reality smaller as predicted by the mentioned models.

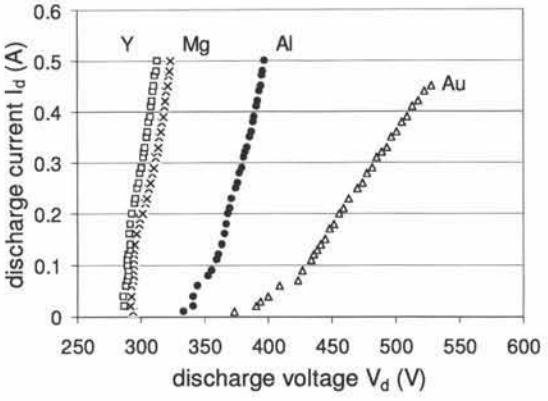

a)

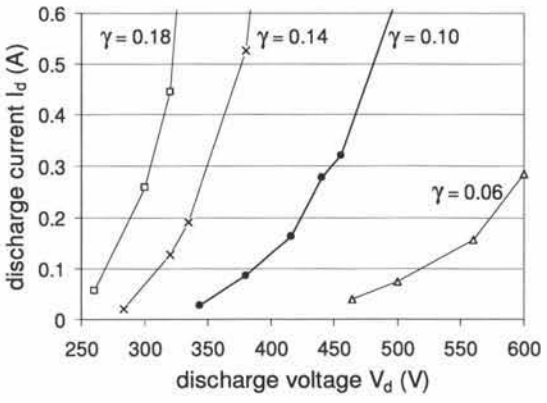

b)

Fig. 6.23 Influence of the SE yield γ on the IV at 0.3 Pa, as measured (*a*) and as simulated (*b*). The experimental curves are obtained with different target materials: Au, Al, Mg and Y. The corresponding γ-values used in the simulation for these materials are 0.06, 0.10, 0.14 and 0.18, respectively.

On the other hand, using again the extended Thornton relation, we can determine for each couple (V_d, γ) the value of $\langle fm \rangle$. The plot of $\langle fm \rangle$ as a function of γ reveals that it is not constant (not shown). Hence, the linear fit to $1/V_d$ vs. γ is not completely physically correct but is a first order approximation. As such, it is an interesting way to investigate the SE yield of materials, see e.g. [Depla05a,b].

Given the uncertainty of the SE yield of a material, it is also interesting to look at the general influence of γ on the MD. Therefore, $1/V_d$ is plotted as a function of γ for a whole range of γ at 0.3 Pa (Fig. 6.24). The experimental results are indicated by diamonds (♦) with a horizontal error bar. The simulated results are represented by circles (O). According to the extended Thornton relation (eq. (3.7)), the factor relating $1/V_d$ and γ is $\langle fm \rangle / W$. The effective ionisation energy W can be considered constant in the range considered. If it is assumed that $\langle fm \rangle$ is constant, there should be a linear relation between $1/V_d$ and γ. Fig. 6.24 shows that the simulated results can indeed be fitted by a linear relation. Also for the experimental results this linear approximation appears acceptable.

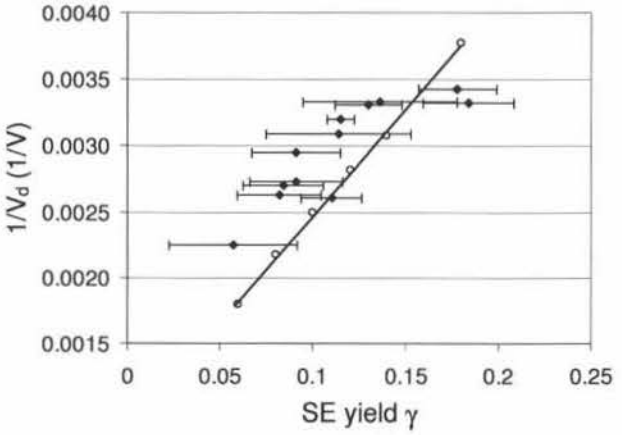

Fig. 6.24 Dependence of $1/V_d$ on the SE yield γ for $I_d = 0.16$ A at 0.3 Pa. The diamonds (♦) represent the experimental points obtained by sputtering different target materials using the laboratory magnetron. Note that because of the uncertainty of the values for the SE yield of the different materials, error bars are shown. The circles (O) represent the simulated dependence. The line is a guide for the eye based on the simulated results.

6.5 Conclusions

In this chapter, Bohm diffusion was introduced in the SCM. This was done on a phenomenological basis. The influence of increasing the "amount of Bohm diffusion" on the MD properties was simulated. These changes could be related to the increased mobility of the electrons in the direction perpendicular to the magnetic field lines. The main advantage of including Bohm diffusion is that it enables the simulation of the extremely steep current-voltage relations that are characteristic for the MD.

The results of the SCM were compared with experimental results. Two input parameters of the SCM, the electron reflection coefficient R and the relative occurrence of Bohm diffusion collisions, were used as tuning parameters.

Given that the SCM takes some aspects of the MD only in a very simplified form into account and others not at all (e.g. the bulk electrons are completely neglected), the agreement between the experimental and simulations is very good. The SCM has the, to our knowledge, unique ability to reproduce self-consistently the influence of the main three external parameters (gas pressure, magnetic field strength and applied electrical power) over a wide range. Also the dependence of the MD on the SE yield γ was reproduced. This indicates that the SCM captures the most important processes occurring in the MD. As such, the model is a valuable tool to gain insight in the generic MD behaviour.

Summary

Magnetron sputtering is a deposition technique based on the generation of a magnetically enhanced discharge at reduced pressure. Given its industrial relevance, efforts are being made to simulate the entire deposition process. The *m*agnetron *d*ischarge (MD), one part of this process, forms the topic of this work.

Objective

More precisely, the objective of the presented work is to obtain a fundamental understanding of the MD, i.e. the identification and modelling of the processes crucial for the generic MD behaviour. This should result in a simplified model that enables the self-consistent simulation of the MD over wide range of external parameters. The emphasis is on the dependence on the magnetic field, the gas pressure and the electrical power input.

Literature review

Fundamental aspects of the MD

The already existing wealth of experimental measurements and proposed theories was studied in order to distil the generic magnetron discharge behaviour from them. From this literature review, it followed that the general processes related to the working of the MD are well-known. However, some issues are not completely clarified. The ones that are of concern here are summarised briefly.

- The *s*econdary *e*lectrons (SE) emitted from the target are brought back to the vicinity of the target because they follow the magnetic field lines. This leads to electron-target interaction, which results in recapture of the electrons. Although it has been known for a long time that this process occurs and that it can strongly influence the discharge voltage, practically no work has been done to quantitatively assess recapture.

- In a MD the Child-Langmuir law cannot be applied because, due to the magnetic field, the cathode sheath is neither electron-free nor source-free. The latter is due to the ionisation within the sheath. In spite of this, the Child-Langmuir law is frequently applied to the MD, mainly by lack of an alternative.

- Characteristic for the MD is the very steep current-voltage characteristic, i.e. at high electrical powers, the discharge current increases very strongly for a small increase of the discharge voltage. Although efforts are made to physically clarify this relationship, basically only phenomenological models exist.

- Due to the E×B drift of the electrons, there exists a Hall current in the MD. Experimental measurements of the ratio of the Hall current and the discharge current (towards the target) reveal values that are substantially lower than theoretically predicted. Consequently, there is anomalous electron diffusion, i.e. the electron transport in the direction perpendicular to the magnetic field lines is larger than theoretically expected. The anomalous transport is especially important at strong magnetic fields and/or low gas pressures. Although it is suggested that this enhanced transport is related to electric field oscillations, no quantitative models exist for this phenomenon.

Modelling of the magnetron discharge

The different techniques and models used for describing the MD were examined. Existing models range from very rudimentary to extremely detailed ones. The most commonly encountered self-consistent models are the *P*article-*I*n-*C*ell *M*onte *C*arlo (PIC-MC) model and the hybrid model. The latter combines a Monte Carlo method for the high energy electrons with a fluid description of the ions and bulk electrons. These models result in a wealth of data; very interesting is the strong sensitivity of the discharge properties on the SE yield γ. Unfortunately, the experimental values of these yields are not known very accurately.

The main disadvantage of these models is the required computational load. As such, they are not so practical to investigate the MD dependence on one or more parameters over a wide range. Moreover, it is not so clear whether they can reproduce accurately the MD behaviour for conditions where the anomalous electron diffusion is important. For the hybrid model this is due to the use of electron diffusion constants. The PIC-MC model should in principle be able to deal with the problem but the time scale at which the process plays is too long to be calculated within a reasonable time.

Description of the simplified self-consistent model and major results

From the literature overview, it follows that a simplified model is required for reproducing the MD dependence on external parameters over a wide range. Consequently, a two-dimensional simplified but *S*elf-*C*onsistent *M*odel (SCM) for the d.c. planar magnetron discharge was developed. Before actually developing the SCM, two issues had to be dealt with: the recapture of the SE and the distribution of the ions generated by the *h*igh *e*nergy *e*lectrons (HEE).

Recapture

The process of recapture was modelled by introducing the *e*ffective *g*as *i*nteraction *p*robability (EGIP) f. It is basically defined as:

$$f = 1 - e^{-\frac{s}{\lambda}}$$

with s the average distance travelled by the electron before it is recaptured by the target and λ the mean free path length of the electron. This shows that with decreasing pressure, the EGIP decreases (increasing λ) and that especially the SE emitted close to the centre of the race-track have a small EGIP (small s) compared to the ones emitted at the edges (large s). Because of the latter, it is more appropriate to use the average EGIP, represented by $\langle f \rangle$. For typical MD conditions (V_d = 300 V, B_{max} = 600 G, p = 0.5 Pa), the EGIP $\langle f \rangle$ is around ⅓, i.e. about ⅔ of the electrons is recaptured.

Ionisation model

The electrons in a MD can be split in HEE and bulk electrons. Due to their low energy, the latter cannot contribute to the ionisation, and thus, they are not considered in the model. To describe the ionisation distribution of the HEE, the discharge area is split in arch-shaped regions. The physical background for this is that the collisionless motion of the HEE is limited to such arch-shaped regions. The effect of the electron interactions with the discharge gas was analytically modelled as a probability for the electron to hop from one arch to

another. This way, a fast *I*onisation *M*odel (IM) was developed to determine the distribution of the ions generated by a single electron emitted from the target.

Using the IM it was found that the ionisation distribution is not directly influenced by the gas pressure. This characteristic could be used by future MD models to reduce the computational load. Moreover, it appeared that electrons emitted close to the centre of the race-track have similar ionisation distributions. Another important result is that a substantial amount of ionisation occurs in the cathode sheath of the MD. This so-called sheath ionisation is important because the ions generated in the cathode sheath can become a HEE and contribute to the ionisation. This effect was characterised by the multiplication factor m. This factor gives the ratio of the total number of ions $n_{ion,tot}$ generated because of the emission of a single SE and the theoretical number of ions n_{ion} it can generate without sheath ionisation:

$$m = \frac{n_{ion,tot}}{n_{ion}}$$

This value is close to one for SE emitted at the edge of the race-track but, for typical MD conditions, it increases to a value of about three to five for SE emitted close to the race-track centre. Because of this, it is useful to introduce the average multiplication factor $<m>$.

Self-consistency

The above described IM does not include electron-electron interactions. Consequently, it does not have to be restricted to a single SE emitted from the target but can be used to determine the ionisation distribution of several SE emitted at once. Hence, for a given emission profile of SE at the target surface, the IM allows the calculation of the resulting ionisation. This way the self-consistent model can be deduced.

Assume a SE emission profile that specifies the (relative) number and the positions of the SE emitted from the target. First, it has to be taken into account that due to recapture not all of these SE become HEE. Then, the IM is used to calculate the ionisation distribution generated by the HEE with taking into account the multiplication factor m. From this, the ion bombardment $\mathcal{B}$ at the target is easily deduced. When an ion hits the target material, the average number of emitted electrons is given by the SE yield γ (typically 0.1 for metals). Thus, from the ion bombardment a new SE emission profile can be deduced. Iterating through this process and demanding that the original and the new SE emission profile should be identical makes the model self-consistent. Indeed, for a given input of the magnetic field geometry, the discharge voltage and the gas pressure, the corresponding MD properties are retrieved, e.g. the cathode sheath thickness, the erosion profile width or the relative ionisation distribution.

By using the SCM, the Thornton relation for determining the minimum discharge voltage at which the MD can be maintained is extended to a general relation for the discharge voltage:

$$V_d = \frac{W}{\gamma < fm > \varepsilon_e \varepsilon_i}$$

with W the effective ionisation energy (≈30 eV for argon), ε_i the ion collection efficiency and ε_e the fraction of the theoretical number of ions that the electron effectively generates before it is lost from the discharge. Both ε_i and ε_e can be assumed equal to one for typical MD conditions. In the original Thornton relation sheath ionisation is not considered ($m = 1$) and

the EGIP f is given a estimated value ($f = 0.5$). Because the SCM is two-dimensional and as it includes the magnetron configuration (geometry and magnetic field strength), f and m can be calculate accurately.

This extended Thornton relation shows that the pressure and magnetic field influence on the MD acts through f and m as all the other quantities at the right hand side of the expression are constant for a given target material and typical MD conditions.

Discharge current

The next challenge was to deduce the discharge current I_d from the obtained MD properties. The line current density j_m was introduced. It is related with I_d through the race-track length L_{rt}:

$$I_d = j_m L_{rt}$$

To determine j_m, the CL law had to be extended. Indeed, the CL law can only be applied when the charge supply requirement is fulfilled, which is a fundamental restriction for its use. As the discharge has to supply the charge carriers, this requirement cannot be taken for granted. We distinguish between the availability of charge carriers "in time" and "in space".

To check the requirement "in time", two time scales are critical: the time the ions need to reach the cathode and the time the electrons need to generate the ions. The charge supply requirement in time is only fulfilled if the latter occurs much faster than the first. In a diode discharge this requirement is met. In a magnetron discharge it is not because the low gas pressures increases the ion generation time. To account for this the factor $A_{//,t}$ was introduced. This factor basically accounts for the considerable fraction of ions (typically between ¼ and ½) that is generated within the sheath.

The requirement "in space" means that the electrons need to generate the ions in such a region that, on average, the ions hit the cathode at the same spot as from where the electron was emitted. This requirement is met in diode discharges but not in magnetron discharges because, due to the E×B drift of the electrons, the ions are generated scattered over the race-track length. This is described by the factor $A_{//,s}$.

Taking into account the above, the following relation is deduced for j_m:

$$j_m = j_d A_{//,t} A_{//,s} \int \mathcal{B}(x) dx$$

with x the direction across the width of the race-track. The integration is needed to convert the surface current density j_d into the line current density j_m and accounts for the non-uniformity across the race-track.

Using this relation for j_m, the discharge current could be calculated. The model was able to reproduce the behaviour of the MD discharge with decreasing pressure at constant current. Also the typical IVs could be simulated. However, it appeared that the extreme steepness of the IVs was missing and that the influence of the magnetic field on the gas pressure dependence was not retrieved.

Effect of anomalous or Bohm transport

In order to resolve the discrepancy between the simulated and experimental results, two processes not included in the model so far were examined: Coulomb collisions and Bohm (or anomalous) diffusion. The first could explain the magnetic field dependence of the pressure influence of the cylindrical (or post) MD but it can be ruled out for planar magnetrons because the HEE are too energetic. The latter was added to the SCM in an empirical way by introducing an artificial type of interactions, the Bohm diffusion collisions. These represent the electron interactions with the electric field oscillations, which are supposed to generate anomalous diffusion. The "amount" of Bohm diffusion is defined by F_B, the occurrence of the Bohm diffusion collisions relative to the standard collisions (ionisations, excitations and elastic collisions). F_B is proportional to the magnetic field and inversely proportional to the gas pressure, indicating that anomalous electron transport is especially important at strong magnetic fields and low pressures.

The influence of increasing the "amount of Bohm diffusion" on the MD properties was simulated. These changes could be related to the increased electron mobility in the direction perpendicular to the magnetic field lines. The main advantage of including Bohm diffusion is that it enables the simulation of the extremely steep current-voltage relations that are characteristic for the MD.

The results of the SCM were compared with experimental results. Two input parameters of the SCM, the electron reflection coefficient R and the relative occurrence of Bohm diffusion collisions, were used as tuning parameters. Given that the SCM takes some aspects of the MD only in a very simplified form into account and others not at all (e.g. the bulk electrons are completely neglected), the agreement between the experimental and simulations is considered very good.

The SCM has the, to our knowledge, unique ability to reproduce self-consistently the influence of the main three external parameters (magnetic field strength, gas pressure and electrical power) over a wide range. Also the dependence of the MD on the SE yield γ was reproduced. This indicates that the SCM captures the most important processes occurring in the MD. As such, the model is a valuable "virtual" tool to gain insight in the generic MD behaviour.

Suggestions for further research

For the simplified self-consistent model

As mentioned, the SCM takes some aspects of the MD only in a very simplified way into account, other aspects are completely neglected. The accuracy and applicability of the SCM could be fundamentally improved by working on these. The most important ones are the self-consistent calculation of the electron temperature and the pre-sheath, the electron contribution to the discharge current and the effect of gas density reduction.

Moreover, the rudimentary model used for certain aspects could be elaborated. This principle was already applied in this work when calculating the recapture of secondary electrons. In general a two-dimensional approximation of the cosine distribution was used but for comparison with the experiments a more accurate three-dimensional approximation was made. Of course, this comes at the pay-off of an increased calculation time.

By making minor, non-fundamental changes to the model, it could also be used to investigate aspects of the MD, like the influence of the erosion groove formation on the target or switching to another (non-reactive) discharge gas.

For general magnetron discharge modelling

From the simulation results obtained with the SCM and with other MD models, it follows that the effective SE yield is crucial for a reliable result. Hence, existing models for the MD should, if not already the case, include recapture of SE. This also means that further experimental research is needed to determine both the SE yield and the reflection coefficient that describes the electron-target interaction.

All models will be helped by a better understanding of the anomalous electron drift. For the PIC-MC approach, this knowledge is, in principle, only needed to confirm the simulation results. For the other approaches, the knowledge is crucial as it is required to describe the electron motion. It would be very interesting to see how including the anomalous electron transport by tuning the electron diffusion coefficients affects the simulation results.

In general, to verify the different models, it is clear that more direct confrontation of simulation and experimental results is needed, something that is very rarely encountered in literature. Moreover, the simulation should be aimed at reproducing trends as this is a good way to detect flaws in the modelling.

For developing a virtual sputter magnetron

From the different modules needed to develop a virtual sputter magnetron, the modelling of the film growth based on the incoming particle fluxes on the one hand and of the magnetron discharge characteristics on the other hand, are the most challenging. Given the required computational load, a workable virtual sputter magnetron can in the foreseeable future, in spite of the increasing computer power, only be realised using (very) simplified models. The actual combining of existing simplified models to obtain a virtual tool describing magnetron sputter deposition appears more an engineering than an academic challenge.

Samenvatting

Magnetronsputteren is een depositietechniek gebaseerd op de generatie van een magnetisch geassisteerde gasontlading bij lage druk. Deze gasontlading wordt aangeduid als "de magnetrononontlading". Gezien het industriële belang van deze depositietechniek wordt heel wat (onderzoeks)werk verricht naar de simulatie ervan. Eén onderdeel daarvan, de studie en modellering van de *m*agnetron*o*ntlading (MO), vormt het onderwerp van dit doctoraatswerk.

Doel

Het doel van het voorgestelde werk is inzicht bekomen in de fundamentele werking van de MO. Dit betekent het identificeren en modeleren van de belangrijkste deelprocessen die het generieke gedrag van de MO bepalen. Dit moet leiden tot een vereenvoudigd model dat toelaat de MO op een zelfconsistente wijze te simuleren over een groot bereik van externe parameters. De klemtoon bij het onderzoek ligt op de invloed van het magneetveld, de gasdruk en het opgelegde elektrische vermogen.

Literatuurstudie

Fundamentele aspecten van de MO

De bestaande overvloed aan experimenteel werk en bijhorende theoretische verklaringen werd bestudeerd met als doel het uitfilteren van het generieke gedrag van de MO. Op basis van deze literatuurstudie besluiten we dat het algemene principe van de MO goed gekend is maar er zijn nog enkele pijnpunten. De voor dit werk relevante ervan worden nu kort toegelicht.

- De *s*ecundaire *e*lektronen (SE) die van op de *target* worden geëmitteerd volgen de magneetveldlijnen en keren bijgevolg terug naar de *target*. De daaruit voortvloeiende elektron-*target* interactie geeft aanleiding tot het opnieuw invangen van SE. Er is nog vrijwel geen onderzoek gedaan naar het effect van dit proces op de MO, ook al is dit proces reeds lang gekend.

- De kathode *sheath* is het gebied aan de kathodezijde waar een netto ruimteladingslaag aanwezig is (in het Nederlands ook aangeduid met de term "donkere ruimte"). In een MO kan de Child-Langmuir wet niet toegepast worden omdat er, door de aanwezigheid van het magneetveld, in de kathode *sheath* elektronen aanwezig zijn en er elektron-ion paren gevormd worden. Toch wordt, bij gebrek aan alternatieven, de Child-Langmuir wet veelvuldig aangewend voor de MO.

- Typisch voor de MO is de extreem steile stroom-spanningskarakteristiek (IV) bij voldoend hoge ontladingsspanning. Ondanks pogingen om deze karakteristiek te verklaren zijn enkel fenomenologische modellen voorhanden.

- In een MO is er naast de ontladingsstroom ook een Hall stroom omdat de elektronen een E×B drift ondergaan. Experimentele metingen van de verhouding van de Hall stroom en de ontladingsstroom geven waarden die veel lager zijn dan theoretisch voorspeld. Dit betekent dat er in de richting loodrecht op de magnetische veldlijnen een anomaal sterke elektronendrift is. Deze anomale elektronendiffusie is vooral van belang bij lage gasdruk en/of sterke magneetvelden en wordt toegeschreven aan oscillaties van het elektrische veld. Helaas ontbreekt een kwantitatieve beschrijving.

Modeleren van de magnetronontlading

De verschillende technieken en modellen voor het beschrijven van de MO werden bestudeerd. Deze modellen variëren van zeer rudimentair tot uiterst gedetailleerd. De meest aangewende zelfconsistente modellen zijn het *P*article-*I*n-*C*ell *M*onte *C*arlo (PIC-MC) model en het hybride model. Dat laatste combineert de Monte Carlo techniek voor het beschrijven van de hoogenergetische elektronen met een continuüm model voor de ionen en de laagenergetische elektronen. Deze modellen laten toe de meeste eigenschappen van de MO te simuleren. Interessant is dat de resultaten van beide modellen aantonen dat de MO sterk afhangt van de SE opbrengst γ. Jammer genoeg zijn de experimentele waarden voor γ niet nauwkeurig gekend.

Het grootste nadeel van deze zelfconsistente modellen is de vereiste rekenkracht waardoor ze niet praktisch zijn om de afhankelijkheid van de MO na te gaan van één of meerdere parameters over een groot gebied. Bovendien is het twijfelachtig of ze de eigenschappen van de MO correct reproduceren in het geval dat het anomale elektronentransport een (grote) rol speelt. Voor het hybride model is dit te wijten aan het gebruik van diffusiecoëfficiënten die bepaald worden op basis van de klassieke theorie. De PIC-MC aanpak is in principe in staat om het anomale transport te reproduceren maar door de tijdschaal waarop het fenomeen zich afspeelt vereist het onredelijk lange rekentijden.

Het vereenvoudigde zelfconsistente model en de voornaamste resultaten

Op basis van de literatuurstudie werd vastgesteld dat een vereenvoudigd model noodzakelijk is om de afhankelijkheid van de MO na te gaan over een groot parameterbereik. Er werd dan ook een tweedimensionaal vereenvoudigd maar zelfconsistent *m*odel (ZCM) ontwikkeld voor de dc vlakke magnetronontlading. Vooraleer het volledige ZCM te bespreken, worden eerst twee deelaspecten nader toegelicht: het invangen van SE en de distributie van de ionen gegenereerd door een *h*oog*e*nergetisch *e*lektron (HEE).

Invangen van SE

Het invangen van de SE werd gekarakteriseerd door het invoeren van de *e*ffectieve *gas*interactie *p*robabiliteit (EGIP) *f*. Deze is gedefinieerd als:

$$f = 1 - e^{-\frac{s}{\lambda}}$$

met s de gemiddelde afstand afgelegd door een elektron vooraleer het ingevangen wordt en λ de gemiddelde vrije weglengte van het elektron. Dit toont dat met dalende druk (toenemende λ) de EGIP daalt en dat voornamelijk de SE geëmitteerd vanuit het midden van de *race-track* (kleine s) ingevangen worden. Omwille van dit laatste is het meer aangewezen om de gemiddelde EGIP $\langle f \rangle$ te gebruiken om het invangen van de SE bij een MO te karakteriseren. Voor een typische MO ($V_d = 300$ V, $B_{max} = 600$ G, $p = 0.5$ Pa) bedraagt de EGIP $\langle f \rangle$ ongeveer ⅓, wat betekent dat ongeveer ⅔ van de SE opnieuw ingevangen wordt.

Ionisatiemodel

De elektronen in een MO kunnen opgesplitst worden in HEE en laagenergetische of bulk elektronen. Deze laatste dragen wegens hun lage energie niet bij tot de ionisatie in de MO en werden bijgevolg niet opgenomen in het model. Om de ruimtelijke spreiding van de ionisatie afkomstig van een HEE te beschrijven werd het ontladingsgebied opgesplitst in boogvormige gebieden. De motivatie daartoe is dat de beweging van een elektron dat geen interactie met het sputtergas ondergaat beperkt is tot dergelijke gebieden. De interactie van

een elektron met het sputtergas werd gemodelleerd als een kans voor het elektron om naar een ander boogvormig gebied over te springen. Deze analytische beschrijving resulteerde in een *i*onisatie*m*odel (IM) dat toelaat om heel snel de distributie van de ionen gegenereerd door een HEE te bepalen.

De resultaten behaald met het IM toonden dat de distributie van de gegenereerde ionen niet rechtstreeks afhangt van de gasdruk. Deze eigenschap kan mogelijks door toekomstige modellen voor de MO gebruikt worden om de vereiste rekenkracht te reduceren. Het bleek ook dat de ionendistributie praktisch onafhankelijk is van de exacte startpositie voor SE geëmitteerd nabij het midden van de *race-track*. Bovendien werd ook aangetoond dat een belangrijk deel van de ionisatie plaatsgrijpt in de kathode *sheath*. Deze *sheath* ionisatie wordt gekarakteriseerd door de multiplicatiefactor m. Deze geeft de verhouding van het totale aantal ionen $n_{ion,tot}$ gegenereerd door de emissie van één SE en het theoretische aantal ionen n_{ion} dat datzelfde SE zou genereren in de veronderstelling dat er geen *sheath* ionisatie is:

$$m = \frac{n_{ion,tot}}{n_{ion}}$$

Voor SE die aan de rand van de *race-track* vertrekken is m niet veel groter dan één maar naar het midden van de *race-track* toe loopt m typisch op tot een waarde van vier à vijf. Om het effect van *sheath* ionisatie te karakteriseren is de gemiddelde multiplicatiefactor $<m>$ dan ook meer aangewezen.

Zelfconsistentie

Het hierboven beschreven IM houdt geen rekening met elektron-elektron interacties. Bijgevolg kan het niet alleen gebruikt worden om de ionisatieverdeling te bepalen van één SE maar ook van een aantal SE die tegelijkertijd van op de *target* geëmitteerd worden. Dit betekent dat het IM toelaat om voor een gegeven emissieprofiel van SE de resulterende ionisatiedistributie te bepalen. Dit vormt de basis voor het afleiden van het ZCM zoals nu wordt uitgelegd.

Om de gedachten te vestigen beschouwen we een SE emissieprofiel. Dit beschrijft het (relatief) aantal en de positie van de SE die vertrekken van op de *target*. Eerst wordt in rekening gebracht dat slechts een fractie f van deze elektronen effectief bijdraagt tot de ionisatie omwille van het invangen van SE. Dan wordt m.b.v. het IM de ionisatiedistributie berekend, daarbij rekening houdend met de multiplicatiefactor m. Van de ionisatiedistributie kan het ionenbombardement $\mathcal{B}$ op de *target* afgeleid worden. Als een ion op de *target* inslaat kan een elektron worden geëmitteerd. Het gemiddelde aantal elektronen per inkomend ion wordt gegeven door de SE opbrengst γ (typisch 0.1 voor metalen). Dit betekent dat het ionenbombardement aanleiding geeft tot een nieuw SE emissieprofiel. De procedure om van een gegeven een nieuw SE emissieprofiel af te leiden kan omgezet worden tot een iteratielus, wat resulteert in het zelfconsistente model. Daarmee kan voor een gegeven invoer (het magneetveld, de gasdruk en de ontladingsspanning) de eigenschappen van de MO (bijvoorbeeld de erosieprofiel of de kathode *sheath* dikte) bepaald worden.

Het ZCM laat toe de uitdrukking van Thornton voor het bepalen van de minimum ontladingsspanning voor de MO uit te breiden tot een betrekking voor de ontladingsspanning in het algemeen:

$$V_d = \frac{W}{\gamma < fm > \varepsilon_e \varepsilon_i}$$

met W de effectieve ionisatie-energie (≈30 eV voor argon), ε_i de ion collectie efficiëntie en ε_e de fractie van het theoretische aantal ionen dat het elektron effectief genereert vooraleer het de ontlading verlaat. De parameters ε_i en ε_e kunnen beide gelijk aan één verondersteld worden voor een typische MO. In de oorspronkelijke Thornton relatie is *sheath* ionisatie verwaarloosd ($m = 1$) en de EGIP f is een geschatte constante waarde ($f = 0.5$). Het ZCM laat toe f en m accuraat te berekenen omdat het rekening houdt met de specifieke magnetronconfiguratie (geometrie en magneetveld).

De uitgebreide Thornton relatie toont dat de invloed van het magneetveld en van de gasdruk op de MO te wijten is aan hun invloed op f en m aangezien de andere grootheden in de rechterzijde van de uitdrukking constant zijn bij een typische MO.

Ontladingsstroom

De volgende uitdaging was het afleiden van de ontladingsstroom I_d uit de berekende karakteristieken van de MO. Daarvoor werd de lijnstroomdichtheid j_m ingevoerd. Deze lijnstroomdichtheid geeft het verband tussen de ontladingsstroom I_d en de lengte L_{rt} van de *race-track*:

$$I_d = j_m L_{rt}$$

Om j_m te bepalen was het noodzakelijk de Child-Langmuir wet (CL wet) uit te breiden. Inderdaad, deze is enkel geldig wanneer er voldoende ladingsdragers ter beschikking zijn. Daar de MO voor deze ladingsdragers moet instaan, is de vervulling van deze voorwaarde helemaal niet vanzelfsprekend. Er werd onderscheid gemaakt tussen de beschikbaarheid van de ladingsdragers "in de tijd" en "in de ruimte".

Voor de vervulling van de voorwaarde "in de tijd" zijn twee tijden cruciaal: de tijd die de ionen nodig hebben om de kathode te bereiken en de tijd die de elektronen nodig hebben om de ionen te genereren. De voorwaarde in de tijd is enkel vervuld als deze laatste tijd korter is dan de eerste. Deze voorwaarde is voldaan in een diode ontlading maar niet in de MO omdat door de veel lagere gasdruk de generatie van de ionen een veel langere tijd in beslag neemt. Om de CL wet toch te kunnen toepassen werd de factor $A_{//,t}$ ingevoerd. Deze factor laat toe in rekening te brengen dat een aanzienlijk deel van de ionisatie (typisch een ¼ tot ½) in de kathode *sheath* plaats heeft.

De voorwaarde voor de beschikbaarheid van de ladingsdragers "in de ruimte" houdt in dat de elektronen de ionen moeten genereren in een gebied zodat, gemiddeld gezien, de ionen de kathode bombarderen op dezelfde plek als vanwaar de elektronen waren geëmitteerd. Deze voorwaarde is vervuld in de diode ontlading maar niet in de MO omdat de ionen gegenereerd worden verspreid langsheen de *race-track* omwille van de ExB drift van de elektronen. Om hiermee rekening te houden werd de factor $A_{//,s}$ ingevoerd.

Rekening houdend met bovenstaande voorwaarden, werd de volgende relatie bekomen voor j_m:

$$j_m = j_d A_{//,t} A_{//,s} \int \mathcal{B}(x)dx$$

met x de plaatscoördinaat langsheen de breedte van de *race-track*. De integratie is noodzakelijk om de oppervlaktestroomdichtheid j_d om te zetten in de lijnstroomdichtheid j_m en laat bovendien toe om de niet-uniformiteit van de *race-track* in rekening te brengen.

Met behulp van deze uitdrukking voor j_m, werd de ontladingsstroom I_d van de MO berekend. Het model reproduceerde bijvoorbeeld de drukafhankelijkheid van de MO bij constante stroom. Ook de stroom-spanningskarakteristiek (IV) werd gesimuleerd. Het bleek dat de extreme steilheid van deze karakteristieken niet werd gereproduceerd. Bovendien werd de invloed van het magneetveld op de drukafhankelijkheid van de IVs niet teruggevonden in de simulatieresultaten.

Invloed van de anomale elektronendiffusie

Om de discrepantie tussen de simulatie en experimentele resultaten te verklaren werden twee processen die (nog) niet in het model waren opgenomen onderzocht: de Coulomb interactie tussen de elektronen onderling en de Bohm of anomale diffusie. Coulomb interacties lieten toe om de experimentele waarnemingen bij cilindrische magnetrons te verklaren maar bij de vlakke magnetron spelen ze geen rol omdat de elektronen hier zelfs bij heel sterke magneetvelden voldoende energetisch zijn. Bohm diffusie werd op een fenomenologische manier aan het ZCM toegevoegd via het invoeren van een artificiële soort interacties, de Bohm diffusie interacties. Deze stellen de interactie voor van de elektronen met elektrische veld oscillaties. De "hoeveelheid" Bohm diffusie werd gedefinieerd via F_B, de relatieve frequentie van Bohm interacties t.o.v. standaard interacties (ionisaties, excitaties en elastische botsingen). F_B is recht evenredig met de magneetveldsterkte en omgekeerd evenredig met de gasdruk, wat aanduidt dat de anomale elektronendrift vooral van belang is bij sterke magneetvelden en/of lage gasdrukken.

De invloed van een toenemend aandeel van Bohm diffusie op de eigenschappen van de MO werd gesimuleerd. De verschillende invloeden konden verklaard worden aan de hand van de toegenomen elektronenmobiliteit in de richting loodrecht op de magnetische veldlijnen. Het in rekening brengen van Bohm diffusie maakt het mogelijk om IVs te simuleren met een steilheid zoals experimenteel geobserveerd.

De simulatieresultaten behaald met het ZCM werden vergeleken met experimentele resultaten. Twee invoerparameters van het ZCM, de elektronreflectiecoëfficiënt R en de relatieve frequentie van de Bohm interacties F_B, werden gebruikt als *tuning* parameters. Aangezien het ZCM bepaalde aspecten van de MO slechts heel rudimentair en andere in het geheel niet in rekening brengt, wordt de overeenkomst tussen de simulatie en experimentele resultaten zeer goed genoemd.

Het ZCM is, voor zover ons gekend, uniek omdat het toelaat om op een zelfconsistente wijze de invloed van de belangrijkste parameters (het magneetveld, de gasdruk en het aangelegde elektrische vermogen) op de MO over een groot parameterbereik te reproduceren. Ook de afhankelijkheid van de SE opbrengst γ werd met goed gevolg gereproduceerd. Dit duidt aan dat de voornaamste processen die van belang zijn voor de MO met voldoende nauwkeurigheid gemodelleerd zijn in het ZCM. Als dusdanig is het ZCM een waardevol "virtueel" instrument om inzicht te verkrijgen in het generieke gedrag van de MO.

Suggesties voor verder onderzoek

Voor het vereenvoudigde zelfconsistente model

Zoals vermeld neemt het ZCM een aantal aspecten van de MO heel sterk vereenvoudigd of zelfs helemaal niet in rekening. De nauwkeurigheid en de toepasbaarheid van het ZCM kunnen verbeterd worden door deze aspecten (preciezer) in het model op te nemen. De voornaamste aspecten zijn de zelfconsistente berekening van zowel de elektronentemperatuur als het potentiaalverval over de *pre-sheath*, de elektronbijdrage in de ontladingsstroom en de verdunning van het sputtergas (*gas density reduction*).

Bovendien kunnen een aantal ruwe benaderingen gemaakt in het ZCM verfijnd worden. Dit principe werd reeds toegepast in dit werk bij de berekening van de EGIP. In het algemeen werd voor deze berekening een tweedimensionale benadering van de cosinusdistributie van de initiële snelheidsvectoren van de elektronen genomen maar bij de vergelijking van de simulatie en experimentele resultaten werd een nauwkeurigere driedimensionale benadering verkozen. Uiteraard vereist deze verhoogde nauwkeurigheid een langere rekentijd.

Door kleine, niet-fundamentele aanpassingen aan het ZCM uit te voeren, moet het mogelijk zijn de invloed na te gaan van bijvoorbeeld de erosievorming op de *target* of het gebruik van een ander sputtergas.

Voor de algemene modellering van de MO

Uit de simulatieresultaten behaald met het ZCM, maar ook met andere modellen, blijkt dat de effectieve SE opbrengst cruciaal is voor een betrouwbaar resultaat. Bijgevolg zouden reeds bestaande modellen voor de MO, voor zover dit nog niet het geval is, het invangen van SE in rekening moeten brengen. De gevoeligheid voor de effectieve SE opbrengst betekent ook dat verder experimenteel onderzoek nodig is om zowel de SE opbrengst γ als de reflectiecoëfficiënt R (die de elektron-*target* interactie beschrijft) nauwkeurig(er) te bepalen.

Alle modellen zijn ook gebaat bij een beter begrip van de anomale elektronendiffusie. Voor het PIC-MC model is deze kennis, in principe, enkel nodig om de simulatieresultaten te bevestigen. Voor andere modellen is deze kennis noodzakelijk voor een accurate beschrijving van de elektronenbeweging. Het zou zeer interessant zijn om te zien hoe het fenomenologisch inbouwen van de anomale elektronendrift via het *tunen* van de diffusiecoëfficiënten de simulatieresultaten beïnvloedt.

In het algemeen is voor het testen van de verschillende modellen een directe confrontatie tussen simulatie en experimentele resultaten noodzakelijk, iets wat maar heel zelden voorkomt in de literatuur. Bovendien moeten afhankelijkheden gesimuleerd worden daar deze, veel meer dan de simulatie van een paar geïsoleerde gevallen, toelaten de betrouwbaarheid van het model in te schatten.

Voor het ontwikkelen van een virtuele sputtermagnetron

Verschillende stappen zijn noodzakelijk om een virtueel sputtermagnetron te implementeren. Het blijkt dat vooral het modelleren van de magnetronontlading en van de filmgroei nog moeilijke stappen zijn. Omwille van de vereiste rekentijd is het duidelijk dat in de nabije toekomst, ondanks de toenemende rekencapaciteit, een werkbaar virtueel sputtermagnetron slechts mogelijk zal zijn op basis van vereenvoudigde modellen. Het eigenlijke combineren van bestaande vereenvoudigde modellen met als doel het magnetron sputterdepositie proces volledig te virtualiseren lijkt meer een technologische dan een wetenschappelijke uitdaging.

Appendix: Magnetic Field Calculation

A.1 Introduction

One of the main parameters of a sputter magnetron is its *magnetic field B*, expressed in Tesla or Gauss. Strictly seen this terminology is not correct as the units Tesla and Gauss refer to the magnetic flux density (Wb/m^2). Hence, the symbol B represents strictly seen a magnetic flux density and is a vector. The magnetic field (intensity) on the other hand is represented by $\bar{H}$ with unit A/m. In a medium with magnetisation $\bar{M}$ these quantities are connected through the relation (see e.g. [Farschtschi98]):

$$\bar{H} = \frac{\bar{B}}{\mu_0} - \bar{M} \qquad \text{(A.1)}$$

with μ_0 the magnetic induction, although other conventions are possible (see e.g. [Feynman64]). In vacuum, the relation:

$$\bar{H} = \frac{\bar{B}}{\mu_0} \qquad \text{(A.2)}$$

holds as there is no magnetisation. Hence, in vacuum, both $\bar{B}$ and $\bar{H}$ have the same physical meaning, which explains the term "*the magnetic field B*". In this appendix we explicitly differentiate between *the magnetic field* $\bar{H}$ and *the magnetic flux density* $\bar{B}$ and the vector notation is used when appropriate. However, in the other parts of this text, the sputter magnetron nomenclature is followed in that the term "*the magnetic field B*" is used.

A.2 Magnetic field calculation of a permanent magnet

To calculate the magnetic flux density $\bar{B}$ in a point outside a permanent magnet with magnetisation $\bar{M}_r$, the magnetic surface charge σ is introduced [Schabes87]. Introducing σ has no physical meaning as up to now no magnetic monopoles have been experimentally observed, in spite of their predicted existence [Giacomelli03]. The reason for introducing σ is that it allows treating magnetostatic problems like electrostatic ones.

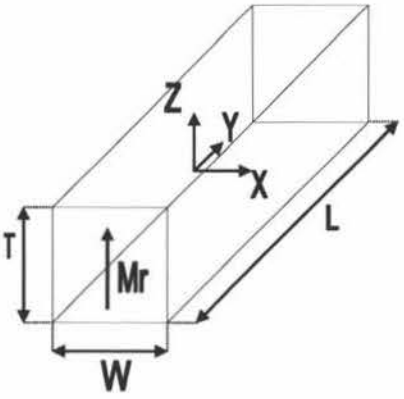

Fig. A.1. Sketch of a permanent magnet with its dimensions *W*, *L* and *T* along the *x*-, *y*- and *z*-axis, respectively. Also the magnetisation $\bar{M}_r$ is indicated.

The magnetic surface charge σ is defined as:

$$\sigma = \bar{M}_r \cdot \bar{n} \tag{A.3}$$

with $\bar{n}$ the outward oriented unit vector perpendicular to the surface of the permanent magnet. For simplicity we will limit the geometry of the permanent magnets to rectangular bars and assume a homogenous magnetisation $\bar{M}_r$ along the z-axis of the magnet with dimensions W, L and T as shown in Fig. A.1. In this case, eq. (A.3) reduces to:

$$\sigma = \pm\left|\bar{M}_r\right| \tag{A.4}$$

This means that there are only magnetic charges on the top $(+\left|\bar{M}_r\right|)$ and bottom $(-\left|\bar{M}_r\right|)$ plane.

Analogue to the electric potential, the magnetic potential V_m can be defined:

$$\bar{B} = -\nabla V_m(\bar{r}) \tag{A.5}$$

This implies that the expression for the electric field $\bar{E}$ caused by an electric surface charge σ' (the prime is used to differentiate the electric surface charge from the magnetic one) on surface S:

$$\bar{E}(\bar{r}) = \frac{1}{4\pi\varepsilon_0}\int_S \frac{\sigma'(\bar{r}')(\bar{r}-\bar{r}')}{\left|\bar{r}-\bar{r}'\right|^3} d\bar{r}' \tag{A.6}$$

can be used to determine the magnetic field $\bar{H}$. This requires replacing ε_0, the dielectric constant, by μ_0 and σ' by σ :

$$\bar{H}(\bar{r}) = \frac{1}{4\pi\mu_0}\int_S \frac{\sigma(\bar{r}')(\bar{r}-\bar{r}')}{\left|\bar{r}-\bar{r}'\right|^3} d\bar{r}' \tag{A.7}$$

Given eq. (A.2) we obtain for the x-component of the magnetic flux density :

$$B_x(x,y,z) = \frac{1}{4\pi}\int_S \frac{\sigma'(x',y',z')(x-x')}{\left[(x-x')^2+(y-y')^2+(z-z')^2\right]^{3/2}} dx'dy'dz' \tag{A.8}$$

For the y- and z-components a similar expression can be obtained. Given the mentioned assumptions for the magnetisation and shape of the magnets, the surface integral is reduced to an integration over the top plane defined by $z = T/2$ and the bottom plane defined by $z = -T/2$ (Fig. A.1). The magnetic surface charge on the top and bottom plane is $+\left|\bar{M}_r\right|$ and $-\left|\bar{M}_r\right|$, respectively, which leads to :

$$B_x = \frac{\sigma}{4\pi}\int_{-W/2}^{W/2}\int_{-L/2}^{L/2} \left[\frac{x-x'}{\left[(x-x')^2+(y-y')^2+\left(z-\frac{T}{2}\right)^2\right]^{3/2}} - \frac{x-x'}{\left[(x-x')^2+(y-y')^2+\left(z+\frac{T}{2}\right)^2\right]^{3/2}}\right] dx'dy' \tag{A.9}$$

as the top and bottom plane are limited to [-W/2, W/2] along the x-axis and [-L/2, L/2] along the y-axis. Use of the integral equations :

$$\int_d^u \frac{t}{\left(t^2+K\right)^{3/2}}dt = -\frac{1}{\sqrt{u^2+K}} + \frac{1}{\sqrt{d^2+K}} \tag{A.10}$$

and

$$\int_d^u \frac{1}{\left(t^2+K\right)^{1/2}}dt = \ln\left(u+\sqrt{u^2+K}\right) - \ln\left(d+\sqrt{d^2+K}\right) \tag{A.11}$$

allows to integrate over x' and y', respectively. Furthermore we introduce X, Y and Z, defined as :

$$X = x + \frac{iW}{2} \quad Y = y + \frac{jL}{2} \quad Z = z + \frac{kT}{2} \tag{A.12}$$

as this allows to write the solution for B_x in a compact form :

$$B_x = \frac{\left|\bar{M}_r\right|}{4\pi} \sum_{i,j,k=\pm 1} ijk \ln\left(Y + \sqrt{X^2+Y^2+Z^2}\right) \tag{A.13}$$

Note that the integration includes eight terms. Similarly, the component B_y is found as x and y can be exchanged :

$$B_y = \frac{\left|\bar{M}_r\right|}{4\pi} \sum_{i,j,k=\pm 1} ijk \ln\left(X + \sqrt{X^2+Y^2+Z^2}\right) \tag{A.14}$$

The calculation of the z-component is different. We find:

$$B_z = \frac{\sigma}{4\pi} \int_{-W/2}^{W/2} \int_{-L/2}^{L/2} \frac{z-z'}{\left[(x-x')^2+(y-y')^2+\left(z-\frac{T}{2}\right)^2\right]^{3/2}} - \frac{z-z'}{\left[(x-x')^2+(y-y')^2+\left(z+\frac{T}{2}\right)^2\right]^{3/2}} dx'dy' \tag{A.15}$$

Regardless whether the integration is started over x' or y', the integral can be solved using the expression:

$$\int_d^u \frac{1}{\left(t^2+K\right)^{3/2}}dt = \frac{u}{K\sqrt{u^2+K}} - \frac{d}{K\sqrt{d^2+K}} \tag{A.16}$$

For the second integration, the expression :

$$\int_d^u \frac{1}{\left(t^2+L+M\right)^{1/2}\left(L+t^2\right)}dt = \frac{1}{\sqrt{LM}} \arctan\left[\frac{u\sqrt{M}}{\sqrt{L(u^2+L+M)}}\right] - \frac{1}{\sqrt{LM}} \arctan\left[\frac{d\sqrt{M}}{\sqrt{L(d^2+L+M)}}\right] \tag{A.17}$$

can be used. The final result for B_z is given by:

$$B_z = -\frac{\left|\bar{M}_r\right|}{4\pi} \sum_{i,j,k=\pm 1} ijk \arctan\left(\frac{XY}{Z\sqrt{X^2+Y^2+Z^2}}\right) \tag{A.18}$$

In conclusion, for a rectangular magnet with a homogenous magnetisation in the z-direction, the components of the magnetic flux density $\bar{B}$ can be calculated using eqs. (A.13), (A.14) and (A.18). Note that if several magnets are placed in the vicinity of each other, this method still can be applied using the principle of superposition. The only limitation is that there should not be any mutual influence on the magnetisation, i.e. the magnets should be spaced far enough from each other such that the magnetisation $\bar{M}_r$ of the magnet is not influenced by the magnetic field created by the other magnets.

A.3 Magnetic field calculation of a permanent magnet on a flux iron

In a magnetron, the permanent magnets are placed on a flux iron. The dimensions of the flux iron are chosen so that it is not in saturation. The magnetic fields lines are perpendicular to the flux iron. This property allows again calculating the magnetic field caused in analogy with calculating the electric field in the vicinity of conductors. In the electrostatic case, this can be done by introducing a so-called image charge. Similarly, to calculate the magnetic field caused by a permanent magnet above a magnetic material (in our case the flux iron), the image of the magnet needs to be introduced as shown in Fig. A.2. If the magnet is placed on the flux iron, the bottom plane of the real magnet and the top plane of the image magnet are at the same position and cancel each other. What remains are two planes at a distance which is twice the thickness of the magnet (see Fig. A.2). Hence, placing a magnet on a flux iron is similar as using a magnet which is twice as thick. This way the problem is reduced to calculating the magnetic field of a single magnet, which was described in the previous section. Note that this method requires that the flux iron is not saturated.

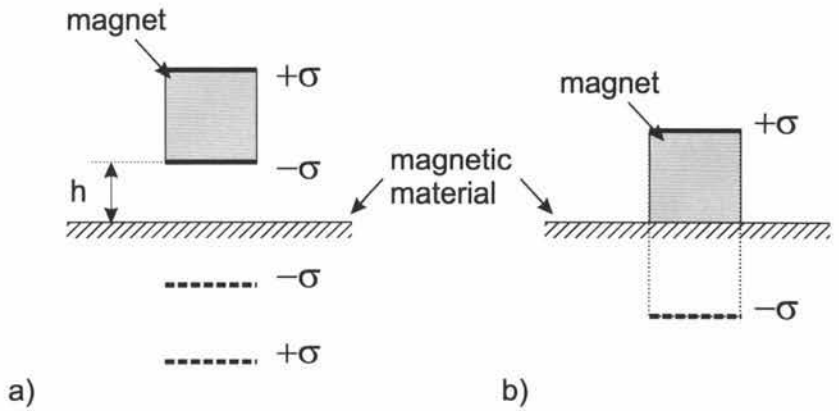

Fig. A.2. The magnetic surface charges σ needed to calculate the magnetic field for a magnet at height h above a magnetic material (*a*) and for a magnet placed on top of the magnetic material (*b*). In both cases, images charges need to be introduced (thick dashed lines). When the magnet is placed on top of the magnetic material, it acts as a magnet with twice its physical length.

Publications and Conference Contributions

List of publications

Journal articles with refereeing (A1-publications):

- "Importance of recapture of secondary electrons in cylindrical and planar magnetron discharges"
  G. Buyle, D. Depla, K. Eufinger, J. Haemers, R. De Gryse, W. De Bosscher
  Czechoslovak Journal of Physics, Vol. 52, Suppl. D, 615-623 (2002).
- "Recapture of secondary electrons by the target in a DC planar magnetron discharge"
  G. Buyle, W. De Bosscher, D. Depla, K. Eufinger, J. Haemers, R. De Gryse
  Vacuum 70 (1), 29-35 (2003).
- "Simplified model for calculating the pressure dependence of a direct current planar magnetron discharge"
  G. Buyle, D. Depla, K. Eufinger, J. Haemers, R. De Gryse, W. De Bosscher
  J. Vac. Sci. Technol. A 21 (4), 1218-1224 (2003).
- "Simplified model for the DC planar magnetron discharge"
  G. Buyle, D. Depla, K. Eufinger, J. Haemers, W. De Bosscher, R. De Gryse
  Vacuum 74 (3-4), 353-358 (2004).
- "Calculation of the effective gas interaction probabilities of secondary electrons in a dc magnetron discharge"
  G. Buyle, D. Depla, K. Eufinger, R. De Gryse
  J. Phys. D: Appl. Phys. 37 (12), 1639-1647 (2004).
- "Discharge voltage measurements during magnetron sputtering"
  D. Depla, G. Buyle, J. Haemers, R. De Gryse
  Surf. Coat. Technol., accepted for publication (2005).
- "Monte Carlo simulation of the transport of atoms in DC magnetron sputtering"
  S. Mahieu, G. Buyle, D. Depla, S. Heirwegh, P. Ghekiere, R. De Gryse
  Nucl. Inst. Meth. Phys. Res. B, accepted for publication (2005).
- "An in-situ reduction/oxidation XAS study on the EL10V8 VO_x/TiO_2(anatase) powder catalyst"
  G. Silversmit, H. Poelman, I. Sack, G. Buyle, G.B. Marin, R. De Gryse
  Catalysis Letters, accepted for publication (2005).
- "Hysteresis behaviour during reactive magnetron sputtering of Al_2O_3 using a rotating cylindrical magnetron"
  D. Depla, J. Haemers, G. Buyle, R. De Gryse
  J. Vac. Sci. Technol A, submitted.
- "Influence of the target composition on the discharge voltage during magnetron sputtering"
  D. Depla, H. Tomaszewski, G. Buyle, R. De Gryse
  Surf. Coat. Technol., submitted.
- "Simplified model for the line current density of a DC planar magnetron discharge"
  G. Buyle, D. Depla, R. De Gryse
  J. Vac. Sci. Technol A, submitted.

Journal articles without refereeing:

- "Simplified model for the DC planar magnetron discharge"
  G. Buyle, D. Depla, K. Eufinger, J. Haemers, R. De Gryse, W. De Bosscher
  Belvac News 19 (2), 8-16 (2003).
- "Uniformity Control in Sputter Deposition Processes"
  W. De Bosscher, A. Blondeel, G. Buyle
  Vacuum & Coating Technology, February issue, 38-44 (2003).
- "Discharge voltage behaviour in poisoned sputtering"
  R. De Gryse, D. Depla, G. Buyle, J. Haemers
  Belvac News 21 (3), 3-12 (2005).

Conference Contributions

- "Uniformity Control in Sputter Deposition Process"
  W. De Bosscher, A. Blondeel, G. Buyle
  45th SVC Annual Techn. Conf. Proc., 135-141 (2002).
  Oral presentation.
- "Influence of Recapture of Secondary Electrons on the Magnetron Sputter Deposition Process"
  G. Buyle, D. Depla, K. Eufinger, W. De Bosscher, J. Haemers, R. De Gryse
  45th SVC Annual Techn. Conf. Proc., 346-353 (2002).
  Oral presentation.
- "Low pressure behavior of the sputter magnetron discharge"
  G. Buyle, D. Depla, W. De Bosscher, K. Eufinger, J. Haemers, R. De Gryse
  29th IEEE Intern. Conf. on Plasma Science Proc., 218 (2002).
  Oral presentation.
- "Importance of Recapture of Secondary Electrons in Planar and Cylindrical Magnetron Discharges"
  G. Buyle, D. Depla, W. De Bosscher, K. Eufinger, J. Haemers, R. De Gryse
  20th Symposium on Plasma Physics and Technology, Prague (2002).
  Poster presentation.
- "Simplified Model for Calculating the Pressure Dependence of a DC Planar Magnetron Discharge"
  G. Buyle, D. Depla, W. De Bosscher, K. Eufinger, J. Haemers, R. De Gryse
  49th AVS International Symposium & Exhibition (2002).
  Oral presentation.
- "Dissection of the Planar Magnetron Discharge"
  G. Buyle, D. Depla, W. De Bosscher, K. Eufinger, J. Haemers, R. De Gryse
  46th SVC Annual Techn. Conf. Proc., 71-77 (2003).
  Oral presentation.
- "Simplified Model for the DC Planar Magnetron Discharge"
  G. Buyle, D. Depla, K. Eufinger, J. Haemers, W. De Bosscher, R. De Gryse
  7th Intern. Symp. on Sputtering & Plasma Processes Proc., 67-70 (2003).
  Oral presentation.

- "Shallow Implantation as a Mechanism for Target Poisoning in Reactive Sputtering"
  R. De Gryse, D. Depla, J. Haemers, G. Buyle
  50th AVS International Symposium & Exhibition (2003).
  Oral presentation.
- "Characterization of the Electron Movement in Varying Magnetic Fields and the Resulting Anomalous Erosion"
  G. Buyle, D. Depla, K. Eufinger, J. Haemers, R. De Gryse, W. De Bosscher
  47th SVC Annual Technical Conf. Proc., 265-270 (2004).
  Oral presentation.
- "Simplified model for the DC Planar Magnetron Discharge"
  G. Buyle, D. Depla, R. De Gryse
  Reactive Sputter Processes and Related Phenomena III, Ghent (2004).
  Oral presentation.
- "Monte Carlo Simulation of Anomalous Erosion in Large Area Sputter Magnetrons"
  G. Buyle, D. Depla, K. Eufinger, R. De Gryse, W. De Bosscher
  48th SVC Annual Technical Conf. Proc., accepted for publication (2005).
  Oral presentation.
- "Simplified Model for the DC Planar Magnetron Discharge"
  G. Buyle, D. Depla, R. De Gryse
  15th Intern. Colloquium on Plasma Processes (CIP), 41 (2005).
  Oral presentation.
- "Simplified Model for the DC Planar Magnetron Discharge"
  G. Buyle, D. Depla, R. De Gryse
  52nd AVS International Symposium & Exhibition (2005).
  Oral presentation.
- "Hysteresis Behavior During Reactive Sputtering Using a Rotatable Magnetron"
  D. Depla, G. Buyle, J. Haemers, R. De Gryse
  52nd AVS International Symposium & Exhibition (2005).
  Oral presentation.

References

[**Ahedo03**] E. AHEDO et al., "Effects of the radial plasma-wall interaction on the Hall thrusters discharge", Phys. Plasmas, 10 (8), 3397 (2003).

[**Anderson78**] P. ANDERSON, Nobel lecture (1978).

[**Andersson69**] S. ANDERSSON, "Low-energy electron diffraction intensities from the clean copper (001) surface", Surf. Sci. 18, 325 (1969).

[**Andersson70**] S. ANDERSSON and B. KASEMO, "Determination of energy gap edges in copper and nickel from specular electron reflectivities", Solid State Commun. 8, 961 (1970).

[**Babout77**] M. BABOUT et al., "Mirror electron microscopy applied to the determination of the total electron reflection coefficient at a metallic surface", J. Phys. D: Appl. Phys. 10, 2331 (1977).

[**Baragiola79**] A. BARAGIOLA et al., "Ion-induced electron emission from clean metals", Surf. Sci. 90, 240 (1979).

[**Baragiola81**] R.A. BARAGIOLA in "Inelastic Particle-Surface Collisions", Springer, Berlin (1981).

[**Baragiola94**] R.A. BARAGIOLA, "Low energy ion-surface interactions" in "Electron emission from ion-solid interactions" (ed. J.W. Rabelais), Chichester: John Wiley & Sons, ISBN 047193891 (1994).

[**Bareilles04**] J. BAREILLES et al., "Critical assessment of a two-dimensional hybrid Hall thruster model: comparisons with experiments", Phys. Plasmas 11 (6), 3035 (2004).

[**Behnke00**] J.F. BEHNKE et al., "A novel system for studies of dc discharge in cylindrical magnetron", Czech. J. Phys., 50/S3, 419 (2000).

[**Berg87**] S. BERG et al., "Modeling of reactive sputtering of compound materials", J. Vac. Sci. Technol. A 5 (2), 202 (1987).

[**Berg05**] S. BERG and T. NYBERG, "Fundamental understanding and modeling of reactive sputtering processes", Thin Solid Films 476, 215 (2005).

[**Bertacco99**] R. BERTACCO and F. CICCACCI, "Large spin asymmetry in electron absorption and reflection from oxidized single crystal Fe/MgO(001) films", Surf. Sci. 419, 265 (1999).

[**Biersack80**] J.P. BIERSACK and L.G. HAGGMARK, "A Monte Carlo computer program for the transport of energetic ions in amorphous targets", Nucl. Instr. Meth. 174, 257 (1980).

[**Bilek02**] M.M.M. BILEK and D.R. MCKENZIE, "Predicting the structure of plasma deposited materials", Czech. J. Phys. 52 Suppl. D, 905 (2002).

[**Bilyk04**] O. BILYK et al., "Fluctuations of the magnetically-supported dc discharge in coaxial configuration", Vacuum 76, 437 (2004).

[**Bingsen92**] H. BINGSEN and C. ZHOU, "Plasma properties in a planar d.c. magnetron sputtering device", Surf. Coat. Technol. 50, 111 (1992).

[**Birdsall05**] C. BIRDSALL et al., homepage of *The Plasma Theory and Simulation Group*: http://ptsg.eecs.berkeley.edu/.

[**Bogaerts96**] A. BOGAERTS, "Mathematical modelling of a direct current glow discharge in argon", PhD-thesis Antwerp University (1996).

[**Bogaerts05**] A. BOGAERTS et al., homepage of the research group *Plasmant*: http://webhost.ua.ac.be/plasma/.

[**Bohlmark04**] J. BOHLMARK, "Measurement of the magnetic field change in a pulsed high current magnetron discharge", Plasma Sources Sci. Technol. 13, 654 (2004).

[**Bowden93**] M.D. BOWDEN et al., "Measurements of the cathode sheath in a magnetron sputtering discharge using laser induced fluorescence", J. Appl. Phys. 73 (8), 3664 (1993).

[**Bradley96**] J.W. BRADLEY, "The plasma properties adjacent to the target in a magnetron sputtering source", Plasma Sources Sci. Technol. 8, 622 (1996).

[**Bradley97**] J.W. BRADLEY et al., "Measurement and modelling of the bulk plasma in magnetron sputtering sources", Surf. Coat. Technol. 97, 538 (1997).

[**Bradley98a**] J.W. BRADLEY, "Study of the plasma pre-sheath in magnetron discharges dominated by Bohm diffusion of electrons", Plasma Sources Sci. Technol. 7, 572 (1998).

[**Bradley98b**] J.W. BRADLEY and M. CECCONELLO, "Modifying the electrical characteristics of magnetron sputtering sources using hollow cathode structured targets", Vacuum 49 (4), 315 (1998).

[**Bradley01**] J.W. BRADLEY et al., "Measurement of the plasma potential in a magnetron discharge and the prediction of the electron drift speeds", Plasma Sources Sci. Technol. 10, 490 (2001).

[**Braithwaite00**] N.St.J. BRAITHWAITE, "Introduction to gas discharges", Plasma Sources Sci. Technol. 9, 517 (2000).

[**Bretagne86a**] J. BRETAGNE, "Relativistic electron-beam-produced plasmas. I: Collision cross sections and loss function in argon", J. Phys. D: Appl. Phys., 19, 761 (1986).

[**Bretagne86b**] J. BRETAGNE, "Relativistic electron-beam-produced plasmas. II: Energy apportionment and plasma formation", J. Phys. D: Appl. Phys., 19, 779 (1986).

[**Bruno03**] D. BRUNO et al., "Particle kinetic modelling of rarefied gases and plasmas", Plasma Sources Sci. Technol. 12, S89 (2003).

[**Buyle05**] G. BUYLE et al., "Monte Carlo Simulation of Anomalous Erosion in Large Area Sputter Magnetrons", 48th SVC Annual Technical Conf. Proc., to be published (2005).

[**Cale00**] T.S. CALE et al., "Topography simulation for the virtual wafer fab", Thin Solid Films 365, 152 (2000).

[**Carman89**] R.J. CARMAN, "A simulation of electron motion in the cathode sheath region of a glow discharge in argon", J. Phys. D: Appl. Phys. 22, 55 (1989).

[**Chable05**] S. CHABLE and F. ROGIER, "Numerical investigation and modelling of stationary plasma thruster low frequency oscillations", Phys. Plasmas 12, 033504 (2005).

[**Chang86**] S.A. CHANG et al., "High rate sputtering deposition of nickel using dc magnetron mode", J. Vac. Sci. Technol. A 4 (3), 413 (1986).

[**Chapman80**] B. CHAPMAN, "Glow Discharge Processes", New York: John Wiley & Sons (1980).

[**Chen03**] F.F. CHEN and J.P. CHANG, "Lecture notes on principles of plasma processing", New York: Kluwer Academic/Plenum Publishers (2003).

[**Choi96**] Y.W. CHOI, "A study of sheath electric fields in planar magnetron discharges", Jpn. J. Appl. Phys. 35 Part 1, 5858 (1996).

[**Christie05**] D.J. CHRISTIE, "Target material pathways model for high power pulsed magnetron sputtering", J. Vac. Sci. Technol. A 23 (2), 330 (2005).

[**Christou00**] C. CHRISTOU and Z.H. BARBER, "Ionization of sputtered material in a planar magnetron discharge", J. Vac. Sci. Technol. A 18 (6), 2897 (2000).

[**Christou02**] C. CHRISTOU and Z.H. BARBER, "A spatially resolved spectroscopic study of ionization in the planar magnetron discharge", Plasma Sources Sci. Technol. 11, 37 (2002).

[**Costin05**] C. COSTIN et al., "Two-dimensional fluid approach to the dc magnetron discharge", Plasma Sources Sci. Technol. 14, 168 (2005).

[**Cramer97**] N.F. CRAMER, "Analysis of a one-dimensional, steady-state magnetron discharge", J. Phys. D: Appl. Phys. 30, 2573 (1997).

[**Cuomo86**] J.J. CUOMO and S.M. ROSSNAGEL, "Hollow-cathode-enhanced magnetron sputtering", J. Vac. Sci. Technol. A 4 (3), 393 (1986)

[**Debal98**] F. DEBAL et al., "Correlation between the cathode erosion, the optical emission and the magnetic field distribution in magnetron sputtering systems", J. Phys. D: Appl. Phys. 31, L31 (1998).

[**Debal00**] F. DEBAL et al., "Spatially-resolved spectroscopic optical emission of dc-magnetron sputtering discharges in argon-nitrogen gas mixtures", Plasma Sources Sci. Technol. 9, 152 (2000).

[**DeBosscher99**] W. DE BOSSCHER and H. LIEVENS, "Advances in magnetron sputter sources", Thin Solid Films 351, 15 (1999).

[**Depla02**] D. DEPLA and R. DE GRYSE, "Cross section for removing chemisorbed oxygen from an aluminium target by sputtering", J. Vac. Sci. Technol. A 20 (2), 521 (2002).

[**Depla04a**] D. DEPLA and R. DE GRYSE, "Target poisoning during reactive magnetron sputtering: Part I: the influence of ion implantation", Surf. Coat. Technol. 183, 184 (2004).

[**Depla04b**] D. DEPLA and R. DE GRYSE, "Target poisoning during reactive magnetron sputtering: Part II: the influence of chemisorption and gettering", Surf. Coat. Technol. 183, 190 (2004).

[**Depla04c**] D. DEPLA and R. DE GRYSE, "Target poisoning during reactive magnetron sputtering: Part III: the prediction of the critical reactive gas mole fraction", Surf. Coat. Technol. 183, 196 (2003).

[**Depla05a**] D. DEPLA et al., "Discharge voltage measurements during magnetron sputtering", Surf. Coat. Technol., accepted for publication (2005).

[**Depla05b**] D. DEPLA et al., "Discharge voltage behaviour during reactive sputtering of oxides", submitted for publication (2005).

[**Devine05**] M. DEVINE and C. LI, "Magnetic field structure during sputter deposition processes involving ferromagnetic target media", 48th SVC Annual Technical Conf. Proc., to be published (2005).

[**Dony95**] M.F. DONY et al., "Optical diagnostics of d.c. and r.f. argon magnetron discharges", Surf. Coat. Technol. 74-75, 479 (1995).

[**Dony97**] M.F. DONY et al., "Comparison of direct current and radio frequency argon magnetron discharges by optical emission and absorption spectroscopy", J. Vac. Sci. Technol. A 15 (4), 1890 (1997).

[**Eckstein91**] W. ECKSTEIN, "Computer Simulation of Ion-Solid Interactions", Heidelberg: Springer Verlag (1991).

[**Ehiasarion02**] A.P. EHIASARIAN et al., "Influence of high power densities on the composition of pulsed magnetron plasmas", Vacuum 65, 147 (2002).

[**Escrivão03**] M.L. ESCRIVÃO et al., "Current-pressure-voltage characteristics in a planar magnetron discharge", J. Vac. Sci. Technol. A 21 (2), 375 (2003).

[**Fan03**] Q.H. FAN et al., "A cross-corner effect in a rectangular sputtering magnetron", J. Phys. D: Appl. Phys. 36, 244 (2003).

[**Fan04**] Q.H. FAN et al., "Computer-aided simulation of a rotary sputtering magnetron", J. Appl. Phys. 95 (11), 6017 (2004).

[**Farschtschi98**] A. FARSCHTSCHI et al., "Berücksichtigung von ferromagnetischem Material in der FNM durch Einführung von Magnetisierungsstromdichten", Electrical Engineering 81, 65 (1998).

[**Fellenberg03**] R. FELLENBERG and G. BRÄUER, "Plasma Surface Technologies in Germany", 46th SVC Annual Techn. Conf. Proc., 462 (2003).

[**Feynman64**] R. FEYNMAN et al., "The Feynman Lectures on Physics", Chapter 36, part 2, Reading, Massachusetts: Addison-Wesley (1964).

[**Field02**] D.J. FIELD et al., "Spatial survey of a magnetron plasma sputtering system using a Langmuir probe", J. Vac. Sci. Technol. A 20 (6), 2032 (2002).

[**Fujita86**] H. FUJITA et al., "Plasma production with dc discharge planar magnetron device for thin film preparation", J. Phys. D: Appl. Phys. 19, 1699 (1986).

[**Fujiyama95**] H. FUJIYAMA and K. KUWAHARA, "Magnetron plasmas for large-area uniform sputtering", Surf. Coat. Technol. 74-75, 75 (1995).

[**Fukami82**] T. FUKAMI and T. SAKUMA, "Target erosion pattern in planar magnetron sputtering", Jpn. J. Appl. Phys. 21 Part 1, 1680 (1982).

[**Fukami87**] T. FUKAMI and F. SHINTANI, "Observations on the operation of a planar magnetron sputtering system by target erosion patterns", Thin Solid Films 151, 373 (1987).

[**Garcia03**] O.E. GARCIA, "Collective motions in non-uniformly magnetized plasmas", Eur. J. Phys. 24, 331 (2003).

[**Giacomelli03**] G. GIACOMELLI and L. PATRIZII, "Magnetic Monopole Searches", Lecture at the: Summer School on Astroparticle Physics and Cosmology, ICTP, Trieste, June-July 2002, hep-ex/0302011 v2 (2003).

[**Gilmer00**] G.H. GILMER et al., "Lattice Monte Carlo models of thin film deposition", Thin Solid Films 365, 189 (2000).

[**Godyak90**] V.A. GODYAK, "Measuring EEDF in gas discharge plasmas" in "Plasma-surface interactions and processing of materials" (eds. O. Auciello et al.), Kluwer Academic (1990).

[**Goeckner90**] M.J. GOECKNER et al., "Laser-induced fluorescence characterization of ions in a magnetron plasma", J. Vac. Sci. Technol. A 8 (6), 3920 (1990).

[**Goeckner91**] M.J. GOECKNER et al., "Monte Carlo simulation of ions in a magnetron plasma", IEEE Trans. Plasma Sci. 19 (2), 301 (1991).

[**Goeckner92**] M.J. GOECKNER et al., "Measurements of ion velocity and density in the plasma sheath", Phys. Fluids B 4 (6), 1663 (1992).

[**Goleman98**] D. GOLEMAN, "Working with emotional intelligence", New York, Bantam (1998).

[**Gopalraja00**] P. GOPALRAJA and J. FORSTER, "Nonlinear wave interaction in a magnetron plasma", Appl. Phys. Lett. 77 (22), 3526 (2000).

[**Goree91**] J. GOREE and T.E. SHERIDAN, "Magnetic field dependence of sputtering magnetron efficiency", Appl. Phys. Lett. 59 (9), 1052 (1991).

[**Graves03**] D.B. GRAVES and M.J. KUSHNER, "Influence of modeling and simulation on the maturation of plasma technology: Feature evolution and reactor design", J. Vac. Sci. Technol. A 21 (5), S152 (2003).

[**Guimarães91**] F. GUIMARÃES et al., "Modeling of the energy deposition mechanisms in an argon magnetron planar discharge", J. Vac. Sci. Technol. A 9, 133 (1991).

[**GüntherSchulze30**] A. GÜNTHERSCHULZE, Reference [67] in [Phelps99].

[**Gvozdev98**] V.V. GVOZDEV et al., "Ion Current through Cathode Dark Space in Magnetron Sputtering Systems", Plasma Physics Reports 25 (5), 443 (1998).

[**Hagelaar03**] G.J.M. HAGELAAR et al., "Role of anomalous electron transport in a stationary plasma thruster simulation", J. Appl. Phys. 93 (1), 67 (2003).

[**Hagstrum56**] H.D. HAGSTRUM, "Auger ejection of electrons from tungsten by noble gas ions", Phys. Rev. 104 (2), 317 (1956).

[**Hammerschmidt05**] T. HAMMERSCHMIDT et al., "Embedded atom simulations of titanium systems with grain boundaries", Phys. Rev. B 71, 205409 (2005).

[**Henrist02**] B. HENRIST et al., "Secondary electron emission data for the simulation of electron cloud", Proc. ECLOUD2002, CERN, Geneva, 15-18 April (2002).

[**Hershkowitz05**] N. HERSHKOWITZ, "Sheaths: more complicated than you think", Phys. Plasmas 12, 055502 (2005).

[**Hoffman85**] D.W. HOFFMAN, "A sputtering wind", J. Vac. Sci. Technol. A 3 (3), 561 (1985).

[**Hong96**] S. HONG et al., "A simulation model for thickness profile of the film deposited using planar circular type magnetron sputtering sources", J. Vac. Sci. Technol. A 14 (5), 2721 (1996).

[**Ido93a**] S. IDO et al., "Measurements of plasma controlled by compressed magnetic field magnetron sputtering technique", Jpn. J. Appl. Phys. 32 Part 1, 2112 (1993).

[**Ido93b**] S. IDO and K. NAKAMURA, "Computational studies on the shape and control of plasmas in magnetron sputtering systems", Jpn. J. Appl. Phys. 32 Part 1, 5698 (1993).

[**Ido96a**] S. IDO and K. NAKAMURA, "Computational studies on electron orbits in the magnetron sputtering plasmas", Vacuum 47 (6-8), 1035 (1996).

[**Ido96b**] S. IDO and K. NAKAMURA, "Computational studies on plasma generation and erosion in a rectangular magnetron sputtering system", Jpn. J. Appl. Phys. 35 Part 1, 2302 (1996).

[**Ido98**] S. IDO et al., "Computational studies on erosion process in a magnetron sputtering system with a ferromagnetic target", Jpn. J. Appl. Phys. 37 Part 1, 965 (1998).

[**Ido99**] S. IDO et al., "Computational studies of plasma generation and control in a magnetron sputtering system", Jpn. J. Appl. Phys. 38 Part 1, 4450 (1999).

[**Itoh96**] A. ITOH et al., "Tomographic imagings of a plasma structure and sputtered particle in a direct current magnetron discharge", IEEE Trans. Plasma Sci. 24 (1), 109 (1996).

[**Ivanov92**] I. IVANOV et al., "Electron energy distribution function in a dc magnetron sputtering discharge", Vacuum 43 (8), 837 (1992).

[**Ivanov94**] I. IVANOV et al., "Influence of an external axial magnetic field on the plasma characteristics and deposition conditions during direct current planar magnetron sputtering", J. Vac. Sci. Technol. A 12 (2), 314 (1994).

[**Jablonski04**] A. JABLONSKI et al., "Differential cross sections for elastic scattering of electrons by atoms and solids", J. Electron Spec. Relat. Phen. 137-140, 299 (2004).

[**Jacobs03**] W. JACOBS et al., "Determination of Ti^+-flux and Ar^+-flux of ionized physical vapour deposition of titanium from multiscale model calibration with test structures", J. Vac. Sci. Technol. A 21 (4), 922 (2003).

[**Janes66**] G.S. JANES and R.S. LOWDER, "Anomalous electron diffusion and ion acceleration in a low-density plasma", Phys. Fluids 9 (6), 1115 (1966).

[**Jepsen61**] R.L. JEPSEN, "Magnetically Confined Cold-Cathode Gas Discharges at Low Pressures", J. Appl. Phys. 32 (12), 2619 (1961).

[**Kadlec95**] S. KADLEC and J. MUSIL, "Optimized magnetic field shape for low pressure magnetron sputtering", J. Vac. Sci. Technol. A 13 (2), 389 (1995).

[**Kadlec04**] S. KADLEC, private communication (2004).

[**Karolewski03**] M.A. KAROLEWSKI, "Collision cascade containment in classical dynamics simulations of sputtering", Nucl. Instr. and Meth. in Phys. Res. B 211, 43 (2003).

[**Karolewski05**] M.A. KAROLEWSKI, "Kalypso: a software package for molecular dynamics simulation of atomic collisions at surfaces", Nucl. Instr. and Meth. in Phys. Res. B 230, 402 (2005). See also: http://www.geocities.com/karolewski/kalypso.htm.

[**Kashiwagi99**] M. KASHIWAGI and S. IDO, "Computational analyses of a magnetron sputtering system with a ferromagnetic target", Vacuum 53, 33 (1999).

[**Keidar01**] M. KEIDAR et al., "Plasma flow and plasma-wall transition in Hall thruster channel", Phys. Plasmas, 8 (12), 5315 (2001).

[**Kelly87**] R. KELLY, "The surface binding energy in slow collisional sputtering", Nucl. Instr. and Meth. B18, 388 (1987).

[**Kelly98**] P.J. KELLY and R.D. ARNELL, "The determination of the current-voltage characteritics of a closed-field unbalanced magnetron sputtering system", Surf. Coat. Technol. 98, 1370 (1998).

[**Kelly00**] P.J. KELLY and R.D. ARNELL, "Magnetron sputtering: a review of recent developments and applications", Vacuum 56, 159 (2000).

[**Kim95**] G.-H. KIM, "Magnetic and collisional effects on presheaths", Phys. Plasmas 2 (8), 3222 (1995).

[**Kishinevsky73**] L.M. KISHINEVSKY, Rad. Eff. 19, 23 (1973).

[**Kisker85**] E. KISKER et al., "Test of the electronic structure of Fe(100) by absorbed current spectroscopy", J. Appl. Phys. 57 (1), 3021 (1985).

[**Kolev04a**] I. KOLEV and A. BOGAERTS, "Numerical models of the planar magnetron glow discharges", Contrib. Plasma Phys. 44 (7-8), 582 (2004).

[**Kolev04b**] I. KOLEV, "Detailed numerical investigation of a dc planar magnetron via PIC/MCC method" oral presentation at "Reactive Sputter Processes and Related Phenomena III", Ghent (2004).

[**Kolev05**] I. KOLEV et al., "Influence of electron recapture by the cathode upon the discharge characteristics in DC planar magnetrons" Phys. Rev. E, submitted (2005).

[**Komath99**] M. KOMATH et al., "Studies on the optimisation of unbalanced magnetron sputtering cathodes", Vacuum 52, 307 (1999).

[**Kondo99a**] S. KONDO and K. NANBU, "A self-consistent numerical analysis of a planar dc magnetron discharge by the particle-in-cell/Monte Carlo method", J. Phys. D: Appl. Phys. 32, 1142 (1999).

[**Kondo99b**] S. KONDO and K. NANBU, "Chaotic dynamics of three-dimensional dc magnetron discharge", IEEE Trans. Plasma Sci. 27 (1), 92 (1999).

[**Kondo01**] S. KONDO and K. NANBU, "Axisymmetrical pparticle-in-cell/Monte Carlo simulation of narrow gap planar magnetron plasmas. I. Direct current-driven discharge", J. Vac. Sci. Technol. A 19 (3), 830 (2001).

[**Kono04**] A. KONO, "Structure of collisional and collisionless sheaths: closed expressions for sheath thickness", J. Phys. D: Appl. Phys. 37, 1945 (2004).

[**Kools04a**] J. KOOLS, "Modeling of sputtering equipment, process and film growth as an engineering tool: building a virtual sputter tool", 47th SVC Annual Techn. Conf. Proc., 31 (2004).

[**Kools04b**] J. KOOLS, "Modeling of sputtering equipment, process and film growth as an engineering tool: building a virtual sputter tool", oral presentation at 47th SVC Annual Techn. Conf. (2004).

[**Kubart04**] T. KUBART et al., "Modelling of magnetron sputtering process", Czech. J. Phys. 54 (Suppl. C), C1027 (2004).

[**Kudrna02**] P. KUDRNA et al., "PIC-MCC modeling of the DC discharge in cylindrical magnetron", Czech. J. Phys. 52 Suppl D, 666 (2002).

[**Kumar02**] T.A.S. KUMAR et al., "Plasma diffusion across inhomogeneous magnetic fields", Phys. Plasmas 9 (7), 2946 (2002).

[**Kumar04**] T.A.S. KUMAR et al., "Trapped electron effects in a magnetic filter field of the plasma source", Phys. Plasmas 11 (4), 1735 (2004).

[**Kushner05**] M.J. KUSHNER et al., homepage of the *Computational Optical and Discharge Physics Group*: http://uigelz.ece.iastate.edu/.

[**Kusumoto04**] Y. KUSUMOTO and K. IWATA, "Numerical study of the characteristics of erosion in magnetron sputtering", Vacuum 74, 359 (2004).

[**Kuwahara94**] K. KUWAHARA and H. FUJIYAMA, "Application of the Child-Langmuir law to magnetron discharge plasmas", IEEE Trans. Plasma Sci. 22 (4), 442 (1994).

[**Kuwahara98**] K. KUWAHARA and H. FUJIYAMA, "Relation between cathode-fall and ion-sheath thicknesses in multi-electrode-type magnetron discharges", Surf. Coat. Technol. 98, 1347 (1998).

[**Kuwata03**] K.T. KUWATA et al., "A comparative study of interatomic potentials for copper and aluminium gas phase sputter atom transport", Nucl. Instr. and Meth. in Phys. Res. B 201, 566 (2003).

[**Kwon05**] U.H. KWON et al., "Multi-scale simulation of plasma generation and film deposition in a circular typed DC magnetron sputtering system", Thin Solid Films 475, 17 (2005).

[**Lakits90**] G. LAKITS et al., "Threshold of ion-induced kinetic electron emission from a clean metal surface", Phys. Rev. A 42 (9), 5780 (1990).

[**LanGu88**] LAN GU and M.A. LIEBERMAN, "Axial distribution of optical emission in a planar magnetron discharge", J. Vac. Sci. Technol. A 6 (5), 2960 (1988).

[**Lee65**] R.N. LEE and H.E. FARNSWORTH, "LEED studies of adsorption on clean (100) copper surfaces", Surf. Sci. 3, 461 (1965).

[**Leroy04**] O. LEROY et al., "Determination of titanium temperature and density in a magnetron vapor sputtering device assisted by two microwave coaxial systems", J. Vac. Sci. Technol. A 22 (1), 192 (2004).

[**Lewis89**] M.A. LEWIS et al., "Measurements of secondary electron emission in reactive sputtering of aluminium and titanium nitride", J. Vac. Sci. Technol. A 7 (3), 1019 (1989).

[**Li95**] J. LI et al., "Simulation of ionization in a magnetron-like glow discharge", J. Phys. D: Appl. Phys. 28, 1121 (1995).

[**Lieberman94**] M.A. LIEBERMAN and A.J. LICHTENBERG "Principles of Plasma Discharges and Materials Processing", New York: John Wiley & Sons (1994).

[**Lister96**] G. LISTER, "Influence of electron diffusion on the cathode sheath of a magnetron discharge", J. Vac. Sci. Technol. A 14 (5), 2736 (1996).

[**Lopp02**] A. LOPP et al., "Plasma Simulation for Planar Sputtering Cathodes", 45th SVC Annual Techn. Conf. Proc., 170 (2002).

[**Luginsland02**] J.W. LUGINSLAND et al., "Beyond the Child-Langmuir law: a review of recent results on multidimensional space-charge-limited flow", Phys. Plasmas 9 (5), 2371 (2002).

[**Macàk99**] K. MACÀK et al., "Monte Carlo simulations of the transport of sputtered particles", Comp. Phys. Comm. 120, 238 (1999).

[**Mahan97**] J.E. MAHAN and A. VANTOMME, "A simplified collisional model of sputtering in the linear cascade regime", J. Vac. Sci. Technol. A 15 (4), 1976 (1997).

[**Mahieu04**] S. MAHIEU et al., "A model for the development of biaxial alignment in yttria stabilized zirconia layers, deposited by unbalanced magnetron sputtering", Surf. Coat. Technol. 187, 122 (2004).

[**Mahieu05**] S. MAHIEU et al., "Monte Carlo simulation of the transport of atoms in DC magnetron sputtering", Nucl. Instr. and Meth. in Phys. Res. B, accepted for publication (2005).

[**Maniv80**] S. MANIV and W.D. WESTWOOD, "Discharge characteristics for magnetron sputtering of Al in Ar and Ar/O_2 mixtures", J. Vac. Sci. Technol. A 17 (3), 743 (1980).

[**Maniv82**] S. MANIV et al., "Calculation of the current-voltage-pressure characteristics of dc diode sputtering discharges", J. Appl. Phys. 53 (2), 856 (1982).

[**Manley93**] B. MANLEY, "Improved planar magnetron sputtering magnet assembly", patent WO9324674 (1993).

[**Martines01**] E. MARTINES et al., "Electrostatic fluctuations in a direct current magnetron sputtering plasma", Phys. Plasmas 8 (6), 3042 (2001).

[**Matsunami84**] N. MATSUNAMI et al., "Energy dependence of the ion-induced sputtering yields of monoatomic solids", Atomic Data and Nuclear Data Tables 31 (1), 1 (1984).

[**McRae76a**] E.G. MCRAE and C.W. CALDWELL, "Very low energy electron reflection at Cu(001) surfaces", Surf. Sci. 57, 77 (1976).

[**McRae76b**] E.G. MCRAE and C.W. CALDWELL, "Absorptive potential in nickel from very low energy electron reflection at Ni(001) surface", Surf. Sci. 57, 766 (1976).

[**Miranda90**] J.E. MIRANDA et al., "Monte Carlo simulation of ionization in a magnetron plasma", J. Vac. Sci. Technol. A 8 (3), 1627 (1990).

[**Miura00**] T. MIURA, "Theory on high-vacuum planar magnetron discharge incorporating the effect of escaping electrons", Jpn. J. Appl. Phys. 39 Part 1, 4890 (2000).

[**Miyagawa03**] Y. MIYAGAWA et al., "Computer simulation of plasma for plasma immersed ion implantation and deposition with bipolar pulses", Nucl. Instr. and Meth. in Phys. Res. B 206, 767 (2003).

[**Miyagawa05**] Y. MIYAGAWA et al., "Particle-in-cell/Monte Carlo simulation of plasma for inner coating of a pipe", Surf. Coat. Technol. 196, 155 (2005).

[**Miyake92**] S. MIYAKE et al., "Diagnostics of direct-current-magnetron discharges by the emission-selected computer-tomography technique", J. Vac. Sci. Technol. A 10 (4), 1135 (1992).

[**Möller88**] W. MÖLLER et al., "TRIDYN – Binary Collision Simulation of Atomic-Collisions and Dynamic Composition Changes in Solids", Comp. Phys. Comm. 51, 355 (1988).

[**Möller02**] W. MÖLLER and M. POSSELT, TRIDYN User Manual, 2002.

[**Muralidhar95**] G.K. MURALIDHAR et al., "An unbalanced magnetron sputtering device for low and medium pressures", Rev. Sci. Instrum. 66 (10), 4961 (1995).

[**Musil95**] J. MUSIL, K. RUSŇÁK, V. JEŽEK and J. VLČEK, "Planar magnetron with additional plasma confinement", Vacuum 46 (4), 341 (1995).

[**Musil98**] J. MUSIL, "Low-pressure magnetron sputtering", Vacuum 50 (3-4), 363 (1998).

[**Musil99**] J. MUSIL, "Rectangular magnetron with full target erosion", J. Vac. Sci. Technol. A 17 (2), 555 (1999).

[**Musil01**] J. MUSIL et al., "Magnetron with gas injection through hollow cathodes machined in sputtered target", Surf. Coat. Technol. 148, 296 (2001).

[**Myers92**] A.M. MYERS et al., "Monte Carlo simulations of sputter atom transport in low-pressure sputtering: the effects of interaction potential, sputter distribution, and system geometry", J. Appl. Phys. 72 (7), 3064 (1992).

[**Nahar87**] S.N. NAHAR and J.M. WADEHRA, "Elastic scattering of positrons and electrons by argon", Phys. Rev. A 35 (5), 2051 (1987).

[**Nakano99**] T. NAKANO and S. BABA, "A hybrid simulation of high pressure sputtering, combining the Monte Carlo method and the diffusive approach", Thin Solid Films 343-344, 24 (1999).

[**Nanbu96**] K. NANBU et al., "Self-consistent particle simulation of three-dimensional dc magnetron discharge", Vacuum 47 (6-8), 1013 (1996).

[**Nanbu97**] K. NANBU and S. KONDO, "Analysis of Three-Dimensional DC Magnetron Discharge by the Particle-in-Cell/Monte Carlo Method", Jpn. J. Appl. Phys. 36 Part 1, 4808 (1997).

[**Nanbu05**] K. NANBU et al., homepage of *Gaseous Electronics Laboratory*: http://www.ifs.tohoku.ac.jp/plasma/.

[**Nishimura96**] K. NISHIMURA et al., "Contribution of kinetic and potential emission to keV singly charged ion-induced electron emission from a metal surface", Jpn. J. Appl. Phys. 35 Part 1, 2284 (1996).

[**Nyaiesh81**] A.R. NYAIESH, "The characteristics of a planar magnetron operated at high power input", Thin Solid Films 86, 267 (1981).

[**Oechsner78**] H. OECHSNER, "Electron yields from clean polycristalline metal surfaces by noble-gas-ion bombardment at energies around 1keV", Phys. Rev. B 17 (3), 1052 (1978).

[**Okhrimovskyy02**] A. OKHRIMOVSKYY et al., "Electron anisotropic scattering in gases: a formula for Monte Carlo simulations", Phys. Rev. E 65, 037402 (2002).

[**Pal04**] A.P. PAL et al., "Observation of instability in presence of ExB flow in a direct current cylindrical magnetron discharge plasma", Phys. Plasmas 11 (10), 4719 (2004).

[**Pekker95**] L. PEKKER, "Longitudinal distribution of plasma density in the low-pressure glow discharge with transverse magnetic field", Plasma Sources Sci. Technol. 4, 31 (1995).

[**Penfold95**] A.S. PENFOLD "Magnetron sputtering" in "Handbook of Thin Film Processing" (eds. D.A. Glocker and S.I. Shah), Bristol: IOP Publishing Ltd (1995).

[**Petrov93**] I. PETROV et al., "Comparison of magnetron sputter deposition conditions in neon, argon, krypton, and xenon discharges", J. Vac. Sci. Technol. A 11 (5), 2733 (1993).

[**Petrov03**] I. PETROV et al., "Microstructural evolution during film growth", J. Vac. Sci. Technol. A 21 (5), S117 (2003).

[**Pflug02**] A. PFLUG et al., "Simulation of reactive magnetron sputtering kinetics in real in-line processing chambers", 45th SVC Annual Technical Conf. Proc., 241 (2002).

[**Pflug03**] A. PFLUG et al., "Process simulation for advanced large area optical coatings", 46th SVC Annual Technical Conf. Proc., 241 (2003).

[**Phelps94**] A.V. PHELPS, "The application of scattering cross sections to ion flux models in discharge sheaths", J. Appl. Phys. 76 (2), 747 (1994).

[**Phelps99**] A.V. PHELPS and Z.Lj. PETROVIĆ, "Cold-cathode discharges and breakdown in argon: surface and gas phase production of secondary electrons", Plasma Sources Sci. Technol. 8, R21 (1999).

[**Porokhova01**] I. A. POROKHOVA et al., "Kinetic simulation model of magnetron discharges", Phys. Rev. E, 63, article 056408, (2001).

[**Porokhova03**] I.A. POROKHOVA et al., "Two-dimensional nonlocal model of axially and radially inhomogeneous plasma of cylindrical magnetron discharge", Phys. Rev. E 68, 016401 (2003).

[**Porokhova05a**] I.A. POROKHOVA et al., "Modeling and diagnostic of the plasma of magnetic field supported discharges", Contrib. Plasma Phys. 45 (5-6), 319 (2005).

[**Porokhova05b**] I. POROKHOVA, private communication.

[**Posadowski93**] W.M. POSADOWSKI and Z.J. RADZIMSKI, "Sustained self-sputtering using a direct current magnetron source", J. Vac. Sci. Technol. A 11 (6), 2980 (1983).

[**Posadowski01**] W.M. POSADOWSKI, "Plasma parameters of very high target power density magnetron sputtering", Thin Solid Films 392, 201 (2001).

[**Posadowski04**] W.M. POSADOWSKI, "Self-sustained magnetron co-sputtering of Cu and Ni", Thin Solid Films 459, 258 (2004).

[**Post04**] D.E. POST et al., "Report of the Fusion Simulation Project Steering Committee ", found on http://fusion.gat.com/comp/daag/seminar_attach/FSPFinalReport.pdf or in J. Fusion Energy 23 (1), 1 (2004).

[**Rabiński98**] M. RABIŃSKI, "Fluid model of plasma in magnetron sputter device", ICPP & 25th EPS Conf. on Contr. Fusion and Plasma Physics, ECA Vol. 22C, 2165 (1998).

[**Redhead58**] P.A. REDHEAD, "The Townsend discharge in a coaxial diode with axial magnetic field", Can. J. Phys. 36, 255 (1958).

[**Reimer85**] L. REIMER, "Scanning Electron Microscopy", Heidelberg: Springer Verlag (1985).

[**Ross03**] P.E. ROSS, "5 Commandments", IEEE Spectrum 40 (12), 30 (2003).

[**Rossnagel86**] S.M. ROSSNAGEL and H.R. KAUFMAN, "Langmuir probe characterization of magnetron operation", J. Vac. Sci. Technol. A 4 (3), 1822 (1986).

[**Rossnagel87a**] S.M. ROSSNAGEL and H.R. KAUFMAN, "Induced drift currents in circular planar magnetrons", J. Vac. Sci. Technol. A 5 (1), 88 (1987).

[**Rossnagel87b**] S.M. ROSSNAGEL and H.R. KAUFMAN, "Charge transport in magnetrons", J. Vac. Sci. Technol. A 5 (4), 2276 (1987).

[**Rossnagel88a**] S.M. ROSSNAGEL, "Gas density reduction effects in magnetrons", J. Vac. Sci. Technol. A 6 (1), 19 (1988).

[**Rossnagel88b**] S.M. ROSSNAGEL and H.R. KAUFMAN, "Current-voltage relations in magnetrons", J. Vac. Sci. Technol. A 6 (2), 223 (1988).

[**Rossnagel89**] S.M. ROSSNAGEL and K.L. SAENGER, "Optical emission in magnetrons: nonlinear aspects", J. Vac. Sci. Technol. A 7 (3), 968 (1989).

[**Rossnagel99**] S.M. ROSSNAGEL, "Sputter deposition for semiconductor manufacturing" IBM J. Res. Dev. 43, 163 (1999).

[**Schabes87**] M.E. SCHABES and A. AHARONI, "Magnetostatic Interaction Fields for a Three-Dimensional Array of Ferromagnetic Cubes", IEEE Trans. Magn. MAG-23 (6), 3882 (1987).

[**Schulte97**] J. SCHULTE et al., "A linear model for the interpretation of optical emission spectroscopy measurements in low pressure dc magnetron sputtering", Contrib. Plasma Phys. 37 (6), 483 (1997).

[**Sellers97**] J.C. SELLERS, "The disappearing anode myth: strategies and solutions for reactive PVD from single magnetrons", Surf. Coat. Technol. 94-95, 184 (1997).

[**Seo04a**] S.-H. SEO et al., "Measurements of electron energy distribution functions and electron transport in the downstream region of an unbalanced dc magnetron discharge", Plasma Sources Sci. Technol. 13, 409 (2004).

[**Seo04b**] S.-H. SEO and H.-Y. CHANG, "Anomalous behavior of plasma parameters in unbalanced direct-currnet magnetron discharge", Phys. Plasmas 11 (7), 3595 (2004).

[**Seo04c**] S.-H. SEO and H.-Y. CHANG, "Electron transport in the downstream region of planar unbalanced magnetron discharge", J. Appl. Phys. 96 (3), 1310 (2004).

[**Serianni00**] G. SERIANNI et al., "Plasma characterisation of a dc closed field magnetron sputtering device", 27th EPS Conf on Contr. Fusion and Plasma Phys. Budapest, 17 (2000).

[**Sheridan89a**] T.E. SHERIDAN and J. Goree, "Low-frequency turbulent transport in magnetron plasma", J. Vac. Sci. Technol. A 7 (3), 1014 (1989).

[**Sheridan89b**] T.E. SHERIDAN and J. GOREE, "Analytical expression for the electric potential in the plasma sheath", IEEE Trans. Plasma Sci. 17 (6), 884 (1989).

[**Sheridan90a**] T.E. SHERIDAN et al., "Model of energetic electron transport in magnetron discharges", J. Vac. Sci. Technol. A 8 (1), 30 (1990).

[**Sheridan90b**] T T.E. SHERIDAN et al., "Electron and ion transport in magnetron plasmas", J. Vac. Sci. Technol. A 8 (3), 1623 (1990).

[**Sheridan90c**] T.E. SHERIDAN et al., "Pressure dependence of ionization efficiency in sputtering magnetrons", Appl. Phys. Lett. 57 (20), 2080 (1990).

[**Sheridan91a**] T.E. SHERIDAN et al., "Observation of two-temperature electrons in a sputtering magnetron plasma", J. Vac. Sci. Technol. A 9 (3), 688 (1991).

[**Sheridan91b**] T.E. SHERIDAN et J. GOREE, "Collisional plasma sheath model", Phys. Fluids B 3 (10), 2796 (1991).

[**Sheridan94**] T.E. SHERIDAN et al., "Langmuir-probe characteristic in the presence of drifting electrons", Phys. Rev. E 50 (4), 2991 (1994).

[**Sheridan95**] T.E. SHERIDAN et al., "Electron distribution functions in a sputtering magnetron discharge", Jpn. J. Appl. Phys. 34 Part 1, 4977 (1995).

[**Sheridan98**] T.E. SHERIDAN et al., "Electron velocity distributions in a sputtering magnetron discharge for the ExB direction", J. Vac. Sci. Technol. A 16 (4), 2173 (1998).

[**Shidoji94**] E. SHIDOJI et al., "Three-dimensional simulation of target erosion in dc magnetron sputtering", Jpn. J. Appl. Phys. 33 Part 1, 4281 (1994).

[**Shidoji99a**] E. SHIDOJI et al., "Two-dimensional self-consistent simulation of a DC magnetron discharge", Jpn. J. Appl. Phys. 38 Part 1, 2131 (1999).

[**Shidoji99b**] E. SHIDOJI et al., "Numerical simulation of the discharge in d.c. magnetron sputtering", Thin Solid Films 351, 37 (1999).

[**Shidoji00**] E. SHIDOJI et al., "An anomalous erosion of a rectangular magnetron system", J. Vac. Sci. Technol. A 18 (6), 2858 (2000).

[**Shidoji01a**] E. SHIDOJI et al., "Influence of gas pressure and magnetic field upon dc magnetron discharge", Vacuum 60, 299 (2001).

[**Shidoji01b**] E. SHIDOJI et al., "A comparative study of an unbalanced magnetron with dielectric substrate with a conventional magnetron through the use of hybrid modelling", Plasma Sources Sci. Technol. 8, 621 (2001).

[**Shidoji03**] E. SHIDOJI and T. MAKABE, "Magnetron plasma structure with strong magnetic field", Thin Solid Films 442 (1-2), 27 (2003).

[**Shidoji04**] E. SHIDOJI, "Plasma simulation of magnetron sputtering" oral presentation at "Reactive Sputter Processes and Related Phenomena III", Ghent (2004).

[**Shon98**] C.H. SHON et al., "Velocity distributions in magnetron sputter", IEEE Trans. Plasma Sci. 26 (6), 1635 (1998).

[**Shon99**] C.H. SHON et al., "Kinetic and steady-state properties of magnetron sputter with three-dimensional magnetic field", Jpn. J. Appl. Phys. 38 Part 1, 4440 (1999).

[**Shon02**] C.H. SHON and J.K. LEE, "Modeling of magnetron sputtering plasmas", Appl. Surf. Sci. 192, 258 (2002).

[**Sieck94**] P. SIECK, "Effect of anode location on deposition profiles for long rotatable magnetrons", 37th SVC Annual Technical Conf. Proc., 233 (1994).

[**Sigmund69**] P. SIGMUND, "Theory of sputtering. I. Sputtering yield of amorphous and polycrystalline targets", Phys. Rev. 184 (2), 383 (1969).

[**Singha02**] B. SINGHA et al., "Experimental observation of sheath and magnetic presheath over an oblique metallic plate in the presence of a magnetic field", Phys. Plasmas 9 (2), 683 (2002).

[**Smirnov04**] A. SMIRNOV et al., "Electron cross-field transport in a low power cylindrical Hall thruster", Phys. Plasmas 11 (11), 4922 (2004).

[**Smith94**] P.C. SMITH et al., "Low-energy ion-induced electron emission from gas-covered surfaces", J. Vac. Sci. Technol. A 12 (5), 2692 (1994).

[**Smy97**] T. SMY et al., "Simulation of sputter deposition at high pressures", J. Vac. Sci. Technol. A 15 (6), 2847 (1997).

[**Špatenka97**] P. ŠPATENKA et al., "A comparison of internal plasma parameters in a conventional planar magnetron and a magnetron with additional plasma confinement", Plasma Sources Sci. Technol. 6, 46 (1997).

[**Spolaore99**] M. SPOLAORE et al., "Automatic Langmuir probe measurement in a magnetron sputtering system", Surf. Coat. Technol. 116-119, 1083 (1999).

[**Sproul03**] W.D. SPROUL et al., "Control of the reactive sputtering process using two reactive gases", 46th Annual Technical Conf. Proc., 98 (2003).

[**Sproul05**] W.D. SPROUL et al., "Control of reactive sputtering processes", Thin Solid Films, 491; 1 (2005).

[**Srivastava81**] S.K. SRIVASTAVA et al., "Elastic scattering of intermediate-energy electrons by Ar and Kr", Phys. Rev. A 23 (5), 2156 (1981).

[**Stepanova01**] M. STEPANOVA and S.K. DEW, "Estimates of differential sputtering yields for deposition applications", J. Vac. Sci. Technol. A 19 (6), 2805 (2001).

[**Surendra90**] M. SURENDRA et al., "Self-consistent model of a direct-current glow discharge", Phys. Rev. A 41 (2), 1112 (1990).

[**Tamura85**] E. TAMURA et al., "Energy-dependence of inner potential in Fe from low-energy electron absorption (target current)", Solid State Comm. 55 (6), 543 (1985).

[**Tao96**] W.H. TAO et al., "Spatial distributions of electron density and electron temperature in direct current glow discharge", J. Vac. Sci. Technol. A 14 (4), 2113 (1996).

[**Thornton78a**] J.A. THORNTON, "Magnetron sputtering : basic physics and application to cylindrical magnetrons", J. Vac. Sci. Technol. 15 (2), 171 (1978).

[**Thornton78b**] J.A. THORNTON and A.S. PENFOLD, "Cylindrical Magnetron Sputtering" in "Thin Film Processes" (eds. J.L. Vossen and W. Kern), New York: Academic Press (1978).

[**Töglhofer93**] K. TÖGLHOFER et al., "Ion-induced electron emission from metal surfaces – insights from the emission statistics", Surf. Sci. 281, 143 (1993).

[**VanderStraaten98a**] T.A. VAN DER STRAATEN et al., "The cylindrical DC magnetron discharge: I. Particle-in-cell simulation", J. Phys. D: Appl. Phys. 31, 177 (1998).

[**VanderStraaten98b**] T.A. VAN DER STRAATEN et al., "The cylindrical DC magnetron discharge: II. The negative space charge mode", J. Phys. D: Appl. Phys. 31, 191 (1998).

[**VanderStraaten00**] T.A. VAN DER STRAATEN and N.F. CRAMER, "Transverse electric field and density gradient induced instabilities in a cylindrical magnetron discharge", Phys. Plasmas 7 (1), 391 (2000).

[**Verboncoeur95**] J.P. VERBONCOEUR et al., "An object-oriented electromagnetic PIC code", Comp. Phys. Comm. 87, 199 (1995).

[**Waits78**] R.K. WAITS, "Planar Magnetron Sputtering" in "Thin Film Processes" (eds. J.L. Vossen and W. Kern), New York: Academic Press (1978).

[**Wang99**] Z. WANG and S.A. COHEN, "Hollow cathode magnetron", J. Vac. Sci. Technol. A 17 (1), 77 (1999).

[**Wendt88a**] A.E. WENDT et al., "Radial current distribution at a planar magnetron cathode", J. Vac. Sci. Technol. A 6 (3), 1827 (1988).

[**Wendt88b**] A.E. WENDT, "Dynamics of a Planar Magnetron Discharge", PhD-thesis University of California at Berkeley (1988).

[**Wendt90**] A. E. WENDT and M.A. LIEBERMAN, "Spatial structure of a planar magnetron discharge", J. Vac. Sci. Technol. A 8 (2), 902 (1990).

[**Westwood83**] W.D. WESTWOOD et al., "The current-voltage characteristic of magnetron sputtering systems", J. Appl. Phys. 54 (12), 6841 (1983).

[**Westwood03**] W. WESTWOOD, "Sputter Deposition", AVS Education Committee Book Series Vol. 2, New York : AVS (2003).

[**Wikipedia05**] http://en.wikipedia.org/wiki/Random_walk

[**Window86**] B. WINDOW and N. SAVVIDES, "Charged particle fluxes from planar magnetron sputtering sources", J. Vac. Sci. Technol. A 4 (2), 196 (1986).

[**Yamauchi83**] Y. YAMAUCHI and R. SHIMIZU, "Secondary electron emission from Aluminium and Oxygen ion bombardment below 3keV", Jpn. J. Appl. Phys. 22 Part 1, L227 (1983).

[**Yamamura83**] Y. YAMAMURA et al., "Theoretical studies on an empirical formula for sputtering yield at normal incidence", Rad. Eff. 71, 65 (1983).

[**Yamamura95**] Y. YAMAMURA and M. ISHIDA, "Monte Carlo simulation of the thermalization of sputtered and reflected atoms in the magnetron sputtering discharge", J. Vac. Sci. Technol. A 13 (1), 101 (1995).

[**Yamazaki02**] O. YAMAZAKI et al., "Modeling of Cu transport in sputtering using a Monte Carlo Simulation", Jpn. J. Appl. Phys. 41 Part 1, 1230 (2002).

[**Yanguas-Gil05**] A. YANGUAS-GIL et al., "An update of argon inelastic cross sections for plasma discharges", J. Phys. D: Appl. Phys. 38, 1588 (2005).

[**Yeom89**] G.Y. YEOM et al., "Cylindrical magnetron discharges. I. Current-voltage characteristics for dc- and rf-driven discharge sources", J. Appl. Phys., 65 (10), 3816 (1989).

[**Ziegler04**] J.F. ZIEGLER, "SRIM-2003", Nucl. Instr. and Meth. in Phys. Res. B 219-220, 1027 (2004).

[**Zollweg64**] R.J. ZOLLWEG, "Electron reflection from tungsten crystals, clean and with adsorbed Cs and CO", Surf. Sci. 2, 409 (1964).

Faculteit Wetenschappen
Vakgroep Vaste-stofwetenschappen
Krijgslaan 281 S1
9000 Gent